ABSTRACT

Title of dissertation: SELF–CONTAINED HYBRID ELECTRO-HYDRAULIC ACTUATORS USING MAGNETOSTRICTIVE AND ELECTROSTRICTIVE MATERIALS

Anirban Chaudhuri, Doctor of Philosophy, 2008

Dissertation directed by: Professor Norman M. Wereley
Department of Aerospace Engineering

Hybrid electro-hydraulic actuators using smart materials along with flow rectification have been widely reported in recent years. The basic operation of these actuators involves high frequency bidirectional operation of an active material that is converted into unidirectional fluid motion by a set of valves. While theoretically attractive, practical constraints limit the efficacy of the solid-fluid hybrid actuation approach. In particular, inertial loads, fluid viscosity and compressibility combine with loss mechanisms inherent in the active material to limit the effective bandwidth of the driving actuator and the total output power. A hybrid actuator was developed by using magnetostrictive TerFeNOL-D as the active driving element and hydraulic oil as the working fluid. Tests, both with and without an external load, were carried out to measure the unidirectional performance of the actuator at different pumping frequencies and operating conditions. The maximum no-load output velocity was 84 mm/s with a 51 mm long rod and 88 mm/s with a 102 mm long rod, both noted around 325 Hz pumping frequency, while the blocked force was close to 89 N. Dynamic

tests were performed to analyze the axial vibration characteristics of the Terfenol-D rods and frequency responses of the magnetic circuits. A second prototype actuator employing the same actuation principle was then designed by using the electrostrictive material PMN-32%PT as the driving element. Tests were conducted to measure the actuator performance for varying electrical input conditions and fluid bias pressures. The peak output velocity obtained was 330 mm/s while the blocked force was 63 N. The maximum volume flow rate obtained with the PMN-based actuator was more than double that obtained from the Terfenol-D–based actuator.

Theoretical modeling of the dynamics of the coupled structural-hydraulic system is extremely complex and several models have been proposed earlier. At high pumping frequencies, the fluid inertia dominates the viscous effects and the problem becomes unsteady in nature. Due to high pressures inside the actuator and the presence of entrained air, compressibility of the hydraulic fluid is important. A new mathematical model of the hydraulic hybrid actuator was formulated in time-domain to show the basic operational principle under varying operating conditions and to capture the phenomena affecting system performance. Linear induced strain behavior was assumed to model the active material. Governing equations for the moving parts were obtained from force equilibrium considerations, while the coupled inertia-compliance of the fluid passages was represented by a lumped parameter approach to the transmission line model, giving rise to strongly coupled ordinary differential equations. Compressibility of the working fluid was incorporated by using the bulk modulus. The model was then validated using the measured performance of both the magnetostrictive and electrostrictive-based hybrid actuators.

Self-Contained Hybrid Electro-Hydraulic Actuators using Magnetostrictive and Electrostrictive Materials

by

Anirban Chaudhuri

Dissertation submitted to the Faculty of the Graduate School of the
University of Maryland, College Park in partial fulfillment
of the requirements for the degree of
Doctor of Philosophy
2008

Advisory Committee:
Dr. Norman M. Wereley, Chair/Advisor
Dr. Alison Flatau
Dr. Christopher Cadou
Dr. Robert M. Sanner
Dr. Balakumar Balachandran

DEDICATION

To my parents

and

all my teachers.

"It is difficult to say what is impossible, for the dream of yesterday is the hope of today and the reality of tomorrow."

- Robert H. Goddard

"The greatest challenge to any thinker is stating the problem in a way that will allow a solution."

- Bertrand Russell

Acknowledgments

I would like to gratefully acknowledge the contributions of my advisor, Dr. Norman Wereley, towards the successful completion of my research. He has been the ideal mentor to me; he encouraged my ideas, gave me enormous freedom to try out different approaches during both the experimental stages and the theoretical work, and was always available to discuss the progress of my research. His caring attitude towards all students is exemplary. I would also like to thank the members of my dissertation committee: Dr. Alison Flatau, Dr. Christopher Cadou, Dr. Robert Sanner and Dr. Balakumar Balachandran. They took keen interest in my work and provided valuable insights into my research, all of which resulted in an organized and complete dissertation.

The work presented in this dissertation would not have been complete without contributions from my colleagues at the University of Maryland. I would like to acknowledge the help from Dr. Jin-Hyeong Yoo, who acquainted me with the actuator designs and worked with me during the first stage of testing. His inputs have been invaluable and I have learnt a lot about practical mechanical design from him. I would also like to thank Dr. Shaju John for introducing me to rheology; he had great faith in the model that I later developed and played an important role in tailoring it for MR-based devices. I would also like to thank Michael Perna of the machine shop for his help in fabrication of the numerous actuator parts. I also appreciate the advice from Dr. Jayant Sirohi regarding the theoretical model.

I made several new friends during my stay at Maryland and their companionship

made sure that graduate student life did not become “all work and no play”. A special word of thanks to all my outstanding officemates - Dr. Wei Hu, Ben Woods, Nick Wilson, Ted Bubert, Robbie Vocke, Dr. Atulasimha Jayasimha, Supratik Datta, Dr. Greg Hiemenz, Grum Gnatu, Amy Ahure, Min Mao, Chaitanya Mudivarthi, Dr. Keejoo Lee and Dr. Young Tai Choi - you have all helped me from time to time and also livened up the lab. The helicopter design experience will never be forgotten - Ben Hein, Nick Rosenfeld, the Eric trio (Parsons, Schroeder and Silberg), Tim Beasman, Anne Brindejonc, Dr. Nagaraj, Dr. Tischenko and Dr. Inderjit Chopra - I learnt a lot from all of you. Shishir Murarka and Ayan Sengupta were my apartment-mates during the bachelor days and they are two of my closest friends today.

I gratefully acknowledge the financial support from the project sponsors: US Army Research Office under a Phase 2 STTR contract (Dr. Gary Anderson, Technical Monitor), the US Army Aviation Applied Technology Directorate under a Phase 1 SBIR Contract (Dr. Louis Centolanza, Technical Monitor) and the Office of Naval Research MURI grant (Jan Lindberg, Technical Monitor). I am also thankful to Dr. Gang Wang and Dr. Peter Chen of Techno-Sciences, Inc., for their help.

My family has provided strong emotional and mental support during all my years as a graduate student. This dissertation is dedicated to my parents who made me a confident person and inspired me to always work with dedication and patience. They instilled a strong sense of independence in me and supported all my career decisions. My younger brother, Apu, maintains an excellent mix of studies and extra-curricular activities and inspired me to do the same. My wife, Sneha, is my endless source of motivation; her love and care have kept me strong and focused all these

years. Although she denies it, she deserves an equal share of the sense of achievement at the completion of the dissertation and I am truly fortunate to have her by my side. We did it !!

Table of Contents

List of Figures

List of Tables

List of Notations

Nomenclature

β	Bulk modulus of fluid
ρ	Density of fluid
c	Damping coefficient
d_A	Piezomagnetic / piezoelectric coefficient of active material
k	Stiffness
m	Mass
r	Reed valve opening
x	Displacement
A	Cross-sectional area
B	Magnetic flux density through magnetostrictive rod
E	Young's modulus
K_L	Minor loss coefficient
L	Length
$\dot{M}$	Mass flow rate through reed port
N	Number of lumps
P	Pressure
Q	Volume flow rate through manifold passages
R	Viscous resistance to fluid flow per unit length and density
V	Volume

Subscripts

acc	Accumulator
ch	Pumping chamber
h	High pressure driving side
l	Low pressure driven side
in	Intake port
out	Exhaust/discharge port
port	Exhaust/intake port from pumping chamber
t	tubing
A	Actuator
D	Metal diaphragn
L	Load
O	Output piston
P	Pumping piston
S	Pre-loading disc spring

Chapter 1

Introduction

The use of solid-state induced-strain actuators based on smart materials has seen a great expansion in recent years, accompanied by extensive research in both actuation and sensing technologies incorporating these novel materials [1–13]. *Smart materials* possess the ability to deliver large blocked forces while their low displacement, high frequency operation makes them extremely attractive in revolutionary concepts for converting electrical input to mechanical output. As a result of this, these *smart* or *active* or *adaptive* materials have been applied to a wide variety of engineering problems [14], including active vibration control [15–18], semi-active vibration and shock isolation [19, 20], precision positioning [21] and control and sensing [22]. While subtle differences may be associated with the individual terms [23], these structures are generally defined as systems whose dynamics can be monitored or modified by distributed sensors and actuators, in accordance with an integrated control law, to accommodate time-varying exogenous inputs or changing environmental conditions. Specific choices for the actuators, sensors and control laws are dictated by the design requirements for the system.

For aeronautic and aerospace systems, control transducers must be lightweight and should typically have minimal effect on the passive system dynamics [24]. Furthermore, actuators must provide the required strain or force outputs using the avail-

able power supplies which, in certain aerospace structures, may require the scavenging of power from other components in the system. Restrictions on size and weight also dictate that transducers in some regimes must be capable of multiple roles. For example, the transducers which monitor and control vibrations in an aircraft fuselage may also be required to act as inputs and sensors for health monitoring or nondestructive evaluation of the structure. The limitations on the mass and size of transducers are often relaxed in industrial applications but output requirements may be more stringent. Hydraulic and pneumatic cylinders offer reliable performance with high force and large displacement capabilities and are the actuator of choice for most aerospace, automotive and robotic applications; however, a major drawback in the use of conventional hydraulic actuators is the need for a separate hydraulic power unit equipped with large electric motors and hydraulic pumps that send the high pressure hydraulic fluid to the actuators through hydraulic lines. A large aircraft can also have a large network of vulnerable hydraulic piping that present a major safety liability, under both civilian and military operation. In ground transportation, similar considerations have spurred automobile designers to promote the *brake-by-wire* concept. In some other applications, the use of conventional actuation is simply not an option. For example, the actuation of an aerodynamic servo-tab at the tip of a rotating blade, such as in helicopter applications, cannot be achieved through conventional hydraulic or electric methods due to the prohibitive high-g centrifugal force field environment generated during blade rotation [4].

Actuators and sensors comprised of smart or active materials can meet many of the design criteria. According to Srinivasan and McFarland [26], a closed-loop *smart*

(a) Smart aircrafts [25]

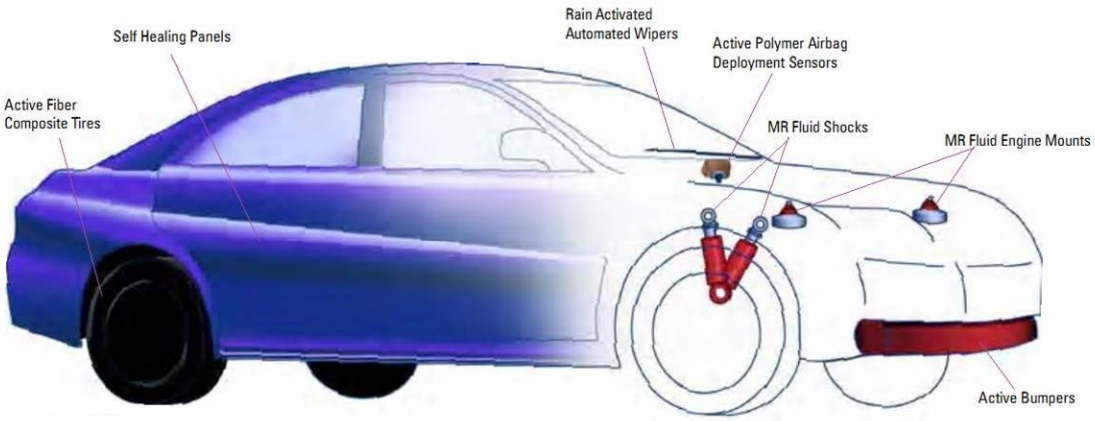

(b) Smart car (*Courtesy: Smart Vehicle Concepts Center, Ohio State University*)

Figure 1.1: Conceptual applications of smart materials in aerospace and ground transportation

structure or component is one which has the ability to sense a physical variable such as temperature, pressure, strain, and so forth, to diagnose the nature and extent of any problem, to initiate an appropriate action to address the problem and "learn" to use the actions taken as a basis next time. Different configurations of the smart materials [27] have been investigated over the years; single layer actuation mechanisms [28, 29], stacked actuators [30–36], cylindrical elements [37,38], and even combinations of these [39, 40]. Standard solid-state ceramic actuators are classified into two groups based on their displacement mechanism [41]: (i) linear type, which exhibit longitudinal or axial displacement, and (ii) bending type, which exhibit bending displacement and reaches the maximum value at the free end of the actuator.

There are many applications for such materials and structures in the man made world. Engineering structures could operate at the very limit of their performance envelopes and to their structural limits without fear of exceeding either. These structures could also give maintenance engineers a full report on performance history, as well as the location of defects, whilst having the ability to counteract unwanted or potentially dangerous conditions such as excessive vibration, and effect self-repair. An aircraft constructed from a *sensual structure* could self-monitor its performance to a level beyond that of current data recording, and provide ground crews with enhanced health and usage monitoring systems (HUMS). This would minimize the overheads associated with current manually conducted HUMS procedures and allow such aircraft to fly for more hours before human intervention is required. Potential applications of such adaptive materials and structures range from the ability to control the aeroelastic form of an aircraft wing [42–44], thus minimising drag and improving operational

efficiency, to vibration control of lightweight structures such as satellites, and power pick-up pantographs on trains. Designing and building aircraft shape changing components is not new; in the past, aircraft have used variable sweep, retractable landing gear, retractable flaps and slats, and variable incidence noses. However, recent work in smart materials and adaptive structures [45–47] has led to a resurgence of interest in more substantial shape changes, particularly changes in wing surface area and controlled airfoil camber [Figure 1.2]. Rotorcrafts are another category of aircraft where adaptive compliant structures technology offers significant promise [48–50]; applying variable geometry technology along both the leading and trailing edge of rotor blades could have great impact on vibration and noise reduction [17, 51, 52]. The concept of smart actuators/sensors distributed over the span of individual rotor blades is particularly attractive to manipulate and sense the mechanical properties and the stress-strain field along the span of the blades [53]. This allows for the use of control algorithms to modify and tune the closed-loop behavior of the blade, along with the additional prospect of monitoring the structural health of the rotor system. Smart materials have also found their way in civil engineering applications [54–57]. The sheer size of most civilian structures of interest presents its own technological challenge in designing a suitable sensing architecture which will both conveniently address the area to be covered and will also provide sufficient sensing points to adequately characterize the structure under test; smart materials like piezoceramics [58] and fiber-optic sensors have been successfully applied to these problems.

Present day hydraulic actuators typically rely on a central supply of high-pressure fluid along with a controllable servovalve distribute this fluid to hydraulic

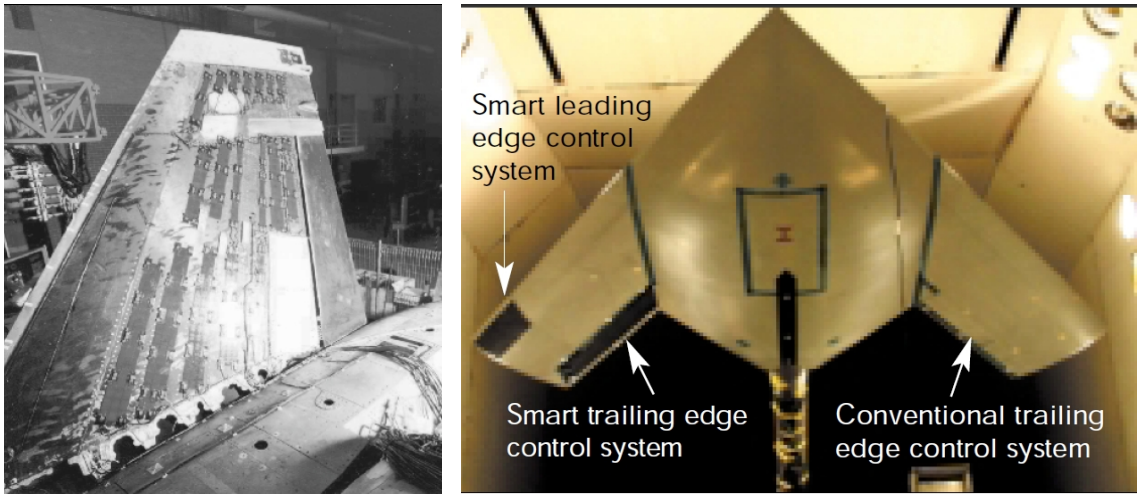

(a) F/A-18 tail with piezo actuators [11]

(b) DARPA Smart Wing model on a UCAV [59]

Figure 1.2: Applications of smart materials in aerospace industry

output devices, where the pressurized fluid does useful mechanical work. While such actuators are effective in numerous applications, such as aircraft and submarines, benefits would accrue from higher efficiency devices and by eliminating the central hydraulic supply. Using inherently energetic smart materials to drive the fluid directly, the complexity of transduction is reduced. Also, by operating in a closed fluid system, central fluid supplies and transfer lines can be eliminated. Applications targeted by this development begin with those currently employing hydraulic and ballscrew actuators as well as those that are not feasible because of limitations in present-day devices. The use of a hydraulic fluid and valve system for frequency rectification is an effective way to overcome the problem of small stroke and develop a moderately high force, large stroke actuator ideal for such applications. Over the last decade, there has been significant research activity in the development of hybrid

hydraulic actuators driven by various smart materials; the Compact Hybrid Actuator Program (CHAP) [60] at DARPA initiated much research and development in the area of developing new types of electromechanical actuators and devices that take advantage of the high energy density of smart material transduction elements. The goal of this technology development was the creation of devices and systems that allow application of mechanical power output through hydraulics without the need for traditional hydraulic distribution lines. The basic operation of these hybrid actuators involves high frequency bidirectional operation of the active material, piezoelectric, magnetostrictive or electrostrictive, which is converted to unidirectional motion of the transmission fluid by a set of valves by flow rectification in each cycle using a set of valves. Through this stepwise actuation process, the high frequency, small stroke of the active material is converted into a lower frequency, larger displacement of the output cylinder. Commercial applications for such a self-contained hybrid actuator range from individual blade control in rotorcrafts [Figure 1.3] to actuation of aerodynamic control surfaces to shock and vibration mitigation equipment.

Some of the compact hybrid actuators developed in recent times are as follows:

(i) One of the first reported hybrid hydraulic actuators was the piezoelectric stack based actuator developed by Konishi *et al.* [61, 62] which had a power output of about 18 W and peak pumping frequency of around 300 Hz and a static bias pressure of 3.0 MPa. The device was constructed using a multiplayer piezoelectric element of 22 mm diameter and 55.5 mm length. The hydraulic circuit was filled with a working liquid and a static pressure was applied to (a) prevent

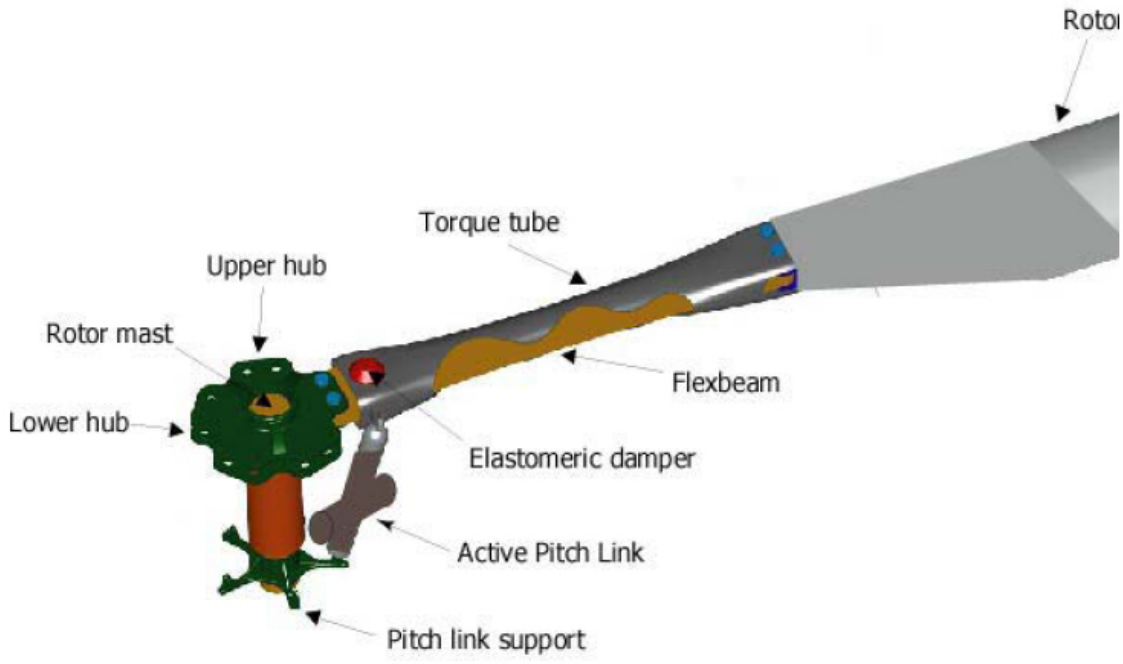

Figure 1.3: Conceptual application of compact hybrid hydraulic actuators as an active pitch link

cavitation in the pump, (b) apply a preset load to the piezoelectric element, and (c) to push the piston rod out of the cylinder. The control valve was operated by the pilot pressure generated by the pump. A simple model based on a single-degree-of-freedom model of the output actuator was used to design an observer and control the output motion.

(ii) Tang *et al.* [63] developed a piezo-hydraulic actuator for active vibration control of rotordynamic systems. The actuator was built to transfer the high force, high frequency capability of the piezoelectric driver to a hydraulic system; the piezoelectric pusher forced the input piston which in turn forced the column of hydraulic fluid into the output piston. PVC-based liquid plastics (LP) were

used in this setup because they have a thick texture that prevents leakage and a high bulk modulus for transmitting even the smallest motions associated with vibration control. From test results, the designers concluded that the output stroke depended on the ratio of the piston areas, compressibility of the LP, tube flexibility and impedance encountered by the output piston.

(iii) A magnetostrictive stack based hybrid pump was developed by Gerver *et al.* [64]; this device employed hydraulic stroke amplification techniques and produced power output of less than 1 W. This design used Terfenol-D as the driving element and employed stroke amplification to obtain high flow rates. The pump achieved a flow rate of 15 ml/s at 5 psi with a power input of 41 W. According to the designers, higher flow rates were obtained by either lowering the pressure (32.5 ml/s at 1.2 psi) or raising the input power (22 ml/s at 5 psi consuming 141 W). To avoid valve inertia at high operating frequencies, thin rigid disks of stainless steel were used. The maximum operational frequency was 150 Hz.

(iv) Mauck and Lynch [65–67] developed a piezoelectric stack based device that produced around 4 W and had a blocked force of 271.7 N (61 lbf); however, it operated at relatively low pumping frequencies (less than 100 Hz) and performed frequency rectification using passive valves. The stack actuator selected was a soft PZT, which maximized output displacement at the cost of a large loss tangent (high hysteresis). This resulted in the generation of significant heat when the operating frequency was increased and verified the belief without the introduction of a cooling system, continuous operation of the stack above 60 Hz

would lead to stack self-heating to the point of failure.

(v) Nasser and Leo [68] developed a piezo based actuator which was capable of 4.5 W output power and operated at slightly higher pumping frequencies around 200 Hz. The major difference between this work and previous research was the use of fluid compressibility to eliminate the need for hydraulic accumulators and four-way control valves. The piezoelectric actuator stack was rated for 100 μm of free displacement and 3000 N of blocked force for a peak-to-peak input voltage of 150 V. A cylinder displacement of 113 μm at a frequency of 10 Hz was measured under these test conditions. Friction was not deemed a limiting factor in the development of the piezohydraulic actuation system. This design was improved upon by the addition of active valves for rectification [69]. Tests were conducted to measure the hydraulic cylinder velocity under no load and with a 12.63 kg load. The timing and phase offset of the active valves was studied; for frequencies lower than 100 Hz, it was concluded that valve timing could change the output velocity by 20–30% when the duty cycle was greater than 50% and the valve offset was positive.

(vi) A compact hybrid hydraulic actuation device that could be driven by piezoelectric, magnetostrictive or electrostrictive stacks was developed by Sirohi and Chopra [70–74] at the University of Maryland [Figure 1.4(a)]. Using piezoelectric stacks, this actuator had an output power of 2.5 W, blocked force of around 138 N (31 lbf) and operated at relatively higher pumping frequencies. The maximum pumping frequency of 1 kHz was dictated by temperature limits of

the piezostacks. Since precise measurement of the blocked force of the device was difficult, the value of blocked force was obtained by fitting a straight line to the force–velocity data and extrapolating it to the zero velocity condition. Two 2-way spool valve were added to the hydraulic circuit for bidirectional operation. A comparison of actuator performance with different smart materials [Figure 1.4(b)] in the same pump body was carried out by John *et al.* [75,76]. In each case, the active material had a length of around 54 mm and cross-sectional area of 25 mm^2. While the maximum power output 2.5 W was obtained for the Terfenol-D and PMN based devices, the latter produced the highest no-load output velocity of 270 mm/s and electromechanical efficiency of 7%.

(vii) Lee and Carman [77] developed a piezoelectric hydraulic pump using active unimorph disc valves for frequency rectification; they reported output flow rate of 3.4 cc/s, specific energy density of 12 W/kg and a stall pressure of 8.3 MPa (1204 psi). According to the authors, the unimorph disc valve concept include a large flow area with low lift and an unidirectional flow from inlet to pumping chamber and to outlet. Application of a voltage to the unimorph disc valves causes the valves (metal disc layer) to deflect away from the seat, opening more rapidly than a conventional check valve and reducing flow resistance. Back flow that normally accompanies passive valve operation could also be suppressed. The outlet valve opened before the piezoelectric stack actuator started its stroke within an optimized duty cycle so that the delivered fluid volume could be maximized. A later version of this piezohydraulic actuator produced power output

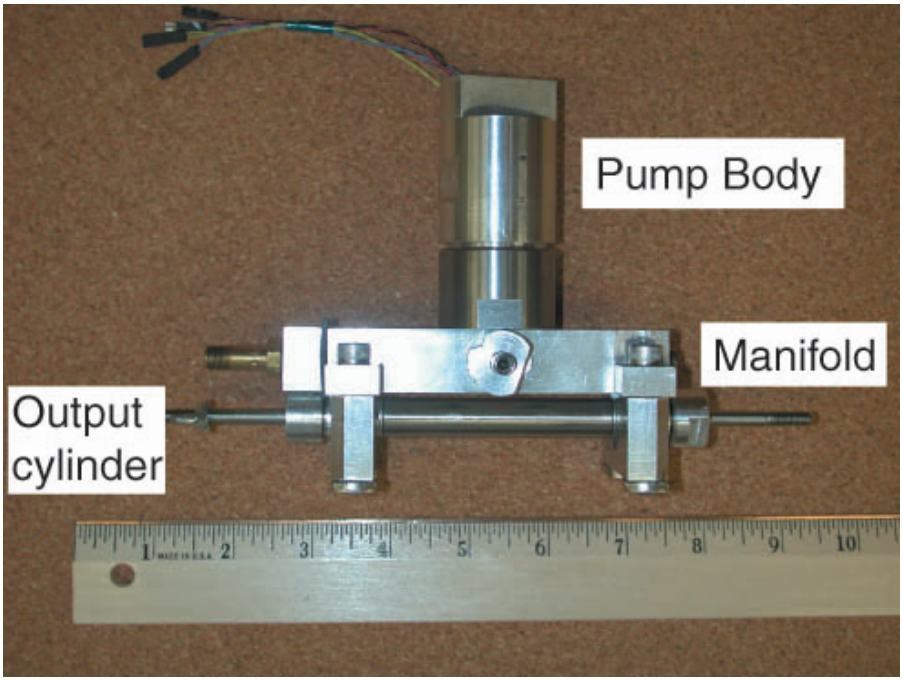

(a) Piezo actuator layout

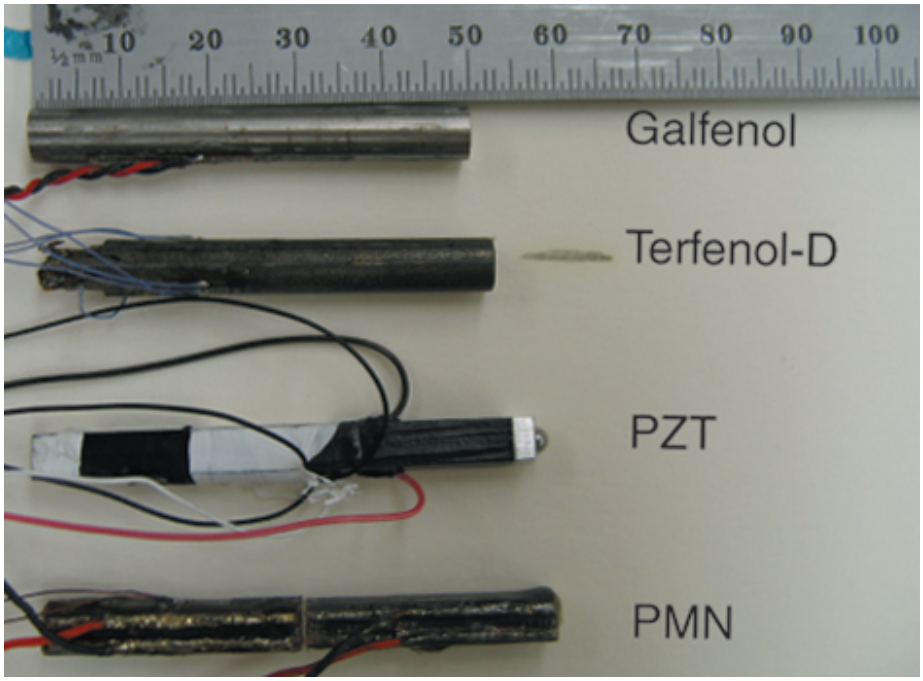

(b) Smart materials used in hybrid pump comparison tests

Figure 1.4: First generation hybrid actuator developed at the University of Maryland, College Park

of 46 W by using proprietary MEMS based valves along with a commercially available piezopump [78]. The MEMS array valve was 1.18 cm in diameter and 0.033 cm thick and held approximately 84 individual valves. The output flow rates were 8.5 cc/s and 17 cc/s at actuation frequencies of 500 Hz and 1 kHz respectively. However, when commercially available check valves were attached to the pump, the maximum flow rate was 0.9 cc/s and the output power was 0.2 W. According to the authors, the reason for this significant drop was the increase of system compliance caused by moving the valves external to the pump housing and air entrapment.

(viii) Ullmann [79] developed a valveless piezoelectric pump that used appropriately shaped and directed nozzles to rectify the flow; this pump was of much smaller scale than the actuators mentioned earlier and had a flow rate of 0.2 cc/s with pressure of around 90 kPa (13 psi). This pump, however, did not have a flow rectification system and worked by transferring fluid from a high pressure source to a low pressure sink at certain frequencies.

(ix) Chapman *et al.* [80] developed three small, low cost piezo-hydraulic pumps to deliver up to 600 psi (4.1 MPa) of blocked pressure and 5.63 cc/s of free flow; the smallest pump weighed less than 90 g. A 4-way spool valve was used for bidirectional control of the output linear actuator. The first set of experiments using check valves produced flow rates up to 1.2 cc/s between 100–120 Hz pumping frequency; it was noted that an increase in bias pressure actually hurt pump performance and was attributed to the increased friction in the hydraulic actuator

seals. A second design incorporating reed valves yielded the best performance at 400 Hz pumping frequency. Though the reed valves (0.010 in and 0.005 in thick) were designed for a natural frequency of 2 kHz in air, it was noticed that their performance dropped sharply for frequencies over 400 Hz and never recovered.

(x) Hybrid actuators driven by piezoelectric [81–83] and magnetostrictive [84–87] materials in conjunction with magnetorheological (MR) fluids for bidirectional control have also been developed in recent times. These designs use the controllable yield stress of MR fluids to effectively open or close the channels that comprise opposite arms of an H-bridge, ultimately leading to directional control of the output shaft. The MR valves used designed in the Smart Structures Laboratory at the University of Maryland, College Park, had an annular gap of 0.5 mm and 25.4 mm outer diameter and were made of high-permeability Hiperco alloy [88]. The maximum output shaft velocity obtainable from the system was around 50 mm/s at a pumping frequency of 125 Hz, which was much lower than the peak velocity and resonant frequency noticed in a piezohydraulic actuator using hydraulic oil. Some of the reasons for the lower performance were (a) leakage through MR valves due to finite yield stress, (b) denser transmission fluid and (c) higher viscous losses.

(xi) There have been hybrid hydraulic actuator developments among commercial establishments too. Active Signal Technologies [89] developed a magnetostrictive water pump operating at 3000 psi (21 MPa) pressure with a no-load flow rate of 57 cc/s (3.5 in^3/s). The Terfenol rod used initially in this test set up was 4

inch (101 mm) long x 1.25 inch (32 mm) diameter, but could not achieve the specifications desired. An inertial-mass (*Tonpilz*) based design was then used to improve performance and increase the operational frequency to ∼2 kHz. Optimum matching for a 1 inch (25.4 mm) diameter x 3.125 inch (79.4 mm) long Terfenol rod was achieved with a 1.25 inch (32 mm) diameter piston and 0.1 inch (2.5 mm) chamber height. Under the Smart Material Actuated Servo Hydraulics (SMASH) program, CSA Engineering [9, 60, 90, 91] reported the development of several hybrid actuators, including a magnetostrictive hydraulic actuator with power output exceeding 100 W [92,93]. The maximum no-load flow rate was 0.4 gpm (25.2 cc/s) and the maximum developed pressure was 1700 psi (11.7 MPa). A 4 inch (102 mm) long, 1 inch (25.4 mm) diameter Terfenol-D rod was used for actuation and the optimal operating frequency was 200 Hz. Reed valves were used for flow rectification; according to the authors, insufficiently stiff reeds can lead to 'valve float' where the valves fail to close completely between cycles allowing back flow through the pump, while excessive stiffness reduces maximum reed displacement causing higher pressure drops. Kinetic Ceramics, Inc. [94] developed piezoelectric fluid pumps with maximum flow rates up to 40 cc/s and a stall pressure of 2500 psi (17.2 MPa). Several patents dealing with hybrid hydraulic actuation utilizing both electroactive and magnetoactive materials have also been published [95–102].

While theoretically attractive, practical limitations arise that limit the efficacy of this hybrid actuation approach. In particular, inertial loads, fluid viscosity and

compressibility combine with loss mechanisms inherent in the active material to limit the effective bandwidth of the driving actuator and the total actuator output power [103, 104]. Also, care must be taken in the design of the system to match the mechanical impedance characteristics of the driving element to the fluid transmission so that maximum efficiency of operation is obtained. Theoretical modeling of the dynamics of the coupled structural-hydraulic system has proved to be extremely complex and several models have been proposed in the literature.

1.1 Smart materials

Due to the increasing demand in smart structures-technology, smart materials have continuously been gaining attention in the past decade, although the physical capabilities of many typical candidate materials have been known for over 50 years [22,105,106]. These materials can be typically used in either sensor or actuator modes. All of these materials are capable of reversibly changing their mechanical properties (viscosity, stiffness, shape) under the influence of an electric field (piezoelectrics and electrostrictives), magnetic field (magnetostrictives, magnetic shape memory alloys, magnetorheological fluids) or thermal field (shape memory alloys). For some of these materials the reverse effect can be used for sensor tasks, meaning that a mechanical load applied to the structure generates an electrical or magnetical field.

Active materials vary widely in their basic mechanism of strain generation as well as their stiffness, strain, hysteresis, and electrical impedance properties. The stiffness and the amount of strain generated by the material are the major factors

that determine its energy output to the actuator. The stiffness of the stack, which is dictated by the Youngs modulus of elasticity of the pure active material and the insulating material as well as the cross-sectional area and length of the stack, determines the amount of energy transferred by the stack to the fluid in the pumping chamber through an impedance matching criteria. The free displacement determines the volumetric displacement produced by the stack under no-load conditions. The input electrical (or magnetic) energy required by the electrostrictive stack (or magnetostrictive rod) depends on the electrical impedance of the stack or the coil and the hysteresis in the active material. Hysteresis constitutes the part of the input energy that is dissipated within the material and is a characteristic of the bulk material. The rest of the energy is available to be transmitted to the load as useful mechanical work. In the case of electro-active stacks, this part of the input energy (non-dissipative part) is determined by the electrical impedance of the stack, which is capacitive in nature. For magnetostrictive rods, the non-dissipative part of the input energy depends on the inductance of the magnetic field generating coil.

This dissertation focuses on compact hybrid actuator design using magnetostrictive and electrostrictive materials, hence these two materials will be examined in depth.

1.1.1 Magnetostrictives

Magnetostrictive materials consist of alloys of iron and rare Earth elements such as terbium and dysprosium, which undergo deformation when exposed to magnetic

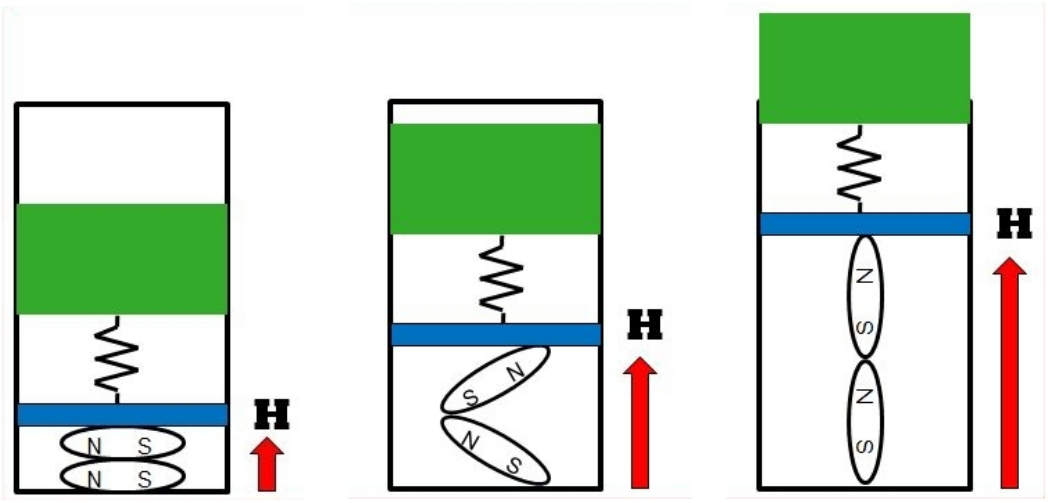

Figure 1.5: Schematic depicting actuation behaviors in magnetostrictive materials as simple rotations of elliptical magnets [107]

field. Without any magnetic field, oblong magnetic domains in the material are randomly oriented (mostly perpendicular to the longitudinal axis). With the application of compressive stress, most of the domains are oriented normal to rods longitudinal axis. In the presence of a magnetic field along the longitudinal axis, these domains rotate and become mostly parallel to this longitudinal axis, causing an induced strain. As the intensity of the magnetic field increases, more magnetic domains rotate, and longitudinal strain increases until saturation is reached (at about 0.2% strain) at high field levels; a schematic of the operation is shown in Figure 1.5. *Magnetostriction* is the change in any dimension of a magnetic material caused by a change in its magnetic state. Since the magnetostrictive forces are molecular in origin, the mechanical response is very fast – a matter of microseconds (∼kHz) [108]. The magnetic field can be produced either by a permanent magnet or by a magnetic coil surrounding the rod. Normally, a permanent magnet is used to create a steady bias field and a time-

varying magnetic field produced by an alternating current in the surrounding coil is superimposed. An extensional strain is induced in the direction of magnetic field. If the field is reversed, the domains reverse direction, but again induce an extensional strain. On the macroscopic level a magnetostrictive material conserves volume, and, as a result, the diameter shrinks due to Poissons effect [109].

James Joule first discovered the magnetostrictive effect in nickel in 1840. Later, cobalt, iron, and their alloys were shown to have significant magnetostrictive effects. The maximum strains were of the order of 50 ppm (parts per million, 0.005%). In early 1970s, Arthur Clark and his research group at Naval Ordnance Lab (later known as NSWC) discovered Terfenol-D, which produced significantly larger magnetostriction resulting in a maximum strain of the order 1800 ppm (0.18 %) [110, 111]; this was almost twice the maximum strain produced by piezoceramics. These materials were also referred to as Giant Magnetostrictive Materials (GMMs). As a result of this behavior, magnetostrictives were used in numerous applications [112–115], including vibration control [116–118], machine tools, servo valves, hybrid motors [119, 120], sonar and tomography [37, 121], automotive brake systems [122, 123], micropositioners [124, 125] and transducers [126, 127]. While the *Joule effect* describes the action of a magnetic field which results in longitudinal extensional strain accompanied by transverse compressive strain, shown in Figure 1.6, the reverse phenomemon is called *Villari effect* where an application of stress (that is, strain) results in a change in its magnetization. This change in magnetization can be sensed, and once calibrated, used to measure the applied stress or force. In other words, the Joule effect transfers magnetic energy to mechanical energy, whereas the Villari effect transforms mechan-

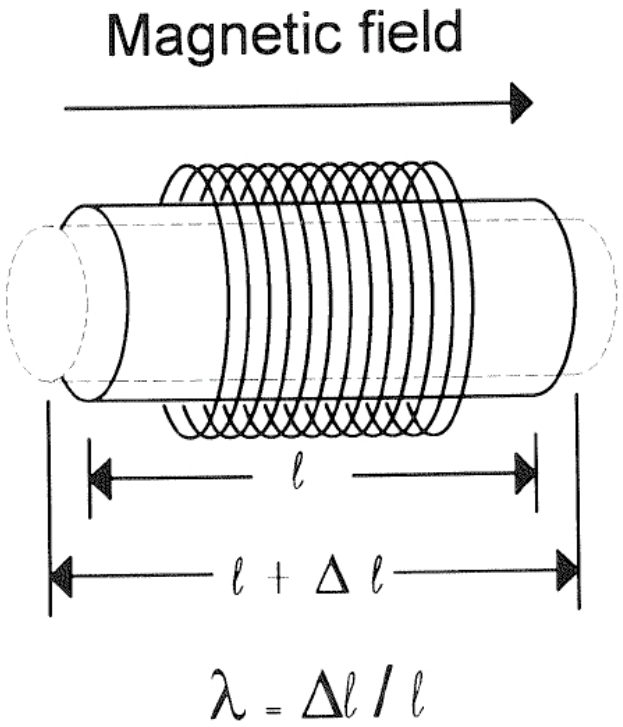

Figure 1.6: Joule magnetostriction of a magnetic rod [129]

ical energy to magnetic energy. The Joule effect is used in actuators, whereas the Villari effect is used in sensor applications [128]; a schematic of the various energy conversion processes in a GMM is shown in Figure 1.7.

The most fundamental measure of a magnetostrictive material is the *saturation strain*, i.e., the maximum magnetostrictive strain that is produced when the material reaches magnetic saturation under the application of a magnetic field. In ferromagnetic materials, an applied field causes rotation of the magnetization towards the field direction within a domain and/or motion of domains with magnetization vectors close to the applied field direction. When the magnetization is completely aligned with the field, magnetic saturation is achieved and no additional magnetostrictive

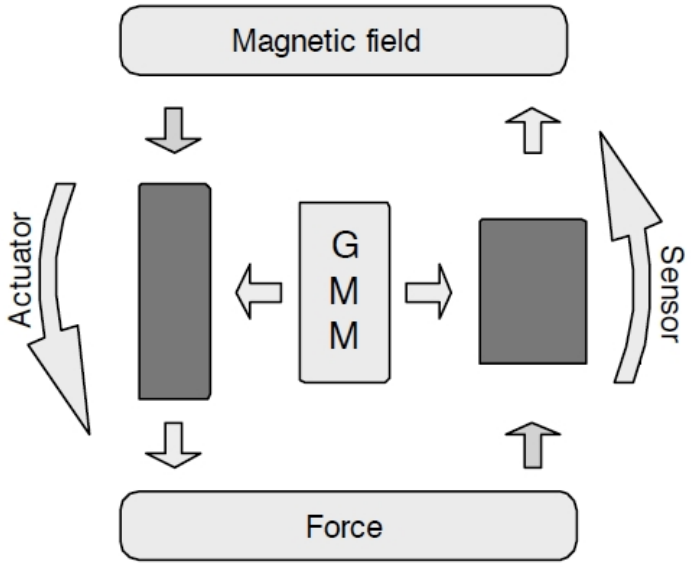

Figure 1.7: Schematic diagram of energy transformation in magnetostrictive materials [130]

strain can be produced by increasing the field magnitude. This property of magnetic saturation means that all ferromagnetic magnetostrictors are intrinsically nonlinear. At finite bias fields, for small changes in applied fields, the resulting strains are approximately linear giving *piezomagnetic* behavior. These materials are, in general, rugged, impervious to adverse environmental conditions, and have a record of high reliability. Although efficiencies are often lower than in electromechanical actuators, magnetomechanical actuators do not suffer from electrical breakdown and malfunction due to arcing. The effects of eddy currents also limit the use of these materials at high actuating frequencies [38, 131, 132]; however, careful design of the magnetic circuit and inclusion of laminations in the material can alleviate this problem to quite an extent [133, 134].

The magnetostrictive process relating the magnetic and mechanical states can

be described with two coupled linearized equations. These equations of state for a magnetostrictive element are expressed in terms of mechanical parameters (strain ϵ, stress σ and Youngs modulus at constant applied magnetic field E_y^H), magnetic parameters (applied magnetic field H, magnetic induction B and permeability at constant stress μ^σ), and two magnetomechanical coefficients (the strain coefficient $d = \partial\epsilon/\partial H$ and $d^\star = \partial B/\partial\sigma$) [135, 136].

$$\epsilon = \frac{\sigma}{E_y^H} + dH \tag{1.1}$$

$$B = d^\star\sigma + \mu^\sigma H \tag{1.2}$$

In these equations, ϵ and B are dependent on σ and H, which are externally applied. The application of a stress will cause a change in the magnetic induction as seen in Equation 1.2. This can also be expressed as a change in permeability by writing the magnetic relation in general case

$$B = \mu H$$

where the effects of stress are included in the permeability μ.

The commercially available giant magnetostrictive material is Terfenol, which derives its name from its constituent elements (**Ter**bium-**Fe**rrous), the place of discovery (**N**aval **O**rdnance **L**aboratory) and the additives (**D**ysprosium); its chemical symbol is $Tb_{0.3}Dy_{0.7}Fe_{1.92}$. Eddy currents lead to the frequency limitation (max. 10 kHz) of bulk Terfenol-D. The Young's modulus is strongly dependent on the magnetic field and the applied compressive stress and can vary between 25–65 GPa [137–140]. Terfenol-D has a specific density of 9.15 - 9.25. The Curie temperature is about 380°C. When heating Terfenol-D beyond this temperature, the magnetostrictive effect is not

permanently eliminated and returns after operating beneath Curie temperature again. However, at high operating regimes hysteresis and nonlinearities are intrinsic to magnetostrictive behaviour. Table 1.1 lists some of the important material properties of Terfenol-D.

Magnetostriction is dependent on applied stress [56]. When there is no applied compressive stress, the jump in magnetostriction does not occur while, above a certain compressive stress value, magnetostriction decreases. The reason for this unusual behavior is that the applied stress changes the alignment of the magnetic domains. The larger the domain rotation, the larger the observed strain. With sufficient compression stress (around 7.6 MPa) and no applied magnetic field, a large percentage of the magnetic domains are oriented perpendicular to the direction of applied stress. When magnetic field is applied, the domains rotate to align with the applied field which is in the direction of the applied stress. Note that as the pre-stress is further increased (e.g., 18.9 MPa), large magnetic fields are required to produce the same strains, since the material performs more mechanical work when pushing against a larger stress [Figure 1.8]. The effects of stress on the hysteresis behavior [142, 143] as well as the elastic modulus [137], popularly called the ΔE *effect*, in Terfenol-D have also been reported in recent times.

1.1.2 Electrostrictives

Materials such as relaxor ferroelectrics undergo strain when an electric field is applied. *Electrostriction* is a general term referring to the elastic deformation of a

Table 1.1: PHYSICAL PROPERTIES OF TERFENOL-D [133, 141]

	Property	Symbol	Value
Mechanical			
	Density	ρ	9250 kg/m^3
	Modulus at constant H	E^H	25 – 35 GPa
	Modulus at constant B	E^B	50 – 70 GPa
	Speed of sound at constant H	c^H	1.72×10^3 m/s
	Speed of sound at constant B	c^B	2.45×10^3 m/s
	Tensile strength		28 MPa
	Compressive strength		700 MPa
Electrical			
	Resistivity		$58 \times 10^{-8}\Omega$-m
Magnetostrictive			
	Piezomagnetic coefficient	d_{33}	1.5×10^{-8} m/A
	Relative permeability	μ	3 – 10
	Coupling coefficient	k	0.70 – 0.75
Thermal			
	Coefficient of thermal expansion		12 ppm/degC
	Thermal conductivity		13.5 W/m-K

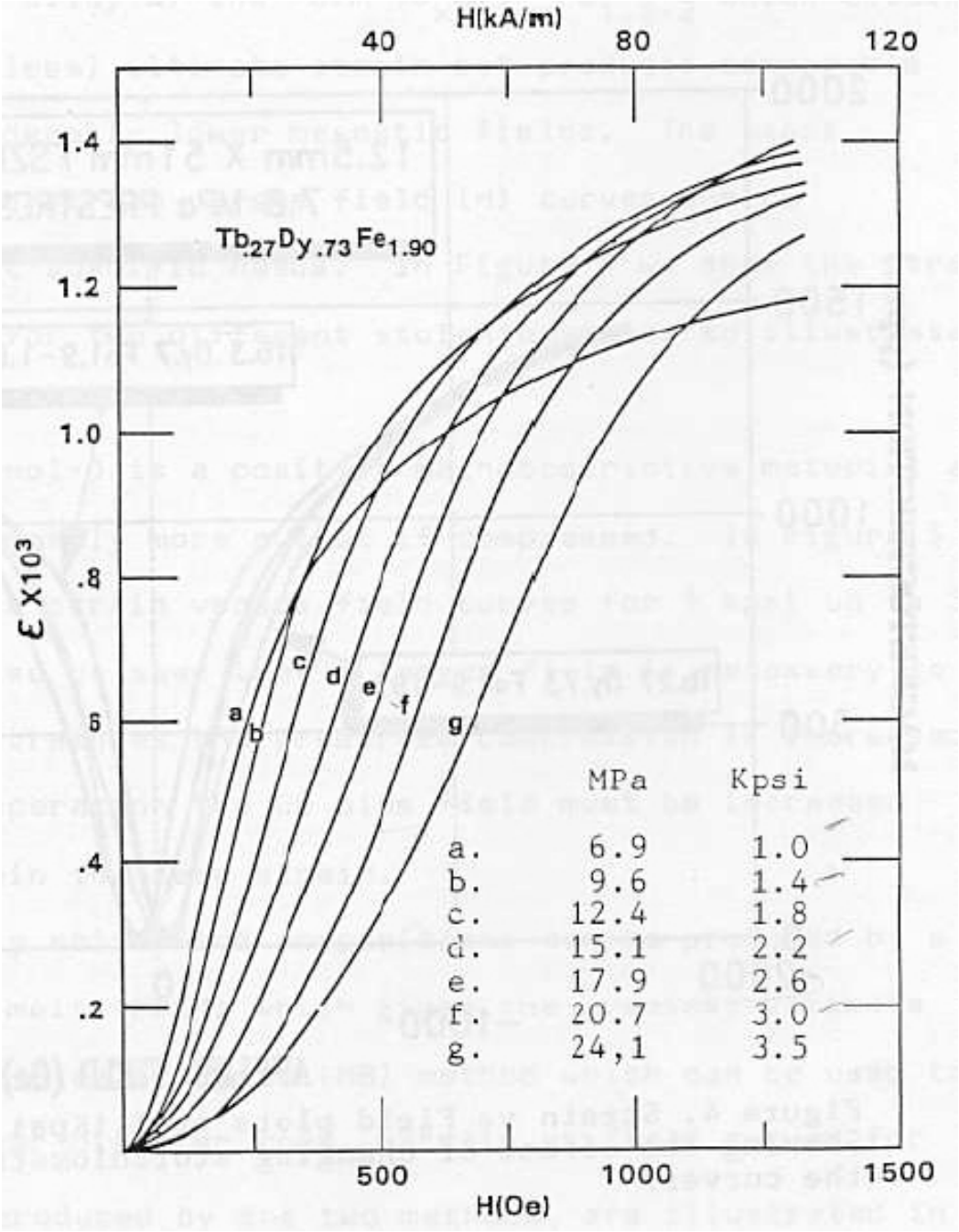

Figure 1.8: Strain vs. magnetic field curves for Terfenol-D under varying compressive stresses [133, 144, 145]

dielectric material under the influence of an electric field. Strictly speaking, PZT therefore also belongs to the category of electrostrictive ceramics since electrostriction exist in almost all materials but is usually very small in effect. In a narrower sense, however, the term electrostrictive ceramics is used to describe ceramics such as those based on lead magnesium niobate (PMN) that, in contrast to piezoelectric ceramics, are not polarized but rather exhibit a change in length due to a spontaneous orientation of dipoles in an electric field. Ferroelectrics consist of subvolumes, called *domains*, that have a uniform, permanent, reorientable polarization. Since the direction of polarization for each domain is randomly oriented in the absence of electric field, the crystal itself has no net bulk polarization. Above a characteristic temperature, called the *Curie temperature*, a ferroelectric undergoes a transition where the spontaneous polarization disappears [146, 147]. With the application of electric field, these domains rotate resulting in a induced strain. Hence, electrostriction is a coupled electromechanical effect, where the induced strain is approximately proportional to the square of the induced polarization. Therefore, the same deformation occurs when the electric field is reversed, in contrast to piezoelectricity i.e. independent of polarity of field. At a sufficiently high field, the induced strain becomes saturated.

The single-crystal behavior depends on various factors and nonlinear processes such as crystal orientation angle, crystal cut, temperature, phase transformation behavior and domain wall motion. The ceramic behavior is the result of a complex arrangement of these effects in addition to effects of intergranular interactions and dispersed inhomogeneities. This creates a complex network of nonlinear local effects which can influence overall material constitutive behavior. Recent studies have

also shown strong dependence of large-signal d_{33} values on uniaxial stress applied on electrostrictive PMN [148–150]; this is an important consideration in transducer applications. Mechanical load in the [001] crystallographic orientation depolarizes the single-crystal by switching it to a perpendicularly polarized phase. At high compressive stress the material is fully depolarized with the orthorhombic crystal variants lying perpendicular to the stress direction. As the electric field is increased the spontaneous polarization begins to rotate through the monoclinic phases towards the rhombohedral phase and results in quadratic electrostrictive behavior [151].

Relaxor ferroelectric single crystals have superior dielectric and electromechanical properties compared to other piezoelectric ceramics and single crystals [152]. Under this category of materials, lead magnesium niobate ($\left[\mathrm{Pb}(\mathrm{Mn}_{1/3}\mathrm{Nb}_{2/3})\mathrm{O}_3\right]_{(1-\mathrm{x})}$ - $\left[\mathrm{PbTiO}_3\right]_{\mathrm{x}}$ $(\mathrm{PMN}-\mathrm{xPT}, 0<\mathrm{x}<0.35)$), alloys provide very large piezoelectric, dielectric and electromechanical coupling coefficients. The outstanding physical properties of these crystals are related to their domain structures and phase states [153–155]. The lack of a spontaneous polarisation means that electrostrictors display little or no hysteretic loss even at very high frequencies of operation [156]. The advantages are however gained at the expense of temperature stability. Relaxors operate best in situations where the temperature can be stabilised to within approximately 10 C. This may seem extremely limiting at first glance, but given that electrostrictors excel at high frequencies and very low driving fields, then the applications tend to be in specialised micro actuators. Temperature stabilisation of such small devices is relatively simple and often presents only a minor problem in the overall design and development process.

Due to their high electromechanical coupling coefficient ($k_{33} > 90\%$), high piezoelectric constant ($d_{33} > 2500$ pC/N) and extremely large piezoelectric strains ($\epsilon_{33} > 1.7\%$), relaxor based ferroelectric single crystals are considered to be the next generation in transducer materials. They are being developed for advanced applications such as medical ultrasonic imaging, underwater communication, high-displacement piezoelectric actuators, and MEMS devices. Electrostrictive materials are well-suited to precise positioning applications in a laboratory environment due to their high stroke and stiffness. In generic applications, special attention must be paid to the design of an appropriate control system to compensate for the large temperature sensitivity of electrostrictives and their inherent non-linearity. The main advantage of these materials is their low drift and low hysterisis, resulting in low self-heating during dynamic actuation.

An electroactive solid-state actuator consists of a stack of many layers of electroactive material (PZT or PMN) alternatively connected to the positive and negative terminals of a high voltage source [27, 103], as shown in Figure 1.9. Such a PZT or PMN stack behaves like an electrical capacitor. When activated, the electroactive material expands and produces output displacement. Typical strains for electroactive materials are in the range 0.075–0.150%. The PZT or PMN stacks are constructed by two methods. In the first method, the layers of active material and the electrodes are mechanically assembled and glued together using a structural adhesive, as shown in Figure 1.9. The adhesive modulus (typically 4–15 GPa) is at least an order of magnitude lower than the modulus of the ceramic (typically 70–90 GPa). This aspect may lead to loss in stack stiffness. In the second method, the ceramic layers

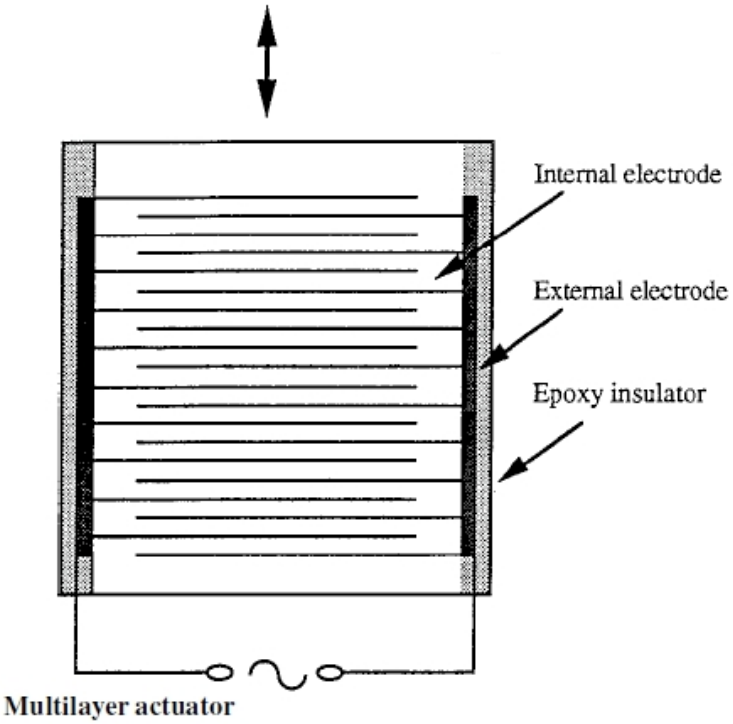

Figure 1.9: Multilayer electroactive ceramic actuator design [41]

and the electrodes are assembled in the *green* state, and then fired together (cofired) in the processing oven. Compaction under high isostatic pressure (HIP process) is sometimes applied to improve mechanical behavior. This process ensures a much stiffer final product and, hence, better actuator performance. However, the processing limitations, such as oven and press sizes, etc., limit the process applicability to large stacks. Some of the important physical properties of single-crystal PMN-PT are listed in Table 1.10.

Material type	Type II PZT ceramics	Type III PZT ceramics	Type VI PZT ceramics	PZN–4.5%PT crystals[a]	PMN–33%PT crystals[a]
Dielectric constant	2050	1000	3900	5000	8000
Dielectric loss	0.018	0.003	0.025	0.01	0.01
Curie temperature (°C)	340	300	210	155	166
Coupling coefficient (k_{33})	0.73	0.64	0.79	0.92	0.94
Piezoelectric coefficient (d_{33}, pC/N)	400	225	690	2200	2200
Young's modulus	59	74	49	8	14
Mechanical quality factor (Q_m)	77	800	46	40	50
Applications	Accelorometer, Actuators, Flow meters, Hydrophones	Sonar projectors, Cleaners, Therapeutic Ultrasound	Medical imaging Transducers, Actuators, Hydrophones	Medical imaging, Actuators, Sonar, Accelerometers	Medical imaging, Actuators, Sonar, Accelerometers

[a] ⟨001⟩ oriented crystals.

Figure 1.10: Electromechanical properties and device applications of PZT ceramics and relaxor PMN-PT single crystals [152]

There are a number of technical hurdles that have to be overcome before single crystals can replace piezoelectric ceramics in commercial applications [152,157]. These issues include:

1. PMN-PT is difficult to grow in single crystal form because of high vapor pressure of PbO and the tendency for chemical segregation resulting from incongruent melting of the solid solution. As a result, the yield of materials from the growth has been fairly small, and crystals have been expensive with variable quality and inhomogeneity

2. Another issue related to the inhomogeneity is the unstable high field performance and over-poling. High perfromance PMN-PT crystals are poled along the non-polar direction and as a result, single crystals exhibit non-linear electric field induced phase transition. This can induce additional heterogeneity in the crystals during high field operation.

3. Low elastic modulus (15 GPa for PMN-PT) makes the crystals susceptible to lateral clamping and leads to degraded performance for bonded devices and/or devices under high compressive preloads. The poling condition is also sensitive to the compressive loads.

1.2 Survey of smart actuator models

Several theoretical models have been proposed in literature to capture the behavior and performance of the hybrid actuator. Some of these will be summarized in the following sections.

1.2.1 Modeling of active material behavior

In many applications, electroactive and magnetoactive materials are often subjected to mechanical loading, either deliberately in the design of the device itself or because the device is used to change shape as in many smart structure applications or is used under environmental stresses. A prior knowledge of how the material properties change under different load conditions is therefore crucial for proper design of a device and for suitable selection of materials for a specific application. Despite this fact, material constants used in many design calculations are often obtained from a stress-free measuring condition, which in turn may lead to incorrect or inappropriate actuator and transducer designs. It is therefore important to determine the properties of these materials as a function of applied electric or magnetic field as well as the involved stresses. Mathematical models of the dynamic behavior of active materials under varying loading conditions have been developed in recent years. These models are used to predict the free strain in the material under different conditions like applied field (electric or magnetic), driving frequency and preload. Most of the active materials show non-linearity in their strain response under large driving inputs along with hysteresis, all of which require a complex formulation that start from considerations of the microstructure and domain level physics. The linearized formulation for induced strain S in active materials under static conditions follows the general format prescribed in the IEEE standards [135, 158, 159] as follows:

Piezoelectric	*Magnetostrictive*
$S = s^E T + dE$	$S = s^H T + dH$
$D = dT + \epsilon^T E$	$B = dT + \mu^T H$

The individual physical properties in the above set of equations depends on the material under consideration e.g. in the case of piezoelectrics and electrostrictives [160–163] the driving input is an electric field, E, while the driving input for magnetostrictives is a magnetic field, B [164, 165].

The strong coupling between magnetic and mechanical properties in certain ferromagnetic materials causes the phenomenon of magnetostriction; strains are generated in response to an applied magnetic field, while conversely, mechanical stresses in the materials produce measurable changes in magnetization [166]. The strains generated due to an applied field are always positive since rotation of the domains from the prestressed perpendicular state leads to an increase in rod length. The vast majority of magnetostrictive materials used in present day applications are operated under a biased condition (ϵ_0, B_0, H_0); this permits the material to exhibit both extension and contraction, unlike operating about a null field where only elongations are possible [136]. The biased condition also permits operating in a strain/field region which more closely approximates a linear relation between the displacement and applied magnetic field, following the linearized expressions used in the IEEE Standard on Magnetostrictive Materials [135,159]. As illustrated in Figure 1.11(a), the relationship between applied magnetic field H and magnetic induction B displays significant

hysteresis at high drive levels. This implies that the permebility μ is a non-linear, multivalued function [167]. The magnetomechanical effect, shown in Figure 1.11(b), is almost quadratic, introducing further nonlinearity into the behavior. Combining these, we arrive at the familiar *butterfly* curves, shown in Figure 1.11(c), that depict the variation of induced strain as a function of the magnetic field.

Magnetostrictives also display strong hysteresis, which makes their effective use quite challenging. The eddy current losses and magnetoelastic dynamics of the magnetostrictive rod were considered to be the origin of the rate-dependent hysteresis in [168], where the eddy current losses were modeled by placing a resistor in parallel with a hysteretic inductor and the magnetoelastic dynamics was modeled by a second-order linear system. The hysteresis models can be roughly classified into physics-based models and phenomenological models; *physics-based models* are built on first principles of physics, an example of which is the Jiles–Atherton model of ferromagnetic hysteresis [169], while *phenomenological models* are used to produce behaviors similar to those of physical systems without necessarily providing physical insight into the problems. [170, 171] The Preisach operator has been applied successfully in the latter case [164, 172].

Using the Jiles-Atherton mean field theory for ferromagnetic materials, the total magnetization M is calculated from the effective magnetic field as follows [167, 170, 173]:

$$H_{eff}(t) = H(t) + \alpha M(t)$$

where $H(t) = NI(t)$ is the magnetic field generated by a solenoid having N turns and

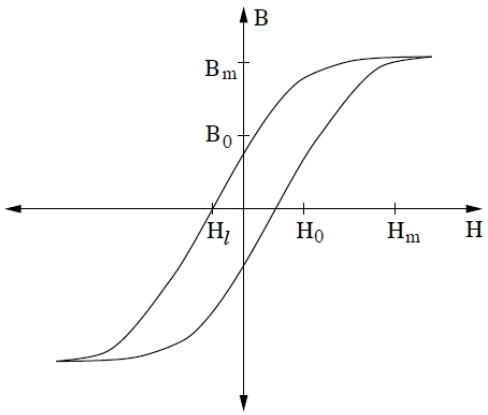

(a) Magnetic field (H) and magnetic induction (B)

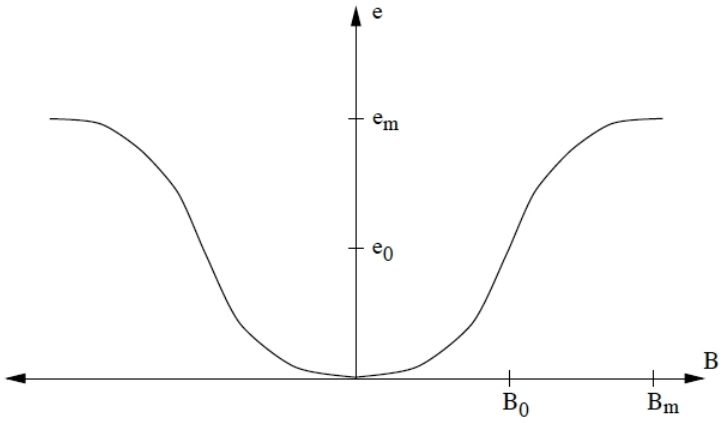

(b) Magnetic induction (B) and induced strain (e)

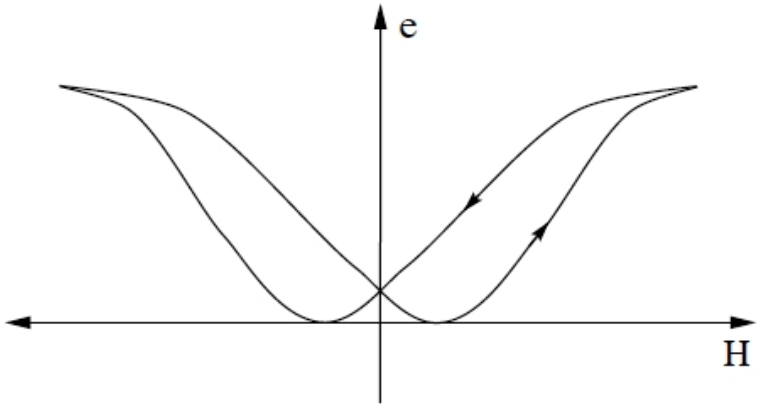

(c) Magnetic field (H) and induced strain (e)

Figure 1.11: Magnetic and mechanical input-output relationships [164]

carrying current $I(t)$. The parameter α quantifies magnetic and stress interactions. The total magnetization is the sum of the reversible and irreversible magnetization levels, the latter being dependent on the anhysteretic magnetization too. In order to extend this formulation to include time-varying stress (σ)-dependent scenarios, Dapino *et al.* [174, 175] derived the rate of change of magnetization as follows:

$$\frac{dM}{dt} = \left(\frac{\partial M}{\partial H}\right)\frac{dH}{dt} + \left(\frac{\partial M}{\partial \sigma}\right)\frac{d\sigma}{dt}$$

The main magnetoelastic component is $\partial M/\partial H$, called the *differential susceptibility*, was identified from the ferromagnetic hysteresis model, while the time rate of change of magnetic field dH/dt was readily determined from the magnetic field input to the transducer based on the input current signal. The damping in these materials have also been considered in several models [176–178].

A three-dimensional, fully coupled, electromechanical constitutive model for isotropic relaxor-ferroelectrics was developed by Hom and Shankar [147, 179]. This model used polarization and strain as the independent state variables and related them to key states like stress, electric field and temperature in a set of nonlinear constitutive equations. The primary assumption was that the electrically induced strain ϵ depends only on the second order polarization P. Summing this with the elastic and thermally induced strains, an expression was obtained for the Helmholtz free energy A as a function of polarization, strain and temperature. The model also assumes that the stress-free dielectric behavior can be expressed by the hyperbolic tangent function

$$|\mathbf{P}| = P_s \tanh\left(k|\mathbf{E}|\right)$$

Electrical testing has shown that the dielectric behavior of relaxor-ferroelectrics is nonlinear [151, 154, 155, 180]. At low fields, the polarization is approximately proportional to the applied electric field. However, at high fields, the induced polarization saturates. According to Hom and Shankar [147], a possible mechanism for such dielectric behavior is as follows:

The individual crystals are divided into domains in which a uniform permanent dipole moment is embedded in the atomic lattice. Since the crystals are randomly oriented, the macroscopic or net polarization is initially zero. An applied electric field induces the permanent dipoles to rotate and stretch towards the direction of the field, resulting in a net polarization in the polycrystal. However, as the field is increased, the lattice structure prevents the complete alignment or further elongation of the dipoles, so the macroscopic polarization eventually saturates.

This approach was later extended to modeling the dynamic behavior in one-dimension [181], where the electrostrictive rod/stack actuator was visualized as fixed at one end with a dashpot at the other end. The mechanical behavior was expressed by

$$S = \frac{T}{s_{33}} + d_{33}P^2$$

where S is the longitudinal strain, T is the axial stress, P is the polarization in the axial direction, s_{33} is the elastic compliance and Q_{33} is the longitudinal electrostrictive coefficient. The inverse electrical behavior was written as

$$E = -2d_{33}PT + \frac{1}{k}\text{arctanh}\left(\frac{P}{P_s}\right)$$

where E is the electric field in the axial direction, P_s is the saturation polarization

and k is a material constant. Applying mechanical equilibrium of the rod/stack and treating the electric portion of the problem as static (for the frequencies of interest), the governing equations for the induced displacement (u) and electric potential (ϕ) become

$$\frac{\partial^2 u}{\partial x^2} = s_{33}\rho\frac{\partial^2 u}{\partial t^2}, \quad E = -\frac{\partial \phi}{\partial x} = -2d_{33}P\left(\frac{\partial u}{\partial x} - d_{33}P^2\right) + \frac{1}{k}\text{arctanh}\left(\frac{P}{P_s}\right)$$

The boundary condition at the free end was included as follows:

$$T = \rho\frac{\partial u}{\partial x} = -CA\frac{\partial u}{\partial t} \quad \text{at} \quad x = L$$

A similar formulation was developed by Deng [182], who assumed the stress (σ) to depend on the electric field (E), strain (ϵ) and strain rate ($\dot{\epsilon}$) by the relation

$$\sigma = -\frac{d}{s}EX_s(E) + \frac{1}{s}\epsilon + F\dot{\epsilon}$$

where d is the piezoelectric coefficient, X_s is the field-dependent phase factor and F is the friction factor. The hysteretic behavior of the material was included through the factor $X_s(E)$. Finally, the above expression for stress was used to calculate the time-varying strain from force balance considerations as follows:

$$\ddot{\epsilon}(t) = \frac{\ddot{x}(t)}{L} = -\frac{A}{mL}\sigma(t)$$

Finite element techniques have also been used in recent times to model the electrostrictive behavior in PMN-PT ceramics [183, 184].

While the material models described above are very useful from a microscopic point of view, their use in the actual design of a smart structure is complicated and involves huge computational loads. The electro-mechanical properties and behaviors

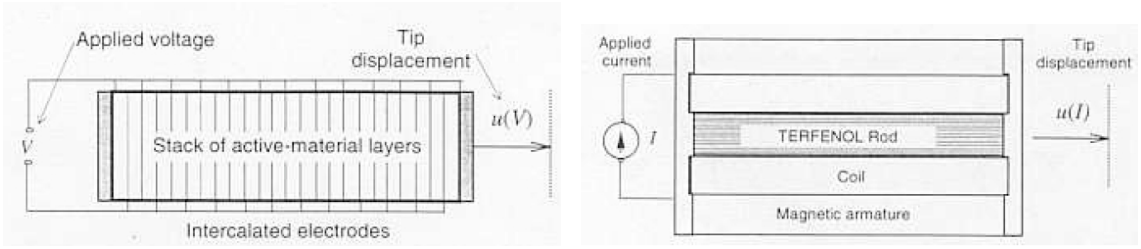

(a) Electroactive (e.g. PZT, PMN) (b) Magnetostrictive (e.g. TerFeNOL)

Figure 1.12: Construction of induced-strain actuators [27]

associated with the interaction of a smart material with a structure has been investigated from more macroscopic methods too. The modeling of smart actuation using an active material, mostly piezoelectrics, was carried out to find the average power, peak power required and total energy consumed, all of which were necessary to get an idea of the energy requirements and overall electro-mechanical efficiencies for structural control applications.

Giurgiutiu and Rogers [27,185] derived expressions for the work output and efficiency of induced-strain actuators [Figure 1.12] under static and dynamic conditions. Starting from the tensorial relation between mechanical and electrical variables (mechanical strain S_{ij}, mechanical stress T_{ij}, electrical field E_i and electrical displacement D_i) in the form [158]

$$\begin{aligned} S_{ij} &= s^E_{ijkl} T_{kl} + d_{kij} E_k \\ D_j &= d_{jkl} T_{kl} + \epsilon^T_{jk} E_k \end{aligned}$$

where s^E_{ikl} is the mechanical compliance of the material measured at zero electric field ($E = 0$), ϵ^T_{jk} is the dielectric permittivity measured at zero mechanical stress ($T = 0$), and d_{kij} is the piezoelectric coupling between the electrical and mechanical variables.

Assuming that the mechanical stress and electric field act only in the 3-direction (the stack axis), the transverse effects were neglected in a first-order analysis and led to the one-dimensional equivalent. Using this simplification, the electromechanical coupling coefficient, κ, became

$$\kappa = \frac{d^2}{s\epsilon}$$

For the static case, when the actuator is energized, the active material expands and produces an output displacement u which generates reaction force F from the mechanical system. Due to actuator compressibility, the force F produces an elastic internal displacement F/k_i, where k_i is the internal stiffness. Hence, in terms of the free displacement u_{ISA},

$$u = \frac{1}{1+r}u_{ISA}, \quad r = \frac{k_e}{k_i}$$

which gives the output energy as

$$E_{out} = \frac{1}{2}F_e u = \frac{1}{2}k_e u^2 = \frac{r}{(1+r)^2}\left(\frac{1}{2}k_i u_{ISA}^2\right)$$

and is maximum for $r = 1$ i.e. perfect stiffness match.

For dynamic analysis of the actuation mechanism shown in Figure 1.13, the authors wrote the output displacement in complex notation as follows:

$$\mathbf{u} = \frac{1}{1+\mathbf{r}(\omega)}\mathbf{u}_{ISA}$$

leading to the total output power

$$\mathbf{P}_{out} = -i\omega\frac{\mathbf{r}(\omega)}{(1+\mathbf{r}(\omega))(1+\mathbf{r}(\omega))^*}\left(\frac{1}{2}k_i\mathbf{u}_{ISA}^2\right)$$

Since the electrical input was a sinusoidal voltage with an offset, the input electrical

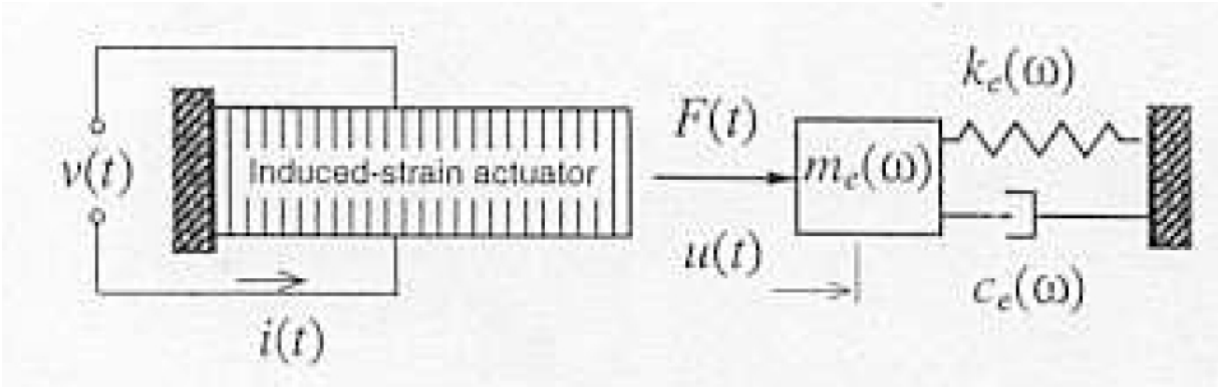

Figure 1.13: Schematic representation of a solid-state induced-strain actuator (PZT stack) operating against a mechanical load under dynamic conditions [27]

power was

$$P(t) = (V_0 + V \sin \omega t) \cdot I \sin(\omega t - \phi),$$

and could be broken up into as active part and a reactive part, the former being $P_{active} = (1/2)VI \cos \phi$.

Leo [186] focused on analyzing the electromechanical coupling between the actuator and the undamped resonant host structure, without reference to the amplifiers used to drive the active material. The structural motion was assumed to be the first mode of vibration and was modeled as a mass-spring oscillator. Similar to the earlier formulation by Giurgiutiu [27], the actuator displacement was written as

$$x = x_0 \frac{1}{1 + R(\omega)} V, \quad F = -K_a R(\omega) x$$

where the mechanical ratio stiffness R included the mass (M) and spring (K) model

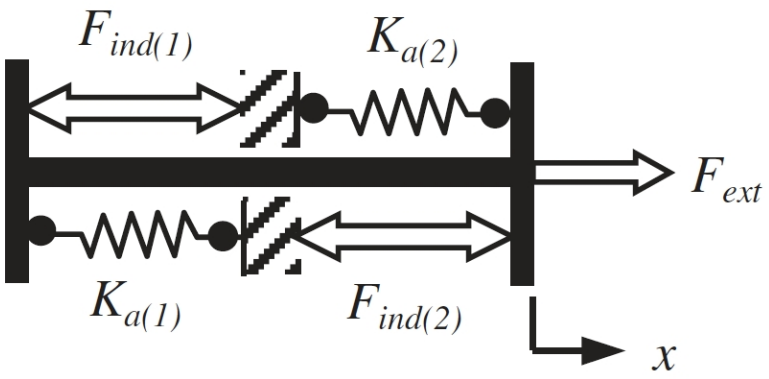

Figure 1.14: Schematic diagram of a dual-stack actuator

of the external impedance, that is,

$$R(\omega) = \frac{K - \omega^2 M}{K_a} = \kappa \left(1 - \omega^2/\omega_n^2\right), \quad \kappa = \frac{K}{K_a}, \omega_n = \sqrt{K/M}$$

Heverley *et al.* [187] analyzed a dual-stack piezoelectric actuation device that utilized a pair of identical piezoelectric stack elements, where both stacks were configured in an opposing fashion within the actuator housing and electrically operated out of phase. During operation of the dual-stack actuator, only the extending stack produces the output force, while the other stack contracts to eliminate opposition to the force generated by the extending stack. The fundamental stack element relation,

$$F_{ext} = K_a x - F_{ind}$$

where K_a is the stack stiffness and F_{ind} is the piezoelectric induced force of the stack, and the schematic diagram [Figure 1.14] were used to conduct a quasi-static analysis and derive the free stroke, x_o, and blocked force, F_b, expressions for the dual-stack actuator. The inputs were applied to the actuator in a four-step process. Assuming identical stack elements, The maximum stiffness-matched output energy and input

electrical energy of the dual-stack actuator are given by

$$\begin{aligned} x_o &= \frac{F_{ind2}}{(K_{a1}+K_{a2})} - \frac{-F_{ind1}}{(K_{a1}+K_{a2})} = \frac{F_{ind}}{K_a} \\ F_b &= (K_{a1}+K_{a2})\frac{-F_{ind1}}{(K_{a1}+K_{a2})} - F_{ind2} = -2F_{ind} \end{aligned}$$

The resultant dual-stack actuator free stroke was equivalent to the free stroke of a single freestanding piezoelectric stack element. The maximum stiffness-matched output energy and input electrical energy of the dual-stack actuator were respectively:

$$\begin{aligned} W_e^{max} &= \frac{1}{8}F_b x_o = \frac{1}{4}\frac{F_{ind}^2}{K_a} \\ W_{in} &= \frac{1}{2}C_1V^2 + \frac{1}{2}C_2V^2 \end{aligned}$$

Liang and Rogers [188–190] developed a dynamic model for the behavior of an active material working against a mechanical impedance. The basic configuration is shown in Figure 1.15. The mechanical aspect of the actuator was described by its short-circuit mechanical impedance, $Z_A(s)$, the host structure was generalized by its driving point mechanical impedance, $Z(s)$, which included the effect of mass stiffness, damping, and boundary conditions, and the actuator was powered by voltage, $V(s)$, or current, $I(s)$. To find the respective impedances, the constitutive equations of the PZT actuator

$$\begin{aligned} S_{11} &= s_{11}^E + d_{31}E \\ d_3 &= d_{31}T_{11} + \epsilon_{33}^T E \end{aligned}$$

were used along with the equation of motion for in-plane vibration

$$\frac{\partial^2 u(x,t)}{\partial x^2} = \frac{1}{c^2}\frac{\partial^2 u(x,t)}{\partial t^2}, \quad c = \left(Y_{11}^E/\rho\right)^{1/2},$$

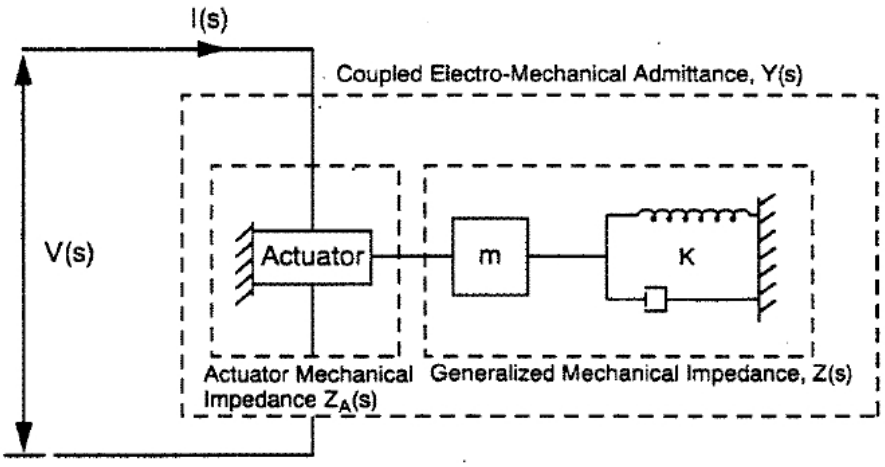

Figure 1.15: Generic electro-mechanical representation of active material systems with integrated actuators

where T_{11} is the stress, S_{11} is the strain and s_{11}^E and Y_{11}^E are the mechanical compliance and elastic modulus of PZT under constant electric field, all in the 1-1 (x) direction. E is the electrical field in the 33 direction. Taking the Laplace transform of the equation of motion along with the boundary conditions

$$\begin{aligned} \bar{u}(s) &= 0 \\ Y_{11}^E w_A h_A \left[\frac{d\bar{u}(x,s)}{dx} - d_{31}\bar{E}_3(s) \right] &= -Z(s)s\bar{u}(l_A,s), \end{aligned}$$

the transformed induced displacement, $\bar{u}(x,s)$, can be written as

$$\bar{u}(x,s) = d_{31}Y_{11}^E w_A \bar{f}(x,s)\bar{V}(s), \quad \bar{f}(x,s) = \frac{\sinh(kx)}{[Z(s)+Z_A(s)]s\sinh(kl_A)}$$

The advantage of the electro-mechanical impedance (EMI) modeling technique was that it could be applied to any linear structure as long as the driving point structural impedance was known; the structural impedance may be determined experimentally or theoretically using any analytical technique.

1.2.2 Static and quasi-static models

The earliest models for hybrid hydraulic actuators were derived from idealized assumptions. Calculations based on stiffness matching of the actuator stack with an incompressible fluid were used for preliminary design and efficiency calculations of piezoelectric based devices [191].

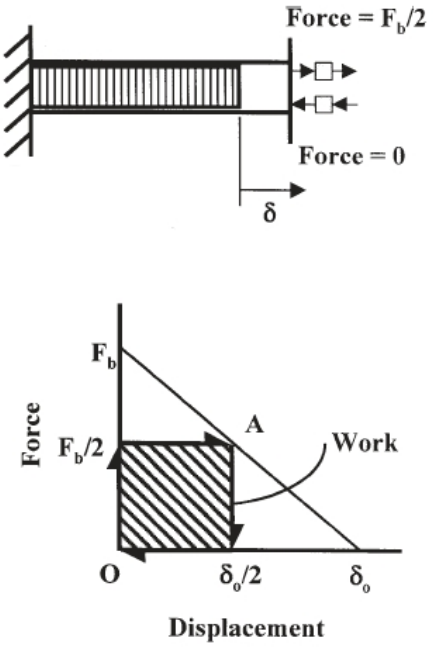

Figure 1.16: Work cycle for an impedance matched stack actuator

In the piezohydraulic pumping theory developed by Mauck and Lynch [67], a piezoelectric stack actuator provided the mechanical driving force for actuation of the pump. The maximum work was obtained from a stack actuator when it was impedance matched to the load it was driving. Figure 1.16 shows the work cycle for an impedance matched PZT stack in a pump cycle where the outlet check valve opens at a pressure corresponding to $F_b/2$ on the loading half of the cycle and the

inlet valve opens at a pressure corres ponding to zero on the unloading half of the cycle. Correspondingly, the work done on the loading half of the cycle is the shaded area under the curve i.e.

$$W = \frac{1}{2}\left(\frac{F_b}{2}\right)\left(\frac{\delta_0}{2}\right)$$

The model developed by Sirohi and Chopra [72] was based on the force-displacement characteristics of the smart material, as shown in Figure 1.17. The equation of the piezostack load line was given by:

$$\delta = \delta_{free}\left(1 - \frac{F_o}{F_{block}}\right)$$

where δ_{free} and F_{block} are properties of the piezostack. Also, the displacement of the active stack is obtained by representing the stack and fluid column as stiffnesses K_p and K_f respectively:

$$\delta_o = \delta_{free} - F_o\left[\frac{1}{K_p} + \frac{1}{K_f}\right], K_f = \beta\frac{A_p}{\Delta_{gap}}$$

The pumping chamber has a cross-sectional area A_p and a displacement δ_p, while the output actuator has a cross-sectional area A_{out} and a displacement δ_{out}. Writing the area ratio as $A_R = A_{out}/A_p$, the output force F_{out} is related to the actuator force F_o by

$$\frac{F_o}{A_p} = \frac{F_{out}}{A_{out}} \implies F_o = \frac{F_{out}}{A_R}$$

The work done per cycle is:

$$\Delta W_{cyc} = F_o\delta_o = F_o\left(\delta_{free} - \frac{F_o}{K_{eff}}\right), K_{eff} = \left(\frac{1}{K_p} + \frac{1}{K_f}\right)^{-1}$$

Writing this in terms of output force, the output work could be obtained from:

$$\Delta W_{cyc} = \frac{F_{out}}{A_R}\left(\delta_{free} - \frac{F_{out}}{A_R K_{eff}}\right)$$

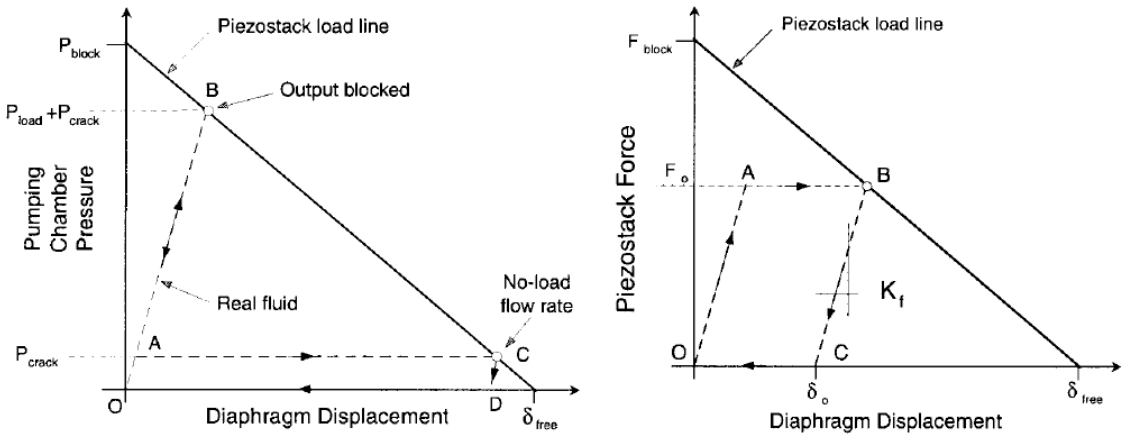

Figure 1.17: Load-line analysis for a piezoelectric actuator [72]

To include effects of the active check valves used for rectification of the flow, a flow factor, C_f was defined to relate the volumetric flow rate, Q, to the differential pressure, ΔP, across the valve by the expression [70]

$$Q = C_f\sqrt{\Delta P}, \Delta P = P_{ch} - P_o$$

where P_{ch} and P_o are the pressure in the chamber and the output tubing. If the inlet valve is open, the pumping chamber would be connected to the low pressure accumulator and $P_o = P_{low}$. Similarly, if the outlet valve is open, the pumping chamber would be connected to the high pressure accumulator, and $P_o = P_{high}$. It was assumed that only one of the valves could be open at any given point in time. Consequently, the flow rate was calculated from the pressure drop and flow direction using

$$Q = C_f\sqrt{|P_{ch} - P_o|}sgn(P_{ch} - P_o)$$

The check valves were modeled by a cracking pressure, P_{crack} and a hysteresis pressure, P_{hys}, that defined the conditions under which they open or close. The inlet

valve was considered open when either of the following two conditions was met

$$P_{ch} < (P_{low} - P_{crack})$$

$$OR$$

$$P_{ch} < (P_{low} - P_{crack} + P_{hys}) \quad AND \quad \frac{dP_{ch}}{dt} > 0$$

Similarly, the outlet valve was considered open if

$$P_{ch} > (P_{high} + P_{crack})$$

$$OR$$

$$P_{ch} > (P_{high} + P_{crack} - P_{hys}) \quad AND \quad \frac{dP_{ch}}{dt} < 0$$

Although this analysis did not assume any dynamics of the valve itself, the flow factor was related to the pressure difference by

$$C_f = \begin{cases} 0 & if \quad \Delta P < P_{crack} \\ \frac{\Delta P - P_{crack}}{P_{full} - P_{crack}} C_{f_0} & if \quad P_{crack} \leq \Delta P < P_{full} \\ 1 & if \quad \Delta P \geq P_{full} \end{cases}$$

where C_{f_0} is the flow factor when the valve was fully open with a differential pressure higher than P_{full}.

Lindler and Anderson [91] calculated the operational efficiency starting from elementary considerations that took into account the compressibility of the chamber fluid and pressure drop in the valves. The maximum work output per cycle (time period T) was obtained from the blocked force F_b and free displacement δ_m on the actuator load line shown in Figure 1.18 and was written as:

$$W_{max} = \frac{F_b \delta_m}{4T} = \frac{P_s \Delta V_m}{4TA^2}$$

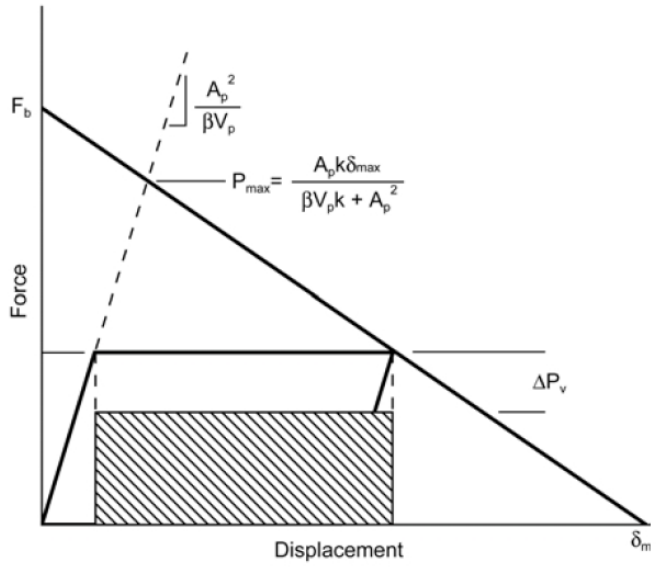

Figure 1.18: Load-line explanation of hybrid-actuator work showing loss elements

where P_s was the stall pressure and ΔV_m was the max volume displacement. By including the viscous pressure loss P_v in the valves, the work output was written as:

$$W_{out} = \frac{(P_s - P_v)A}{4T}\left[\delta_m - \beta P_s \frac{V}{A}\right]$$

A quasi-static two-stage hybrid actuator model was developed by Cadou and Zhang [192]; the intermittent opening and closing of the check valves was assumed to produce impulsively accelerated flow through the fluid tubing and the corresponding velocity profile was used to calculate viscous losses. The authors also noted that that actuation occurs in two steps during each pumping cycle; the first step is associated with pump discharge while the second is associated with pump intake. The intermittent opening and closing of the check valves means that the pressure gradient that accelerates the fluid in the connecting tube is applied impulsively. As the piezo-stack

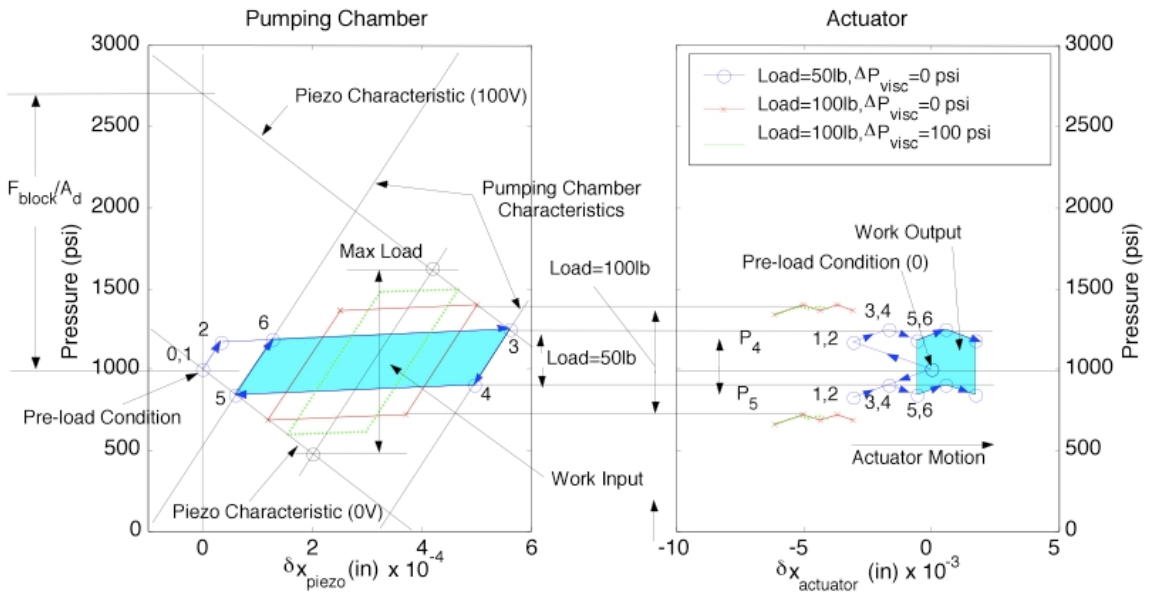

Figure 1.19: Illustration of pumping and stepwise actuation cycle

is energized, the pressure-displacement characteristic of the stack, shown in Figure 1.19, sweeps upward along the pressure-displacement characteristic associated with the fluid in the pumping chamber. Viscous and inertial forces increase the *effective* load on the piezo stack further reducing the displacement per stroke and hence the actuation velocity. This explains the tendency of the actuation velocity to *roll off* at high frequencies since viscous and inertial forces increase rapidly (and nonlinearly) with operating frequency.

Assuming that the fluid is incompressible and that the velocity profile develops uniformly along the length of the tube, a closed-form expression for the fluid velocity response u to an impulsively applied pressure gradient was obtained following Szymanskis [193–195] solution:

$$u(x,y) = \frac{h}{4}\left[x^2 - 1 - 8\sum_{n=1}^{\infty}\left(\frac{J_1(a_n x)}{a_n^3 J_1'(a_n)} e^{-a_n^2 y}\right)\right] \tag{1.3}$$

where h and the non-dimensional parameters x, y, were defined as follows:

$$\begin{aligned} x &= \frac{r}{R} \\ y &= \frac{\mu t}{\rho R^2} \\ h &= \frac{R^2}{\mu}\frac{\Delta P_{tube}}{L} = 4U_{max} \end{aligned}$$

In these expressions, R is the tube radius, ρ is the density, ΔP_{tube} is the fluid pressure drop along the tube, and L is the length of the tube. x and y are, respectively, the non-dimensional radial position and time. The first two terms in Equation 1.3 correspond to steady-state Poiseuille flow while the unsteady component of the velocity field is represented by the third term: a series expansion in first order Bessel functions $J(x)$ with coefficients a_n chosen such that the solution converges to the steady Poiseuille flow solution as $t \to \infty$. The product of density and velocity over the tube cross-sectional area and the valve opening time t_{open} gave the mass moved per piezo stroke while the mass moved per stroke times the frequency gave the overall mass flow rate of the system. Viscous losses were neglected in all of the components except the valves and the tube connecting the open valve with the actuator. The pressure drop across the valve was estimated using the standard assumption that the mass flow rate through the passive check valves is proportional to the square root of the pressure drop through the valve as follows:

$$\dot{m} = C_v\sqrt{\Delta P_{valve}} \tag{1.4}$$

where C_v is the flow coefficient for the valve. The small cracking pressure and inertia of the valve were not included in this analysis. The system model was then built

up by balancing pressures associated with each component in terms of its volume and mass and at the interface with each component, and conservation of mass in the overall system. This led to two sets of equations, one for the *discharge* stroke and one for the *intake* stroke, which were formulated in state-space and solved. Although this model did not formally address the dynamic behavior of the fluid system, the quasi-static approximation did a reasonably good job of predicting actuator performance at frequencies below 150 Hz.

1.2.3 Dynamic actuator models in frequency domain

A dynamic model to find the induced strain of a stacked actuator shown in Figure 1.20 was developed by Tang *et al.* [196]. The model started by considering the total energy per unit volume as:

$$P_v = \frac{1}{2}\sigma^T \mathbf{S}^E \sigma + \frac{1}{2}\mathbf{E}^T \mathbf{C}^\eta \mathbf{E} - \frac{1}{2}\mathbf{E}^T \mathbf{C}^\eta \mathbf{E}$$

where $V_v = (1/2)\sigma^T \mathbf{S}^E \sigma$ is the mechanical energy density, $W_v = (1/2)\mathbf{E}^T \mathbf{C}^\eta \mathbf{E}$ is the electric energy density and $Z_v = (1/2)\mathbf{E}^T \mathbf{C}^\eta \mathbf{E}$ is the electromechanical energy density.

For the ith thin piezoelectric ceramic plate or disk of thickness d_{0i} in the overall stack, the stress σ_i can be related to the displacement u_i' by

$$\sigma_i = E_A u_i'(x,t), \quad \text{where} \quad u_i'(x,t) = \frac{\partial u_i(x,t)}{\partial x}$$

and the corresponding elastic, electric, electromechanical and kinetic energies were

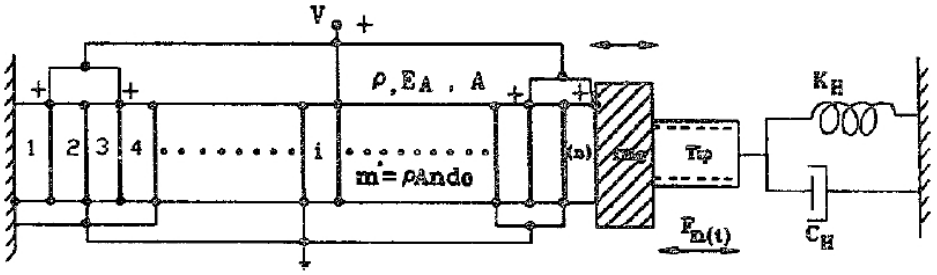

Figure 1.20: Model of piezoelectric actuator for dynamic analysis with tip stiffness

written as:

$$
\begin{aligned}
V_{Ti} &= \int_{x_i}^{x_i+d_{0i}} \frac{1}{2} E_{Ai} A_i \left(u_i'(x,t)\right)^2 dx. \\
W_{Ti} &= \frac{1}{2} \frac{q_i^2}{c_i(dx_i + u_i(x_i+dx_i,t))} = \frac{1}{2}\frac{q_i^2}{c_i dx_i} \\
Z_{Ti} &= -d_{33_i} E_i E_{A_i} A_i \int_{x_i}^{x_i+d_{0i}} u_i'(x,t) d\Omega \\
T_{Ti} &= \frac{1}{2} \int_{x_i}^{x_i+d_{0i}} \rho_i A_i \dot{u}_i^2(x,t) dx
\end{aligned}
$$

Assuming a stack with uniform density ρ, cross-sectional area A and elastic modulus E_A. Correspondingly, the total energies

$$
\begin{aligned}
V_T &= \frac{1}{2} E_A A \int_0^{nd_0} \left(u'(x,t)\right)^2 dx \\
T_T &= \frac{1}{2}\rho A \int_0^{nd_0} + \frac{1}{2} m_e \dot{u}^2(nd_0,t) \\
Z_T &= -d_{33} E_A A \sum_{i=1}^{n} \frac{q_i}{c_i d_0} \int_{(i-1)d_0}^{id_0} u'(x,t) dx
\end{aligned}
$$

can be used to write the Lagrangian

$$L = T_T - V_T - W_T - Z_T$$

and the virtual work is

$$\delta W = -(-K_H - C_H \dot{u}(x,t))\delta u(x,t)|_{x=nd_0} + \sum_{i=1}^{n} V_i \delta q_i$$

This was used to derive the mode shapes and displacement of the complete stack under the application of a electric field. The transfer functions between relating the output force $F_{out}(s)$ and displacement $X_{out}(s)$ to the input force $F_{in}(s)$ and stack displacement $X_{in}(s)$ were found from tests where measurement probes were present within the setup; the input probe was used in sensing the input piston displacement through a extension bar, while the output piston probe was used directly to measure output displacement.

A dynamic system model that coupled the piezoelectric stack actuator with the mechanical and fluid compliances and the viscous effects of the working fluid was developed by Oates and Lynch [197] using state space analysis. Equations of motions of the electromechanical and fluid sub-systems were derived. The stack actuator/piston subsystem was modeled as a second-order masspringdamper with a driving force provided by an input voltage. The stack itself was modeled as a spring (stiffness k_1) in series with a displacement producing actuator (x_1) that was extended by a voltage input (V). The voltage input was converted to mechanical displacement of a stack actuator using the constitutive law of the piezoelectric material. This provided a driving force to the piston mass m_p on the actuating side. A second force on the right hand side of the piston was generated by the fluid pressure in the cylinder head (P_1) applied to the piston area (A_{pi}). The friction associated with the o-ring and fluid between the piston and cylinder walls was represented by a viscous damping coefficient,

b_p. The resulting equation of motion for the stack actuator/piston assembly is

$$m_p\ddot{x}_1 + b_p\dot{x}_1 + k_1x_1 = cV - P_1A_{pi}$$

where the constants c and k_1 were derived from the linear constitutive law of the piezoelectric material

$$S_{33} = s^E_{3333}T_{33} + d_{333}E_3$$

S_{33} is the axial strain component, T_{33} is the axial stress component, E_3 is electric field component, s^E_{3333} is the compliance component at fixed electric field, and d_{333} is the piezoelectric coefficient in this formulation. The stress and electric field were applied in the uniaxial direction. In terms of force (F), displacement (x_1) and voltage (V), this becomes

$$F = \frac{nA_{PZT}Ed_{333}}{L}V - \frac{A_{PZT}E}{L}x_1$$

The spring constant, k_1, is equivalent to $\frac{A_{PZT}E}{L}$ and was based on the effective modulus and geometry of the stack actuator. The piston in the hydraulic actuator was modeled as a mass and damper in parallel, with the o-ring and fluid friction represented by the damping.

The flow resistance through the rectifying check valves was modeled as a finite resistance in one direction and an infinite resistance in the opposing direction. Lumped parameter fluid subsystems were developed for coupling the fluid dynamics with the electromechanical subsystems. Equations of mass continuity and definition

of bulk modulus were used to develop the fluid dynamic equations as follows:

$$\begin{aligned} \dot{m}_{in} - \dot{m}_{out} &= \frac{d\left(\rho V\right)}{dt} \\ \beta_e &= \rho_0 \frac{dP}{d\rho} \\ \frac{\rho_0 V_0}{\beta_e}\dot{P} = C\dot{P} &= \sum_{i=1}^{n} \dot{m}_i = \frac{\Delta P}{R} \end{aligned}$$

Mass flow was represented by m_i and the pressure and rate of pressure change were ΔP and $\dot{P}$, respectively. Capacitance (C) values were calculated for each control volume within the pump system. The effective bulk modulus ($\beta_e = 70$ MPa) of the system used by Oates and Lynch was two orders of magnitude lower than the fluid bulk modulus specified by the manufacturer; this reduction in stiffness was attributed to he presence of O-rings and entrained air in the system.

A different approach was applied by Ullman *et al.* [79, 198] to the valveless piezopump system, where a sinusoidal force was assumed to drive the fluidic systems and the natural frequency of the pumping system was calculated; pressure drops in different sections of the pump were well-represented in these formulations. The driving voltage supplied to the piezoelectric device was assumed to be converted into periodic force acting on the center of the disk, whose elasticity was simulated by a spring with a spring-constant. The fluid was considered to be incompressible and its inertia was included in force-balance equations for different sections of the pipes. For the outlet pipe section with cross-sectional area A_p and at pressure P_1, force balance yielded

$$P_1 A_p = P_{out} A_p + m_p \ddot{x}_p + \frac{32\mu L_p}{D_p^2}\dot{x}_p A_p,$$

while the nozzle section, of cross-sectional area A_n, was represented by

$$P_2 A_p = P_1 A_p + m_n \ddot{x}_n + \frac{1}{2} K_L \dot{x}_n A_n$$

where x_p and x_n are the mean displacements of the fluid in the pipe and nozzle respectively. On the right hand side of both equations, the second term represents the fluid inertia while the third term represents the viscous losses. For the pipe, the viscous losses were calculated assuming laminar flow, while an empirical constant K_L was used for the squared losses in the nozzle. The fluid was assumed to be incompressible, hence, by applying the continuity equation:

$$\dot{x}_p = \frac{A_n}{A_p} \dot{x}_n \quad \text{and} \quad \ddot{x}_p = \frac{A_n}{A_p} \ddot{x}_n$$

Using these relations, the two force balance equations were combined to obtain a single governing ODE for the mass flow rate out of the pump. A similar formulation was used for the inlet line and nozzle. Finally, the force balance on the piezoelectric membrane, which contained the piezoelectric element and supporting disk, resulted in

$$K_D m_D \ddot{x} = F \sin(\omega t) - Kx - A_D K_P P_3$$

where F is the amplitude of the force acting on the center of the disk, K is the equivalent spring constant, K_D is a correction factor that takes into account that not all of the parts of the membrane are displaced as the center (x) and K_P is a correction factor that converts the continuous force (due to pressure difference) that acts on the membrane into a fictitious force acting centrally.

Nasser *et al.* [199] developed a lumped parameter based dynamic model for the

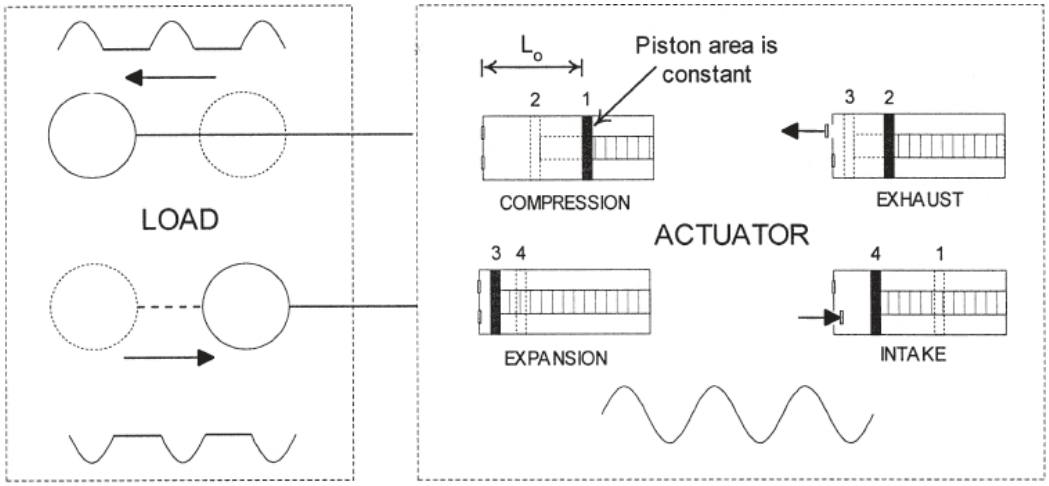

Figure 1.21: Frequency rectification concept using piezoelectric actuation

hydraulic and active components of the systems by linearizing the non-linear behavior of the fluid and using the resulting variables to calculate work done and output efficiency of the device. The operation of the hybrid pump was broken up into four distinct regimes shown in Figure 1.21, along with rectification by a set of unidirectional valves. Work and energy expressions were derived from a one-dimensional model of a piezoelectric actuator. Overall system efficiency of the device was calculated for two different scenarios. An idealized model of incompressible fluid illustrated that the mechanical efficiency of the rectification process is 100% but the electrical efficiency varied between 5% and 29% depending on the actuator coupling coefficient. The mechanical efficiency was between 4% and 40% when using compressible gas as the transmission media, while the electrical efficiency of the process was between 1% and 7% for this process.

Fluid transfer matrix models were used by Sirohi *et al.* [200, 201] to obtain a frequency domain model of the pump operation. Starting from the basic fluid

equations of continuity, momentum, and energy, the relation between the pressure, P, and volume flow rate variables, V, at the ends of the fluid line can be derived in terms of a transfer matrix as:

$$\begin{Bmatrix} P_1 \\ Q_1 \end{Bmatrix} = T_{12} \begin{Bmatrix} P_2 \\ Q_2 \end{Bmatrix} \tag{1.5}$$

where

$$T_{12} = \begin{bmatrix} \cosh\Gamma & -Z_c \sinh\Gamma \\ -\frac{1}{Z_c}\sinh\Gamma & \cosh\Gamma \end{bmatrix}$$

This is a standard representation used in hydraulic analyses, where the assumptions are:

- Fluid velocity is lower than acoustic velocity
- Laminar flow in a rigid tube of circular cross-section
- Length of tube is larger than the diameter ($l/r \gg 1$)
- Normalized density variations are small ($\Delta\rho/\rho \ll 1$)

The behavior of the fluid line is governed by two quantities, the characteristic impedance Z_c and the propagation parameter Γ, both of which can be calculated from density and bulk modulus of the fluid. The complete model was then built by connecting the fluid matrices with SDOF matrices of piston motion, which was achieved in frequency domain by simple multiplication of corresponding transfer matrices. The frequency response of the device was calculated by assuming a harmonic excitation at a frequency ω. The accumulator was treated as a section of tubing with a local compliance much higher than the surrounding fluid. Such an approximation resulted in a

constant pressure across the accumulator, and a difference in the flow rate upstream and downstream of the accumulator. Force equilibrium on the piezo stack was used to obtain the governing equation:

$$c_v - P_c a_p = m_p \ddot{x}_p + b_p \dot{x}_p + k_p x_p$$

where P_c denoted the pressure in the pumping chamber. Assuming the output mechanical load to be lumped together with the output piston, force equilibrium on the output piston yielded

$$\left(P_{lp} - P_{up}\right) A_o = m_o \ddot{x}_o + b_o \dot{x}_o + k_o x_o$$

where x_o is the output displacement. The pressure drops at the check valves are linearly related to the volume flow rates:

$$\text{Exhaust}: \quad P_c - P_1 = R_{out} Q_1$$

$$\text{Intake}: \quad P_4 - P_c = R_{in} Q_4$$

Using the state vector $\mathbf{q} = [x_p \quad x_o \quad P_c \quad P_1 \quad P_4 \quad P_{lp} \quad P_{up}]$, the above linear equations were combined and written in simple form as follows:

$$\mathbf{M}\ddot{\mathbf{q}} + \mathbf{C}\dot{\mathbf{q}} + \mathbf{K}\mathbf{q} = \mathbf{F}$$

Rupinsky and Dapino [202] further extended this formulation to include a transduction model for electromechanical coupling using the equations

$$\begin{aligned} V &= Z_e I + T_{em} v_t \\ F &= T_{em} I + Z_m v_t \end{aligned} \tag{1.6}$$

where V is the applied voltage to the transducer, I is the current flow through the transducer, F is the force on the transducer, v_t is the velocity, Z_e and Z_m are the

blocked electrical and mechanical impedances, and T_{em} and T_{me} are transduction coefficients that describe the electromechanical coupling. The coefficients were calculated from actual mechanical and electrical properties of the material, which, in case of a magnetostrictive material, are analogous to coefficients of the linear piezomagnetic constitutive relations combining the elastic and magnetic effects on the strain ϵ and magnetic induction B:

$$\begin{aligned} \epsilon &= s^H \sigma + d_a H \\ B &= d_a^* \sigma + \mu^\sigma H \end{aligned} \tag{1.7}$$

where σ is the stress on the Terfenol-D rod, H is the magnetic field through the rod, s^H is the elastic compliance at constan magnetic field, $d_a = d_a^*$ are piezomagnetic coupling coefficients, and μ^σ is the magnetic permeability at constant stress.

1.2.4 Dynamic actuator models in time domain

Models for hybrid pumps formulated in time-domain and taking into consideration fluid compressibility and inertial elements also exist in literature. Nasser *et al.* [203, 204] developed a dynamic model of a piezohydraulic pump by considering both inertia and compressibility of the transmission fluid along with the linearized equations for a smart piezo stack. A lumped parameter approach was applied to the fluid system, which was then solved using an electrical network analogy. The resistance, capacitance and inductance were defined and related to the mechanical

variables as follows:

$$\begin{aligned} Resistance &: R_f = \frac{128\mu l}{\pi D^4}\left(1 + D\sum(l/d)_{eq}\right) \sim b \\ Capacitance &: C_f = \frac{Al}{\beta} \sim \frac{1}{k} \\ Inductance &: I_f = \frac{\rho l}{A} \sim m \end{aligned}$$

Using these, the pressure drop through any lump with flow rate Q was written as:

$$\Delta P = R_f Q + I_f \frac{dQ}{dt} \quad \equiv \quad \Delta V = RI + L\frac{dI}{dt}$$

where the current I in equivalent to the flow rate in the analogous electrical circuit. The compliance C_f was added to the electrical network using a capacitor C, thereby arriving at the overall expression by considering a current source (flow rate), as depicted in Figure 1.22:

$$L\frac{d^2Q_1}{dt^2} + \frac{1}{C}(Q_1 - Q_2) + R_1\frac{dQ_1}{dt} = 0$$

The lumped parameter approach was extended to the pumping stack, the end effector and the fluid volumes on the input and output sides of the hydraulic cylinder, resulting in force-balance ODEs for all cases. The model was seen to work well in the case of one-sided operation for frequencies up to 100 Hz. When the action of the active valves was included in the simulation by incorporating valve timing, the model captured the pump behavior up to 8 Hz. One of the problems noted was due to time lag in cylinder motion whenever the frequency of valve operation was increased, possibly due to inertia of the fluid. The authors noted that a model of the valves should include reverse motion for more accurate representation.

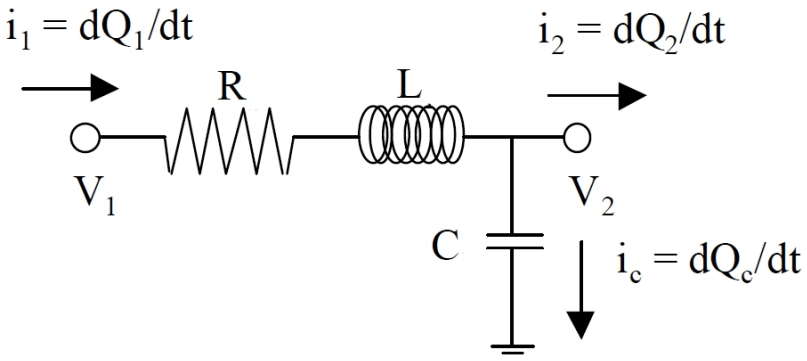

Figure 1.22: Lumped parameter fluid mode using electrical network analogy

Regelbrugge *et al.* [205] derived a simple, physics-based model to describe basic operating characteristics of piezohydraulic actuators. The bulk modulus of the hydraulic fluid along with mass flow rates through different control volumes were used to calculate the pressures in the corresponding sections of the actuator. The input was assumed to be sinusoidal displacement of the piston driven by a piezoelectric stack. Motion of the mechanical components and fluid volumes were modeled using single-degree-of-freedom (SDOF) equations from dynamic force equilibrium considerations. Pressure drops through the valve orifices connecting volume elements were modeled using a momentum-conserving relation (Bernoulli's equation) with empirical corrections for viscous flow losses and jet contraction; the mass flow rate through a valve, $\dot{M}$, was calculated as a function of the pressure difference, ΔP, across it as follow:

$$\dot{M} = \frac{2A}{2+\pi}\text{sgn}(\Delta P)\sqrt{2\rho\left(\Delta P - P_v\right)} \tag{1.8}$$

where ρ is the instantaneous density of the fluid in the valve, A is the valve opening

area and P_v is the viscous pressure loss in the valve. The model progresses between time steps using the governing ODEs and kept track of the mass of fluid, M, in each section using the relation:

$$M = \rho\,(V - Ax) \tag{1.9}$$

where V is the volume and x is the displacement of a boundary. The bulk modulus of the fluid was used to calculate the pressure in any fluid volume based on the instantaneous density in the same volume from the following relation:

$$\begin{aligned} dP &= -\beta\frac{dV}{V} = \beta\frac{d\rho}{\rho} \\ \implies P - P_0 &= \beta \ln\left(\frac{\rho}{\rho_0}\right) \end{aligned}$$

A similar approach was used by Tan, Hurst and Leo [69,206]; in addition to the losses in valves, this model did a thorough analysis of the major and minor losses in the fluidic system and included them in momentum and mass continuity equations as follows:

$$v_2^2 + \frac{P_2}{\rho_2} + \frac{1}{2}K_L\overline{v}^2 = v_1^2 + \frac{P_1}{\rho_1} \tag{1.10}$$

where v_1, v_2 and P_1, P_2 are corresponding fluid velocities and pressures at sections 1 & 2, $\overline{v}$ is the mean velocity and K_L is the minor loss coefficient. Although the acceleration of fluid elements was neglected, the acceleration of solid components, such as piston and load, were incorporated into the model. Active valves made with piezo material were used in this setup; hence, the opening and closing of the valves were controlled by controlled electrical signals. Tan's model is in two forms: while both of them assume the fluid in the pumping chamber to be compressible, the first form (IVF) assumed the fluid in the tubing to be incompressible while the second

form (CVF) considered compressibility in all fluidic parts. In both formulations, the operation of the piezohydraulic pump was broke up in to four stages, similar to the approach used earlier by Nasser and Leo [68]. For both the IVF and CVF models, the rate of change of fluid pressure in the pumping chamber, P_{ch}, due to displacement x of the driving piezostack was obtained from:

$$\dot{P}_{ch} = \beta \frac{A_{ch}}{\forall - A_{ch}x} \dot{x}$$

where A_{ch} and $\forall$ are the cross-sectional area and total initial volume of the pumping chamber respectively. However, for the incompressible model (IVF), there is no change in fluid density when either of the valves are open i.e. $\dot{\rho} = 0$. The compressibility model (CVF), on the other hand, takes into account the change in fluid density in the pumping chamber due to corresponding flow rates and the corresponding rate of change is given by

$$\dot{\rho}_{ch} = \frac{-V_1 A_p + \dot{x} A_{ch}}{A_{ch}(L_o - x)}$$

where V_1 is the velocity at the entrance / exit of the pipe (positive for outflow, negative for inflow) and A_p is the cross-sectional area of the pipe. This method was shown to be accurate up to $\sim$150 Hz pumping frequency, with the CVF model yielding better results than the IVF model as the frequency increased. According to the authors, the reason for this discrepancy is that the CVF model assumed a linear bulk modulus to pressure model while the IVF model assumed an infinite modulus.

1.2.5 Use of CFD

Numerical solutions (using CFD) of the fluid flow in the pumping chamber and its interaction with the active driving element hav been used in some recent studies. Oates and Lynch [197] developed a two-dimensional axi-symmetric model using ANSYS FLOTRAN which uses a finite element method to solve for velocity and pressure within a fixed control volume. A uniform velocity boundary condition was applied to the piston face and the pressure generated in the cylinder head was calculated. No slip conditions were applied on all other boundaries. The input velocity was based on the mean piston velocity during the outlet stroke when the stack was driven at different frequencies. This study resulted in the assessment of viscous losses and loss factors could be calculated. Separate loss coefficients for a sharp and a filleted corner were calculate empirically and compared with CFD results.

A complete 3-D simulation of the flow inside the fluid pumping chamber and the effects of geometrical parameters was carried out in depth by John *et al.* [84, 207] at the University of Maryland using CFD-ACE, a commercial Navier-Stokes solver with multi-physics capabilities. The study showed that pressure losses increase non-linearly with driving frequency, pumping chamber height and radial location of discharge tube, and are much greater when 3D effects are considered. Simple analytical expressions for pressure losses in the pumping chamber during discharge in the 2D and 3D cases were derived, assuming steady, fully developed, incompressible fluid flows only in the

radial direction, as follows:

$$\begin{aligned}\Delta P_{chamber,2D} &= \frac{3\mu Q}{\pi h^3}\left(\frac{d_p - d_o}{d_p + d_o}\right) \\ \Delta P_{chamber,3D} &= \frac{6\mu Q}{\pi h^3}\ln\left(\frac{d_p}{d_o}\right) + \frac{\rho}{60}\left(\frac{6Q}{\pi h d_p}\right)^2\left[\left(\frac{d_p}{d_o}\right)^2 - 1\right]\end{aligned}$$

where Q is the volume flow rate, d_p is the diameter of the pumping chamber, d_o is the diameter of the discharge orifice, h is the pumping chamber height and ρ is the fluid density. In the 2D case, viscous shear is the only contributor to the pressure loss, whereas, in the 3D case, an additional inertial term arises that is associated with the change in flow cross-sectional area with radial position. At low frequencies, the difference between the 2D and 3D representations results from differences between the viscous terms; at high frequencies, the difference arises because the 2D model does not include the effects of the flow area change across the piston face. The frequency at which the inertial effects become stronger than the viscous effects is around 100 Hz. From these analytical derivations, the authors conclude that a simple analytical expression for the pressure loss, ΔP, should have the form

$$\Delta P = AQ + BQ^2$$

where the coefficients A and B are functions of the geometry (d, d_p, h, l) and fluid properties (μ) as follows:

$$\begin{aligned}A &= \frac{6\mu}{\pi h^3}\ln\left(\frac{d_p}{d_o}\right) + \frac{128\mu l}{\pi d_o^4} \\ B &= \frac{\rho}{60}\left(\frac{6Q}{\pi h d_p}\right)^2\left[\left(\frac{d_p}{d_o}\right)^2 - 1\right]\end{aligned}$$

John *et al.* have also demonstrated that a major source of pressure loss in the pumping chamber is the change in effective flow area caused by vortex rings that form in either

the discharge tube or the pumping chamber. During discharge, a vortex ring forms in the entrance of the discharge tube that reduces the effective area of the tube. Similarly during intake, a vortex ring forms in the pumping chamber that reduces the effective height of the pumping chamber. To take care of these effects, correction factors k_{dis} and k_{in} are applied to the actual orifice diameter, $d_{o,nom}$, and actual chamber height, h_{nom} as follows:

$$d_o = \left(\frac{k_{dis}}{k_{dis} + Q}\right) d_{o,nom} \quad , \quad h = \left(\frac{k_{in}}{k_{in} + Q}\right) h_{nom}$$

1.3 Motivation and objectives of current research

The objectives of the present research was twofold:

1. To develop compact self-contained electro-hydraulic actuation systems using magnetostrictive and electrostrictive materials as the driving elements and characterize their performance under varying operating conditions

2. To identify and model the physical phenomena governing the dynamic operation of such a smart actuator

We present the design and test of two prototype actuators based on the giant magnetostrictive material TerFeNOL-D and the electrostrictive material PMN-32%PT. For the first prototype driven by Terfenol-D rods [208, 209], two different lengths, 51 mm (2 inch) and 102 mm (4 inch), with the same diameter, 12.7 mm (0.5 inch), were used. Both the rods were laminated to minimize the effects of eddy currents. Passive reed valves made of spring steel were used to rectify the fluid flow

initiated by oscillatory motion of the Terfenol-D rods. The pumping frequency is varied by controlling the electrical input signal to the magnetizing coil. The displacement of the output shaft is measured and the mean velocity is computed as the slope of a linear fit to the displacement data. Tests with no-load and with external load are carried out to measure the maximum flow rate and the blocked force of the actuator. Dynamic tests, with only the driving rod in the pump body, were also performed to characterize the strain and magnetic flux variation with frequency. Frequency sweeps were carried out at different control voltages and the induced strain and magnetic flux density in the Terfenol-D rods were measured. A significant roll-off was seen in the material strain with frequency, comparable to the magnetic circuit response, was observed which led to the conclusion that the maximum frequency of operation of the pumping device depends on the limitations of the driving circuitry as well as those of the mechanical sub-system. The main conclusions from this set of experiments was that the output performance of the actuator does not scale linearly with operational frequency and dynamic effects of different components come into play at higher frequencies.

While previous research efforts have established the viability of the hybrid actuation concept, the power density achievable from such devices still remains far below that of the conventional electromagnetic actuators. Though it is theoretically possible to surpass the power density of electromagnetic actuators by operating the hybrid devices at high pumping frequencies, a major challenge is the nonlinear behavior of fluid flow rate with pumping frequency. In order to improve the performance of these devices, accurate modeling of the behavior of the device as a function of pumping fre-

quency is essential. Simulations using the currently available models are not always accurate at high frequencies of operation (>200 Hz) where the inertia of the transmission fluid become dominant and becomes strongly coupled with the compliance of the fluid passages. Also, all these models had been developed for active valves that control the fluid flow and are operated by electrical signals; hence, they are either completely open or completely closed and their operation is fully determined by actuating signals rather than the fluid pressure with the system. This is not the case with passive reed valves, where the valve openings are dependent on pressure differences across the reed ports and hence, vary continuously with time depending upon their dynamics. Hence, it was concluded that a complete dynamic model of the hybrid actuator that takes into account the physical properties of the active material and the transmission fluid, inertia of the moving parts and an accurate representation of flow losses needs to be developed.

The second prototype actuator was then built with two PMN stacks, each 12 mm in diameter and 60 mm overall length. The mechanical design of this actuator incorporated lessons learned from the previous experiments:

- better stiffness matching between driving element and driven fluid,

- reduce the effect of fluid pressure on the prestress on the active material,

- lowering fluid compliance by using higher fluid bias pressures,

- improved seals to reduce leakage, and

- mechanical design for compatibility with higher fluid pressures.

The simulation model was used exhaustively to identify a set of optimum geometrical sizing parameters and operating conditions. The new design was tested under both no-load and externally loaded conditions, while varying the pumping frequency, applied voltage and fluid bias pressure, to measure the output performance of the device. The data from the tests was used to validate the comprehensive mathematical model.

1.4 Outline of Dissertation

In Chapter 2, we present the design and experimental studies on a prototype compact hybrid actuator built using the magnetostrictive material Terfenol-D. The construction of the pump, bench top setup and tests are described. Results of the experimental study under different loading conditions are presented. Data from dynamic characterization of the Terfenol-D rods are also presented.

In Chapter 3, a comprehensive mathematical model of the hybrid actuation is formulated by incorporating the major physical phenomena occurring inside the device and representing them as ordinary differential equations. Physical properties of the active element, dynamics of the moving parts, inertial and viscous effects of fluid flow, compressibility in high pressure sections, behavior of reed valves, and friction phenomena in the output shaft are taken into account. The time-domain model is solved with the material properties and geometrical dimensions as inputs and the results are compared with experiment data.

The development and performance tests of a new actuator with PMN as the

driving element are presented in Chapter 4. The design of the new actuator is optimized with respect to the active driving element and it is built to withstand high pressures and seal off hydraulic oil leakage. Results of the dynamic tests performed to analyze stack response with frequency without any fluid coupling are also included. The test data is used to validate the numerical model developed earlier.

Chapter 5 presents a study of the results using the experimentally validated simulation model with variations in important design parameters. It also includes a sensitivity study with non-dimensional parameters.

Chapter 6 provides the conclusion to the thesis and ideas for future work.

Chapter 2

Design and Testing of a Magnetostrictive Hydraulic Actuator

2.1 Overview

This chapter outlines the design of a hybrid actuator using the giant magnetostrictive material Terfenol-D ($Tb_{0.3}Dy_{0.7}Fe_{1.92}$) as the driving element and the tests performed to measure the device output. Two different Terfenol-D rods were used; the first one was 51 mm (2 inch) long with 12.7 mm (0.5 inch) diameter, while the second one was 102 mm (4 inch) long with 12.7 mm (0.5 inch) diameter. Both rods were laminated (5 laminations) to minimize the effects of eddy currents. Passive reed valves made of spring steel were used to rectify the fluid flow initiated by cyclic motion of the Terfenol-D rods. A hydraulic cylinder with 19.05 mm (3/4 inch) bore and 6.35 mm (1/4 inch) stroke was used as the output device. The pumping frequency was varied by controlling the electrical input signal to the magnetizing coil. The displacement of the output shaft was measured and the mean velocity was computed as the slope of a linear fit to the displacement data. Tests with no-load, and with externally suspended loads, were carried out to measure the maximum flow rate and the blocked force of the actuator.

Dynamic tests, with only the driving rod in the pump body, were also performed to characterize the strain and magnetic flux variation with frequency. Frequency sweeps were carried out at different control voltages and the induced strain and mag-

netic flux density in the Terfenol-D rods were measured. A significant roll-off was seen in the material strain with frequency, which is comparable to the frequency response of the magnetic circuit; this led us to to the conclusion that the maximum frequency of operation of the pumping device depends on the limitations of the driving circuitry as well as those of the mechanical sub-system.

2.2 Actuator Operation

The starting point of a smart material driven hydraulic actuator is the initiation of flow due to the oscillation of a mechanical piston being driven by the extension / contraction of a smart material upon application of an periodic electrical input. In case of a magnetostrictive material like Terfenol-D, this actuation is obtained using a magnetizing coil placed around a cylindrical element; a well-designed low reluctance flux return path also has to be in place to complete the magnetic circuit [103,133,210]. A typical hybrid pump uses the principle of frequency rectification to produce a net flow rate out of the pump; this is performed by passive unidirectional reed valves housed inside the pumping head (Figure 2.1) which allow fluid flow either out of the pumping chamber (through the discharge port) or into the pumping chamber (through the intake port).

The pumping device operates in four distinct stages as follows [68, 69, 86, 211]:

1. Compression (Figure 2.2(a)): The first stage involves the expansion of the hybrid material stack/rod as an increasing magnetic field is applied. This in turn compresses the fluid in the chamber, resulting in an increase in chamber pres-

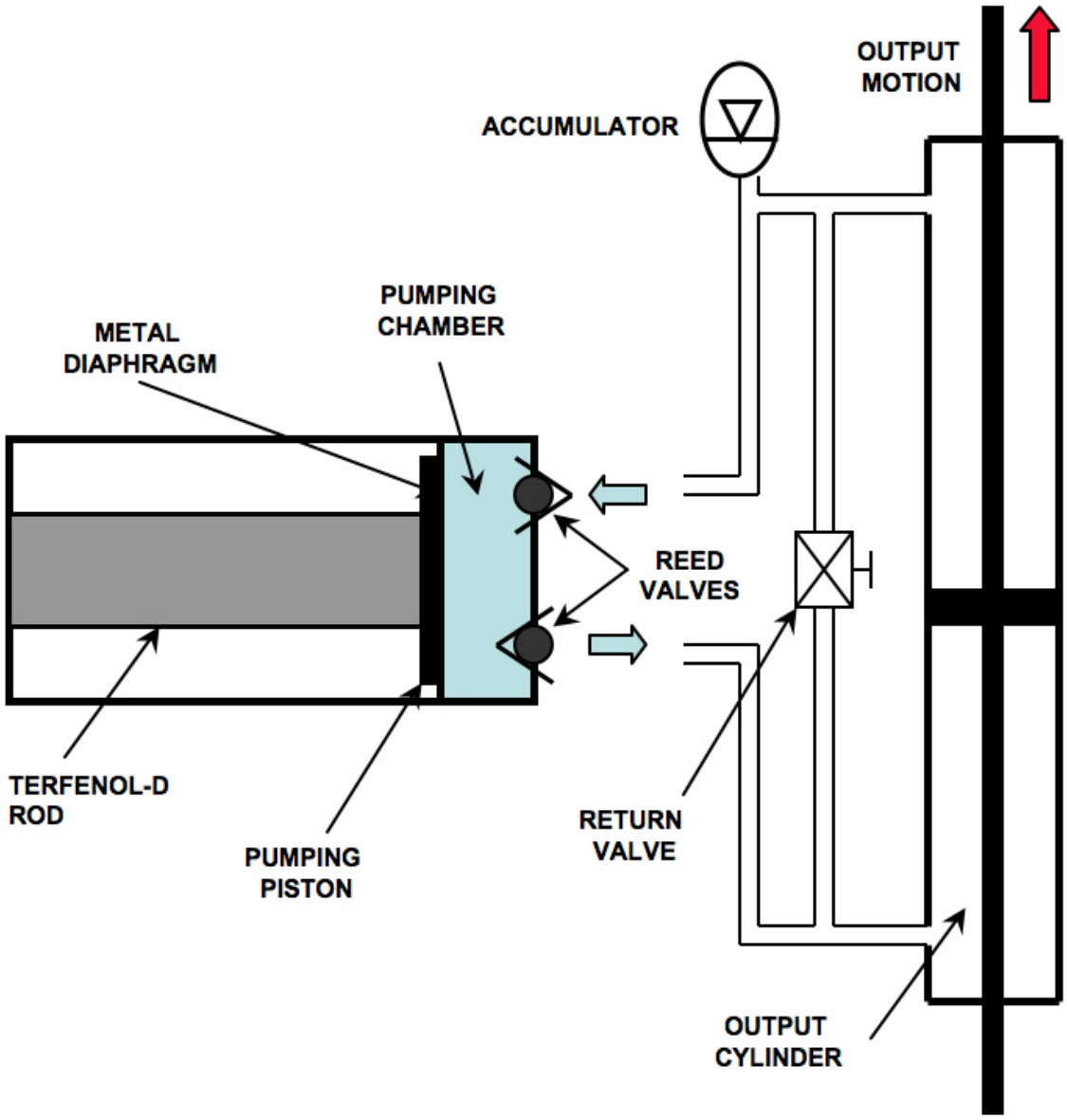

Figure 2.1: Schematic of unidirectional actuator test setup

sure, P_{ch}. This stage continues as long as the pressure difference across the valve is less than the valve cracking pressure, P_{crack}. The intake reed valve is closed during this stage as the pressure in the chamber is greater than the pressure in the intake tube of the pump.

2. Discharge (Figure 2.2(b)): In the second stage, the pressure difference between the chamber and the discharge tube becomes large enough to crack open the discharge reed valve and fluid starts to flow out of the chamber into the discharge tube. Pressure builds up in the high pressure side of the output cylinder and results in motion of the output shaft, causing fluid to move from the low pressure driven side of the output cylinder into the highly compliant accumulator which is maintained at almost constant pressure P_{acc}.

3. Expansion (Figure 2.2(c)): In this stage, the current in the coil starts decreasing causing the hybrid stack to retreat and the pumping chamber pressure, P_{ch}, to reduce. The intake reed valve is designed to only allow flow of fluid into the pumping chamber while the discharge reed valve port does not allow any fluid to come into the chamber. However, the intake port is still closed as the difference $(P_{acc} - P_{ch})$ is still lower than the cracking pressure. This stage is similar to the compression stage, except that the stack/rod is contracting instead of expanding as in Stage 1.

4. Intake (Figure 2.2(d)): In the *intake* stage, the pumping chamber pressure drops further and the pressure difference between the chamber and the intake tube becomes large enough to crack open the intake reed valve and allow fluid flow

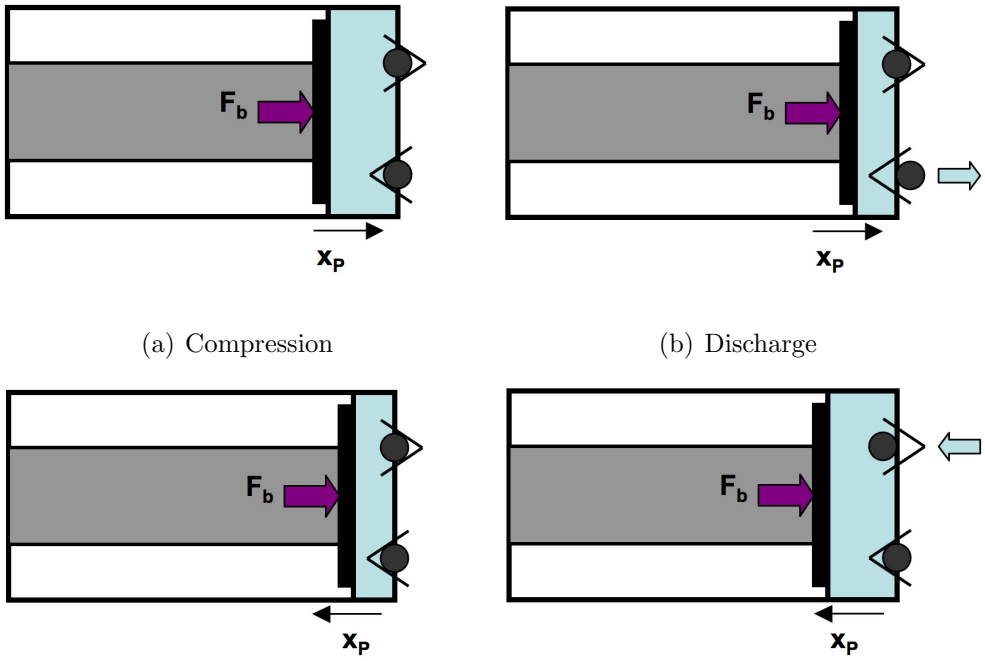

(a) Compression (b) Discharge

(c) Expansion (d) Intake

Figure 2.2: Stages of hybrid pump operation

back into the chamber.

These four stages are repeated every pumping cycle and result in a net mass flow rate out of the pump through the discharge tube and an equivalent mass flow rate into the pump through the intake tube.

A manifold is used to connect the hybrid pump to the output cylinder; this manifold also houses the return valve and the accumulator port. The return valve is closed during normal operation and is only used to reset the output piston to its original position at the end of one stroke. The accumulator consists of a chamber with a rubber diaphragm that separates the fluid filled manifold from a nitrogen tank; the pressure in the tank decides the bias pressure being applied to the fluid. Fluid

from the output port of the hybrid pump flows through the manifold and into the output cylinder, causing an increase in pressure. Since the other end of the output cylinder is connected to the highly compliant accumulator which is maintained at the bias pressure, the output piston shaft moves due to the pressure difference between the two chambers of the cylinder.

2.3 Experimental Setup

2.3.1 Hybrid Pump

The hybrid hydraulic actuator used in this study was driven by a Terfenol-D rod [208]. Figure 2.3 shows an exploded view of the pumping section of the actuator. The Terfenol-D rods used were 50.8 mm (2 inch) and 101.6 mm (4 inch) long, while the diameter was 12.7 mm (0.5 inch) in both cases. The hydraulic oil used was Mobil DTE-20, which has a specific gravity of 0.86 and kinematic viscosity of 36.1 cSt. The pumping section houses the Terfenol-D rod, magnetizing coil, pump body, piston and reed valve assembly. The pump body and bottom cap were made of high permeability steel (12L14 grade) and acted as the return path for the magnetic flux. The stack was pre-loaded by tightening the end cap and using disc springs present within the housing; the disc springs also aided in retracting the pumping piston assembly during the *intake* stage when the Terfenol-D rod undergoes contraction. The reed valves were made of spring steel and served as unidirectional ports for flow of fluid in to and out of the pumping chamber (Figure 2.4). They were cut out of 0.102 mm (4 mil) thick spring steel sheet and then sandwiched between two steel plates in the pump

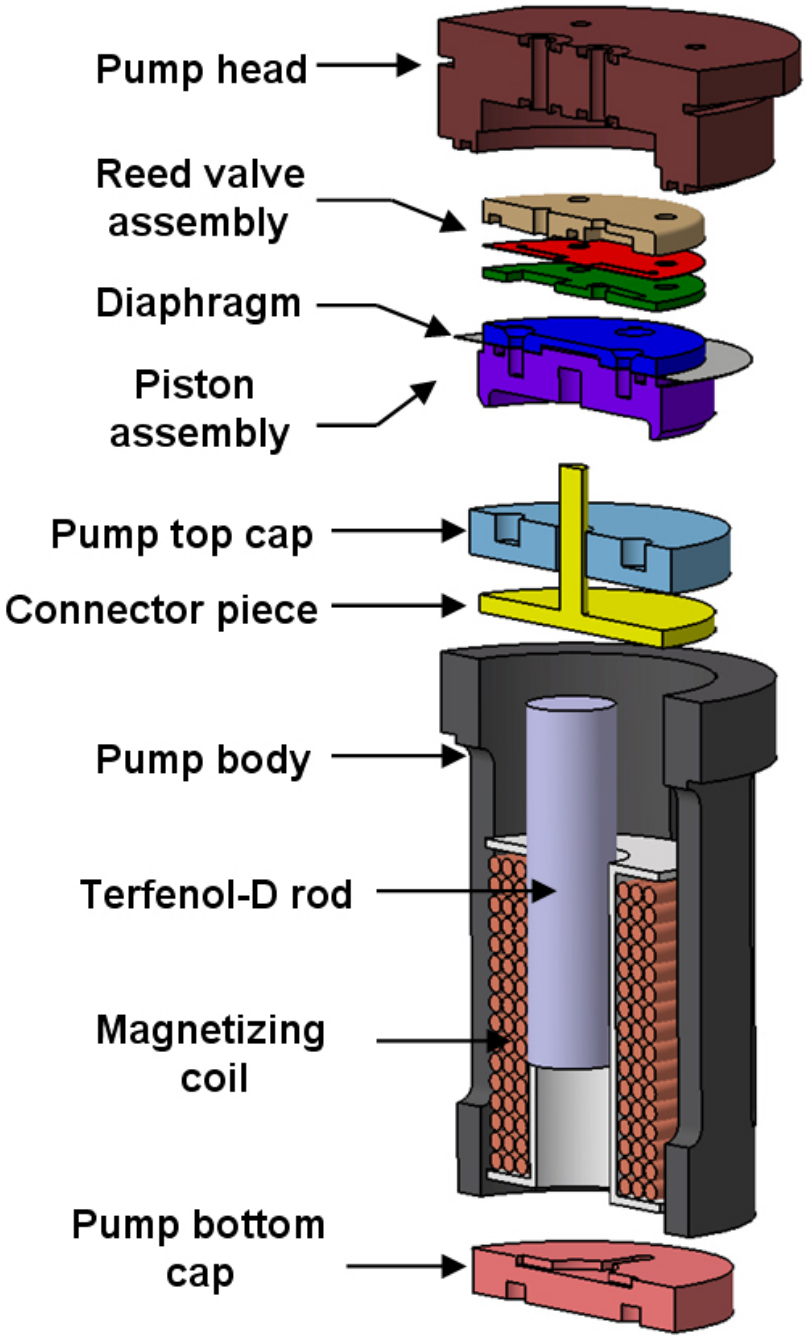

Figure 2.3: Exploded section view of Terfenol-D driven pump assembly

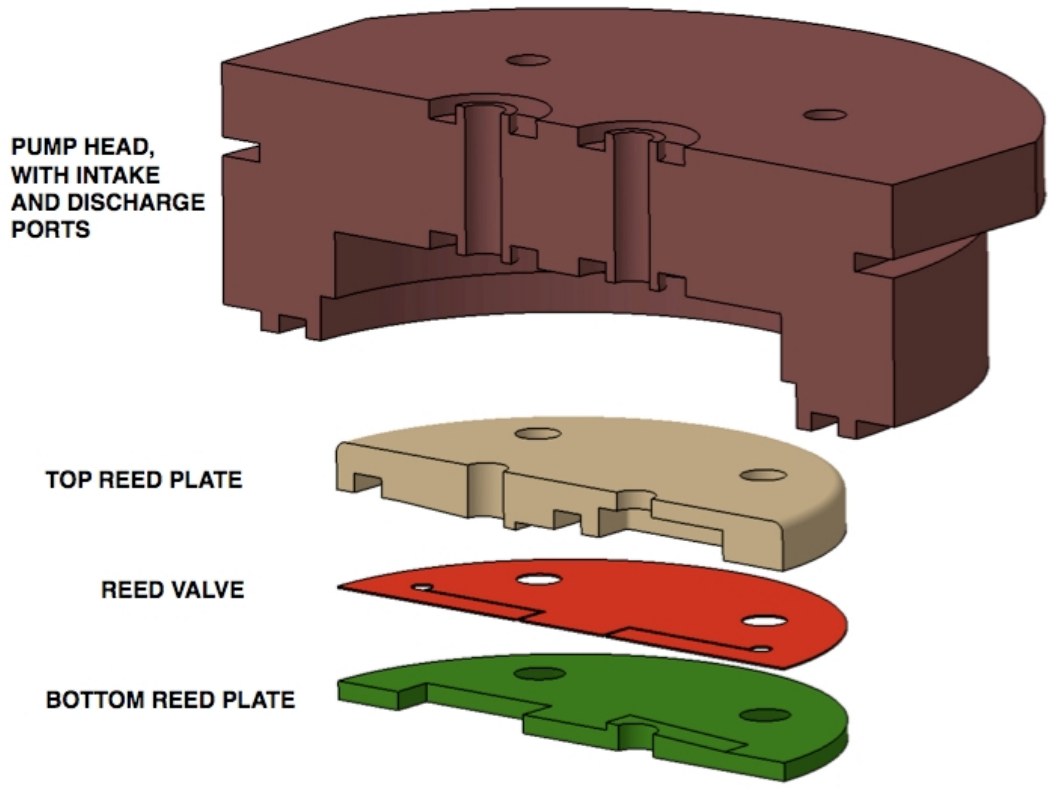

Figure 2.4: Exploded section view of pump head assembly with reed valve

head assembly shown in Figure 2.5(a). The pumping piston assembly consisted of a precision machined piston head and a base plate, with the metal diaphragm in between (Figure 2.5(b)). The pumping piston was 38.1 mm (1.5 inch) in diameter and the height of the pumping chamber was 0.51 mm (0.02 inch). The motion of the Terfenol-D rod was transferred to the pumping piston using a rigid connector piece that can slide within the pump top cap; this, in turn, affected the stress on the material due to variations in fluid pressure within the pumping chamber. The only differences in the actuator setups for the two different sized rods were the lengths of the pump bodies and the dimensions of the magnetizing coils.

The pump was mated to a hydraulic cylinder via a manifold. Fluid from the

(a) Pump head assembly with discharge and intake reed ports

(b) Pumping piston assembly with metal diaphragm

Figure 2.5: Assembled parts of the hybrid pump

pump flowed through 3.05 mm (0.12 inch) diameter holes drilled into the manifold. A port was present on the manifold to connect the accumulator and pressurize the fluid. The accumulator consisted of a 12.7 mm (0.5 inch) diameter chamber with a rubber diaphragm that separated the fluid filled manifold from a nitrogen tank; the pressure in the tank decided the bias pressure being applied to the fluid. Since the actuator does not have any flow control mechanism, it had to be manually returned back to its original position at the end of each test run; a return valve was present on the manifold for position reset at the end of a complete stroke. A double ended dual stroke hydraulic cylinder (Bimba DXDE) with 19.05 mm (3/4 inch) bore and 6.4 mm (1/4 inch) shaft was used for output motion; the overall length available for piston travel was 50.8 mm (2 inch). The fully assembled actuator test setup is shown in Figure 2.6.

The ability to apply and vary the pre-stress on a magnetostrictive driving element is important as the magnetically induced strain, or magnetostriction, is a direct function of the pre-stress applied [142, 145, 210, 212–215]. Pre-stressing the magnetostrictive material increases the peak magnetostriction obtainable from the active rod; the striction, however, decreases beyond a certain level of pre-load as seen in Figure 2.7. Pre-stressing the Terfenol-D sample is also important because it ensures that the rod is always under compressive stress, which is important because the tensile strength of Terfenol-D is much lower than the compressive strength [84].

In our setup, the prestress was controlled by three factors:

(i) Tightening the bottom cap of the pump body: Moving the bottom plate into

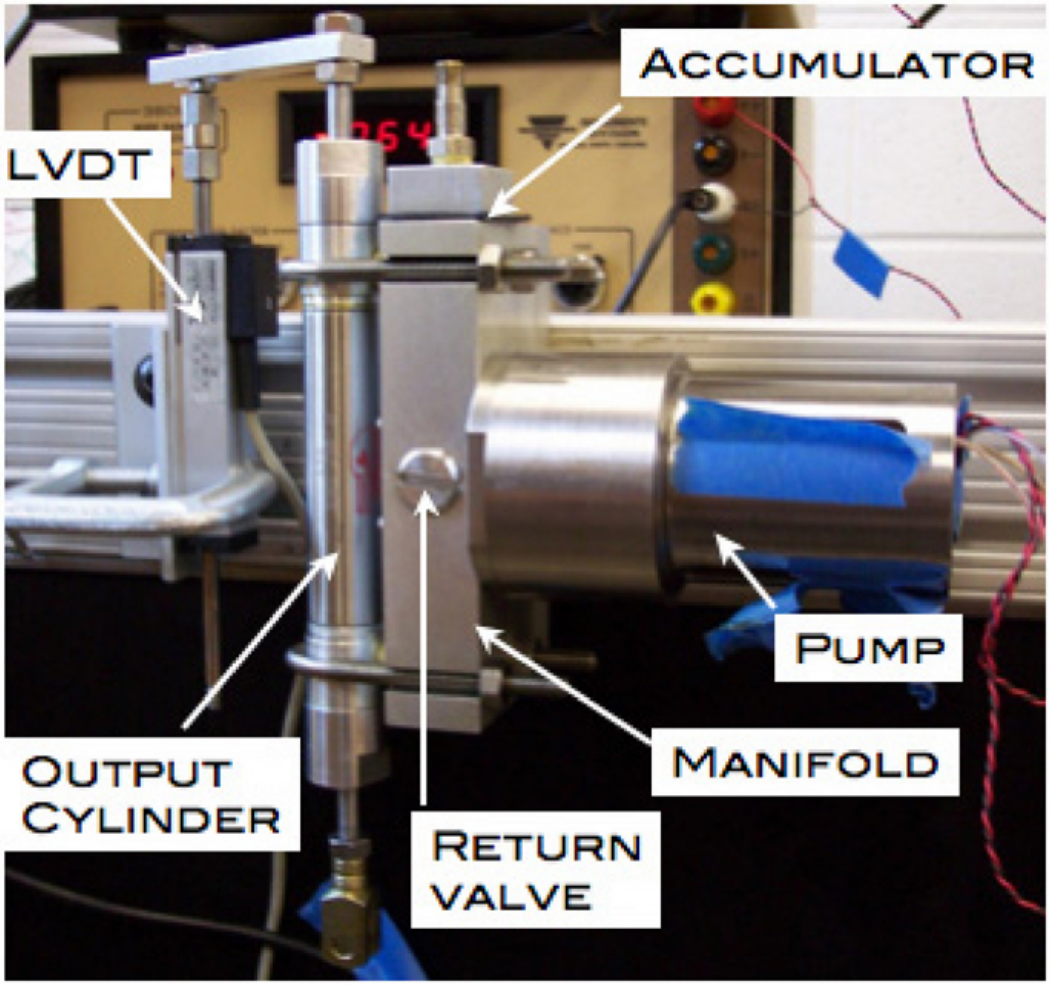

Figure 2.6: Assembled view of Terfenol-D driven actuator test setup

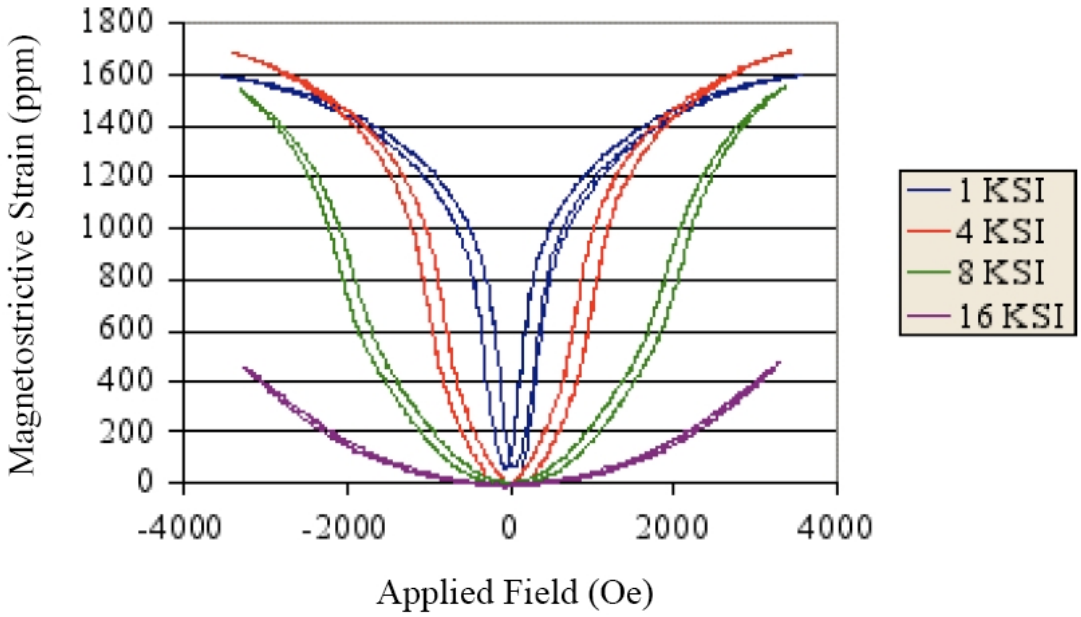

Figure 2.7: Terfenol-D strain under various preloads [141]

the pump body results in an increase of pre-strain on the rod.

(ii) Using disc springs of varying stiffness placed in the pre-stress mechanism (between the movable pre-stress connector piece and the fixed pump top cap).

(iii) Bias pressure on the fluid: Since the bias pressure acts on the entire fluidic system, it is also felt on the pumping piston. This, in turn, directly applies a force on the Terfenol-D rod through the pre-stress connector piece and affects the pre-strain.

Several physical parameters were measured during the experiments. Motion of the output shaft was measured using a linear displacement transducer (Novotechnik T-50). The induced strain in the Terfenol-D rods was measured using two strain gages mounted on the body of the rods, opposite to each other, as seen in Figure 2.8; this

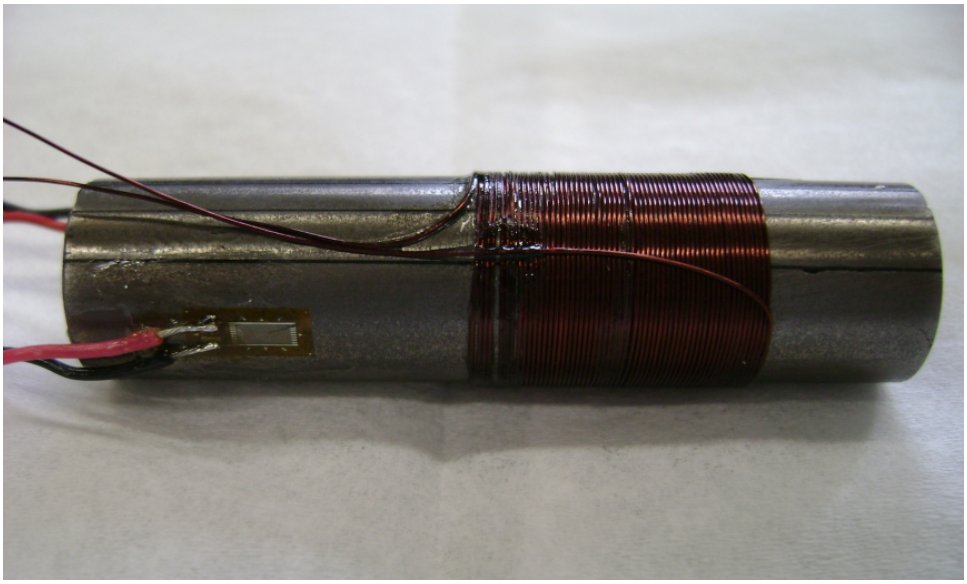

Figure 2.8: Laminated 51 mm (2 inch) long Terfenol-D rod with strain gages and sense coil

arrangement allowed us to prevent any bending of the rod while pre-stressing it during assembly. Wide Range Strain Indicators (Model 3800) from Vishay Measurement Group were used to monitor the strain gages. The flux density was measured using a 80 turn sense coil wrapped around the rods, the voltage across which is read by a fluxmeter (Model MF-50, Walker LDG Scientific Inc.). All the instruments produce voltage outputs proportional to the measurements and NI LabVIEW software was used for sampling, acquisition and storage of all the output data signals.

2.3.2 Input

The use of different power amplifiers was seen to have profound effects on the actuator performance. While initial tests were carried out with an LVC 623 amplifier manufactured by AE Techron, Inc., the second round of tests were carried out using

Table 2.1: Specifications of magnetizing coils

Parameter	51 mm Terfenol-D rod	102 mm Terfenol-D rod
Wire gauge	24	22
Number of turns	500	800
Resistance	7.2 Ω	7.8 Ω
Inductance (in air)	10.8 mH	12.3 mH

a higher capacity LVC 5050 power amplifier from the same manufacturer. It was clearly seen that the higher capacity amplifier could source required coil current at much higher frequencies, thus increasing the operational bandwidth of the pumping device. Tests on the actuator with external loads were carried out with the LVC 5050 amplifier only.

Different coil dimensions for the two different lengths of magnetostrictive rods were also a factor in the performance of the device. The coil for actuating the 51 mm rod is made of smaller diameter wire to accommodate more turns in a smaller size spool, while a larger diameter wire is used for the longer 102 mm rod actuation coil to reduce resistance while maintaining the required number of turns. Hence, the electrical parameters of the coils varied greatly, as shown in Table 2.1.

2.4 Test Results

Tests were carried out under no-load and externally loaded conditions to measure the performance of the hybrid actuator. While the no-load tests give the maximum obtainable velocity and flow rate from the hybrid pump, the load tests are used to determine the blocked force and power output of the actuator. The sampling frequency for data acquisition during all these tests was 1 kHz.

2.4.1 No-Load Tests

In the tests with no external load, the output cylinder shaft was allowed to move freely and the output motion of the actuator was measured. The only load was due to the friction from the lip seals that present on the output shaft. The frequency of the actuating signal driving the Terfenol-D rod was changed in a systematic manner to map out the entire frequency range of interest; this frequency will be referred to as the *pumping frequency*. Two different bias pressures of 345 kPa (50 psi) and 690 kPa (100 psi) were used for the tests. The displacement of the output shaft was measured using a displacement transducer. The motion of the shaft resembled a step jump that was repeated in every cycle; two representative cases at different pumping frequencies and bias pressures of 345 kPa (50 psi) and 690 kPa (100 psi) are shown in Figure 2.9(a) and Figure 2.9(b) respectively. In both cases, we can also observe the differences in the displacement profiles with changes in the driving frequency; the motion at lower frequencies has a large peak (resembling lightly damped behavior), while the motion at higher frequencies has smooth motion in every pumping cycle

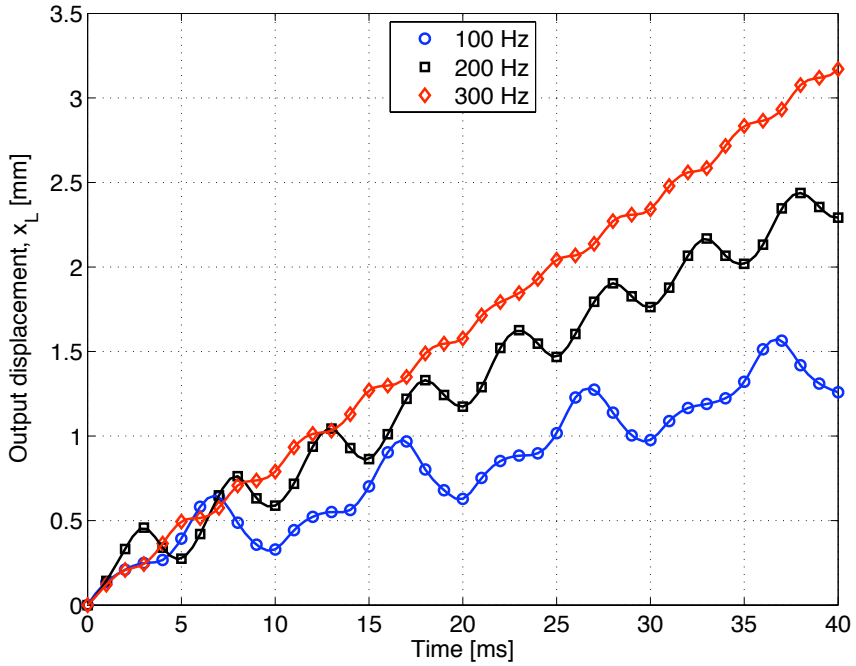

(a) 345 kPa (50 psi) bias pressure

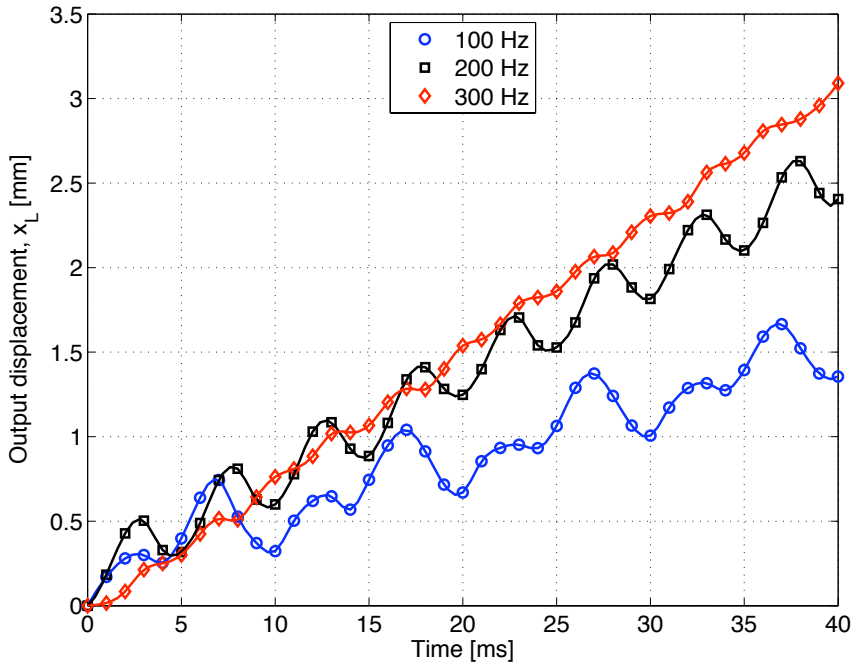

(b) 690 kPa (100 psi) bias pressure

Figure 2.9: Displacements of output shaft driven by 51 mm (2 inch) long Terfenol rod at different pumping frequencies

without any oscillations (highly damped characteristics).

The mean output velocity, v_L, was calculated as the slope of the best linear fit to the displacement data. The maximum no-load velocity is 84 mm/s (3.31 inch/s) at 325 Hz for the 2 inch long rod [Figure 2.10(a)] and 88 mm/s (3.45 inch/s) at 350 Hz for the 4 inch long rod [Figure 2.10(b)]; the corresponding values of volume flow rate were 21.3 cc/s (1.30 inch^3/s) and 22.1cc/s (1.35 inch^3/s) respectively.

A second higher power amplifier LVC 5050 was used for a second round of tests; this amplifier had higher current ratings and a broader frequency bandwidth. The bias pressures used were 690MPa (100 psi) and 1379 kPa (200 psi) for the shorter 51 mm rod, and 345 kPa (50 psi), 690 kPa (100 psi), 1035 kPa (150 psi) and 1379 kPa (200 psi) for the longer 102mm rod. The results with this power source are shown in Figure 2.11. The maximum output velocity was 98 mm/s (3.86 inch/s) at 500 Hz with the 51 mm (2 inch) rod and 90 mm/s (3.53 inch/s) at 525 Hz with the 102 mm (4 inch) rod; the corresponding values of volume flow rate were 24.8 cc/s (1.52 inch^3/s) and 22.7 cc/s (1.39 inch^3/s) respectively. The maximum pumping frequencies at which any motion of the pump is observed were 650 Hz with the shorter rod and 800 Hz with the longer rod, which were higher than the frequency limitations noticed in the case of the lower rated power amplifier.

The peak-to-peak values of induced strain, S_{ac}, under no-load test conditions were also calculated from the measured strains in the actuating rods [Figure 2.12]. These values were obtained by breaking up the total strain S_{tot} into a constant component, S_{dc}, and an oscillating component, S_{ac}, such that $S_{dc} + 0.5S_{ac} = S_{tot}$. While the strains in the 51 mm long rod were close to the maximum obtainable free strain

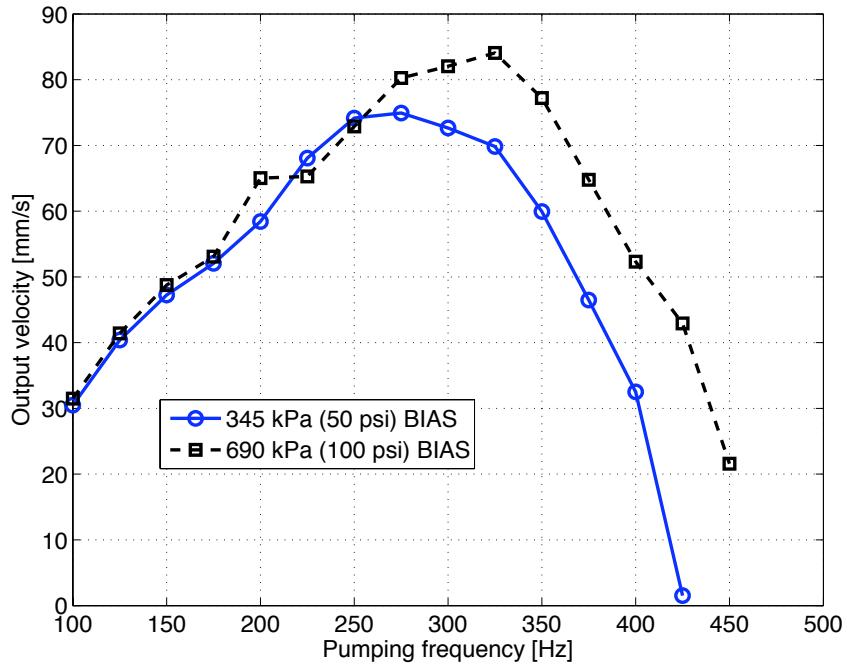

(a) 51 mm (2 inch) long Terfenol-D rod

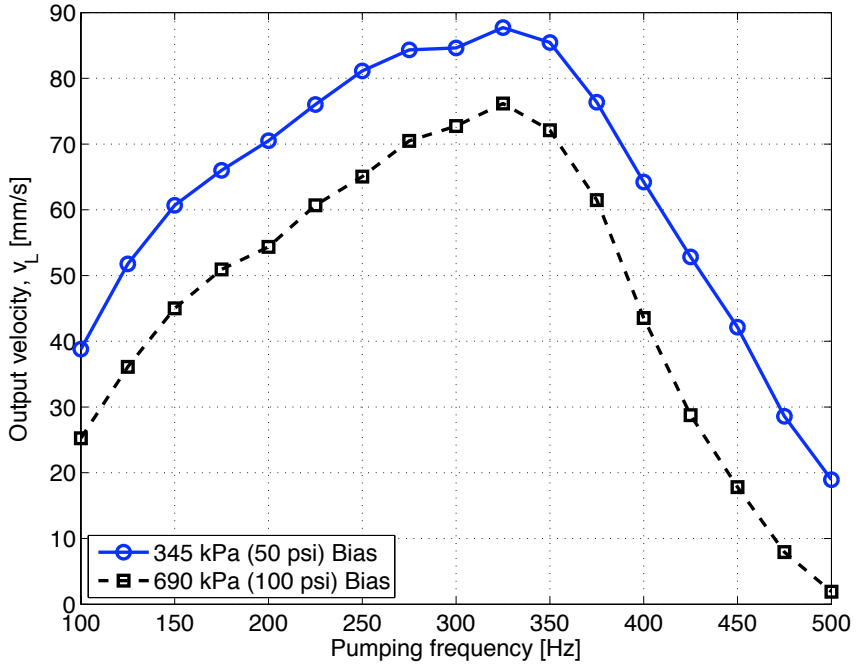

(b) 102 mm (4 inch) long Terfenol-D rod

Figure 2.10: No-load test results with LVC623 amplifier

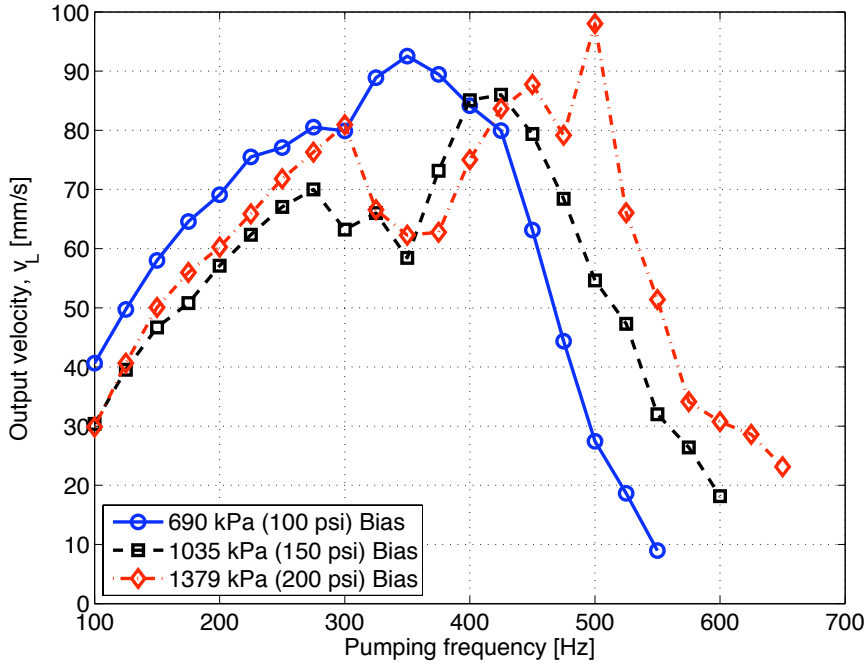

(a) 51 mm (2 inch) long Terfenol-D rod

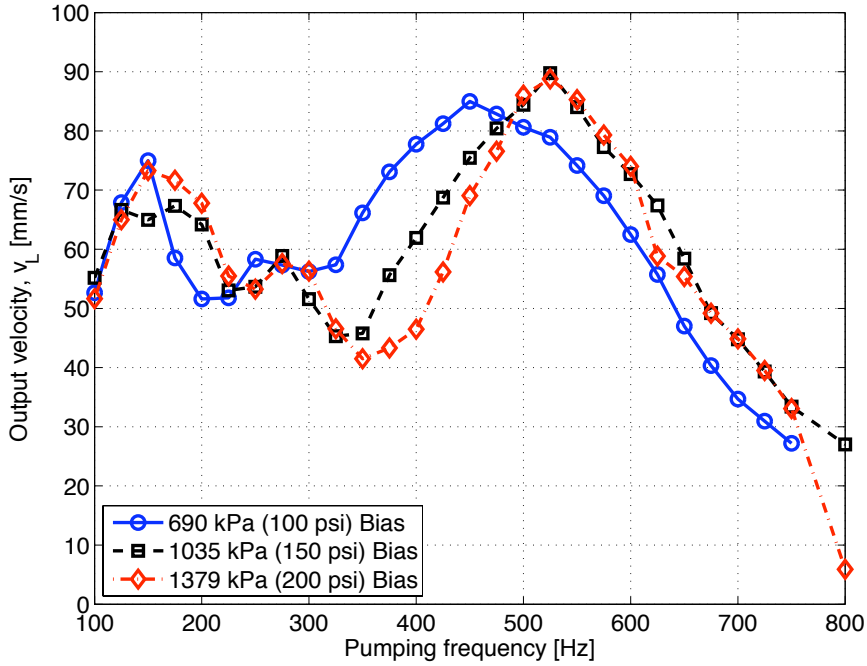

(b) 102 mm (4 inch) long Terfenol-D rod

Figure 2.11: No-load test results with LVC5050 amplifier

values for Terfenol-D, the strains in the 102 mm long rod were considerably lower. The drop in strain in the case of the 102 mm rod was also observed to be steeper than the 51 mm rod. The total induced strains are plotted for the two different actuating rods in Figure 2.13.

Under ideal conditions, the volume flow rate, Q, from the pump would be directly proportional to the pumping frequency, f, i.e.

$$Q = A_{ch} \times \epsilon \times L_a \times f \tag{2.1}$$

where A_{ch} is the cross-sectional area of the pumping chamber, ϵ is the strain in the active material and L_a is the length of the the rod. If we assume the fluid to be incompressible, then the velocity of the output shaft, v_L, is related to the flow rate Q as follows:

$$Q = A_o \times v_L \tag{2.2}$$

where $A_o = 0.25\pi(d_o^2 - d_i^2)$ is the cross-sectional area of the output cylinder available for fluid flow, d_o and d_i being the diameters of the bore and shaft respectively.

From Equation 2.1 and Equation 2.2, the output velocity v_L is directly proportional to the pumping frequency f under ideal conditions. However, the results of our tests indicate that the output increases only over a certain frequency range and then decreases rapidly. This phenomenon can be attributed to the following causes:

1. Fluid inertia: The mass of fluid in the tubing is accelerated in every cycle, hence, the inertia of this volume of fluid becomes important. In the most simple case, the fluid block in the manifold resembles a single-degree-of-freedom (SDOF) system and can be associated with a resonant peak frequency, beyond which

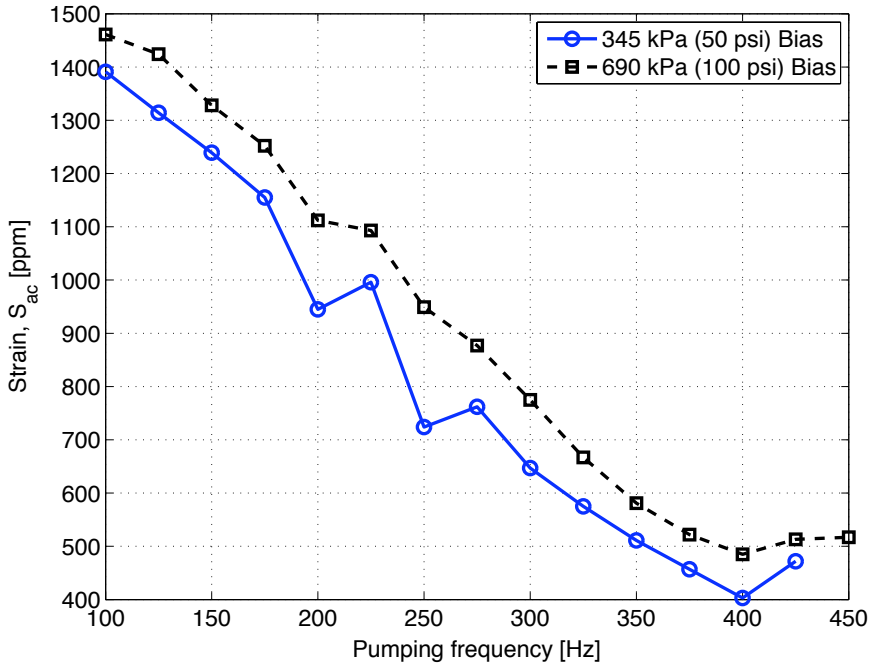

(a) 51 mm (2 inch) long Terfenol-D rod

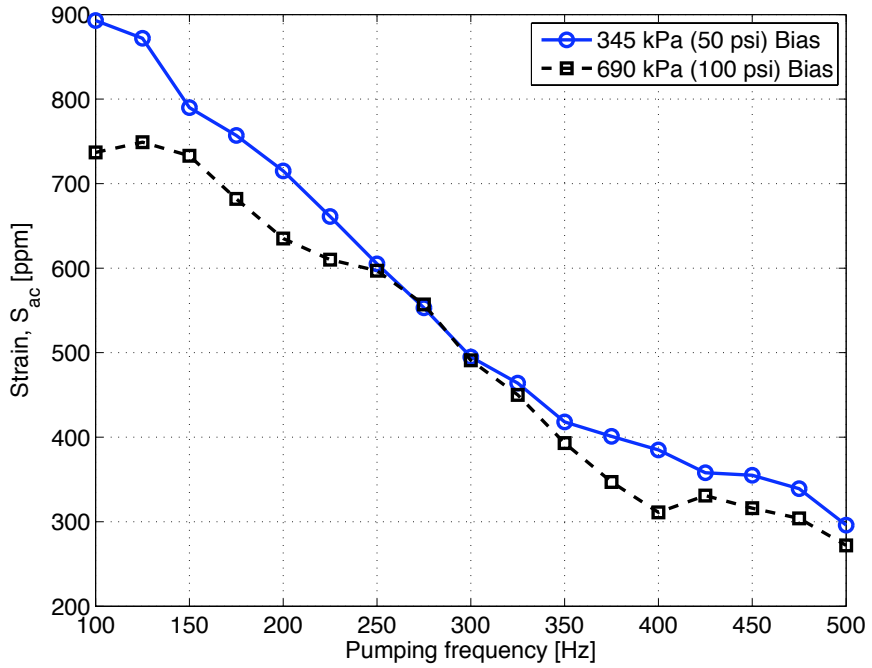

(b) 102 mm (4 inch) long Terfenol-D rod

Figure 2.12: Measured peak-to-peak strain with LVC623 amplifier

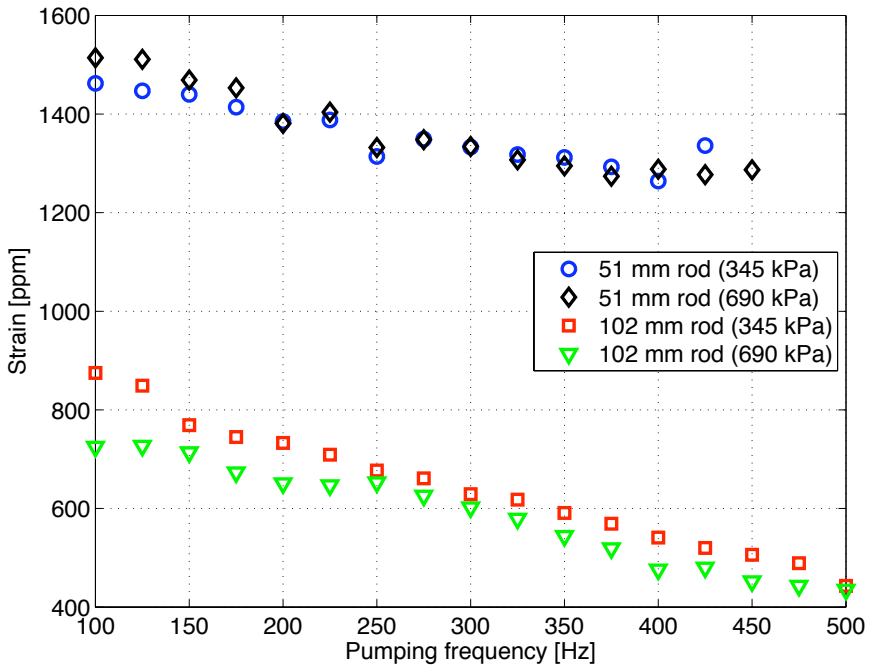

(a) Using LVC623 amplifier

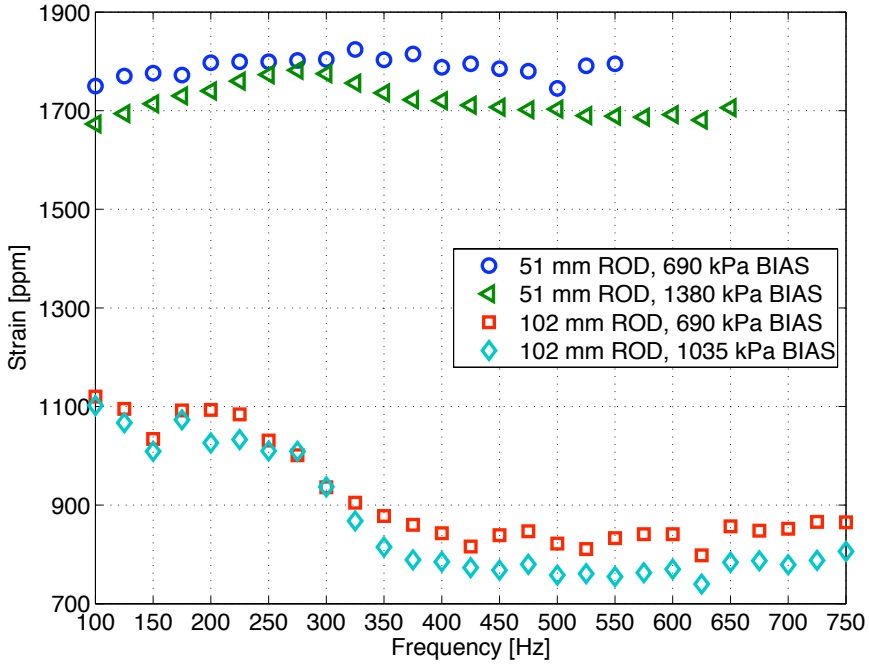

(b) Using LVC5050 amplifier

Figure 2.13: Variation of total measured strain with frequency, no-load operation

the energy required to drive the system increases exponentially. Consequently, there is a sharp drop in the movement of fluid in these sections as the frequency of operation increases and places an upper limit on the maximum frequency of operation of the pumping device.

2. Magnetic circuit properties: Due to the presence of a high inductance magnetizing coil, the input circuitry behaves as a low-pass system that prevents the build up of magnetic field in the magnetic circuit when the input signal increases, and vice versa. Hence, the driving force drops with frequency, resulting in further lowering of system performance. This effect will be further investigated in a later section.

3. Mechanical subsystems: There are three mechanical subsystems that might limit system performance:

    - Reed valves: The reed valves can be visualized as cantilever beams oscillating in a fluid. The natural frequency of the spring steel reeds (0.39 inch$\times$0.2 inch$\times$0.004 inch) vibrating in air is calculated to be 850 Hz, but the presence of hydraulic fluid reduces the resonant frequency drastically. Using empirical relations [216], we can recalculate the modified natural frequency to be $\sim$250 Hz, which is within the range of pumping frequencies used in our test setup and is definitely a limiting factor in the pump performance.

    - Output shaft: Since the output shaft undergoes a start-stop motion in every cycle, the associated friction force increases due to the stiction effect.

Though the mass of the output shaft has inertial effects too, it is much lower compared to the seal friction; however, with the addition of external loads to the output cylinder, the combined inertia of the output shaft will also be of equal importance.

- Pumping section: The natural frequency of axial vibration of the Terfenol-D rod placed within the pump body is also an important factor for efficient operation. Using Rayleigh's coefficient, we can approximate the modal frequency of the pumping section using the axial rigidity $EA(x)$ and linear mass density $m(x)$ as follows:

$$\omega_r^2 = \frac{K[Y_r(L)]^2 + \int_0^L EA(x)[Y_r'(x)]^2 dx}{M[Y_r(L)]^2 + \int_0^L m(x)Y_r^2(x)dx} \tag{2.3}$$

where M is the end mass, K is the stiffness of the disc spring(s) used for pre-stressing and L is the overall length of the rod. The end mass consists of the pre-stress connector and flux return pieces. Since the rod has uniform cross-sections and can be assumed to have same mechanical properties throughout, we have $EA(x) = EA$ and $m(x) = m$. For our test setup, we have $M = 93.2$ g, $K = 10.4 \times 10^6$ N/m, $L = 2$ inch (51 mm), $E = 30$ GPa, $A = 0.2$ inch^2 (127 mm^2) and $m = 1.2$ kg/m. Assuming the first mode as $Y_1(x) = \left(1 - \cos\frac{\pi x}{L}\right)$ for axial vibration with one end fixed and putting in the values of material properties in 2.3, we can calculate the first eigenfrequency to be 4.7 kHz. Since this value is much higher than the pumping frequencies used, we can neglect any frequency limitations of the pumping section.

An important trend noted in the results with the 102 mm rod was the presence of two distinct peaks in the velocity response of the actuator (Figure 2.11(b)). While the first peak occured at the same frequency (∼150 Hz) for all bias conditions, the second peak shifted to higher frequencies as the bias pressure increased. This suggests that the system performance was driven by two separate dynamics; the phenomenon at higher frequency (second peak) was more dependent on the fluid properties while the lower frequency effect (first peak) was independent of the mechanical system and was probably a manifestation of input dynamics.

Though the free displacement of the 102 mm Terfenol-D rod is double that of the 51 mm rod, we did not see a proportional increase in output velocity from our experiments. The reason is that the stiffness of the longer rod is half that of the shorter rod (both having the same diameter) and, hence, the blocked force is also halved. If we compare the load lines of the two actuator rods, the shorter one had lower free displacement but higher blocked force, and vice versa for the longer rod, leading to almost the same operating point for both actuators rods on a load-displacement diagram. This was verified from strain measurements from the tests using both amplifiers LVC623 (Figure 2.13(a)) and LVC5050 (Figure 2.13(b)) where we note that the actual strain of the 102 mm rod was much lower (almost half) than that of the 51 mm rod, resulting in nearly the same pumping piston displacement and consequently, similar output velocities.

2.4.2 External Load Tests

The procedure for these tests is similar to uni-directional no-load testing. Here, measured weights are hung at the end of the vertically oriented output cylinder shaft so that the actuator has to work a fixed external load. Maintaining constant load, the pumping frequency is increased (in steps of 25Hz) to the point where the motion of the actuator becomes negligible. This process is then repeated for other values of loads to get the uni-directional load performance for all pumping frequencies in the range of interest.

In our tests, graduated weights of 1.4 kg (3 lb), 2.5 kg (5.5 lb), 3.6 kg (8 lb), 5.9 kg (13 lb) and 8.2 kg (18 lb) were used to evaluate the system performance. The test results, plotted in Figure 2.14, showed a decrease in output velocity at all pumping frequencies along with a shift in the velocity peak to lower frequencies i.e. there was a clear decrease in operational bandwidth with the addition of external loads. This shift in peak response towards lower frequencies is analogous to the effect of adding mass in a SDOF system. We also noticed that at the lower frequencies, the velocity-frequency response flattened as external mass increased, while the roll-offs at higher frequencies were similar. Further, the results with the 102 mm long rod (Figure 2.14(b)) showed a shift in the second peak towards lower frequencies (from 525 Hz at no-load to 450 Hz with 5.9 kg external load), while the region of the first peak only showed a marginal decrease in output velocity.

The velocities of the output cylinder shaft versus the externally applied loads at two distinct pumping frequencies are shown in Figure 2.15. The experimentally

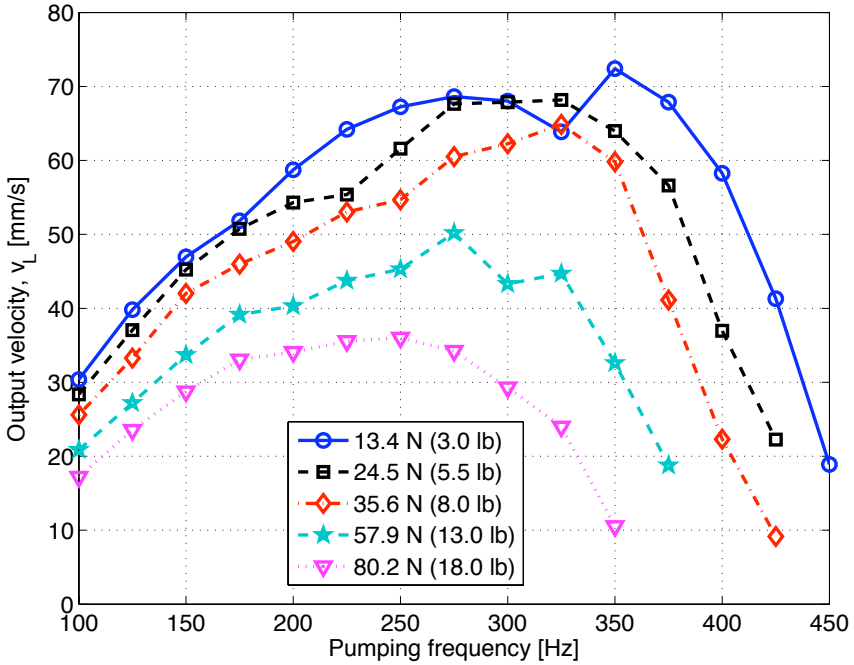

(a) 2 inch long Terfenol-D rod

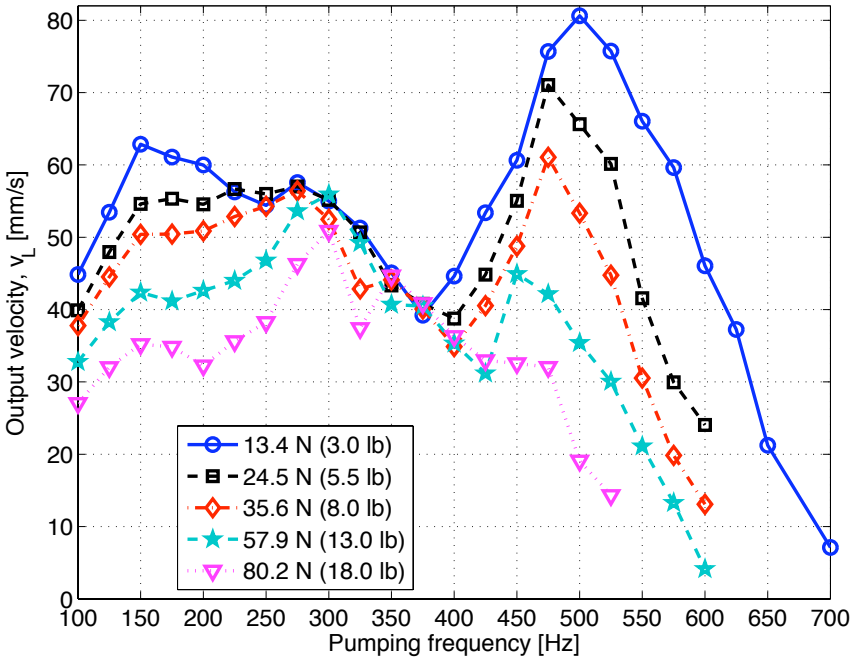

(b) 4 inch long Terfenol-D rod

Figure 2.14: Load test results with LVC5050 amplifier

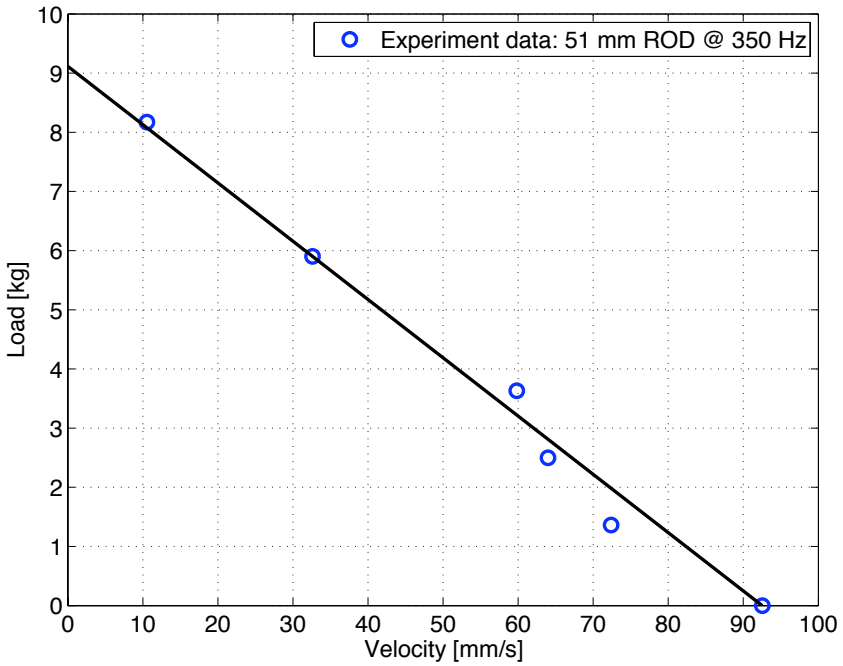

(a) 51 mm long Terfenol-D rod

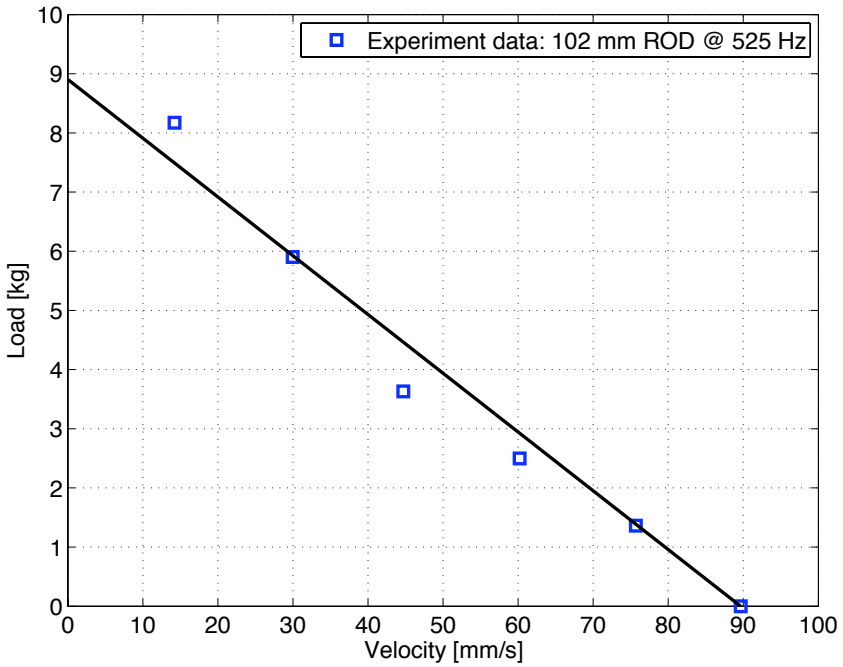

(b) 102 mm long Terfenol-D rod

Figure 2.15: Force-velocity diagrams

obtained data points were fitted with a straight line, which was then extrapolated to the horizontal velocity axis and the vertical load axis. The point where the line intersects the velocity axis gave the maximum *no-load velocity* obtainable from the system at that particular pumping frequency. The point where the line intersects the load axis is called the *blocked force* of the actuator; this denoted the maximum force that can be exerted by the actuation system. From our tests, the blocked force was calculated to be close to 20 lbf (89 N) for actuation by both Terfenol-D rods. The operating point for the actuator under any external load can then be calculated from the force-velocity diagram.

Information obtained from force-velocity diagrams were also used to calculate the maximum power output from the device. Since the actuator works on the basis of frequency rectification, the maximum power that can be obtained from the system is the area of the biggest rectangle that can be enclosed inside the linear load line [72, 76, 85]. Thus, maximum power output, P_{out}, is half the area enclosed under the load-velocity diagram i.e.

$$P_{out} = \frac{1}{4} \times F_{block} \times v_{no-load} \tag{2.4}$$

where F_{block} is the blocked force and $v_{no-load}$ is the maximum output velocity (under no-load conditions) of the actuator. This method was used to calculate the maximum power output from the device for all the pumping frequencies investigated and the variations are shown in Figure 2.16. We can see that the maximum power obtainable (theoretically) from the system are 2.78 W and 3.36 W with the 51 mm and 102 mm Terfenol-D rods respectively.

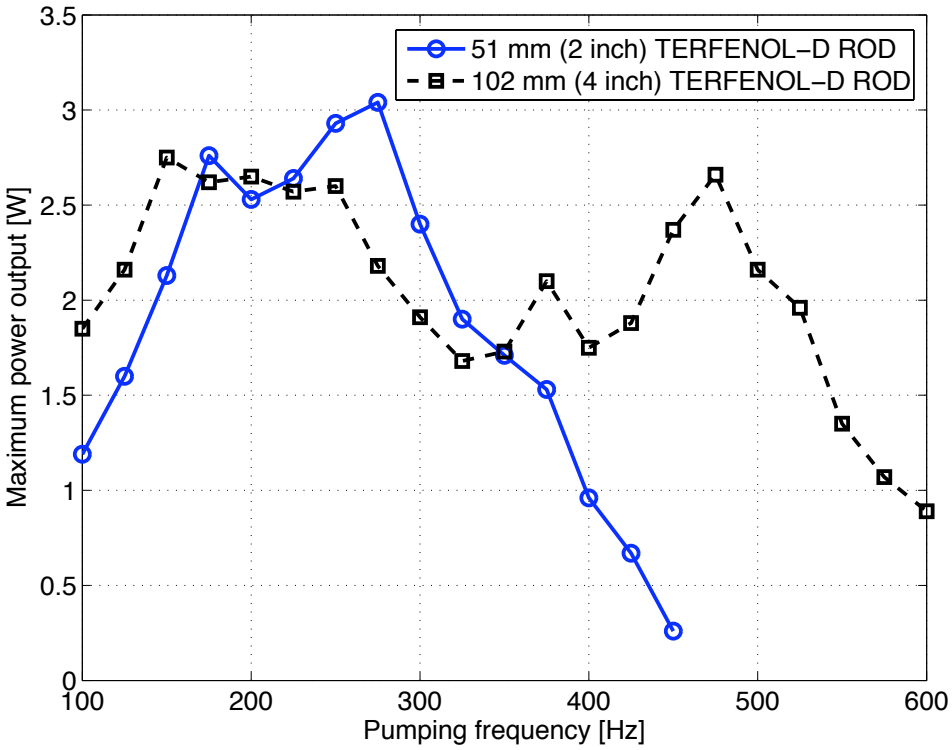

Figure 2.16: Maximum output power from hybrid actuator at different frequencies

2.4.3 Characteristics of Driving Magnetic Circuit

Due to the presence of a highly inductive magnetizing coil, the magnetic circuit within the pump body was seen to have a low-pass filter effect on the input driving signal. Since magnetizing coils and enclosing pump bodies of two different sizes were used for the 51 mm and 102 mm long Terfenol-D rods, the properties of the magnetic circuits are different too. The magnetic flux density through the active material was measured at all the test conditions using a sense coil and a fluxmeter. As the driving signal was a sinusoid with a dc offset, the measured flux density could be broken up into a constant part (B_{dc}) along with an oscillating component (B_{ac}) at each frequency of operation. The amplitudes of B_{ac} at different frequencies for the two amplifiers used are shown in Figure 2.17 and Figure 2.18.

The roll-off observed in the driving flux density was a major factor responsible for the decrease in output performance of the actuator at higher frequencies and placed a limit on the maximum pumping frequency that could be used to drive the pumping section. The primary reasons for this are as follows:

1. Coil inductance: The magnetizing coil can be viewed as an R-L circuit having the characteristics of a low-pass filter. Hence, as we increase the frequency of the input signal keeping input voltage a constant, the output current decreases considerably. This, in turn, reduces the magnetic field generated by the coil and ultimately results in lower induced strain.

2. Eddy currents and skin effect: The reluctance of the magnetic circuit also increases with frequency due to the magnetic skin effect [217,218]. More and more

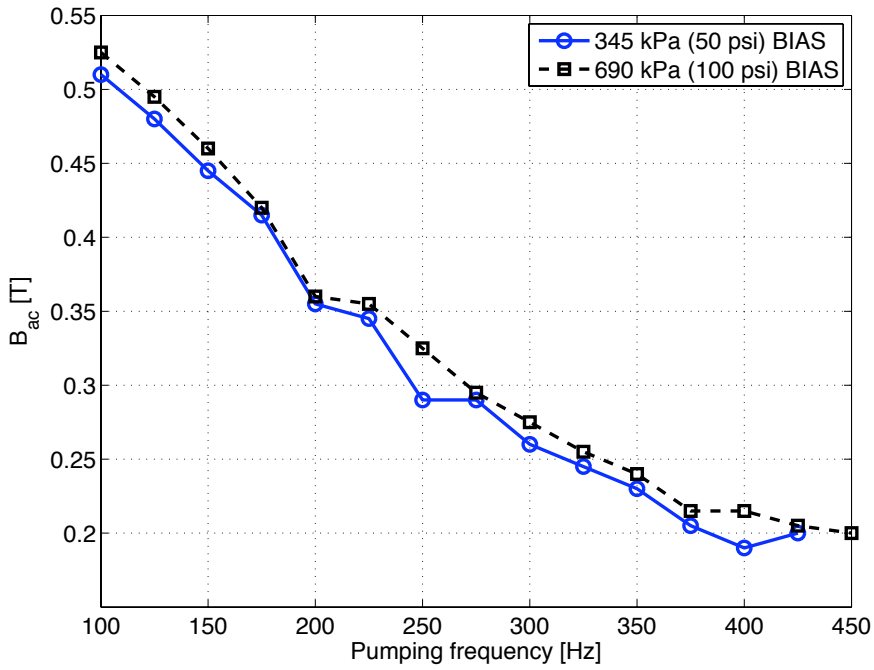

(a) 51 mm (2 inch) long Terfenol-D rod actuation

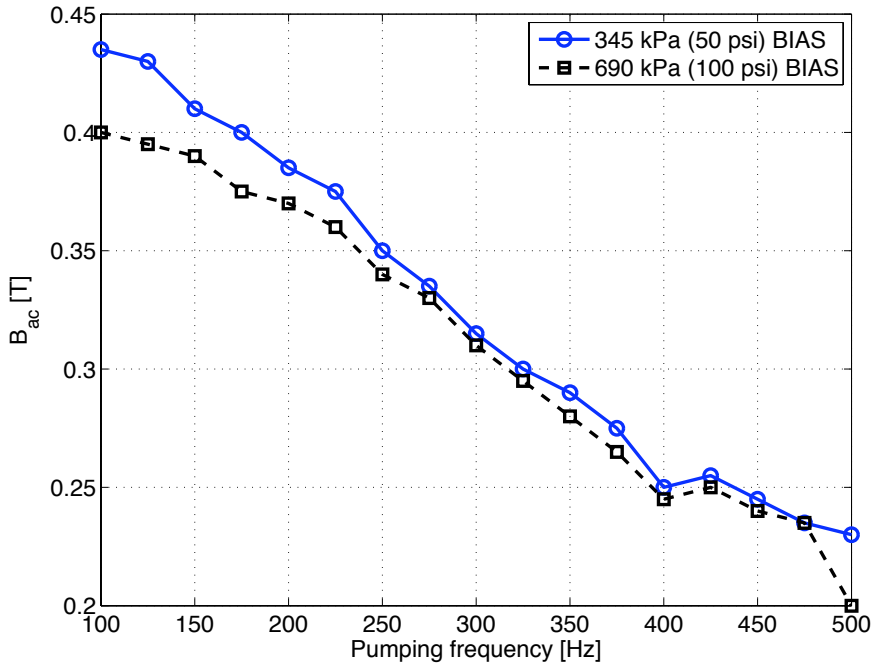

(b) 102 mm (4 inch) long Terfenol-D rod actuation

Figure 2.17: Variation of AC component of flux density with frequency using LVC 623 amplifier

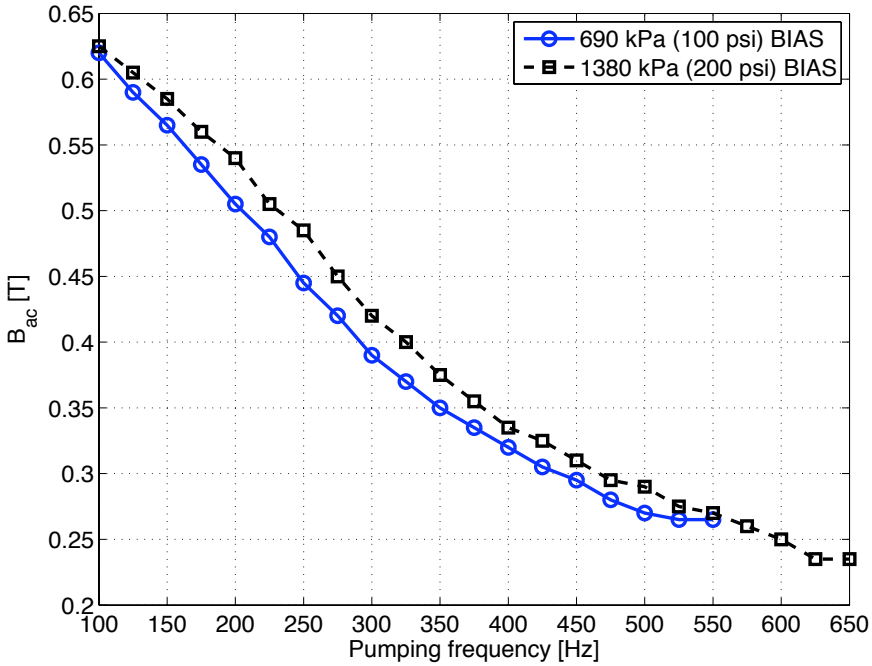

(a) 51 mm (2 inch) long Terfenol-D rod actuation

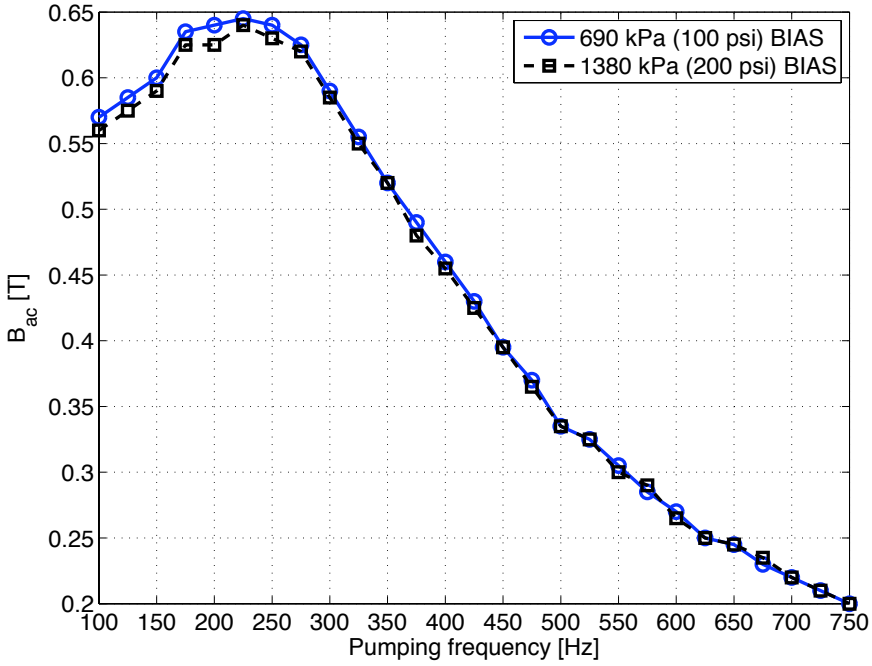

(b) 102 mm (4 inch) long Terfenol-D rod actuation

Figure 2.18: Variation of AC component of flux density with frequency using LVC 5050 amplifier

flux lines tend to get concentrated towards the outer surfaces of the magnetic flux return paths, thus lowering the effective cross sectional area available. This effect, however, should affect the cross-sectional flux density distribution in the Terfenol-D rods to a lesser extent than the return flux path in our frequency range of interest due to the lower permeability and lower electrical conductivity of the former [219]. To reduce the effect of eddy currents, the Terfenol-D rods are laminated and slots are cut into the pump body.

The use of higher capacity power amplifiers and better compensating circuits can help to reduce these effects; however, this reduces the effective energy density of the actuator and makes the overall system inefficient. These results clearly corroborate the fact that the magnetostrictive tranducer and the electronic power amplifier cannot be designed independently from each other [220].

2.5 Dynamic Tests

2.5.1 Experimental Data

In order to further investigate the frequency response of the mechanical pumping device which houses the Terfenol-D rod and magnetizing coil, we carried out a set of frequency sweeps at different control voltage levels. Such tests have also been carried out earlier to find the material properties under different driving conditions and pre-stress levels [137, 142, 143, 221–223]; however, our aim was to determine the characteristics of our particular experiment setup. In our tests, frequency sweeps from 100 Hz to 1 kHz, in steps of 100 Hz, were run on the pump setup at three different

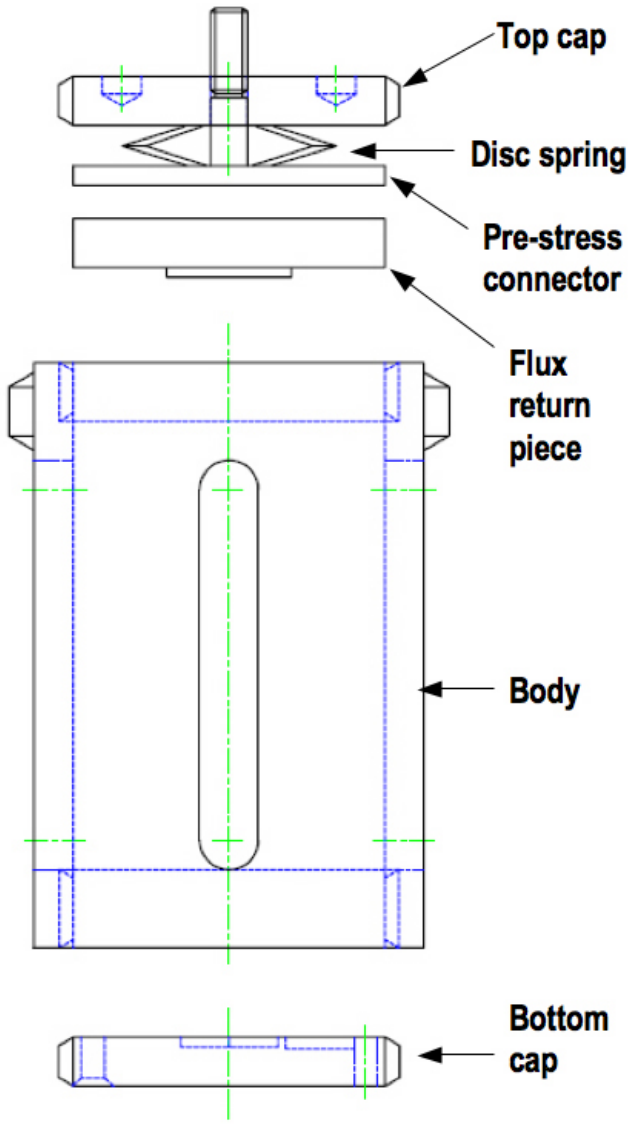

Figure 2.19: Section view of dynamic test setup for pumping section

control input voltage levels (2V, 4V, 5V). A single stainless steel disc spring was placed between the pump top cap cap and the connector piece to provide an axial load on the Terfenol-D rods [Figure 2.19]; the manufacturer rated value of spring stiffness is 3.21×10^7 N/m. The body, bottom cap and flux return piece were made of high permeability steel, with the Terfenol-D placed between the bottom cap and flux return piece for testing. The pre-strain for both Terfenol-D samples was $\sim$600 ppm. The LVC5050 amplifier was used for all the dynamic tests.

From the results with the 51 mm long rod, we noticed that while the input current to the magnetizing coil was almost held constant over the entire frequency range (Figure 2.20(a)), the magnetic flux density in the Terfenol-D rod dropped rapidly with increasing frequency (Figure 2.21(a)); this phenomenon was expected because of the highly inductive nature of the magnetizing coil and the dynamics of the magnetic circuit. A corresponding drop was also noticed in the measured strain (Figure 2.22(a)), which was because the induced strain in the sample was directly driven by the corresponding magnetizing input.

A similar roll-off was also seen in the results with the 102 mm long rod. An additional effect seen in this case is the presence of a peak in the amplifier output current [Figure 2.20(b)]. The peak occurred near between 150 Hz and 200 Hz for control input voltages between 4 V and 5 V, and coincided with the first peak in the output velocity results with the 102 mm rod driven by the LVC5050 amplifier [Figure 2.11(b)]; hence, we can conclude that this phenomenon was purely due to characteristics of the input circuitry and magnetizing coil. The effect of the frequency response of the coil current is directly seen in the measured flux density and the strain

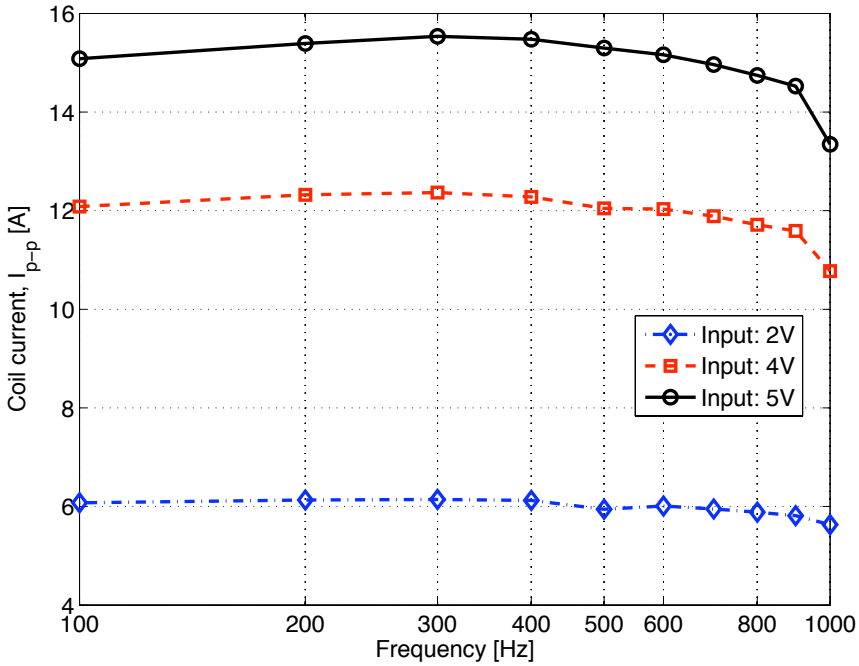

(a) 51 mm (2 inch) long Terfenol-D rod

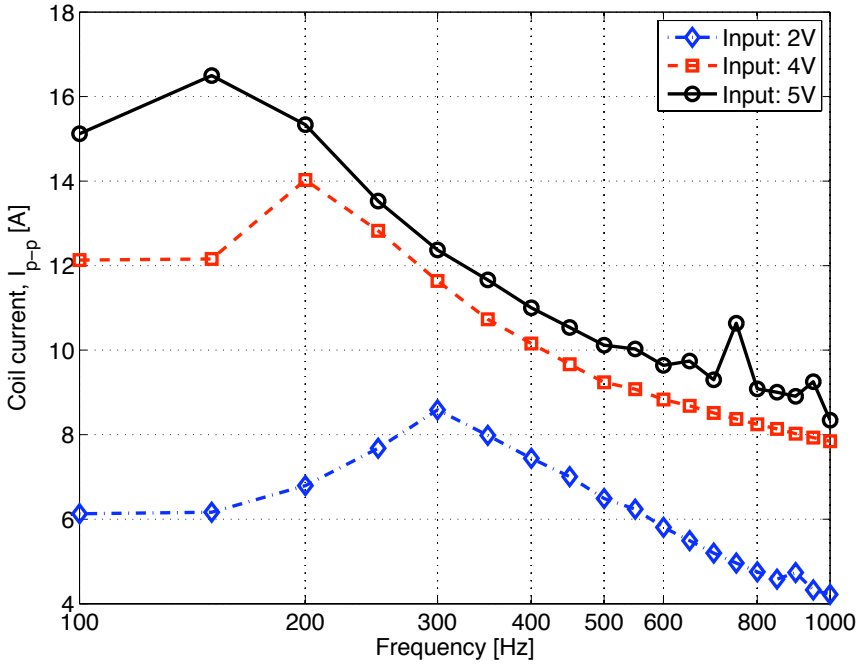

(b) 102 mm (4 inch) long Terfenol-D rod

Figure 2.20: Dynamic test results for amplifier current with different lengths of Terfenol-D rod

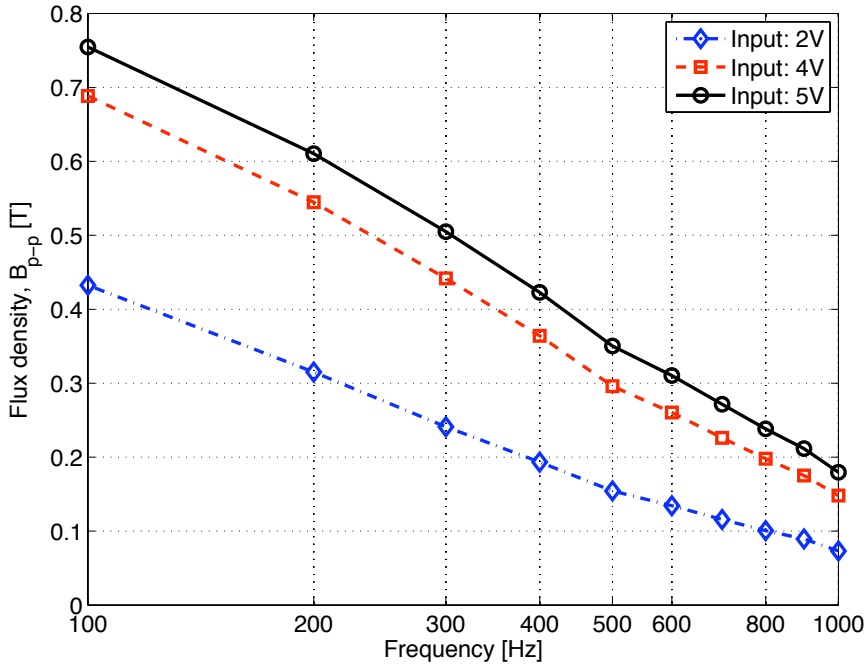

(a) 51 mm (2 inch) long Terfenol-D rod

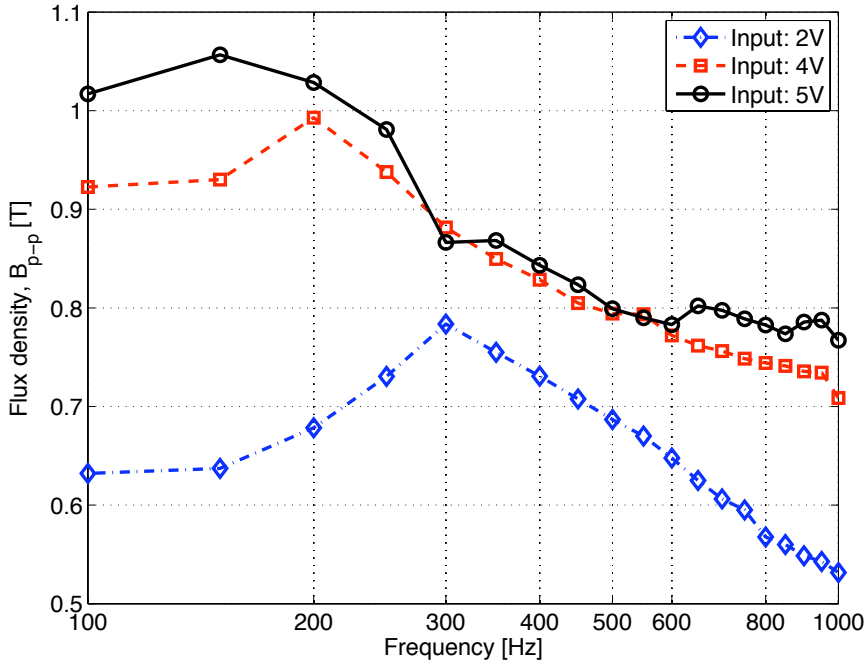

(b) 102 mm (4 inch) long Terfenol-D rod

Figure 2.21: Dynamic test results for flux density with different lengths of Terfenol-D rod

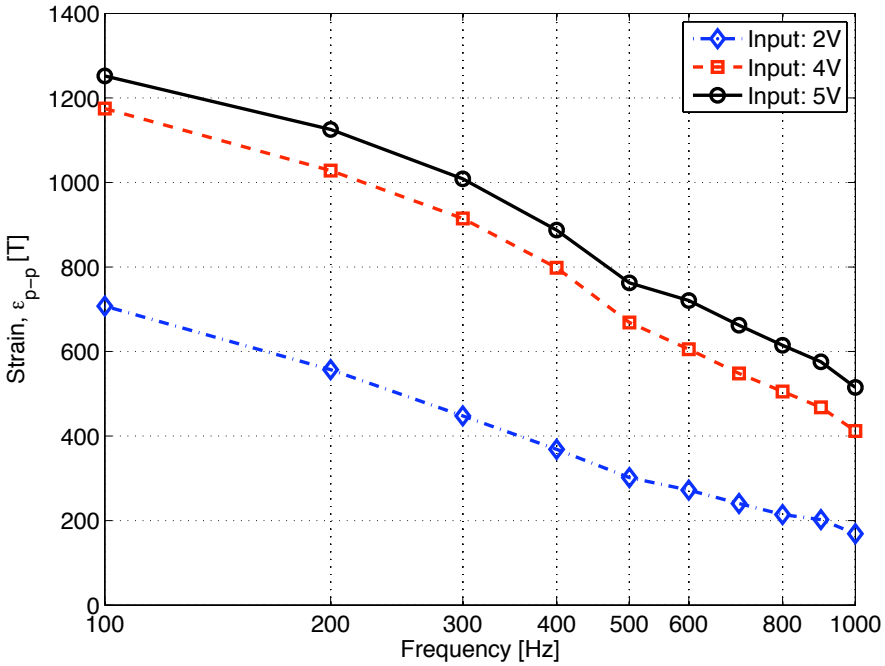

(a) 51 mm (2 inch) long Terfenol-D rod

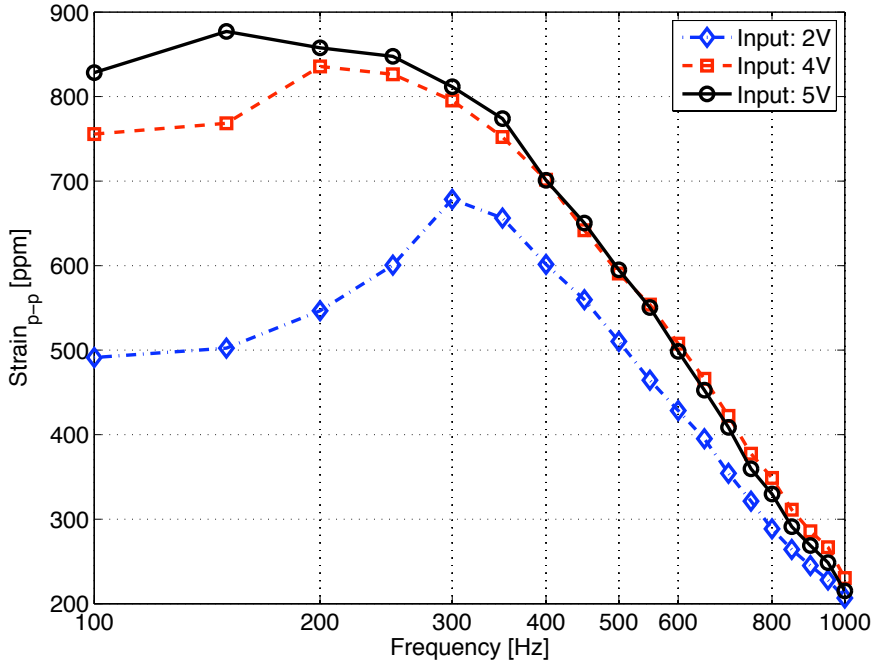

(b) 102 mm (4 inch) long Terfenol-D rod

Figure 2.22: Dynamic test results for induced strain with different lengths of Terfenol-D rod

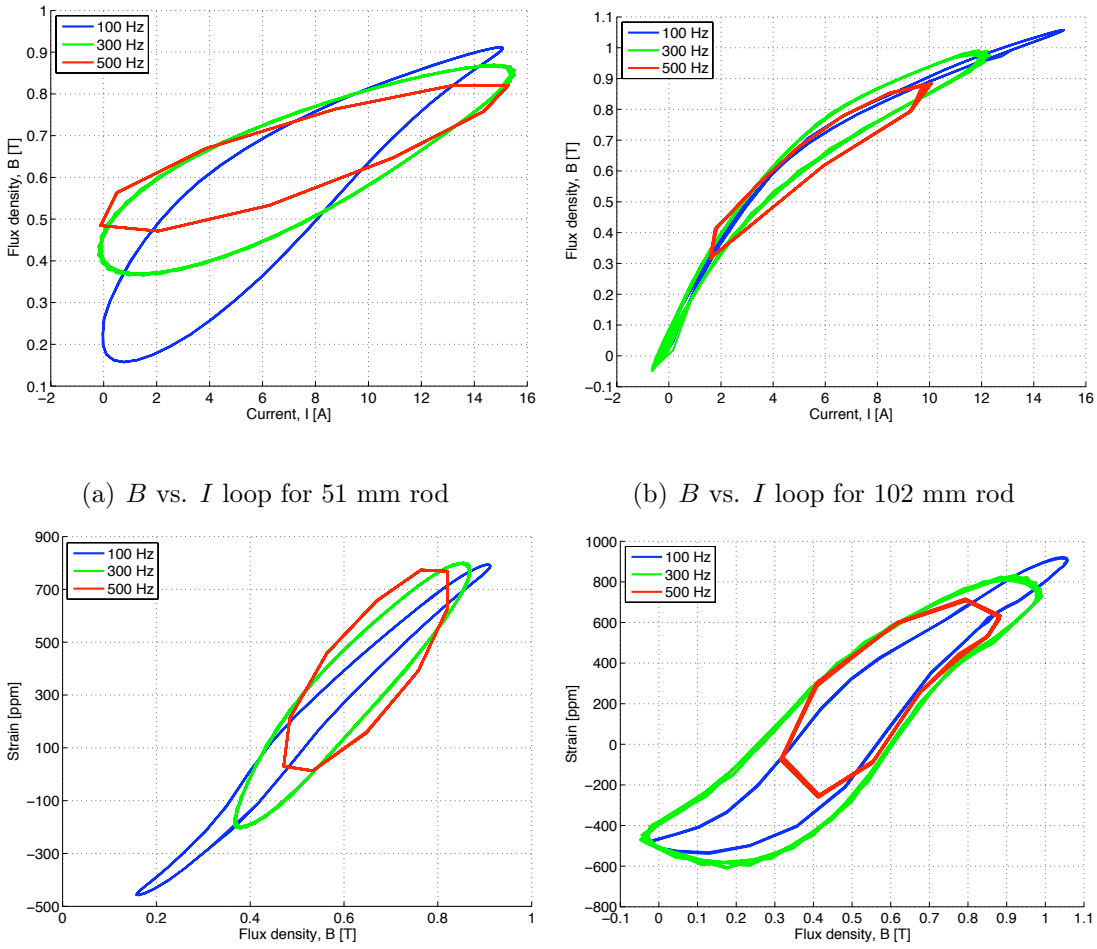

(a) B vs. I loop for 51 mm rod

(b) B vs. I loop for 102 mm rod

(c) *Strain* vs. B loop for 51 mm rod

(d) *Strain* vs. B loop for 102 mm rod

Figure 2.23: Hysteresis loops from dynamic tests

in the active material, as seen in Figure 2.21(b) and Figure 2.22(b) respectively.

The difference in magnetic and actuation behaviors of the driving rods are also observed from their hysteresis loops; the magnetization loops are shown in Figure 2.23(a) and Figure 2.23(b), while the corresponding strain vs. flux density characteristics are shown in Figure 2.23(c) and Figure 2.23(d) for the 51 mm and 102 mm long rods respectively. The magnetic flux density developed in the samples was a very strong function of frequency, as is noted by the extremities of the loops. Although

the current changed from zero to the maximum value of 15 A at all frequencies for the 51 mm rod, the amplitude of the magnetic flux density through the rod decreased with frequency. As a result of this magnetic *inertia*, the corresponding induced strain in the magnetostrictive rod also dropped with frequency.

2.5.2 Magnetic path calculations

2.5.2.1 Reluctance method

Since Terfenol-D is a material with very low permeability, the magnetic circuit has to be carefully designed for maximum efficiency [133]. The first calculations are based on classical techniques where the magnetic reluctance of each part of the magnetic circuit is calculated from the corresponding geometric dimensions and magnetic properties of the material. The pre-stressed pump body is axisymmetric; a sectional view is shown in Figure 2.24. These calculations are done assuming both the core material, Terfenol-D, to have constant relative permeability (μ_{r_A}) of 5 while the flux return path, made of magnetic steel (12L14 grade), has relative permeability (μ_{r_S}) of 1200; the distribution of the magnetic flux is also assumed to be uniform over the entire cross-section.

With respect to the geometry shown in Figure 2.24, the reluctances of the different parts are as follows:

1. Terfenol-D rod: The reluctance of the core material, $\Re_A$, depends on the length

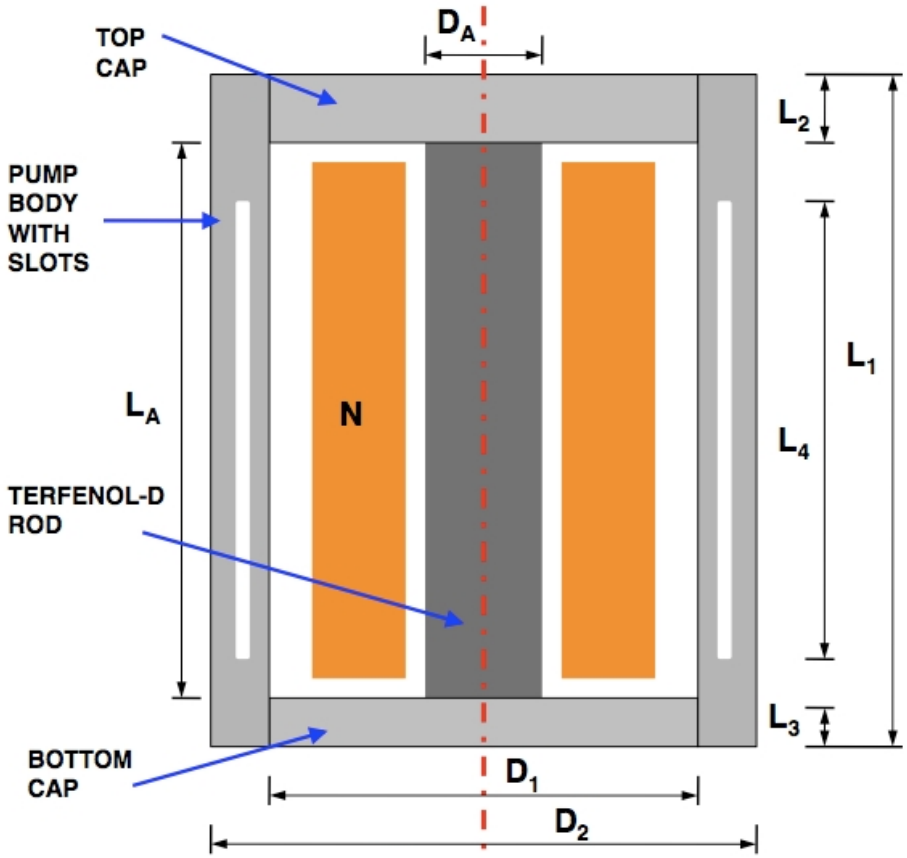

Figure 2.24: Cross-sectional view of pump body with Terfenol-D rod

L_A and cross-sectional area A_A as follows:

$$\Re_A = \frac{L_A}{\mu_0 \mu_{r_A} A_A} \tag{2.5}$$

2. End caps: In case of the top and bottom end caps, the flux flows in the radial direction. If we consider a circular element of thickness dr at radius r [Figure 2.25], the the reluctance of the element is given by

$$d\Re = \frac{dr}{\mu_0 \mu_r (2\pi r t)}$$

where t is the thickness of the element. Upon integrating from $r = R_1$ to $r = R_2$,

the reluctance of an end cap is given by

$$\Re = \int d\Re \int_{r=R_1}^{R_2} = \frac{1}{2\pi\mu_0\mu_r t} \log\left(\frac{R_2}{R_1}\right)$$

Hence, the reluctances of the top and bottom cap are

$$\begin{aligned} \Re_{TOP} &= \frac{1}{2\pi\mu_0\mu_{r_S} L_2} \log\left(\frac{D_2}{D_A}\right) \\ \Re_{BOTTOM} &= \frac{1}{2\pi\mu_0\mu_{r_S} L_3} \log\left(\frac{D_2}{D_A}\right) \end{aligned} \tag{2.6}$$

3. Body: The outer pump body has an inner diameter D_1 and outer diameter D_2, and its overall length can be divided into two parts; length L_4 has slots cut into it for reducing eddy currents and its cross-sectional area can be assumed to be half that of the remaining part. Using these dimensions, we get

$$\Re_{BODY} = \frac{1}{\mu_0\mu_{r_S}} \left(\frac{L_1 - L_4}{A_{BODY}} + \frac{L_4}{0.5A_{BODY}}\right) \tag{2.7}$$

If N be the number of turns present in the magnetizing coil and I is the current through the coil, the the flux ϕ in the magnetic circuit is given by

$$\phi = \frac{NI}{\Re_A + \Re_{TOP} + \Re_{BOTTOM} + \Re_{BODY}} \tag{2.8}$$

The flux density through the core Terfenol-D rod is then given by

$$B_A = \frac{\phi}{A_A} \tag{2.9}$$

Putting corresponding values in Equation 2.9, the flux density in the Terfenol-D rod for current $I = 15$ A in the coil is calculated to be 0.9 T.

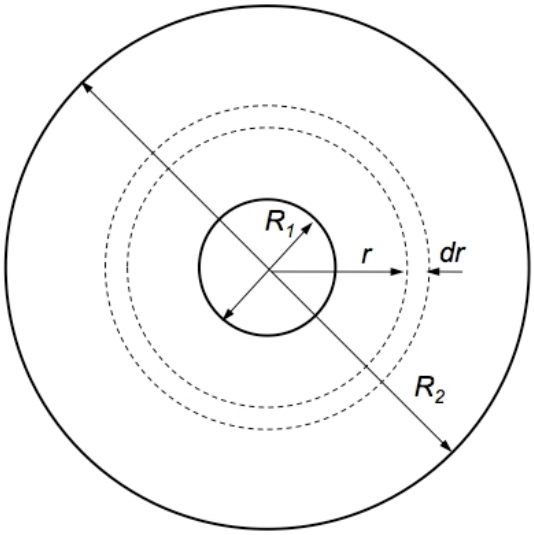

Figure 2.25: End cap with elemental cross section

2.5.2.2 FEA of Magnetic Circuit

Since the permeabilities of both materials (Terfenol-D and steel) depend on the actual magnetic field in the samples, the simple calculations might not be sufficient to find accurate values of magnetic flux densities in different parts of the magnetic circuit, especially because we wish to operate near the saturation regime of the core Terfenol-D material. Also, the distribution of magnetic field within the sample is non-uniform in reality and numerical computational tools can be used to obtain more accurate results. Finite element models have previously been used for magnetic analysis of magnetostrictive devices [224]. Using COMSOL Multiphysics, a simple 2-D axisymmetric model of the pumping section was analyzed to calculate the magnetic variables under different conditions and check for any effects of eddy currents within our frequency range of interest. The complete B-H curves of Terfenol-D and 12L14

steel were used for the simulations; these were provided to the FEA software as a table containing B vs μ_r data. The cross-sectional dimensions of the magnetizing coil are 8 mm (in radial direction) by 45.7 mm (in axial direction); for simulation, the current density in the coil is calculated assuming 500 turns. Three different values of coil currents are used; 5 A, 10 A and 15 A. The simulations were carried out in the absence of any eddy currents.

The first noticeable result is the uniformity of the magnetic flux density at all magnetizing currents, both in the Terfenol-D core as well as the outer steel body [Figure 2.26]. This is verified from the plot of magnetic flux densities across a radial section, as shown in Figure 2.27. The effect of magnetic saturation of the materials is also seen clearly in Figure 2.27 which shows a radial cross-section of the simulation model; even though the coil current is increased linearly in steps of 5A, the peak flux densities in the magnetostrictive core are 0.47 T, 0.68 T and 0.80 T, which is clearly not a proportional increase and shows the effects of magnetic saturation.

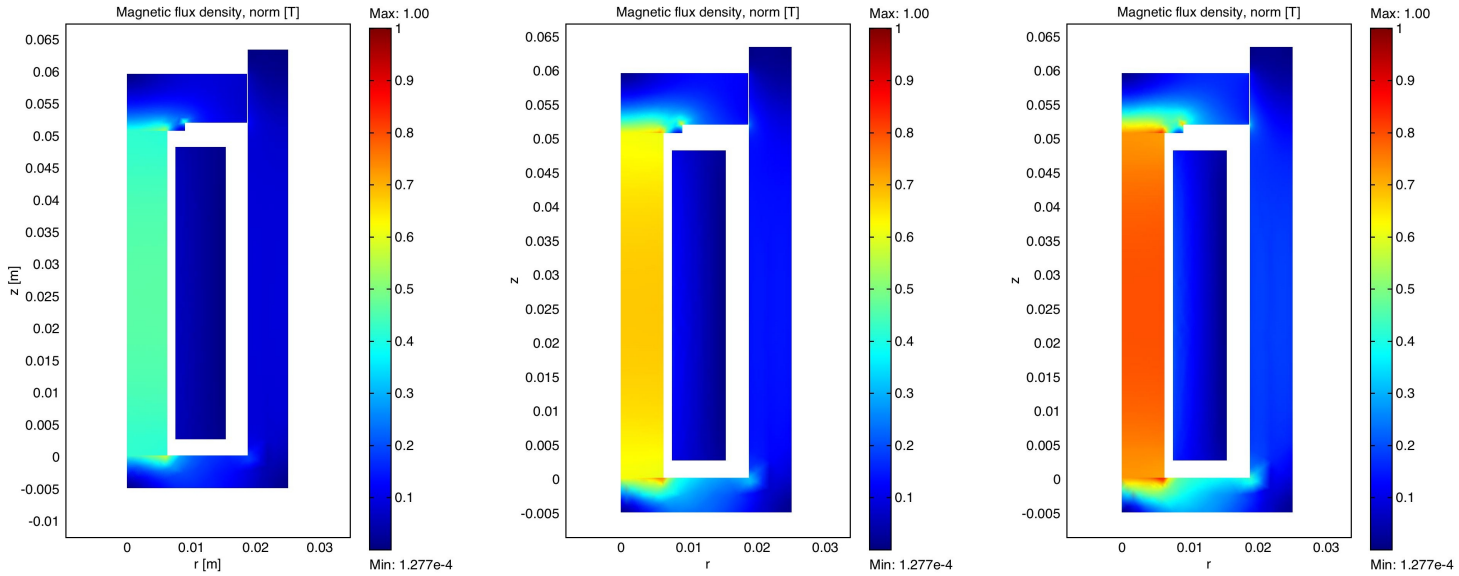

(a) 5 A (b) 10 A (c) 15 A

Figure 2.26: Flux density distribution with varying coil currents, no eddy currents

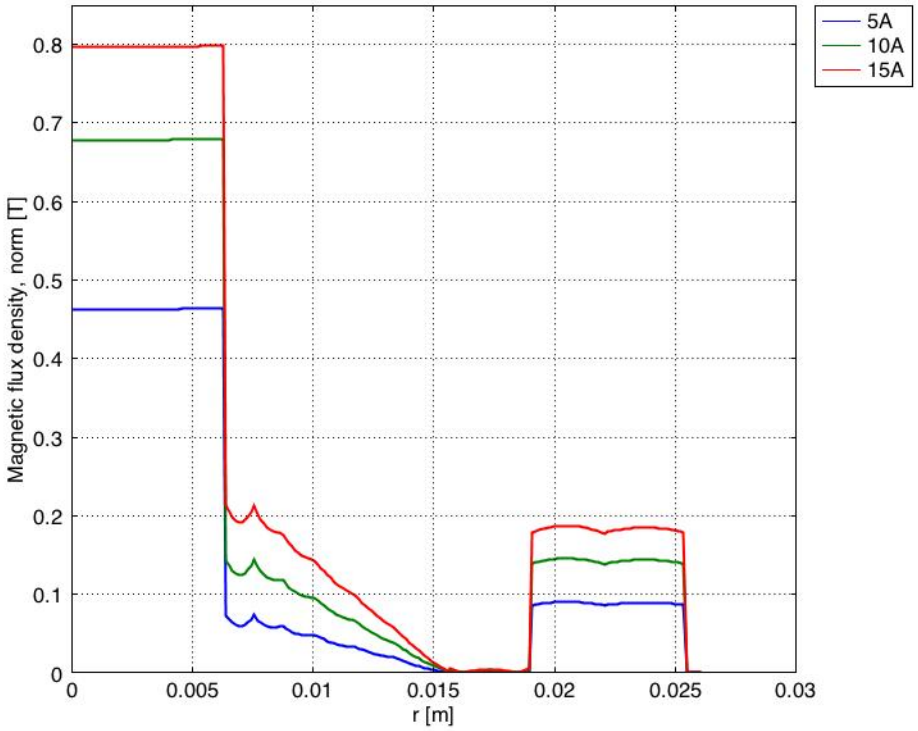

Figure 2.27: Flux density distribution in magnetic path from r = 0 to r = 30 mm, z = 25 mm (no eddy currents)

2.6 Conclusions

A hybrid hydraulic actuation system was developed using a Terfenol-D actuated hybrid pump as the fluid pressure source and hydraulic fluid as the force transmission medium. Extensive experimental studies in uni-directional mode were performed on this actuation system. No-load and external load tests were carried out over a wide range of pumping frequencies to measure the output performance as well as the calculate the force limitations of such a hybrid actuation system.

1. No-load testing established the maximum output velocity of the system to be

98 mm/s for a 51 mm long rod and 90 mm/s for a 102 mm long rod, occurring at pumping frequencies close to 700 Hz; the corresponding flow rates were 24.8 cc/s (1.52 $inch^3$/s) and 22.7 cc/s (1.39 $inch^3$/s). Though two different lengths of the active material were used, the actuator performance remained almost unchanged due to a balance between the actual strain in the rods and their stiffnesses; a shorter actuating rod has higher stiffness and can extend more into the fluid pumping chamber, and vice versa.

2. Frequency limitations of the device are attributed to the effects of fluid inertia, the characteristics of the magnetic circuit and the dynamics of the reed valves oscillating in a dense fluid.

3. External load tests were also carried out to find the power output and blocked force of the system. The highest recorded power outputs from the tests were calculated to be 1.96 W at 275 Hz pumping frequency with the 51 mm rod and 1.02 W at 300 Hz pumping frequency with the 102 mm rod. Using force-velocity plots obtained from uni-directional load tests, maximum obtainable power output of the actuator was determined as 2.78 W and 3.36 W with the 51 mm and 102 mm Terfenol-D rods respectively.

4. The dynamics of the input electrical and magnetic parameters were monitored; the low-pass behavior of the magnetizing coil and the inertia of the magnetic circuit have considerable influence on the performance and bandwidth limitations of the overall actuation system.

Chapter 3

Dynamic Modeling of a Hybrid Electro-Hydraulic Actuator

3.1 Overview

The experimental results from tests conducted on the prototype Terfenol-D actuator clearly showed a strong dependence on certain test conditions. Frequency of actuation was the most dominant factor affecting performance of the device. The test results show that the output performance, measured in terms of output velocity, initially increase with frequency but roll off beyond a certain point. This is clearly deviant from idealized assumptions and static calculations that suggest that the fluid flow rate from the hybrid pump, all geometrical parameters remaining unchanged, should increase proportional to pumping frequency. Hence, we can conclude that there are several physical phenomena occurring in the actuator which have strong frequency dependence. A simple qualitative look at the actuator operation also supports this conclusion; during every cycle of the pumping operation, the pumping piston, hydraulic fluid and output piston are accelerated by on the force exerted by the blocked active material. All these parts can be viewed individually as single degree of freedom (SDOF) systems which are associated with mass and stiffness parameters that determine the corresponding frequency response. The operational pumping frequencies ranged from 100 Hz to 800 Hz, and any static analysis will surely deviate from real world results due to dynamic effects.

The operation of the actuator also involves several non-linear phenomena. The change of pressure in the hydraulic fluid due to change in density (caused by compression or expansion) can be shown to follow a logarithmic function; this is one of the the primary sources of non-linearity. There is a considerable amount of friction acting between the output shaft and the hydraulic seals and this is another major source of non-linearity. Also, the pressure losses due to flow through the reed valves and manifold passagess, also referred to as *minor losses*, vary as the square of the mean flow velocity. The use of the reed valves to rectify the fluid flow from the pumping chamber also introduces a discontinuity in the fluid flow during every pumping cycle; representing this operation in linearized domain is extremely complicated. Theoretical modeling of the hybrid system is extremely complex and several models have been proposed in literature. Models based on stiffness matching of the actuator stack with an incompressible fluid under static conditions were used for preliminary design and work output of piezoelectric based devices [67, 72, 185, 187, 188, 199]. Though these formulations were useful for a first hand understanding of the device physics and to estimate operational efficiency, the complete operation of the coupled electro-hydraulic actuator could only be modeled by more comprehensive schemes, some of which are listed below.

(i) One of the earliest models by Tang *et al.* [196] presented a very detailed dynamic model of a multi-layered piezoelectric stack. The total induced displacement of the overall active stack was calculated by considering it as a structural element undergoing axial motion due to an input electric field; the appropriate stiffness

and inertia values were used as boundary conditions. The transfer functions between relating the output force and displacement to the input force and stack displacement were found from experiments where measurement probes were used within the setup during characterization tests.

(ii) Nasser *et al.* [204] developed a lumped parameter based dynamic model for the hydraulic and active components of the systems. The fluid system was broken up into lumps, each being represented by the corresponding flow resistance, compliance and inertia, which were then combined together and solved using an electrical network analogy. The moving mechanical parts (pumping stack and output shaft) as well as the fluid masses in the hydraulic end effector were modeled as single-degree-of-freedom (SDOF) systems and the corresponding governing ODEs were used.

(iii) Oates and Lynch [197] derived a system model from equations of motion of the electromechanical and fluid sub-systems. The stack actuator/piston subsystem was modeled as a second-order mass–spring–damper with the driving force provided by an input voltage to the piezoelectric stack and an opposing force being generated by the fluid pressure inside the pumping chamber. The friction associated with the o-ring and fluid between the piston and cylinder walls was represented by a viscous damping coefficient. The flow resistance through the rectifying check valves was modeled as a finite resistance in one direction and an infinite resistance in the opposing direction. The authors also used CFD to analyze a two-dimensional axisymmetric model of the pumping chamber and

compute the pressure generated when a uniform velocity boundary condition was applied to the piston head.

(iv) A quasi-static two-stage hybrid actuator model was developed by Cadou and Zhang [192], where the intermittent opening and closing of the check valves was assumed to produce impulsively accelerated flow through the fluid tubing and the corresponding velocity profile was used to calculate viscous losses. The pressure losses in the open valves was assumed to be proportional to the square of the volumetric flow rate.

(v) A different approach was taken by Ullman *et al.* [79, 198] to model a valveless piezopump, where forces driving the fluidic systems were sinusoidal and the natural frequency of the pumping system was calculated; pressure drops in different sections of the pump were well-represented by loss coefficients in these formulations. The fluid was considered to be incompressible and its inertia was included in force-balance equations for different sections of the pipes.

(vi) Fluid transfer matrix models were used by Sirohi *et al.* [200, 201] to obtain a frequency domain model of the pump operation. A quasi-static linearized model was used to calculate the strain in the piezoelectric stack. The coupling between the fluid inertia and compliance was modeled by using the two-port transmission line model of the fluidic subsystem. To linearize the model, pressure losses in the valves were assumed proportional to the flow rate; the proportionality constant were obtained by assuming laminar Poiseuille flow through a circular tube.

(vii) Regelbrugge *et al.* [205] formulated a model of the hybrid actuation system in time domain. The bulk modulus of the hydraulic fluid along with mass flow rates through different control volumes were used to calculate the pressures in the corresponding sections of the actuator. The input was assumed to be sinusoidal displacement of the piston driven by a piezoelectric stack, while the motion of the mechanical components and fluid volumes were modeled using single-degree-of-freedom (SDOF) equations from dynamic equilibrium considerations. Pressure drops through the valve orifices connecting volume elements were modeled using a momentum-conserving relation (Bernoullis equation) with empirical corrections for viscous flow losses and jet contraction.

(viii) Tan and Leo [69] developed two models for a electro-hydraulic actuation system by starting from the linearized equations for a piezoelectric stack; in addition to the losses in valves, this model did a thorough analysis of the major and minor losses in the fluidic system and included them in energy equations for hydraulic flow in a circular pipe. While the first model (IVF) assumed fully developed incompressible viscous flow, and in the second model (CVF) incorporated the compressibility of hydraulic fluid. Each actuation stage was modeled separately and then combined together to simulate the full cycle operation. The CVF model was much closer to experimental data than the IVF model in terms of both velocity and power.

In recent times, CFD has also been used in some studies to derive loss coefficients for flow in and out of the pumping chamber [197, 207]. These computations, however,

are very specific to the geometry and size of the control volume and the flow path.

A comparison of some of the important actuator modeling schemes and their features, along with the model developed in this paper, has been summarized in the chart shown in Figure 3.1. Several important aspects of the models have been considered; they are (i) static or dynamic formulation, (ii) time or frequency domain, (iii) modeling of the active material (non-linear dynamic model or quasi-staic linearized model), (iv) SDOF representation of pumping piston and output load, (v) fluid compressibility, (vi) fluid inertia, (vii) flow losses (viscous and/or minor), (viii) use of CFD, (ix) dynamics of the rectifying valves, and (x) friction in output hydraulic cylinder. A full (or half) circle means that the corresponding feature was included completely (or partly) in the model, while an empty box refers to absence of that property in the formulation. As seen from the chart, a majority of the models incorporated frequency-dependent dynamic effects; the models by Sirohi [72] and Cadou [192] were static in nature, and hence, used a time-domain approach. Almost all the models used the quasi-static linearized equations governing the behavior of the active material; the model by Tang [196] took a more exhaustive look at the dynamics of a stacked actuator (as shown by the complete circle). Both the pumping piston and the output load were represented by spring-mass-damper equivalents in [79, 197, 198, 201, 204, 205]; Tan and Leo [69] modeled only the output load using this approach. Fluid compressibility was included in most cases; Sirohi [72] and Cadou [192], however, assumed the fluid to be compliant only in the pumping chamber and incompressible in the rest of the manifold. Fluid inertia was also included in some of the models; however, the coupling (shown by the dashed boxes encircling the

two corresponding entries in the chart) between the inertia and compressibility was previously considered only by Nasser and Leo [204] and Sirohi *et al.* [201].

Numerical simulations using these models were not always accurate at high frequencies of operation (>200 Hz) where the inertia of the transmission fluid become dominant and the material characteristics become highly non-linear. Also, all these models were either developed for active valves that control the fluid flow or were operated by electrical signals, or assumed the valves to have instantaneous response; hence, they are either completely open or completely closed and their operation was fully determined by actuating signals rather than the fluid pressure with the system. This is not the case with passive reed valves used in our hybrid pump, where the valve openings are strongly dependent on pressure differences across the ports and the dynamics of the metal reeds [225].

All the above reasons suggest that a linearized, static analysis of the actuator physics is not adequate to model the complex behavior of the hybrid actuator. Each section of the hybrid actuator has strong frequency dependence and its behavior is also strongly coupled with the rest of the device. Hence, the most comprehensive method would be to identify all the physical phenomena occurring in the actuator and derive a model based on the mathematical representation of each phenomenon. The goal of this modeling effort was threefold:

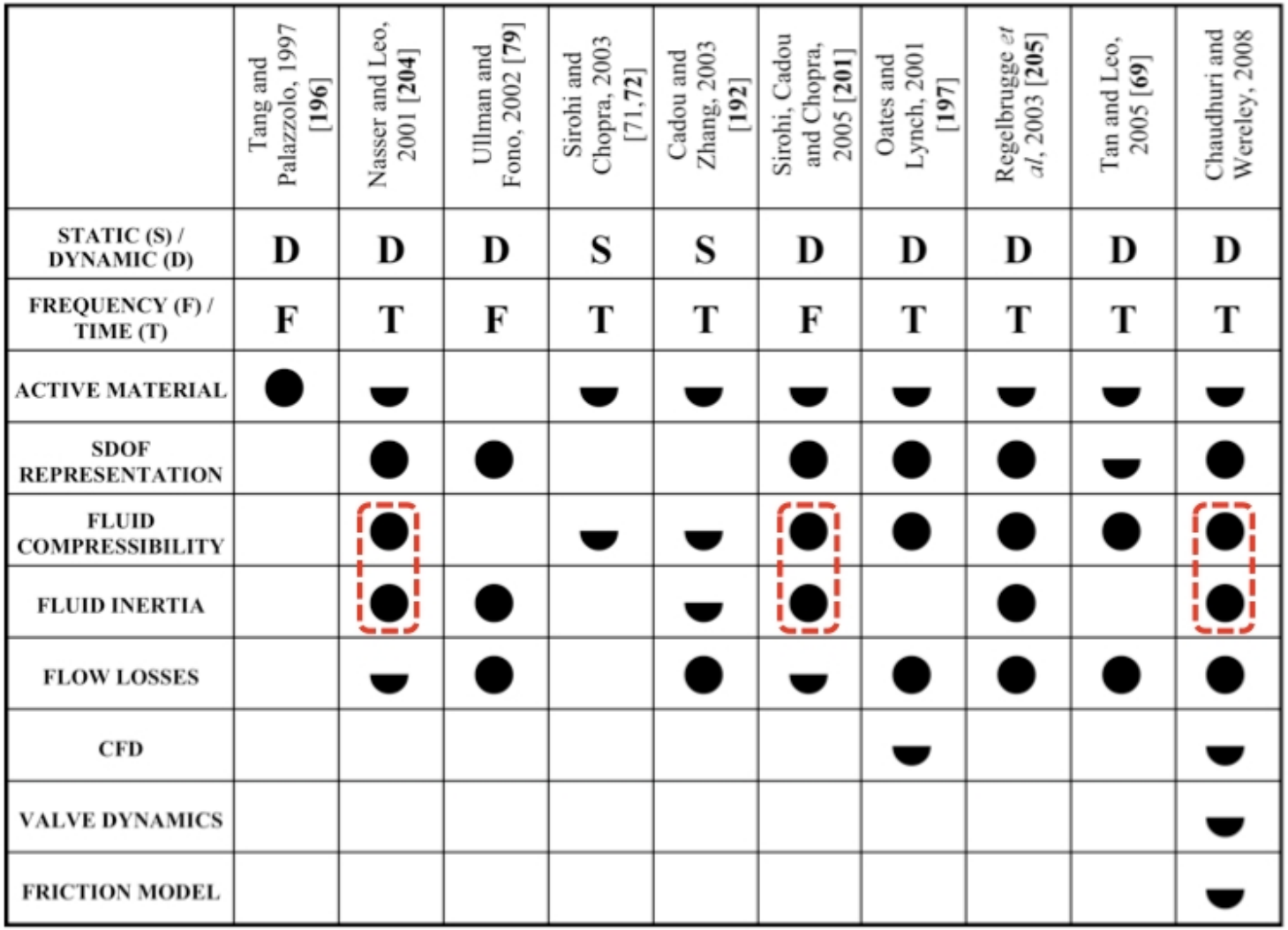

Figure 3.1: Models for smart electrohydraulic actuation systems

- Identify the physical phenomena governing the operation of the hybrid device, with special emphasis on dynamic effects at high actuation frequencies
- Validate the mathematical model by comparing simulation results with experimental data at different conditions
- Utilize the model to design similar actuators with different force and velocity specifications, including selection of appropriate active material for driving the pump

This chapter presents the formulation of a non-linear time-domain model for the hybrid actuators designed and tested in our laboratory [208,209]. The active material was modeled using linearized quasi-static equations, since the natural frequency of this section was found to be much higher than our frequency range of interest. This model takes into account the motion of the pumping piston head mass and the output shaft along with any load mass by considering them as SDOF systems and the respective governing force-balance equations. Friction in the output hydraulic cylinder was represented using the Karnopp model [226–229]. Further, compressibility of the fluid in the pumping chamber, the high pressure driving side and the manifold tubing have been taken into account by incorporating the bulk modulus of the fluid. A coupled lumped parameter approach was used to represent inertia and compliance of the hydraulic fluid in the long manifold passages and the output cylinder. In order to model the continuously varying openings of the passive reed valves in contrast to on-off type valves, two dynamic variables, r_{out} and r_{in}, were introduced to express the opening of the reed valves as a function of the time-varying pressure difference

across the reed ports. This feature allowed us to simulate the frequency dependent behavior of the output piston motion, as noted in our experiments [86, 209, 211, 230], and also captured the back flow through the pressure-dependent passive valves, as has been reported in earlier papers [202, 204]. Two-dimensional CFD models with fluid-structure coupling were used for the first time to estimate the critical pressures required for opening the reed valves in these hybrid devices, while their dynamic response characteristics were obtained from empirical results. The pressure losses incurred in the manifold passages were also computed by applying CFD to 3-D models of the respective geometries. The model of flow though these valve ports includes the inertia as well as minor losses. The bandwidth of the power amplifier and the frequency response of the magnetic circuit were also included in the overall system model. Simulations were carried out and results were compared with experimental data to validate the model.

3.2 Actuator Operation

The starting point of a smart material driven hydraulic pump is the initiation of flow due to the oscillation of a mechanical piston being driven by the extension / contraction of a smart material upon application of an periodic electrical input. A typical hybrid hydraulic pump uses frequency rectification of the oscillatory behavior to produce a net flow rate out of the pump; this is performed by passive uni-directional reed valves housed inside the pumping head of the actuator. A manifold is used to connect the pump to the output cylinder; this manifold also houses the return

valve and the accumulator port. The important variables in different sections of the actuator, shown in Figure 3.2, are selected as the parameters that govern the physical phenomenon in the respective section and are as follows:

1. Forces and displacements of moving parts

2. High pressure regions with fluid compressibility

3. Volume and mass flow rates

The driving force in the actuation system arises from the displacement of the pumping piston, represented by x_p, which results in a change of fluid pressure, P_{ch}, in the pumping chamber. The fluid flows through the manifold tubing into the driving side of the output cylinder, resulting in a change in the pressure P_h. The pressure difference between the high pressure driving side and the low pressure driven side, which is connected to a low stiffness accumulator at pressure P_{acc}, provides the driving force to the output shaft and any connected load. The mean output velocity of the output shaft is calculated as the slope of a linear fit to the shaft displacement, x_L.

The operation of the passive reed valves used in our prototype actuator are dependent on the pressure differences across the respective ports; a positive pressure differential causes the reed to deflect and allows flow through the corresponding port. Using this reasoning, the two fundamental mechanisms that contribute to the flow of hydraulic fluid through the manifold are as follows:

(i) Discharge [Figure 2.2(b)]: $P_{ch} - P_{th} > 0$

(ii) Intake [Figure 2.2(d)]: $P_{acc} - P_{ch} > 0$

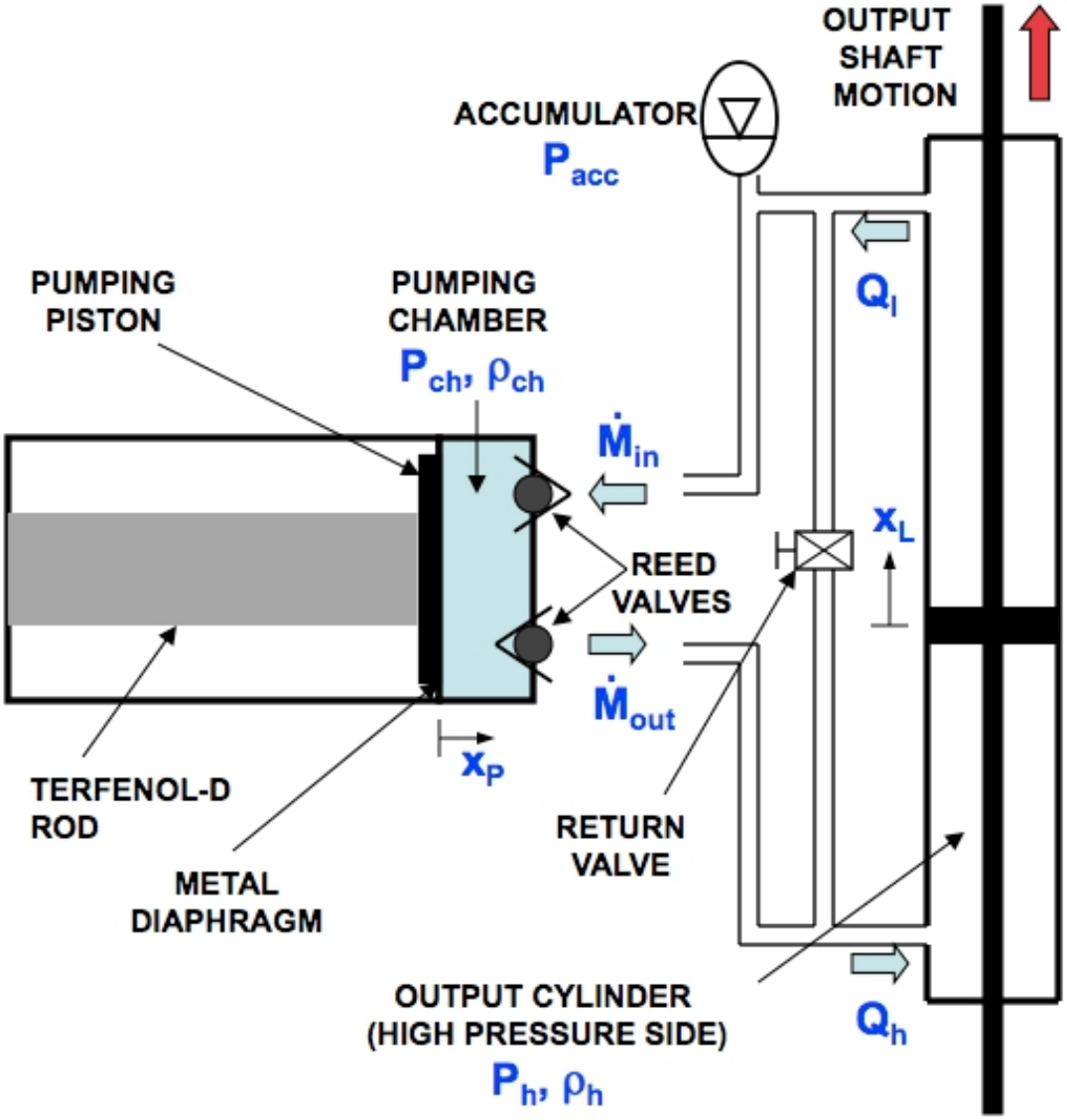

Figure 3.2: Schematic and important physical variables of hybrid actuator test setup

where P_{ch} is the pressure in the pumping chamber, P_{th} is the entry pressure in the discharge manifold (also the pressure at the discharge reed port exit) and P_{acc} is the pressure in the accumulator. These stages are repeated every pumping cycle and result in a net mass flow rate $\dot{M}_{out}$ out of the pump through the discharge tube and an equivalent mass flow rate $\dot{M}_{in}$ into the pump through the intake tube. The duration of any stage depends on the pressure differential across the valve port and varies with operating conditions.

3.3 Characteristics of Driving Magnetic Circuit

Due to the presence of a highly inductive magnetizing coil, the magnetic circuit within the pump body was seen to have a low-pass filter effect on the input driving signal. Since the magnetizing coils and enclosing pump bodies of two different sizes were used for the 51 mm (2 inch) and 102 mm (4 inch) long Terfenol-D rods, the properties of the magnetizing circuit are different too. Also, two different amplifiers with different power ratings resulted in completely different input dynamics, as shown in Figure 3.3. The magnetic flux through the samples was measured at all test conditions. The driving signal was a sinusoid with a dc offset, hence the measured total flux density B could be broken up into a fixed (B_{dc}) and an alternating (B_{ac}) component at each frequency of operation. The resulting harmonic data was fitted with a second order transfer function of the form

$$G(s) = \frac{B_{ac}(s)}{V_{in}(s)} = \frac{K_{dc}}{1 + 2\zeta(s/\omega_n) + (s/\omega_n)^2} \tag{3.1}$$

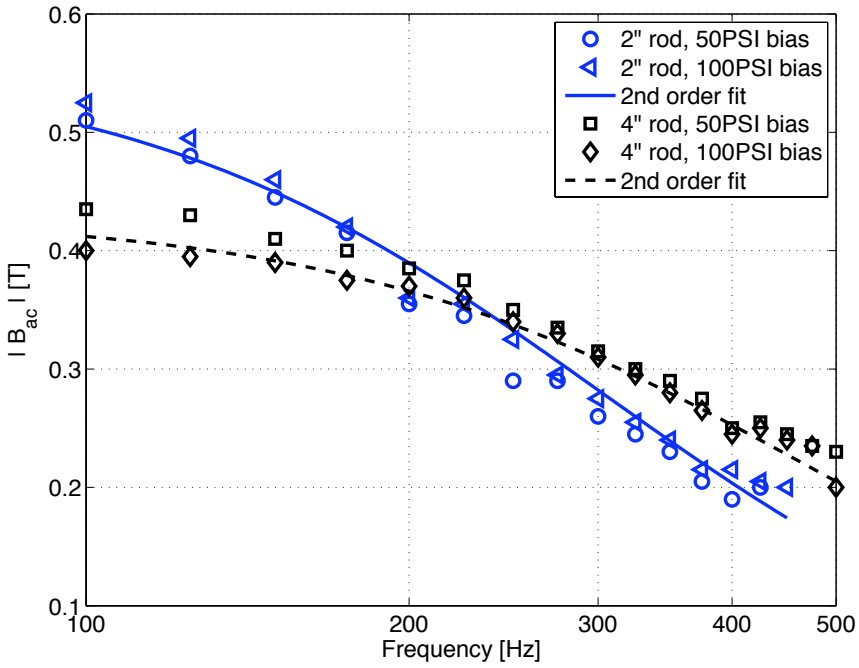

(a) LVC623 amplifier

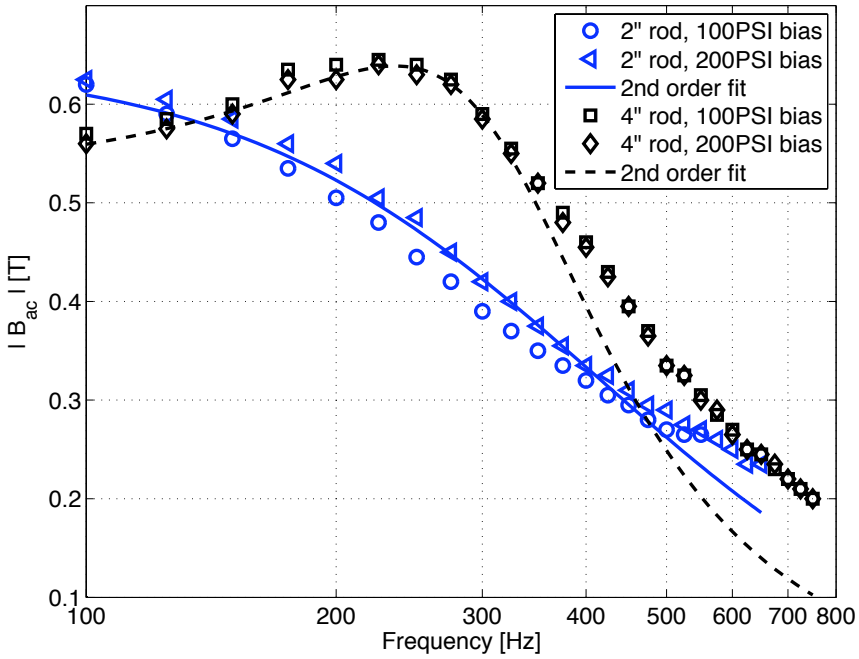

(b) LVC5050 amplifier

Figure 3.3: Variation of amplitude of B_{ac} with frequency

Table 3.1: ESTIMATED INPUT CIRCUIT PARAMETERS

	Parameter	51 mm Terfenol-D rod	102 mm Terfenol-D rod
LVC623	ω_n	1.9x10^3 rad/sec	3.0x10^3 rad/sec
	ζ	1.0	1.0
	K_{dc}	0.56	0.43
LVC5050	ω_n	2.6x10^3 rad/sec	2.0x10^3 rad/sec
	ζ	1.0	0.47
	K_{dc}	0.65	0.53

and its parameters were estimated; Table 3.1 lists the estimated values for the different magnetizing coils when driven using the two amplifiers. The objective function was defined as the squared difference between the observed and expected values at each frequency step, while the *lsqcurvefit* function in MATLAB was used for constrained minimization.by applying the least squares technique. These transfer functions were then used to represent the combined input dynamics of the amplifier and magnetizing coil in time-domain using ODE's.

3.4 System Model

3.4.1 Pump piston and Output piston

Since the movement of the active material provides energy to the whole system, we start by modeling the pumping action of the active rod. Denoting the pressure

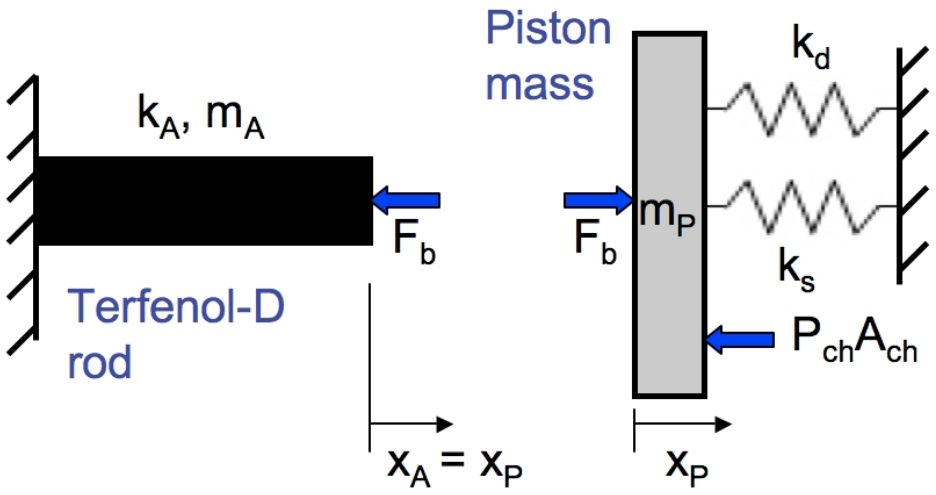

(a) Pumping piston

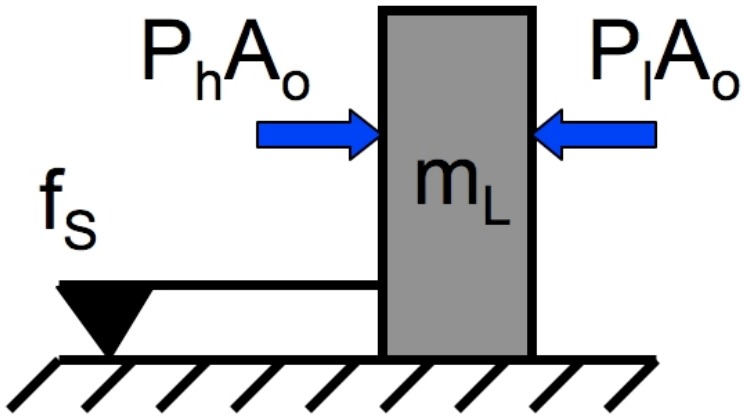

(b) Output cylinder shaft

Figure 3.4: Free-body diagrams for the pumping piston and output cylinder shaft motion

inside the pumping chamber as P_{ch}, we can write the equation of motion of the pumping piston [Figure 3.4(a)] by considering it as a SDOF system as follows:

$$\left(m_P + \frac{m_A}{3}\right)\ddot{x}_P + c_P\dot{x}_P + (k_D + k_S)\,x_P = F_b - P_{ch}A_{ch} \tag{3.2}$$

where F_b is calculated as the force acting on the active material that prevents it from reaching its free strain [8, 231]. Hence, the blocking force acting of the smart material at any instant is given by:

$$F_b = K_A\,(d_A B L_A - x_P) \tag{3.3}$$

where d_A is the *induced strain coefficient* of the smart material. The parameter d_A is also referred to by the symbol d_{33} in literature and referred to as piezoelectric coefficient (for piezoelectric material) and piezomagnetic coefficient (for magnetostrictive materials) [135, 158]. Though the magnetostriction induced in the Terfenol-D rod is a dynamic non-linear phenomenon that varies with the stress acting on the material, we assumed the piezomagnetic coefficient, d_A, of the material to be a constant in our model. This was done in order to obtain a simpler macroscopic view of the physical phenomenon without going into the details of microscopic material properties that govern the magnetostrictive effect. For the same reason, we neglect any variation in Young's modulus, E_A, of the Terfenol-D material, popularly referred to as the ΔE effect [145, 222, 232], and use the value of 30 GPa as quoted by the manufacturer Etrema Products, Inc [141].

Using Equation 3.3 in Equation 3.2, we get the complete ODE governing the motion of the pumping piston as follows:

$$\left(m_P + \frac{m_A}{3}\right)\ddot{x}_P + c_P\dot{x}_P + (k_A + k_D + k_S)\,x_P = k_A d_A B L_A - P_{ch}A_{ch} \tag{3.4}$$

The stiffness of the actuator is calculated from its material properties (E_A) and geometrical dimensions (A_A, L_A) using the following expression:

$$k_A = \frac{E_A A_A}{L_A}$$

The stiffness of the metal diaphragm, k_D, is calculated from empirical relations [216] while the spring stiffness k_S is obtained from manufacturer supplied data. Note that the mass of the actuating rod/stack, m_A, is also included in the inertial component, since the active material can be assumed to behave like a spring with a non-zero mass [233–236].

The fluid pressures on either side of the output cylinder piston constitute the forcing for the output cylinder shaft and the equation of motion of the output cylinder shaft can be obtained from force equilibrium:

$$m_L \ddot{x}_L + c_L \dot{x}_L = (P_h - P_l)A_o - F_f - F_{ext} \tag{3.5}$$

where F_{ext} includes any external forces that might be acting on the output cylinder e.g. $F_{ext} = m_L g$ for a mass hung from the cylinder shaft.

To model the motion of the output cylinder shaft, an accurate representation of the the friction force acting on the output shaft piston is needed. Friction arising from surface contact is a very complicated phenomenon and experiments indicate a functional dependence on a large variety of parameters, including sliding speed, acceleration, critical sliding distance, temperature, normal load, humidity, surface preparation and material combination [237]. Parameter dependence on friction becomes an important issue and a large number of researchers have investigated friction from

a variety of viewpoints. Several models for friction have been proposed in literature [Figure 3.5]; these can be divided into static and dynamic models [227–229, 238–240].

The frictional force arises mainly due to the seals in the assembly that are in contact with the moving piston shaft [241–244]. According to O-ring manufacturers [245, 246], it is generally accepted that the increase of friction on standing is caused by the rubber O-ring flowing into the microfine grooves or surface irregularities of the mating part. As a general rule for a 70 durometer rubber against an 8 micro-inch surface, the maximum break-out friction that will develop in a system is 3 times the running friction. In order to preserve the computational simplicity of our overall model while maintaining accuracy, the frictional force in the output piston is computed from the static symmetric Karnopp model [226, 227, 229, 247, 248] and depends on the applied force F and velocity v as follows:

$$F_f = \begin{cases} \text{sgn}(v)F_d & , \mid v \mid > v_{min} \\ \text{sgn}(F)\max(F, F_s) & , \mid v \mid \leq v_{min} \end{cases} \tag{3.6}$$

where $F = (P_h - P_l)A_O - F_{ext}$ is the total force acting on the output piston and F_s and F_d are the static and dynamic friction in the output hydraulic cylinder respectively. The force-velocity diagrams for different friction models, including the Karnopp model, are shown in Figure 3.5.

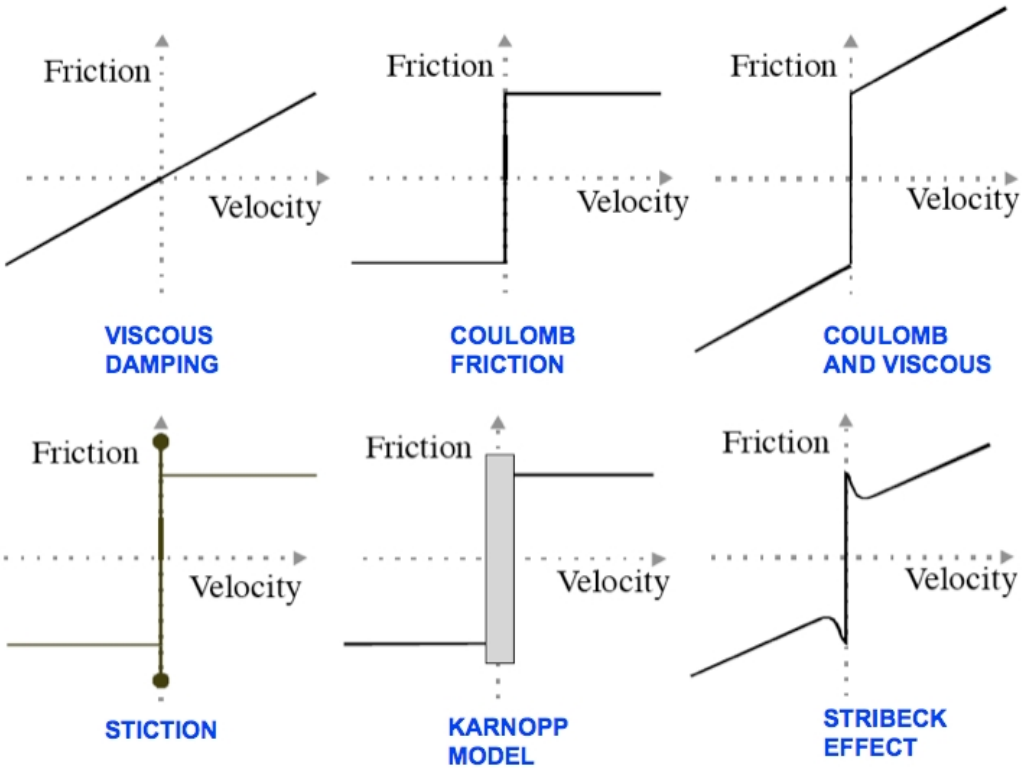

Figure 3.5: Classical friction models [249]

3.4.2 Pumping chamber and output cylinder (high pressure driving side)

The mass of fluid m in any control volume V is $m = \rho V$, ρ being the instantaneous fluid density. Differentiating and rearranging, we get an expression for the rate of change of fluid density in the control volume [69, 205, 250]:

$$\dot{\rho} = \frac{\dot{m} - \rho\dot{V}}{V} \tag{3.7}$$

where $\dot{\rho}$, $\dot{m}$ and $\dot{V}$ give the rate of change of density, mass and volume respectively. This formulation allows us to take into consideration the compressibility of the fluid along with any fluid flowing into and out of a particular part of the actuation system and is similar to the approaches in formerly developed models that included fluid compressibility [69, 205]. If we consider an enclosed volume of fluid where there is no net inflow or outflow of mass, we can rewrite 3.7 as

$$\dot{\rho} = -\rho\frac{\dot{V}}{V} \tag{3.8}$$

The bulk modulus of the fluid, β, is defined as follows:

$$dP = -\beta\frac{dV}{V} \tag{3.9}$$

Using this definition in (3.8), we get

$$dP = \beta\frac{d\rho}{\rho} \implies \dot{P} = \beta\frac{\dot{\rho}}{\rho} \tag{3.10}$$

Upon integrating and applying the condition that $\rho = \rho_0$ when $P = P_{bias}$, we get

$$\frac{\rho}{\rho_0} = exp\left(\frac{P - P_{bias}}{\beta}\right) \tag{3.11}$$

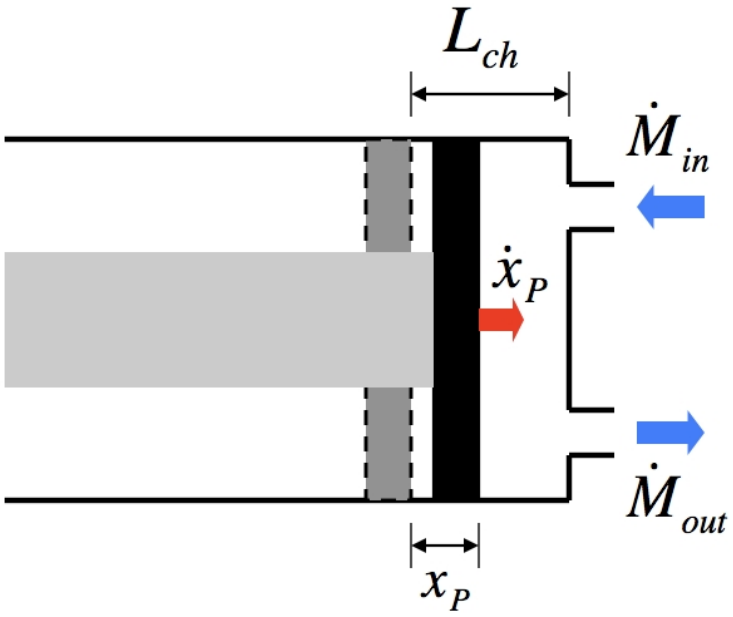

(a) Pumping piston

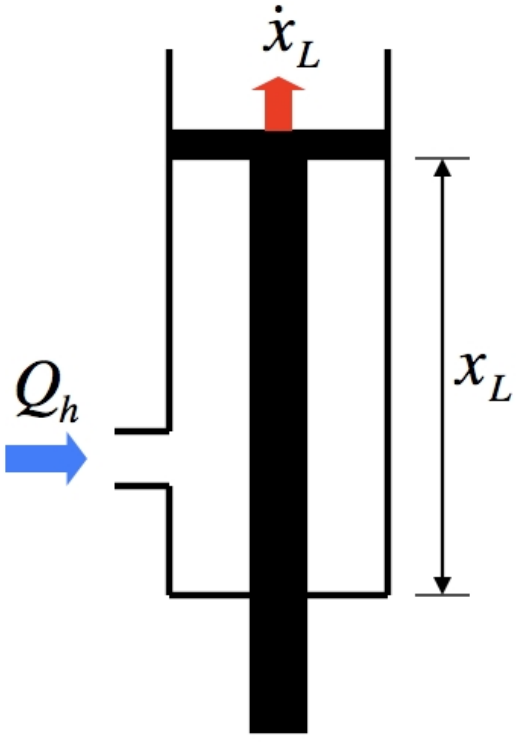

(b) Output cylinder (high pressure driving side)

Figure 3.6: Volume changes and flow rates in compressible sections

In the fluid pumping chamber, the density of the fluid, ρ_{ch}, changes due to the following reasons [Figure 3.6(a)]:

(i) Instantaneous change in volume of the pumping chamber due to axial motion of the pumping piston which is proportional to the velocity of the piston, $\dot{x}_P$,

(ii) Fluid flow rate out of the pumping chamber during the *exhaust stroke* i.e. $\dot{M}_{out}$, and

(iii) Fluid flow rate in to the pumping chamber during the *intake* stroke i.e. $\dot{M}_{in}$.

Using 3.7, the equation governing the rate of change of fluid density in the pumping chamber can be written as follows [69]:

$$\dot{\rho}_{ch} = \frac{\rho_{ch} A_p \dot{x}_p - \dot{M}_{out} + \dot{M}_{in}}{A_p \left(L_{ch} - x_P\right)} \tag{3.12}$$

and the corresponding rate of pressure change inside the chamber can be obtained by applying 3.10 and 3.11 as shown below:

$$\dot{P}_{ch} = \beta \frac{\dot{\rho}_{ch}}{\rho_{ch}} = \beta \frac{\left(\rho_{ch} A_{ch} \dot{x}_P - \dot{M}_{out} + \dot{M}_{in}\right)}{\rho_{ch} A_{ch} (L_{ch} - x_P)} \tag{3.13}$$

The fluid density in the pumping chamber is calculated from the instantaneous pressure by using Equation 3.11 as follows:

$$\rho_{ch} = \rho_0 e^{\left(\frac{P_{ch} - P_{bias}}{\beta}\right)} \tag{3.14}$$

and applied in Equation 3.13.

Similarly, in the driving side of output cylinder [Figure 3.6(b)], the density of the fluid is governed by the volume flow Q_h from the manifold and the volumetric

change due to output piston motion $\dot{x}_L$. The following equation represents this time rate of change of fluid density in the high pressure driving side of the output piston:

$$\dot{\rho}_h = \frac{\rho_h Q_h - \rho_h A_O \dot{x}_L}{A_O x_L} \tag{3.15}$$

where $A_O = \pi(D_o^2 - D_i^2)/4$, D_o and D_i being the bore and shaft diameter of the hydraulic cylinder. The corresponding change in pressure P_h is given by

$$\dot{P}_h = \beta \frac{\dot{\rho}_h}{\rho_h} = \beta \frac{(Q_h - A_O \dot{x}_L)}{A_O x_L} \tag{3.16}$$

It should be noted that the right-hand side of Equation 3.16 cannot be computed for $x_L = 0$; hence, a reasonable positive starting value of x_L should be chosen for the numerical simulation. In our case, a value of $x_L = 0.005$ was chosen; this value represented the additional volume inside the hydraulic cylinder used for external manifold fittings and/or receptacles for linear bearings.

3.4.3 Fluid passages

The equations governing unsteady flow of a fluid through a tube of uniform circular cross-sectional area A can be calculated from the basic equations of continuity and momentum from fluid dynamics. This model of flow takes into account the inertia of the fluid mass and the viscous losses.

The variables of interest are pressure, $p(x,t)$, and velocity, $v(x,t)$, at any point x in the conduit and at any time instant t, as shown in Figure 3.7. Consider the following assumptions:

- One-dimensional flow

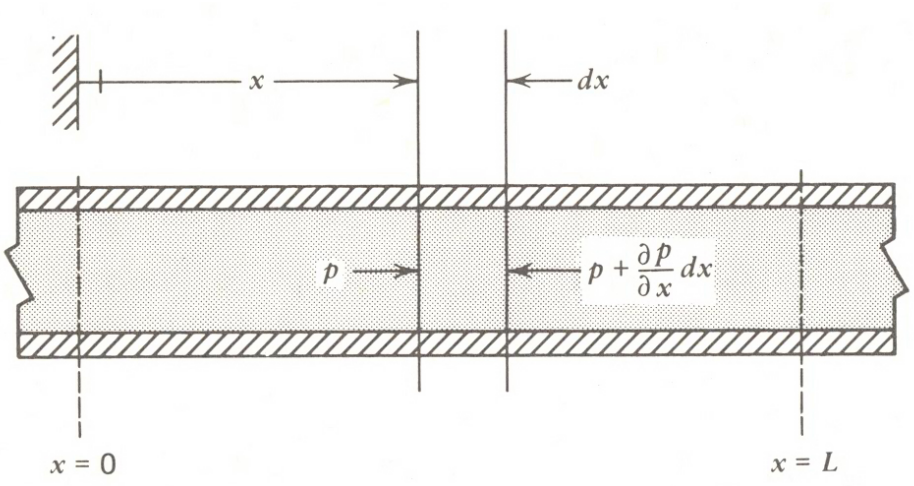

Figure 3.7: Distributed parameter model of hydraulic conduit [251]

- No action-at-a-distance forces
- Constant cross-sectional area
- No longitudinal motion of pipe wall

Using these, the only force, f_p, acting on the element of length dx at a distance x in the longitudinal direction is due to the pressure difference across its area A i.e.

$$f_p = \left[p - \left(p + \frac{\partial p}{\partial x}dx\right)\right] A = -\frac{\partial p}{\partial x}Adx \tag{3.17}$$

Since velocity is a function of both x and t, hence the accelaration a is obtained from:

$$\begin{aligned} a = \frac{dv}{dt} &= \frac{\partial v}{\partial x}\frac{dx}{dt} + \frac{\partial v}{\partial t} \\ &= v\frac{\partial v}{\partial x} + \frac{\partial v}{\partial t} \end{aligned} \tag{3.18}$$

The pressure force has to overcome fluid inertia and the viscous forces associated with the elemental volume. Applying Newton's law,

$$-A\frac{\partial p}{\partial x}dx = \rho A dx\left(v\frac{\partial v}{\partial x} + \frac{\partial v}{\partial t}\right) + \tau_0 \pi D dx$$

where D is the effective diameter of the section and τ_0 is the shear stress. On rearranging and simplifying, we get

$$\frac{\partial p}{\partial x} + \rho\frac{\partial v}{\partial t} + \rho v\frac{\partial v}{\partial x} + \frac{\tau_0 \pi D}{A} = 0 \tag{3.19}$$

In transient flow calculations, the shear stress τ_0 is considered to be the same as if the flow field were steady [252], so in terms of the Darcy-Weisbach friction factor f_f,

$$\tau_0 = \frac{\rho f_f v|v|}{8} \tag{3.20}$$

This equation can be developed from the Darcy-Weisbach equation

$$\Delta p = \frac{\rho f_f L}{D}\frac{v^2}{2}$$

with L as the horizontal length of the pipe, and from a force balance on the pipe in steady flow

$$\Delta p\frac{\pi D^2}{4} = \tau_0 \pi D L$$

by eliminating Δp. The absolute value on the velocity term in Equation 3.20 ensures that the shear stress always opposes the direction of velocity. Using Equation 3.19 and Equation 3.20, we get

$$\frac{1}{\rho}\frac{\partial p}{\partial x} + \frac{\partial v}{\partial t} + v\frac{\partial v}{\partial x} + \frac{f_f v|v|}{2D} = 0 \tag{3.21}$$

In the case of laminar flow, the friction factor f_f is a function of the Reynold's number, Re, as follows [253],

$$f_f = \frac{64}{Re}$$

By definition,

$$Re = \frac{\rho v D}{\mu} = \frac{vD}{\nu}$$

Using these in Equation 3.21, we get the following equation for unsteady laminar flow:

$$\frac{1}{\rho}\frac{\partial p}{\partial x} + \frac{\partial v}{\partial t} + v\frac{\partial v}{\partial x} = 0 \tag{3.22}$$

Applying mass continuity to the space dx,

$$\begin{aligned} \rho A v - \left(\rho A v + \frac{\partial}{\partial x}\left(\rho A v\right) dx\right) &= \frac{\partial}{\partial t}\left(\rho A dx\right) \\ \implies \frac{\partial \rho}{\partial t} + \rho\frac{\partial v}{\partial x} + v\frac{\partial \rho}{\partial x} &= 0 \end{aligned} \tag{3.23}$$

Using the definition of bulk modulus [Equation 3.9] applied to a fixed mass [Equation 3.10] in Equation 3.23, we get:

$$\frac{1}{\beta}\frac{\partial p}{\partial t} + \frac{\partial v}{\partial x} + v\frac{\partial p}{\partial x} = 0 \tag{3.24}$$

Assuming that the average flow velocity is low enough, the *convective effect* can be neglected i.e. $v = 0$. We then obtain the fundamental *waterhammer* equations [251, 254, 255]:

$$\begin{aligned} \frac{1}{\beta}\frac{\partial p}{\partial t} + \frac{\partial v}{\partial x} &= 0 \\ \frac{1}{\rho}\frac{\partial p}{\partial x} + \frac{\partial v}{\partial t} &= 0 \end{aligned}$$

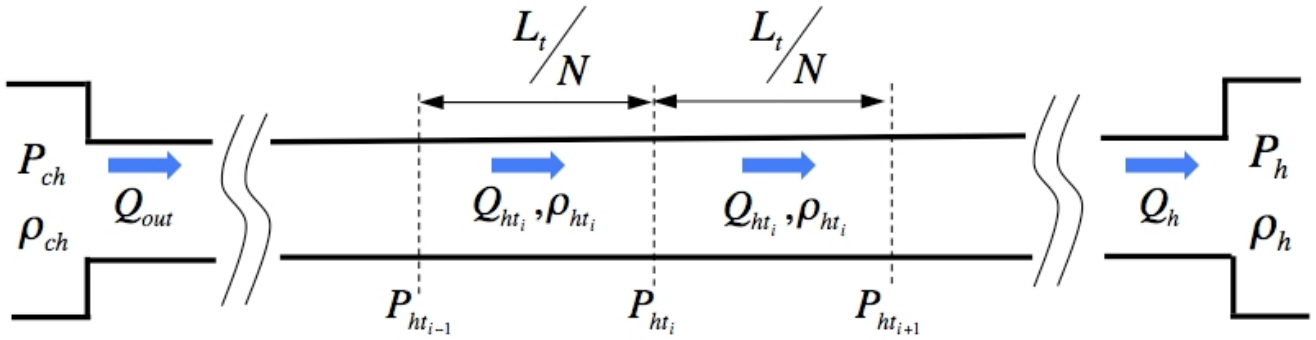

(a) Manifold tubing

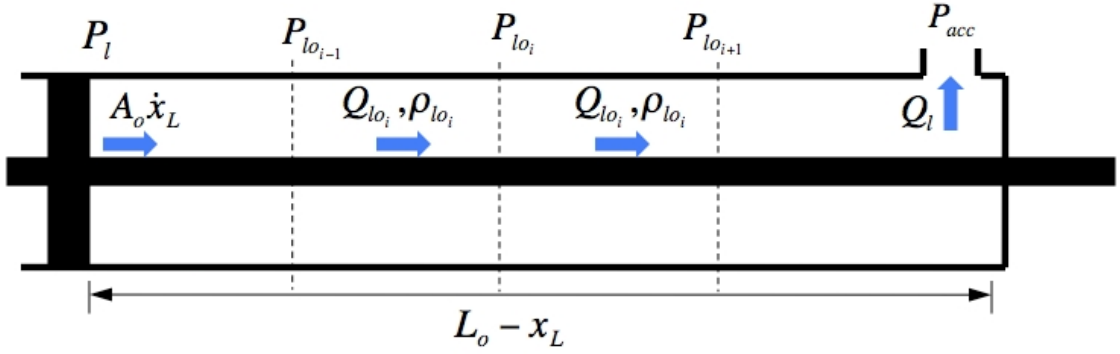

(b) Output cylinder (high pressure side)

Figure 3.8: Lumped model of fluid flow through passages

Since the above approach results in strongly coupled partial differential equations, it is too complex for a model based on ODEs for simulation. Hence, we use the transmission line model, wherein each length of tubing is broken up into N_t equal sections along its length [Figure 3.8(a)] and rate equations for the volume flow rate (Equation 3.25) and pressure (Equation 3.29) though each section are formulated [251, 256, 257]. The pressure drop across any section can be accounted by the effects of fluid inertia and viscous losses as follows [85, 86, 211]:

$$P_i - P_{i+1} = \frac{(L_t/N_t)}{A_t}\rho_i \dot{Q}_i + R_t \left(\frac{L_t}{N_t}\right) \rho_i Q_i \tag{3.25}$$

The viscous resistance to fluid flow in the tubing per unit length is represented by R_t in Equation 3.25. From the measured velocities, the maximum Reynolds number for flow through the tubing was found to be 150. Hence, the viscous fluid resistance can be calculated from the Hagen-Poiseuille solution for laminar flow through a circular tube [253] i.e.

$$\Delta P_{lamimar} = \frac{128\nu}{\pi D^4} L\rho Q \implies R_t = \frac{8\pi\nu}{A^2} \tag{3.26}$$

The number of lumps, N_t is chosen based on the length of the tubing, L_t, and the wavelength of pressure waves in the fluid. The propagation velocity, c, is given by

$$c = \sqrt{\frac{\beta}{\rho}} \tag{3.27}$$

and the corresponding wavelength, λ, at excitation frequency f is

$$\lambda = \frac{c}{f} \tag{3.28}$$

Following a general rule of thumb that satisfies the Courant condition [251, 258, 259],

the length of each lump should be an order smaller than the wavelength of the pressure wave.

The change in pressure in section i is dependent on the flow of fluid in/out of the section and can be derived by applying Equation 3.7 and Equation 3.10 with Q_{ht_i} and $Q_{ht_{i+1}}$ as the corresponding volume flow rates as follows:

$$\dot{P_{ht_i}} = \beta \frac{\left(Q_{ht_i} - Q_{ht_{i+1}}\right)}{A_t \left(L_t/N_t\right)}, \tag{3.29}$$

A similar approach is applied to the output cylinder too, where the length of the driven side, $L_o - x_L$, is broken up into N_o sections, each having a uniform circular cross section with area A_o. Differential equations for the pressure P_{lo_i} and volume flow rate Q_{lo_i} through each section of the output cylinder can then be written.

The known boundary values for the manifold tubing are:

$$Q_{ht_1} = Q_{out} \ , \qquad P_{ht_{N_t}} = P_h$$

while the calculated boundary variables are:

$$P_{th} = P_{ht_0} \ , \qquad Q_h = Q_{ht_{N_t}}$$

A similar approach is applied to the output cylinder too, where the length of the driven side, $L_o - x_L$, is broken up into N_o sections, each having a uniform circular cross section with area A_o. Differential equations for the pressure P_{lo_i} and Q_{lo_i} can then be written. For the fluid in the driven side of the output cylinder, the known boundary values are:

$$Q_{lo_1} = A_o \dot{x}_L \ , \qquad P_{lo_{N_o}} = P_{acc}$$

while the calculated variables are:

$$P_l = P_{lo_1} \ , \qquad Q_l = Q_{lo_{N_o}}$$

For actuation systems with very low volume flow rates, we can assume that the fluid volume flowing through all sections is the same i.e. $Q_i = Q_t \ \forall \ i = 1, 2, ...N_t$. Using this, we can now sum up the pressure drops from Equation 3.25 over the entire length of the manifold tubing to get an expression for the overall loss in pressure ΔP_t as a function of the volume flow rate Q_t as follows:

$$\begin{aligned} \Delta P_t &= \sum_{i=1}^{N_t} (P_i - P_{i+1}) \\ &= \left(\frac{1}{N_t} \sum_{i=1}^{N_t} \rho_i \right) \left[\frac{L_t}{A_t} \dot{Q}_t + R_t L_t Q_t \right] \end{aligned} \tag{3.30}$$

Further, if we assume that the fluid density varies linearly along the length of the tube i.e.

$$\rho = \rho_1 - \frac{(\rho_1 - \rho_{N_t})}{L_t} x$$

where x represents distance along the tubing from the high pressure end, then we can replace the summation term in Equation 3.30 by the arithmetic mean of the fluid densities at either end of the valve i.e.

$$\Delta P_t = \frac{(\rho_1 + \rho_N)}{2} \left[\frac{L_t}{A_t} \dot{Q} + R_t L_t Q_t \right] \tag{3.31}$$

These assumptions simplify the equations representing the flow through the manifold and reduce the number of corresponding states from $2N_t$ to 1. Such an improvement in computational load is highly desirable, since the number of states used to model the tubing is a considerable part of the total number of states in the overall model.

This approach was applied successfully [86, 260] to model an actuation system using magnetorheological fluids, where the low driving frequencies were used (< 250 Hz) and the flow rates were also very low [85].

3.4.4 Reed valves and ports

The reed valves perform the function of flow rectification, wherein the bi-directional motion of the active stack is converted to uni-directional flow of fluid. The reed valves respond to the pressure difference across the valves. We define the parameter P_{open} as the pressure difference at while the reed valve is fully open and hence, the pressure loss through the valve is the least. Unlike on/off valves, a reed valve allows a continuously varying flow through it depending on the amount of deflection of the reed and the geometry of the flow path [230]. Since the behavior of the reed valve in our system is analogous to a cantilever beam fixed at one end, hence, the dynamics of the reed can be represented by a second-order system characterized by a natural frequency, ω_{nr}, and damping coefficient, ζ. To implement this behavior of the reed valve, we define a parameter, r_c, which denotes the commanded amount of deflection of the reed depending on the pressure difference, ΔP, across the reed port as follows [86, 211, 230]:

$$r_c = \begin{cases} 1 & \text{if } \Delta P > P_{open} \\ \Delta P / P_{open} & \text{if } |\Delta P| \leq P_{open} \\ -1 & \text{if } \Delta P < -P_{open} \end{cases} \tag{3.32}$$

The actual reed valve opening, r, is then related to the input or commanded reed deflection using the second order transfer function as follows:

$$\frac{r(s)}{r_c(s)} = \frac{1}{1 + \frac{2\zeta}{\omega_{nr}} s + \frac{s^2}{\omega_{nr}^2}} \tag{3.33}$$

and leads to two state equations (r and $\dot{r}$) for each reed valve.

For the discharge reed valve, the opening r_{out} is determined by the pressure difference $\Delta P_{out} = P_{ch} - P_{th}$ across the valve, while the intake valve opeing r_{in} is controlled by the pressure difference $\Delta P_{in} = P_{acc} - P_{ch}$. The parameters, r_{in} and r_{out}, are then used to derive equations for the volume flow rate in and out of the pumping chamber based only on the pressure differences across the reed valve ports. The values of P_{open} and ω_{nr} are strongly dependent on the geometry of the reed valve; an estimate of ω_{nr} is obtained from empirical formulae [216, 261] while the value of P_{open} is obtained from results of a fluid-structure interaction study between the reed and the hydraulic oil (discussed in a later section).

The parameters, r_{out} and r_{in}, can be used to derive equations for the volume flow rate into and out of the pumping chamber. The pressure drop incurred in the reed valves due to only minor losses can now be written in terms of r_{out} and r_{in} as follows:

$$(\Delta P_{out})_{minor} = \frac{1}{2}\rho_{ch}\left(\frac{K_{Lvalve}}{r_{out}}\right)\left(\frac{\dot{M}_{out}}{\rho_{ch} A_{port}}\right)^2 \tag{3.34}$$

$$(\Delta P_{in})_{minor} = \frac{1}{2}\rho_{0}\left(\frac{K_{Lvalve}}{r_{in}}\right)\left(\frac{\dot{M}_{in}}{\rho_{0} A_{port}}\right)^2 \tag{3.35}$$

where K_{Lvalve} is the minor loss coefficient for a fully open reed valve. This is similar to the empirical equation used in [205] or the explicit loss coefficients used in [71] to

calculate the volume flow rate corresponding to a certain pressure difference; in our formulation, we expressed the pressure drop as a function of the mass flow rate by inverting the sides of the equation, because this makes a logical way to sum up all the pressure drops in any fluid line.

The governing equations for the pulsating flow through the reed ports are then obtained by summing up the inertial, viscous and quadratic losses as follows:

$$P_{ch} - P_{th} = \frac{L_{port}}{A_{port}} \ddot{M}_{out} + R_{port} L_{port} \dot{M}_{out} + (\Delta P_{out})_{minor} \tag{3.36}$$

$$P_{tl} - P_{ch} = \frac{L_{port}}{A_{port}} \ddot{M}_{in} + R_{port} L_{port} \dot{M}_{in} + (\Delta P_{in})_{minor} \tag{3.37}$$

where P_{tl} is the manifold fluid pressure at the intake reed port entry.

3.4.5 Accumulator

Since the fluid stiffness is much higher than the accumulator on the low pressure driven side of the manifold, we can assume that the motion of fluid in this section results only in deformation of the accumulator diaphragm and consequently, fluid compressibility effects are negligible in this section [86, 201]. The stiffness of the accumulator, K_{acc}, can be calculated from its geometry as follows:

$$K_{acc} = \frac{\beta_{air} A_{acc}}{L_{acc}} \tag{3.38}$$

where β_{air} is the bulk modulus of the air filling the accumulator. Since this value is less than a thousandth of the hydraulic fluid and the volume of the accumulator is comparable to the fluid volume, hence the stiffness of the accumulator is a small fraction of the fluid stiffness.

Applying mass continuity for this section of the actuator, we can write:

$$\rho_0 A_{acc} \dot{x}_{acc} = \rho_0 Q_l - \dot{M}_{in} \tag{3.39}$$

and the resulting accumulator pressure variation as as:

$$\dot{P}_{acc} = \frac{K_{acc} \dot{x}_{acc}}{A_{acc}} = \frac{K_{acc} \left(\rho_0 Q_l - \dot{M}_{in} \right)}{\rho_0 A_{acc}^2} \tag{3.40}$$

3.4.6 Manifold tubing (intake)

Due to the presence of a highly compliant accumulator in the intake side, the fluid in this part of the manifold can be assumed to be incompressible [69,201,211,230]. If P_{tl} be the pressure at the entry of the intake reed port, then the intake mass flow rate $\dot{M}_{in}$ is governed by the equation

$$P_{acc} - P_{tl} = \frac{L_t}{A_t} \ddot{M}_{in} + R_t L_t \dot{M}_{in} + \frac{1}{2} \rho_0 K_{L_t} \left(\frac{\dot{M}_{in}}{\rho_0 A_t} \right)^2 \tag{3.41}$$

where K_{L_t} is the loss factor associated with minor losses in the intake tubing. The minor losses include the losses due to sudden expansion or contraction in the pipe sections, entry or exit from pipe to a fluid holding volume (e.g. accumulator, output cylinder) as well as pipe bends. A list of such losses is shown in Figure 3.9. Since the fluid in the intake side of the actuator was assumed to be incompressible due to the presence of the more compliant accumulator, hence, Equation 3.41 is expressed in terms of the baseline fluid density ρ_0. This formulation is similar to the approaches used by Ullmann *et al.* [198] and Regelbrugge *et al.* [205] to model accelerated flow of an incompressible fluid.

By summing the pressure drops in the intake passage from Equation 3.37 and Equation 3.41, we arrive at a single governing ODE for the intake mass flow rate,

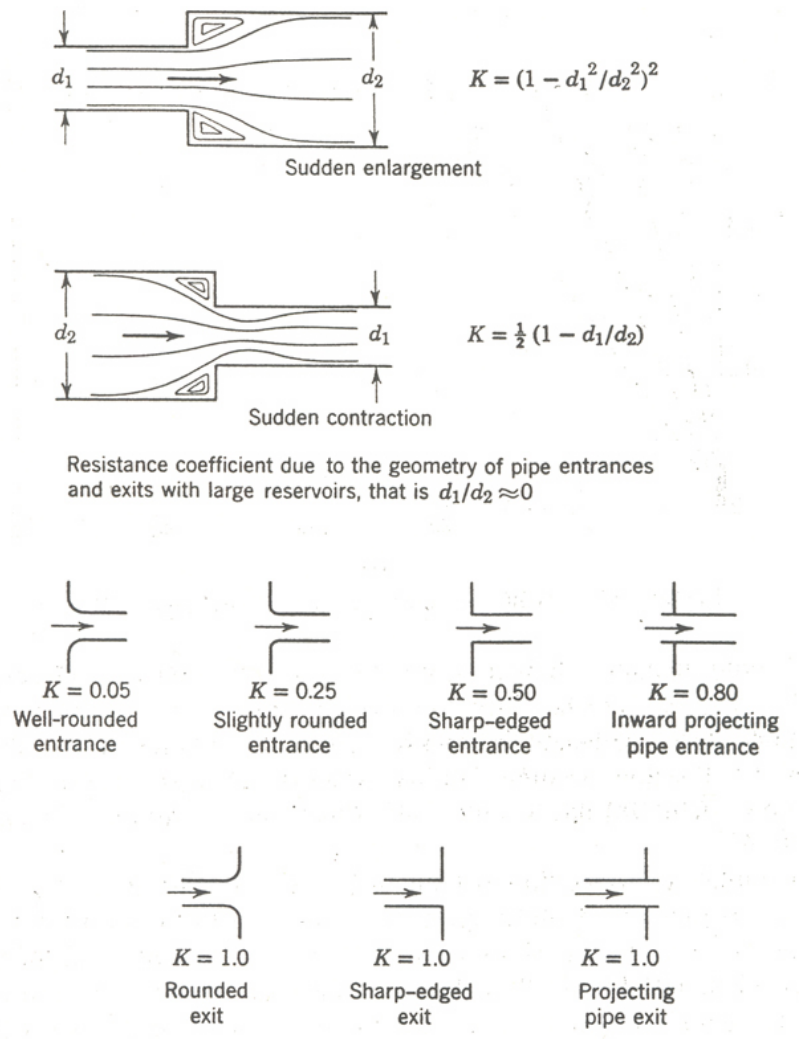

Figure 3.9: Minor losses for flow through a pipe [262]

$\dot{M}_{in}$, as a function of the pressures P_{acc} and P_{ch} at its two ends and the intake reed valve opening, r_{in}.

$$P_{acc} - P_{ch} = \left(\frac{L_t}{A_t} + \frac{L_{port}}{A_{port}}\right)\ddot{M}_{in} + \left(L_t R_t + L_{port} R_{port}\right)\dot{M}_{in} + \frac{1}{2}\rho_0\left(\frac{K_{Lvalve}}{r_{in}} + K_{L_t}\right)\left(\frac{\dot{M}_{in}}{\rho_0 A_t}\right)^2 \quad (3.42)$$

3.4.7 State space formulation

We define state variables for all the time-varying physical variables as follows:

$$
\begin{aligned}
x_1 &= x_P \\
x_2 &= \dot{x}_P \\
x_3 &= x_L \\
x_4 &= \dot{x}_L \\
x_5 &= P_{acc} \\
x_6 &= P_{ch} \\
x_7 &= P_h \\
x_8 &= \dot{M}_{out} \\
x_9 &= \dot{M}_{in} \\
x_{10} &= r_{out} \\
x_{11} &= r_{in} \\
x_{12} &= \dot{r}_{out} \\
x_{13} &= \dot{r}_{in} \\
x_{13+i} &= P_{hp_i}, i = 1, 2, \ldots, N_t \\
x_{13+N_t+i} &= Q_{hp_i}, i = 1, 2, \ldots, N_t \\
x_{13+2N_t+i} &= P_{lo_i}, i = 1, 2, \ldots, N_o \\
x_{13+2N_t+N_o+i} &= Q_{lo_i}, i = 1, 2, \ldots, N_o
\end{aligned}
\tag{3.43}
$$

where N_t and N_o are the number of equal length lumps into which the manifold tubing and output cylinder are broken up.

Table 3.2: STATE-SPACE REPRESENTATION OF MODEL EQUATIONS FOR PRIMARY STATES

$$\dot{x}_1 = \dot{x}_P = x_2$$

$$\dot{x}_2 = \ddot{x}_P = \frac{K_A d_A B L_A - x_6 A_{ch} - c_P x_2 - (k_A + k_D + k_S) x_1}{\left(m_P + \frac{m_A}{3}\right)}$$

$$\dot{x}_3 = \dot{x}_L = x_4$$

$$\dot{x}_4 = \ddot{x}_L = \frac{(x_6 - x_5) A_O - F_{fric} - F_{ext} - c_L x_4}{[m_L + \rho_0 A_O (L_O - x_4)]}$$

$$\dot{x}_5 = \dot{P}_{acc} = \frac{k_{acc}(A_O x_4 - x_9)}{A_{acc}^2}$$

$$\dot{x}_6 = \dot{P}_{ch} = \beta \frac{\left[A_{ch} x_2 - x_8 - x_9 exp\left(\frac{x_6 - P_{bias}}{\beta}\right)\right]}{(L_{ch} - x_1)}$$

$$\dot{x}_7 = \dot{P}_h = \beta \frac{(x_{9+2N_t} - A_O x_4)}{A_O x_3}$$

$$\dot{x}_8 = \ddot{M}_{out} = \frac{A_{port}}{L_{port}} \left[(x_6 - x_{14}) - R_{port} L_{port} x_8 - \frac{1}{2}\rho \left(\frac{K_{L_{valve}}}{r_{out}} + K_{L_t}\right) \left(\frac{x_8}{\rho A_{port}}\right)^2\right]$$

$$\dot{x}_9 = \ddot{M}_{in} = \left(\frac{L_{port}}{A_{port}} + \frac{L_t}{A_t}\right)^{-1} \left[(x_5 - x_6) - (R_{port} L_{port} + R_t L_t)\, x_9 - \frac{1}{2}\rho_0 \left(\frac{K_{L_{valve}}}{r_{in}} + K_{L_t}\right) \left(\frac{x_9}{\rho_0 A_{port}}\right)^2\right]$$

Table 3.3: STATE-SPACE REPRESENTATION OF MODEL EQUATIONS FOR REED VALVE STATES

$$
\begin{aligned}
\dot{x}_{10} &= \dot{r}_{out} = & x_{12} \\
\dot{x}_{11} &= \dot{r}_{in} = & x_{13} \\
\dot{x}_{12} &= \ddot{r}_{out} = & \left[r_{out_c} - \frac{2\zeta}{\omega_{nr}} x_{12} - x_{10} \right] \omega_{nr}^2 \\
\dot{x}_{13} &= \ddot{r}_{in} = & \left[r_{in_c} - \frac{2\zeta}{\omega_{nr}} x_{13} - x_{11} \right] \omega_{nr}^2
\end{aligned}
$$

Table 3.4: STATE-SPACE REPRESENTATION OF MODEL EQUATIONS FOR FLUID PASSAGES

$$
\begin{aligned}
\dot{x}_{13+i} &= \dot{P}_{hp_i} = & \beta \frac{(x_{13+N_t+i} - x_{14+N_t+i})}{(A_t L_t / N_t)}, \quad i = 1, \ldots, N_t \\
\dot{x}_{13+N_t+i} &= \dot{Q}_{hp_i} = & \left[(x_{13+i} - x_{14+i}) \frac{N_t}{L_t \rho_i} - R_t x_{13+N_t+i} \right] A_t \\
\dot{x}_{13+2N_t+i} &= \dot{P}_{lo_i} = & \beta \frac{(x_{13+2N_t+N_o+i} - x_{14+2N_t+N_o+i})}{(A_o (L_o - x_L)/N_o)}, \quad i = 1, \ldots, N_o \\
\dot{x}_{13+2N_t+N_o+i} &= \dot{Q}_{lo_i} = & \left[(x_{13+2N_t+i} - x_{14+2N_t+i}) \frac{N_o}{\rho_i (L_o - x_L)} - R_{cyl} x_{13+2N_t+N_o+i} \right] A_o
\end{aligned}
$$

The ordinary differential equations obtained in the previous sections can be written together in state space form, as shown in Table 3.2, Table 3.3 and Table 3.4. These equations are then solved in time-stepped manner using a 4^{th} order Runge-Kutta numerical scheme. The complete numerical solution scheme was written in C and the code has been provided in Appendix B.

3.5 Flow analysis using CFD

Commercially available CFD tools have been successfully used in earlier attempts at modeling the hybrid pumping device, primarily to find out the pressure losses in the pumping chamber [197, 207]. Compared to empirical values, the use of these numerical tools allows more accurate computation of fluid flow parameters specific to the current design geometry. In our analysis of the hybrid pump and fluid flow through the manifold, we used CFD to model the flow through the reed valve ports and the manifold passages.

3.5.1 Reed valves

The flow of hydraulic oil through the reed valves is an extremely complex phenomenon involving the interaction between the fluid and the reed structure. The pressure drop across the reed valve port and the determination of the valve opening pressure, P_{open}, are critical inputs to the simulation model.

The behavior of the reed valves under varying flow rates depends strongly on the geometrical parameters of the assembly. Everything else remaining the same, the thickness of the reed (and hence, its stiffness) governs the force required to fully open the valve. To model the strongly coupled behavior, we considered a 2-D section of the reed port and simulated the flow behavior at different pressure differences. The inlet boundary on the left was set at the desired value of pressure, while the outlet boundary on the right was maintained at zero pressure. The height of the reed chamber is 0.15 mm (0.06 inch) and the port width is 3.81 mm (0.15 inch); Figure

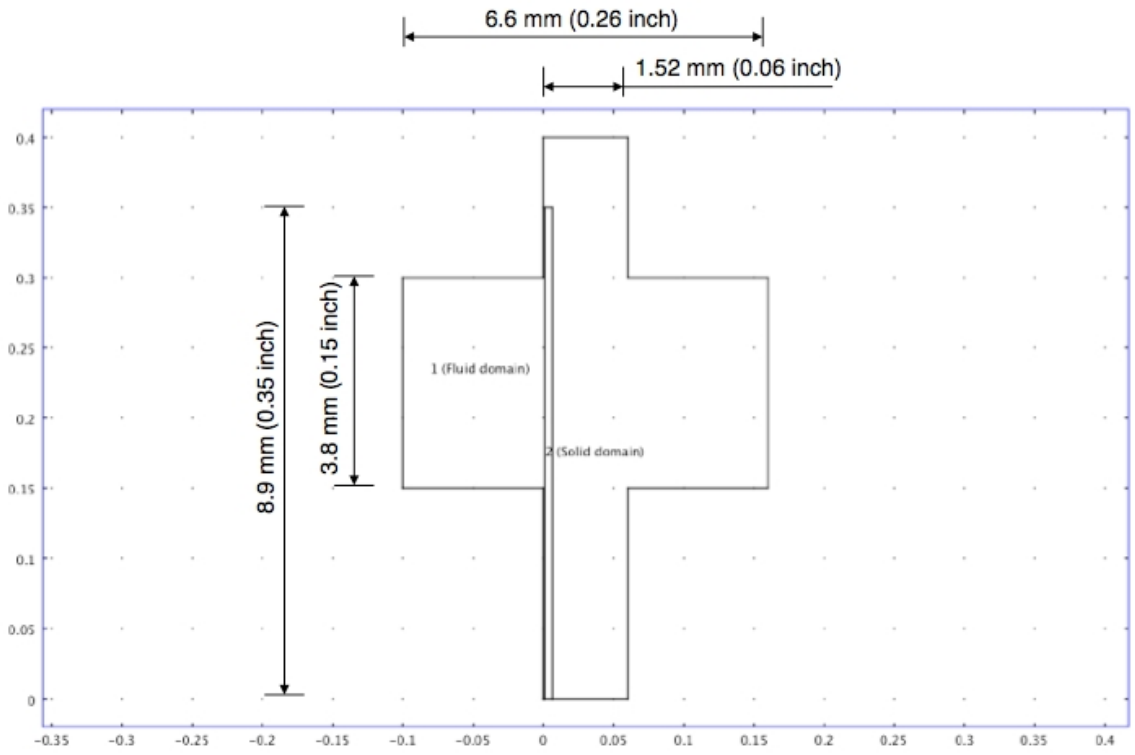

Figure 3.10: Sectional view and dimensions of exhaust reed port used for CFD studies

3.10 shows the geometry of the 2-D cutaway section of the reed port. The flow was assumed to be laminar, since the Reynolds number at the highest operating fluid velocities was found to be much lower than 500. Also, to maintain simplicity of the model, the fluid was assumed to be incompressible. The fluid-structure-interaction module in COMSOL Multiphysics was used for all the simulations.

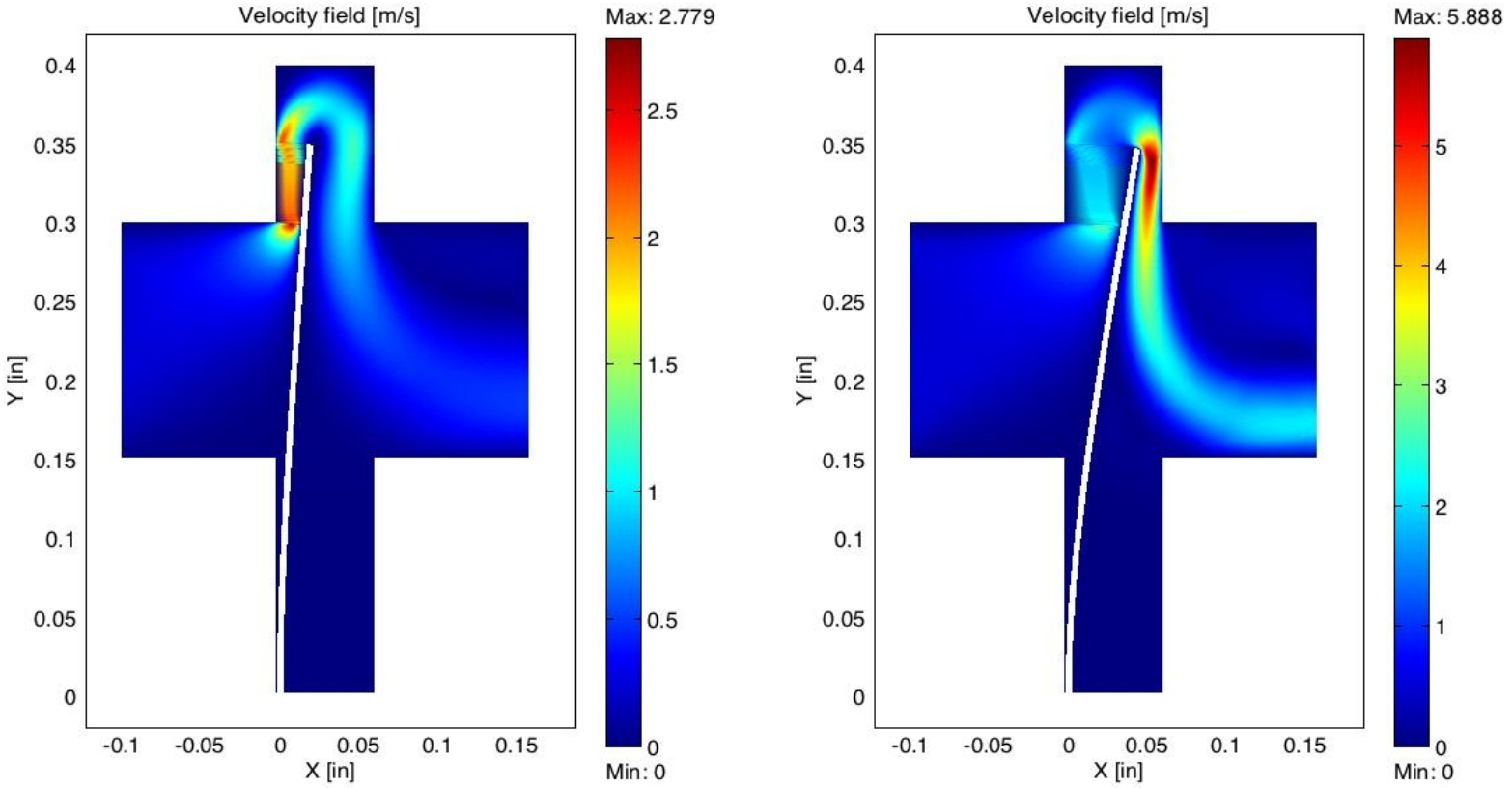

(a) Pressure = 13790 Pa (2 psi)

(b) Pressure = 27580 Pa (4 psi)

Figure 3.11: Flow study with 0.10 mm (4 mil) thick reed valve

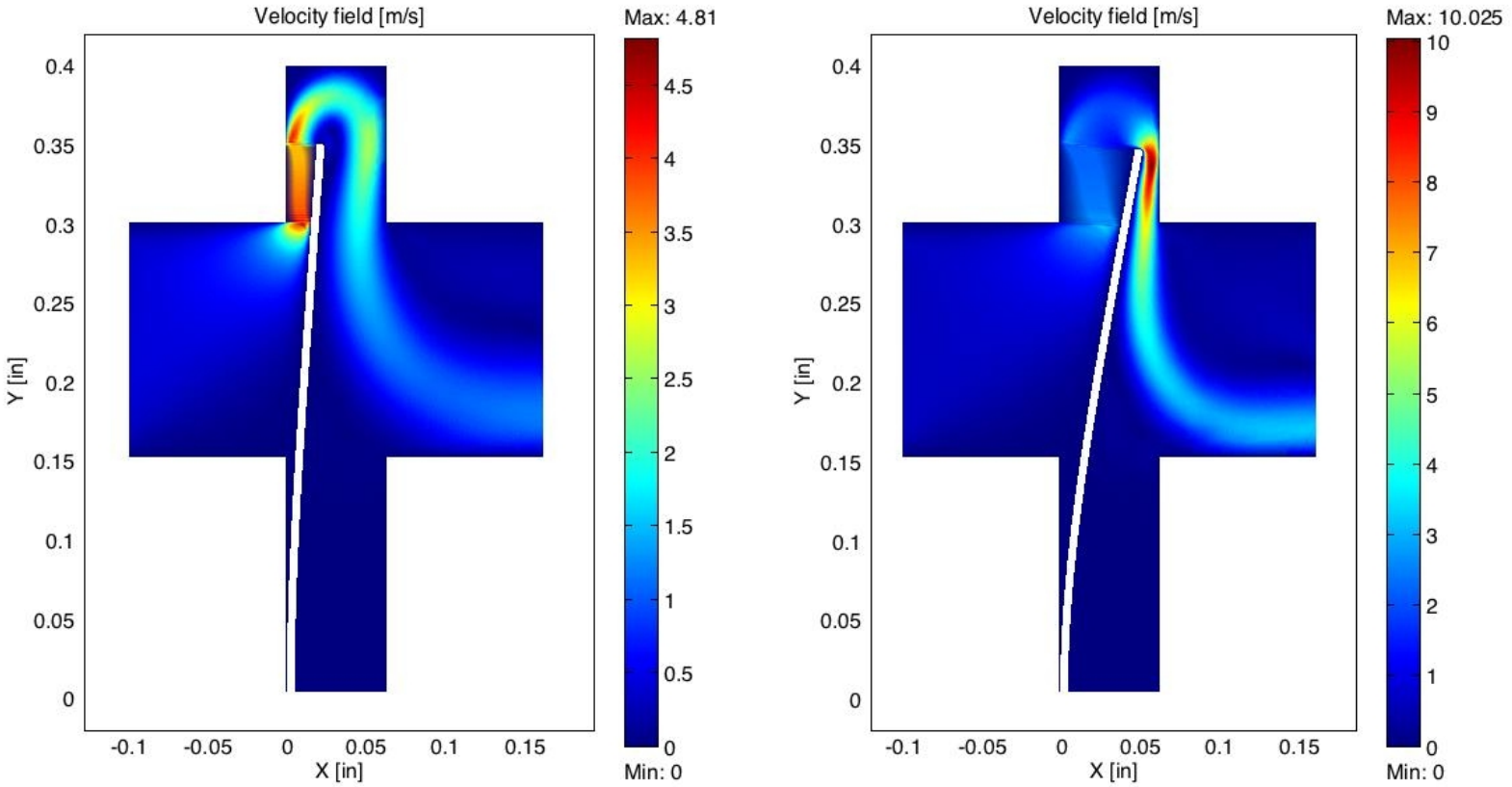

(a) Pressure = 27580 Pa (4 psi)

(b) Pressure = 55160 Pa (8 psi)

Figure 3.12: Flow study with 0.13 mm (5 mil) thick reed valve

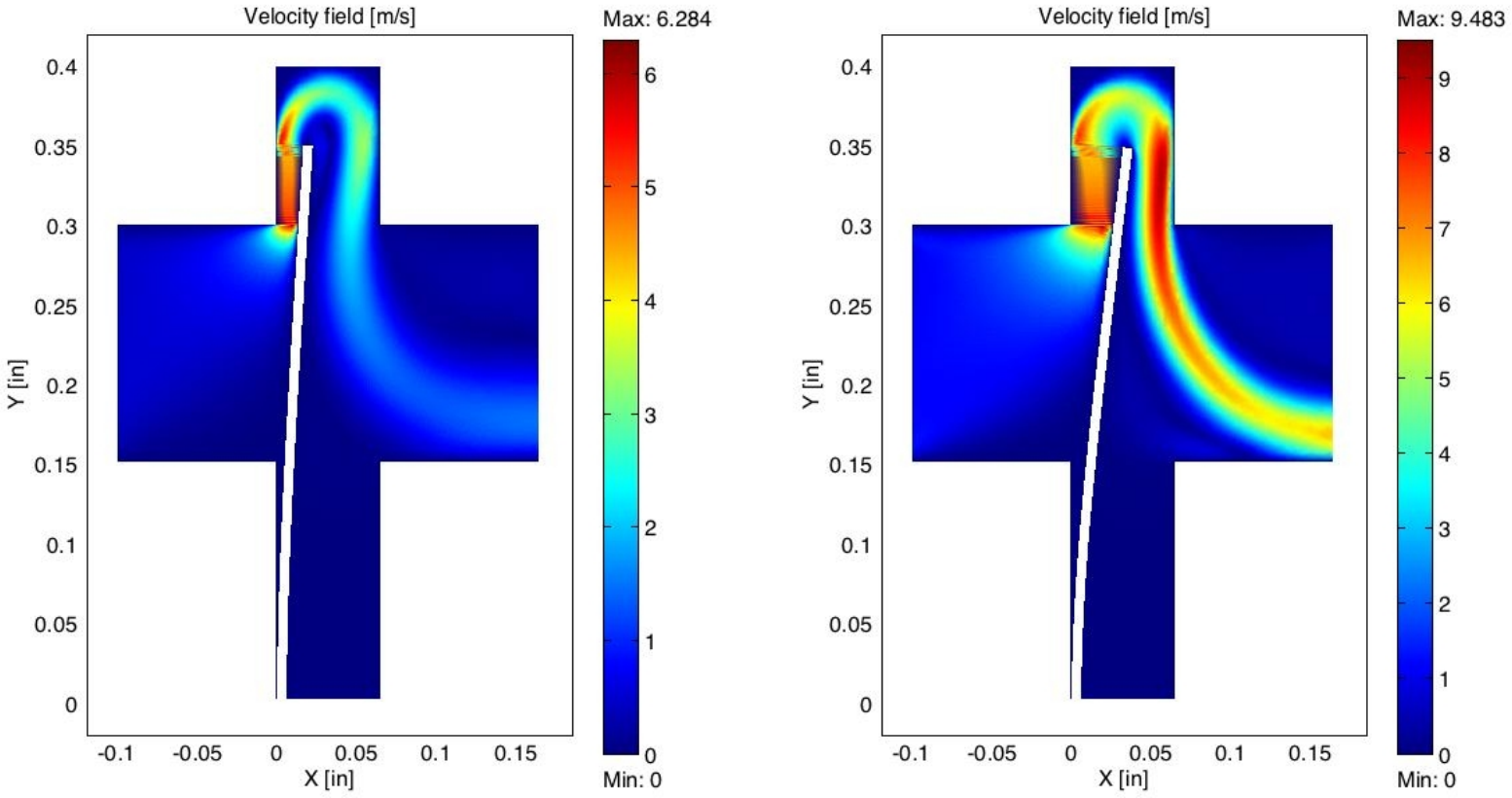

(a) Pressure = 41370 Pa (6 psi)

(b) Pressure = 82740 Pa (12 psi)

Figure 3.13: Flow study with 0.15 mm (6 mil) thick reed valve

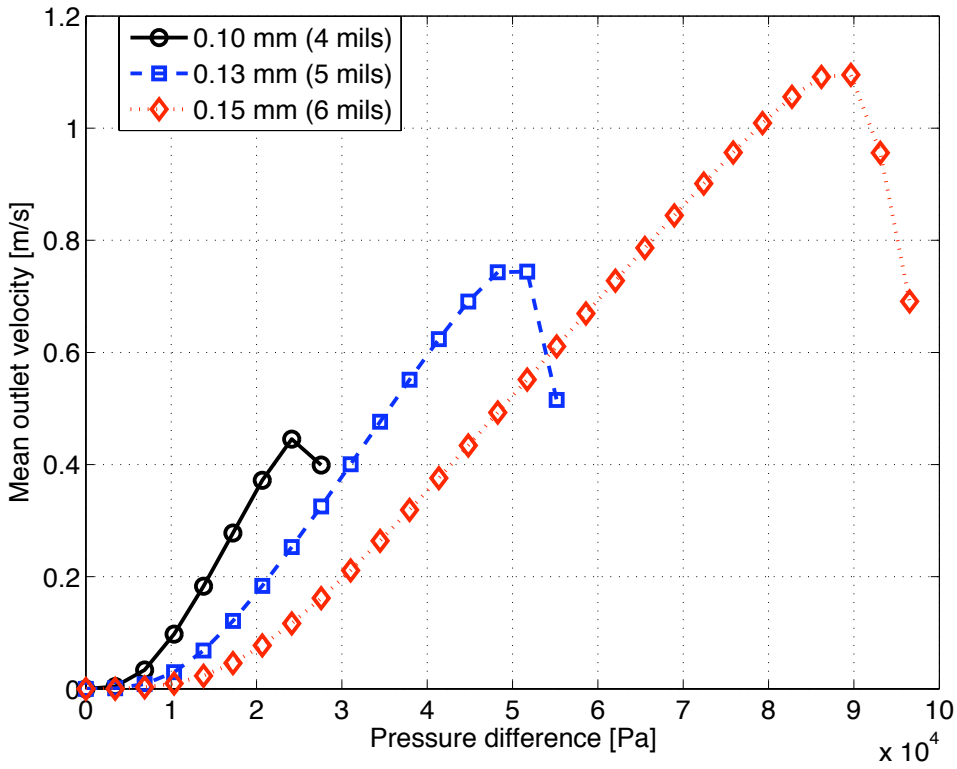

Figure 3.14: Behavior of reed valves of different thicknesses

The behavior of three different thicknesses of reed valves, 0.10 mm (4 mils), 0.13 mm (5 mils) and 0.15 mm (6 mils) are shown in the velocity field plots in Figures 3.11, 3.12 and 3.13 respectively. Initially, increase in pressure difference across the reed port causes a increase in the volume flow rate, proportional to the mean velocity, through the port. However, due to limited space within the reed port, the flow is highly constricted when the reed valve opens fully, resulting in a decrease in flow rate beyond a certain value of pressure [Figure 3.14]. In other words, there is a particular value of pressure at which the valve can be assumed to be completely open and the viscous losses are least; this value of pressure was used as representative of the parameter P_{open} in our dynamic simulation model.

The comparative study of reed valve behavior also clearly shows the dependence on reed thickness and reed port geometry. While a thiner reed requires lower pressure difference to open completely, the maximum volume flow rate through it is also more limited than a thicker reed. Hence, the choice for reed thickness has to be made by comparing the flow rate requirements with the allowable pressure losses in the reed valve. The geometry of the port can also be modified to improve the performance of the valve; filleting the sharp edges of the reed port will help in improving flow rate [207]. According to the previous research [92, 202], insufficiently stiff reeds can lead to *valve float* where the valves fail to close completely between cycles allowing back flow through the pump, while excessive stiffness reduces maximum reed displacement causing higher pressure drops.

The transient behavior of the reed valve and corresponding fluid flow rate are strongly dependent on the time-varying pressure difference across the valve port. This dynamic behavior was also simulated using CFD tools for two reed valve thicknesses, 0.10 mm (4 mil) and 0.13 mm (5 mil). The geometry of the flow path remained the same as the static studies; the pressure (ΔP) at the inlet boundary on the left was a sinusoidally varying parameter in this case while the outlet boundary was maintained at zero pressure. The fluid was assumed to be entering the reed port uniformly at the inlet with $v_y = 0$ The mean flow velocity in the x-direction (v_x) was calculated as the average of the velocity values (along x-axis) at the grid points on the outlet boundary; since the fluid was assumed to be incompressible, this value is the same even if calculated at the inlet boundary.

The *percentage reed displacement* was calculated as the ratio of the instanta-

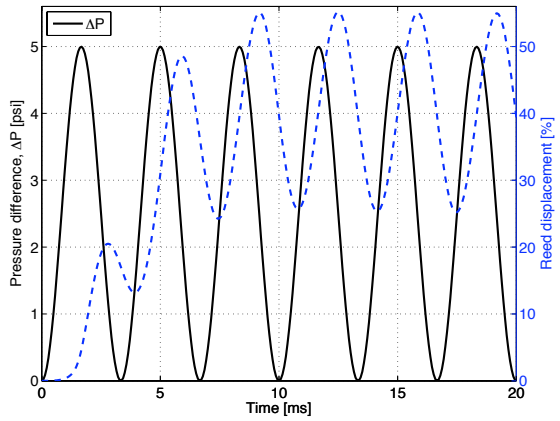

(a) Reed displacement at 300 Hz

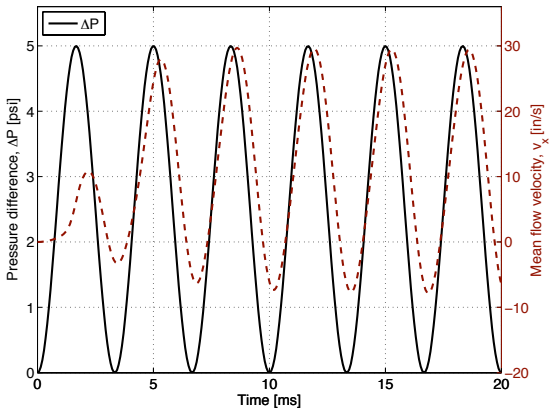

(b) Mean flow velocity at 300 Hz

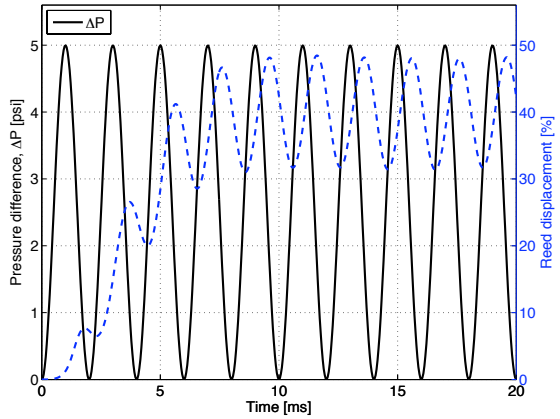

(c) Reed displacement at 500 Hz

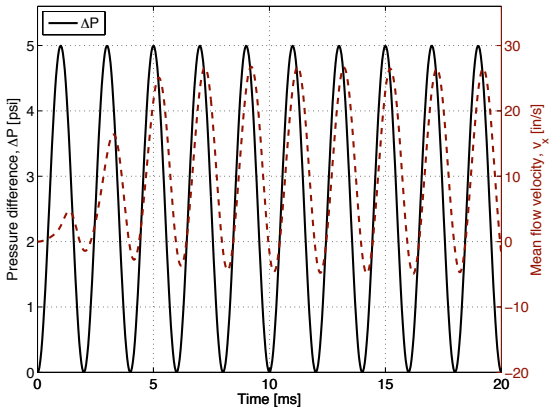

(d) Mean flow velocity at 500 Hz

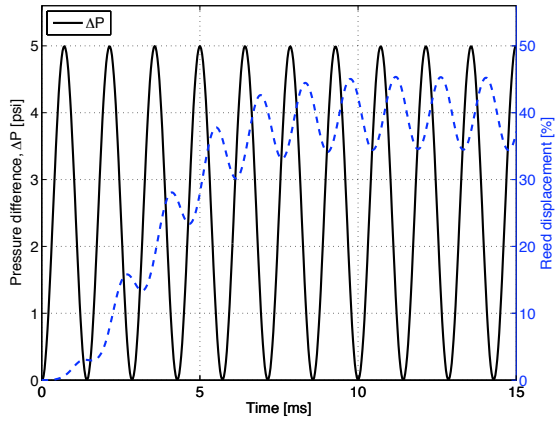

(e) Reed displacement at 700 Hz

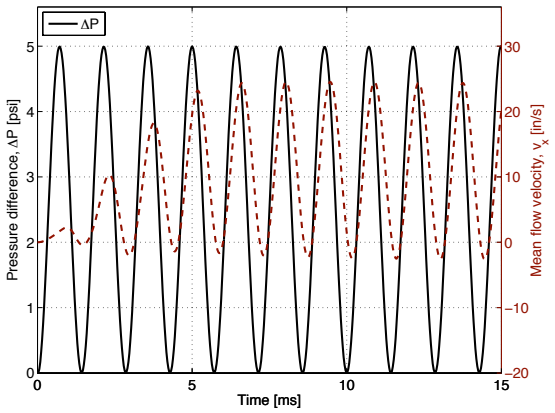

(f) Mean flow velocity at 700 Hz

Figure 3.15: Transient behavior of 4 mil reed valve at different frequencies; $\Delta P_{max} = 5$ psi, $\Delta P_{min} = 0$ psi

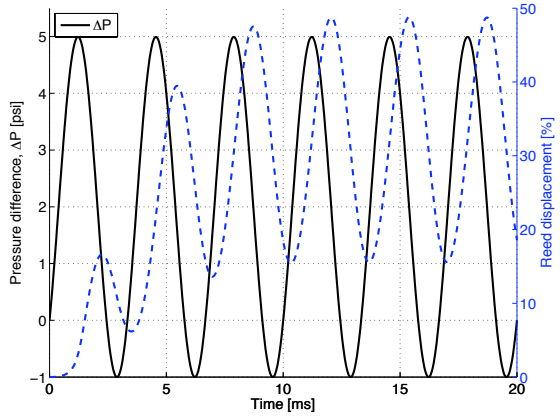

(a) Reed displacement at 300 Hz

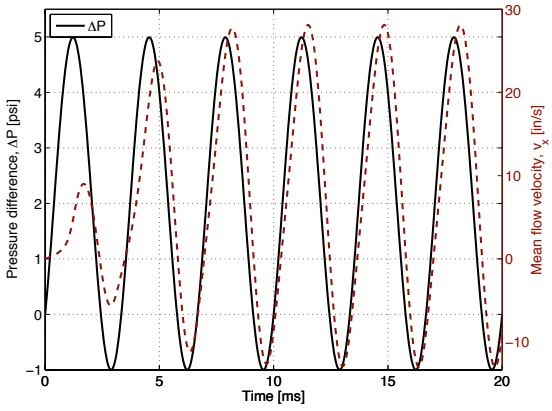

(b) Mean flow velocity at 300 Hz

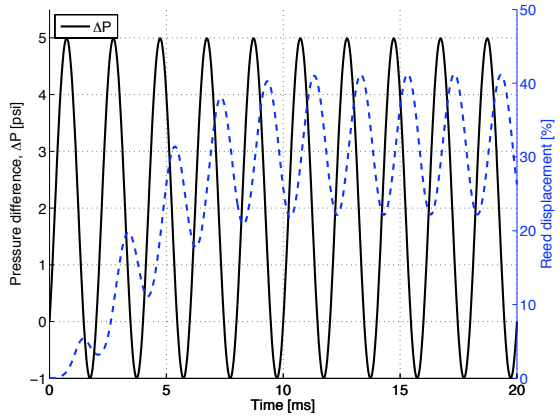

(c) Reed displacement at 500 Hz

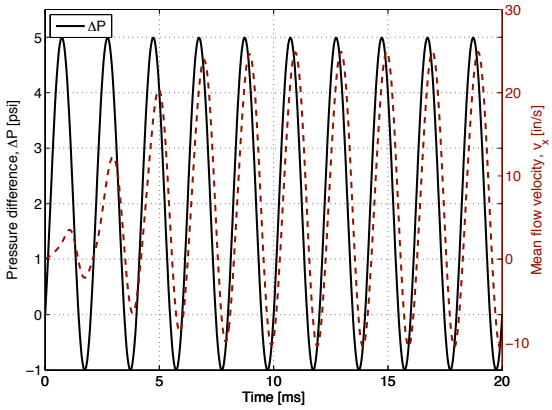

(d) Mean flow velocity at 500 Hz

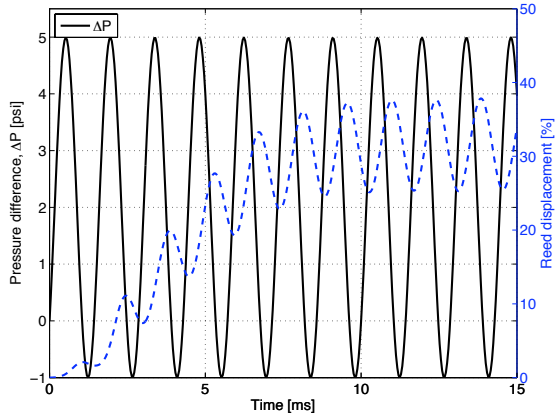

(e) Reed displacement at 700 Hz

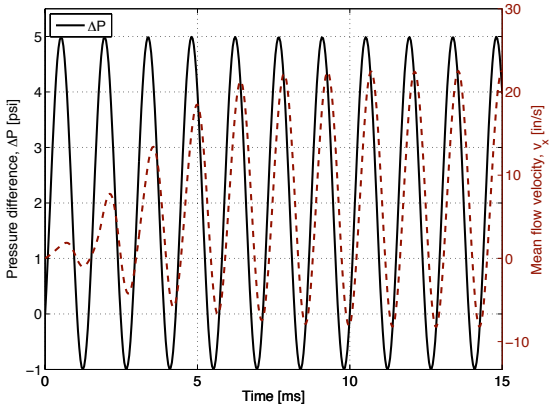

(f) Mean flow velocity at 700 Hz

Figure 3.16: Transient behavior of 4 mil reed valve at different frequencies;

$$\Delta P_{max} = \textbf{5 psi}, \Delta P_{min} = \textbf{-1 psi}$$

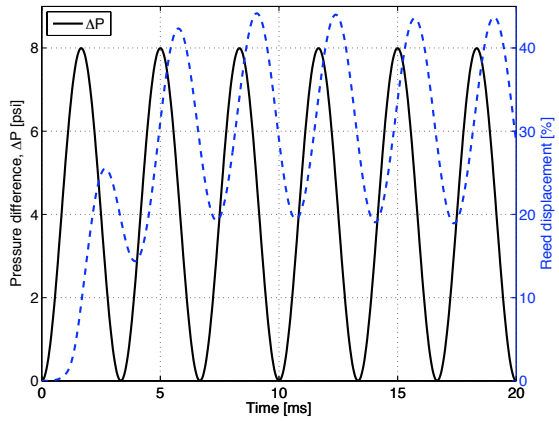

(a) Reed displacement at 300 Hz

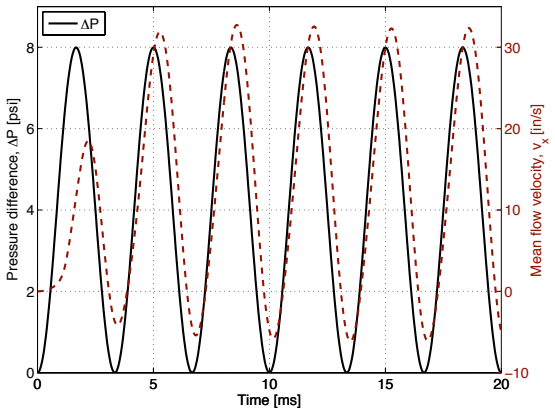

(b) Mean flow velocity at 300 Hz

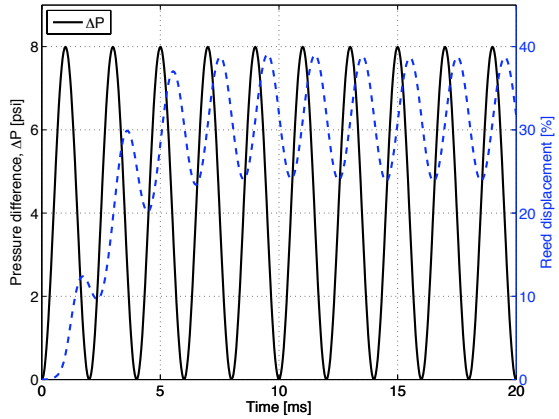

(c) Reed displacement at 500 Hz

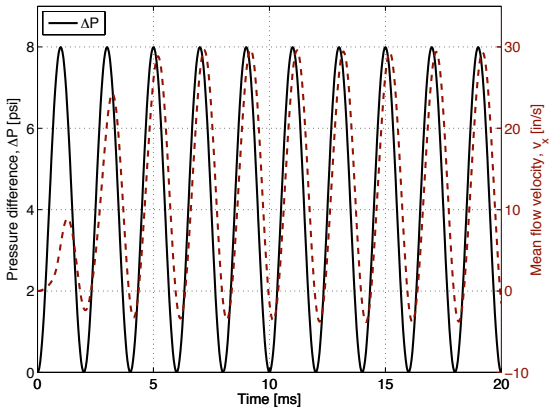

(d) Mean flow velocity at 500 Hz

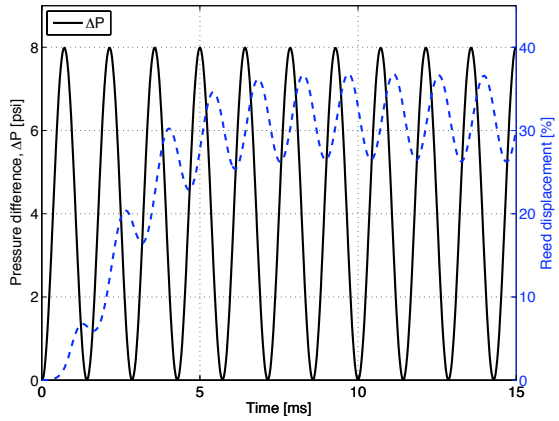

(e) Reed displacement at 700 Hz

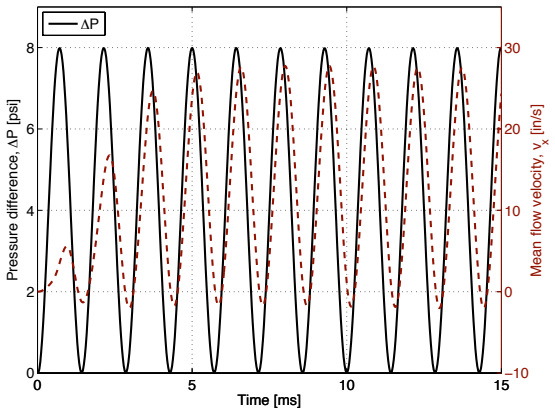

(f) Mean flow velocity at 700 Hz

Figure 3.17: Transient behavior of 5 mil reed valve at different frequencies; ΔP_{max} = 8 psi, ΔP_{min} = 0 psi

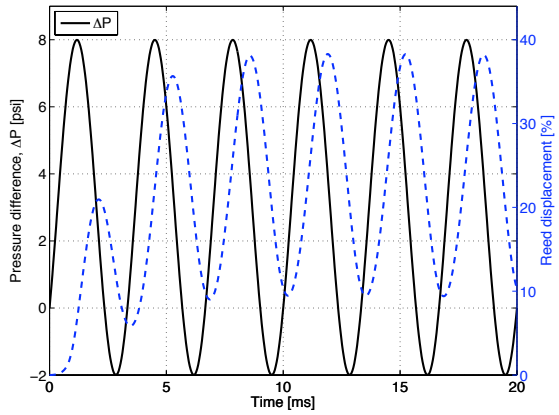

(a) Reed displacement at 300 Hz

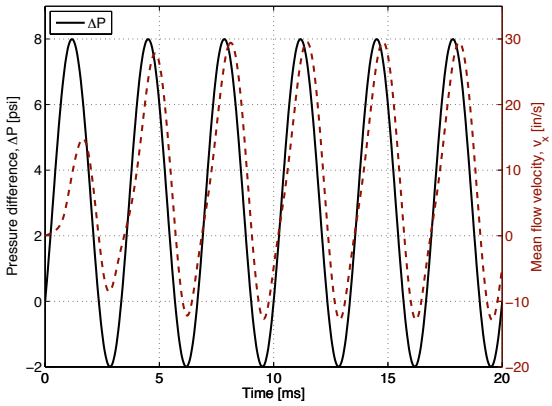

(b) Mean flow velocity at 300 Hz

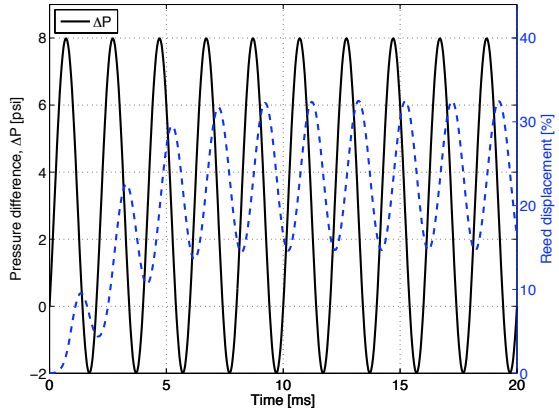

(c) Reed displacement at 500 Hz

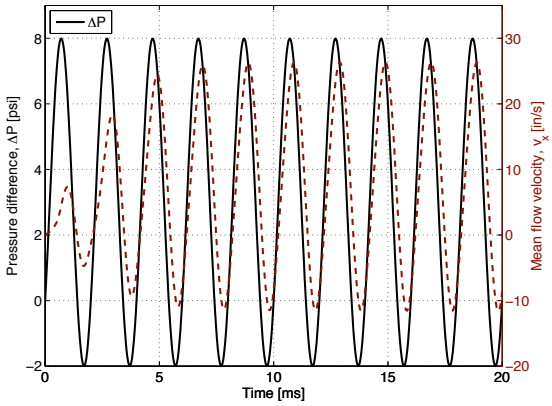

(d) Mean flow velocity at 500 Hz

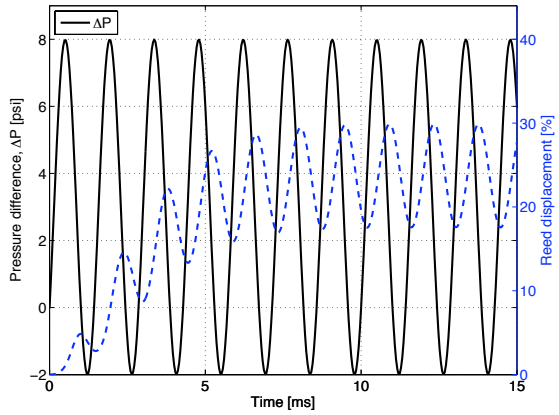

(e) Reed displacement at 700 Hz

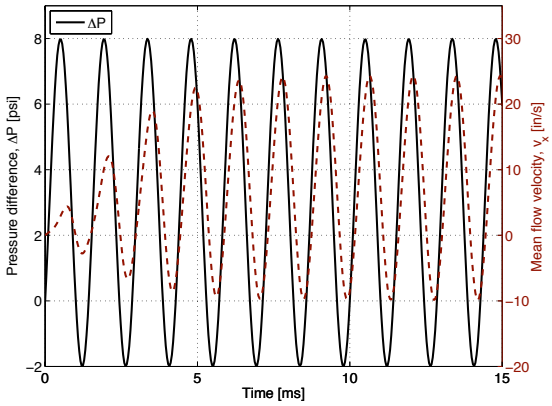

(f) Mean flow velocity at 700 Hz

Figure 3.18: Transient behavior of 5 mil reed valve at different frequencies;

ΔP_{max} = 8 psi, ΔP_{min} = -2 psi

neous displacement of the free end of the reed plate to the overall length of the valve port, which was 1.52 mm (0.06 in). This measure gave us a good comparison of reed valve opening for the two different reed thicknesses studied. Both the reed displacement and the mean flow velocity, v_x, have been plotted for four cases and three pumping frequencies (300 Hz, 500 Hz and 700 Hz). The time-varying pressure difference is shown with the solid black line in all cases, while the reed displacement and mean velocity are shown in blue and brown dashed lines respectively. For the 4 mil thick reed, two different sinusoidal pressure values were used: the first one had a peak value of 5 psi with a minimum value of zero [Figure 3.15], while the second study had a slightly offset pressure signal with highest value of 5 psi and least value of -1 psi [Figure 3.16]. A similar set of computations were carried out for the 5 mil thick reed; the first had maximum value of 8 psi with a minimum value of zero [Figure 3.17], while the second set had an offset pressure signal with high value of 8 psi and low value of -2 psi [Figure 3.18].

All the results clearly show frequency-dependent effects on the reed and flow parameters. Even though the pressure input remained the same for any particular set, the amplitude of steady-state response of both reed displacement and flow velocity decrease with frequency. The results also show that though the pressure drops to zero or even lower in every cycle, the valve does not close fully and there is some reverse flow over the reed. This implies that a considerable reverse pressure gradient is required to completely close the valve in every cycle. The combined frequency-dependent effects of fluid inertia and reed valve motion ultimately result in lower flow rates through the reed port at higher frequencies of operation for the same pressure

condition.

3.5.2 Manifold tubing

To find the minor loss coefficients associated with the flow through the exhaust and intake tubings, models were built in COMSOL Mutiphysics and solved for the different volume flow rates within the designed manifold geometry at varying pressure differentials. For simplicity, the fluid was assumed to be incompressible (density ρ = 860 kg/m^3) in the exhaust manifold too. For the exhaust manifold, the pressure at the entry was varied at different positive values and the corresponding mean flow velocity was computed; one representative case with 1.4 kPa (0.2 psi) is shown in Figure 3.19(a). For the intake tube simulations, the pressure at intake boundary was set at different negative values with the accumulator boundary maintained at zero; a representative case at a pressure difference of 3.4 kPa (0.5 psi) is shown in Figure 3.19(b). Using the results from these simulations at different pressure differences, we calculated the corresponding mean flow velocities in the exhaust / intake ports. The results are plotted in Figure 3.20, where we clearly see a nonlinear variation of pressure difference with mean flow velocity.

Assuming the quadratic form

$$\Delta P = Av + Bv^2$$

the coefficients A and B were calculated using least squares regression techniques. If v_i is the computed mean velocity at pressure difference ΔP_i, $i = 1, \ldots, N$, then we

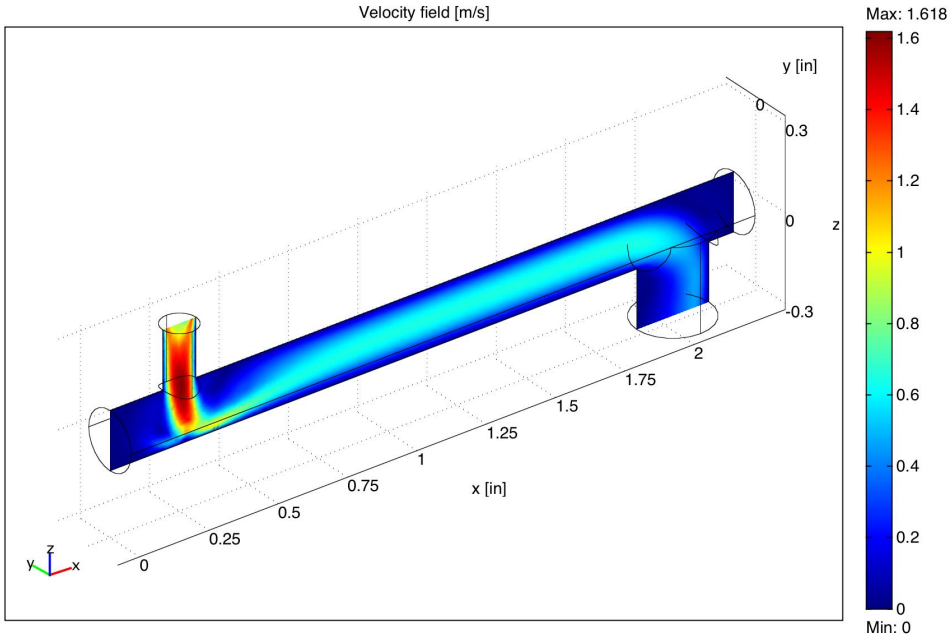

(a) Flow through exhaust manifold tube

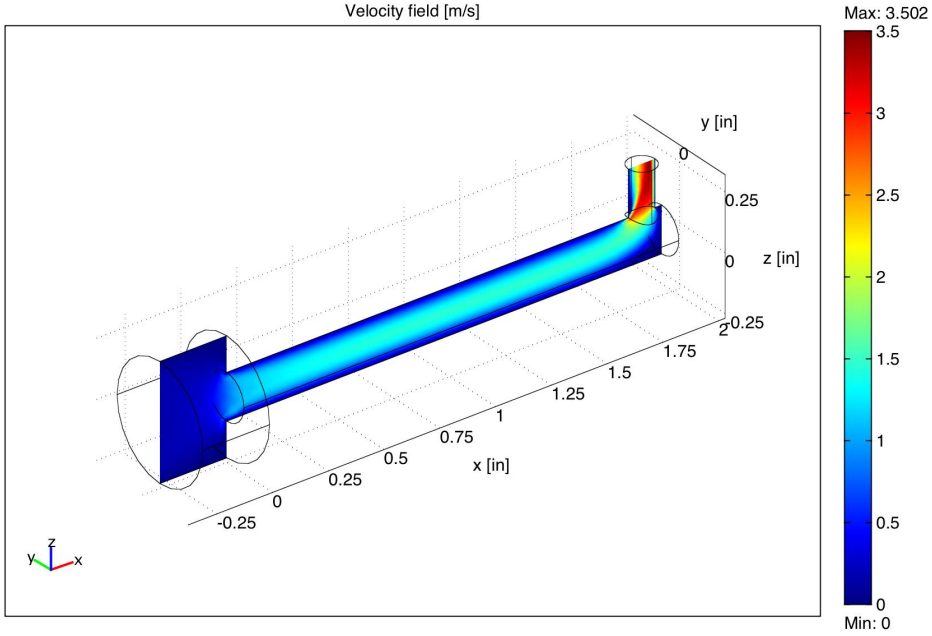

(b) Flow through intake manifold tube

Figure 3.19: Simulations of fluid flow through manifold passages

can write the total squared error as:

$$E = \sum_{i=1}^{N} \left[\Delta P_i - (Av_i + Bv_i^2)\right]^2,$$

which can be minimized with respect to the unknown coefficients A and B to get the following equation for best-fit parameters:

$$\begin{bmatrix} \sum_{i=1}^{N} v_i^2 & \sum_{i=1}^{N} v_i^3 \\ \sum_{i=1}^{N} v_i^3 & \sum_{i=1}^{N} v_i^4 \end{bmatrix} \begin{Bmatrix} A \\ B \end{Bmatrix} = \begin{bmatrix} \sum_{i=1}^{N} P_i v_i \\ \sum_{i=1}^{N} P_i v_i^2 \end{bmatrix} \tag{3.44}$$

The minor loss coefficient, K_{L_t}, relates the flow velocity v with the pressure drop ΔP using the quadratic relation:

$$\Delta P = \frac{1}{2} K_{L_t} \rho v^2$$

Hence, for flow through the respective manifold passage, the loss coefficient was then calculated as follows:

$$K_{L_t} = \frac{2B}{\rho}$$

3.6 Simulation results

The model was used to predict the uni-directional performance of the actuator using material properties and geometric parameters given in Table 3.5. The Terfenol-D rod is actuated at a particular pumping frequency. The flux density, B, used in the simulations is a sinusoid with a dc offset; the magnitude of the sinusoidal portion depends on the pumping frequency and varies according to the transfer function derived in Section 3.3. Since the reed valves used in the experimental setup were 0.10 mm (4 mil) thick, the value of P_{open} was set at 20.7 kPa (3 psi). The simulation was

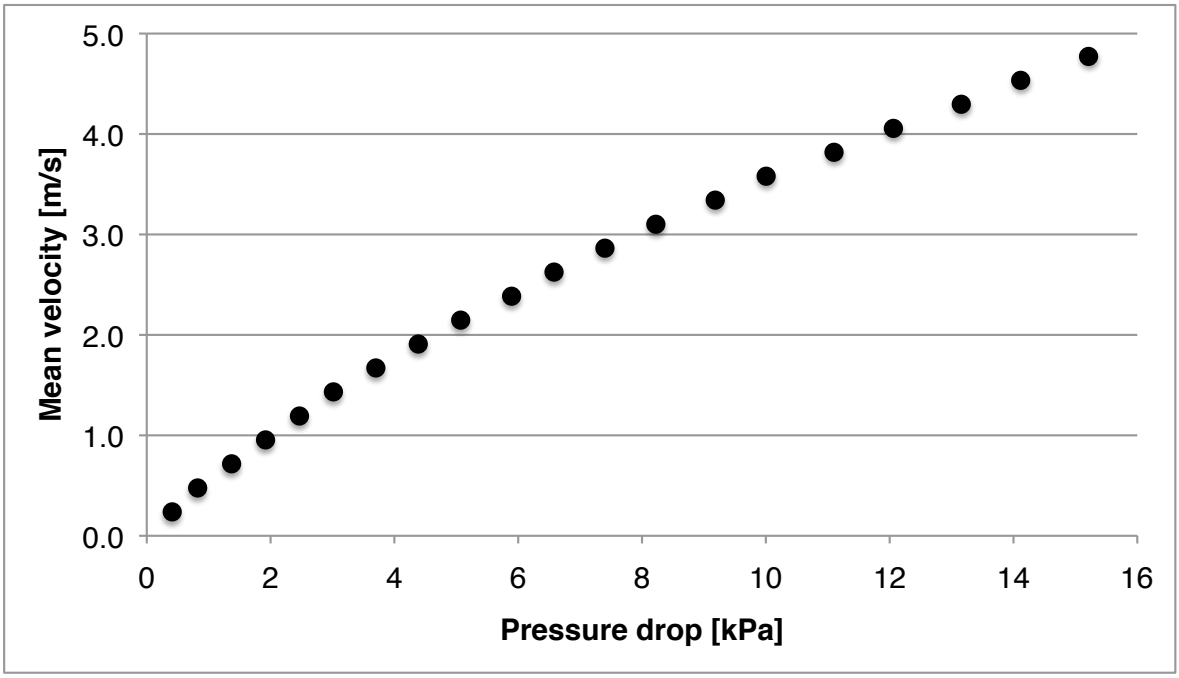

(a) Exhaust manifold tube

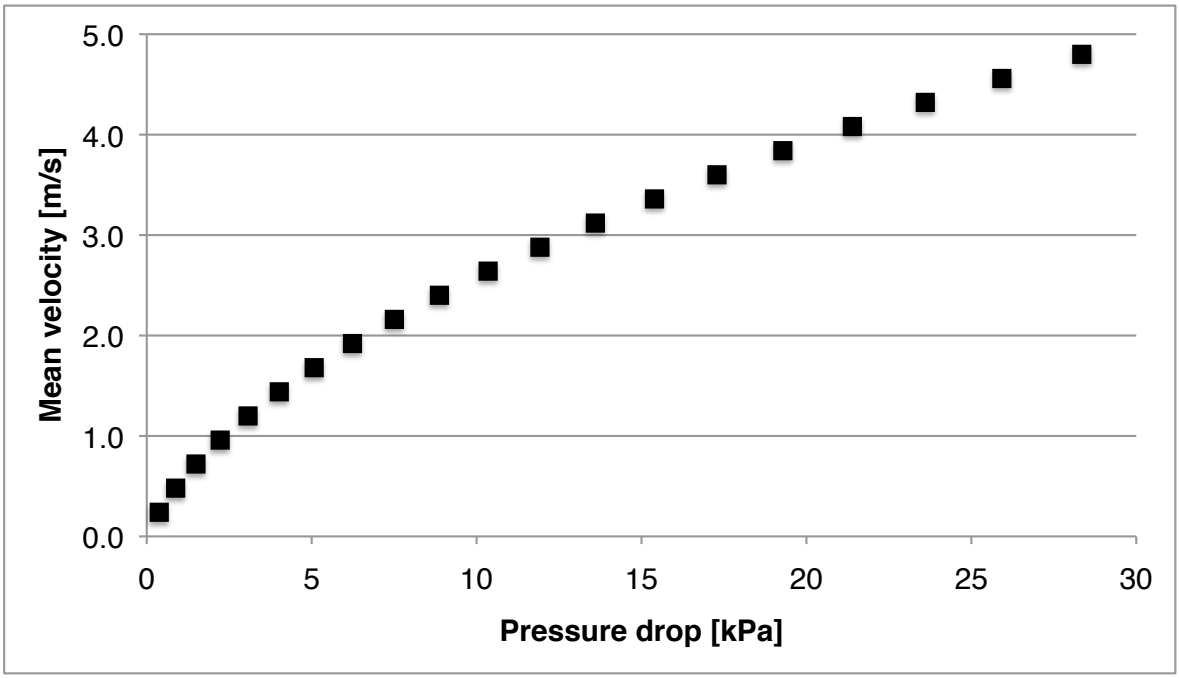

(b) Intake manifold tube

Figure 3.20: Results of flow simulations through manifold passages

done for with a sinusoidal driving input B and the values of the states were updated at each computation step. This was carried out over the entire frequency range of interest. The output velocity was calculated from the slope of the linear fit to the output displacement variable, x_L. The simulation time was varied for each frequency and the states are computed for at least 50 complete cycles of the input signal. The simulation frequency was 1 MHz.

The value of static friction, F_s, in the output cylinder was pre-determined by adding measured weights on to the output shaft (aligned vertically) and noting the point at which it started to move; the critical weight was found to be 1.36 kg (3 lb). Hence, the value of static friction F_s used for our simulations was 13.36 N. The value of the dynamic friction, F_d, however, could not be determined experimentally and was estimated to be 4.45 N (1 lbf) from the simulation studies.

The simulation results for the 51 mm (2 inch) and 102 mm (4 inch) Terfenol-D rods operated using the LVC623 amplifier are superimposed on the experimental data and shown in figures 3.21(a) and 3.21(b) respectively, while the results for the 51 mm (2 inch) and 102 mm (4 inch) Terfenol-D rods operated using the LVC5050 amplifier are shown in figures 3.22(a) and 3.22(b) respectively. The fluid bulk modulus was changed for simulation at different bias pressures; the chosen values were 68.9 MPa (10,000 psi) and 103.4 MPa (15,000 psi) corresponding to 345 kPa (50 psi) and 690 kPa (100 psi) bias pressure respectively. We see a very good match for the output velocity versus frequency data between test data and model calculations. Both the maximum no-load velocity and the location of the peak frequency were accurately captured for all the no-load cases.

Table 3.5: SIMULATION PARAMETERS

Properties		
	β	34.5–68.9 MPa (5–10 ksi)
	ρ_0	860 kg/m^3
	ρ_a	9250 kg/m^3
	ν	21.0 cSt
	E_A	30.0 GPa
Dimensions		
	L_a	51 mm (2 inch), 102 mm (4 inch)
	D_a	12.7 mm (0.5 inch)
	L_{ch}	0.50 mm (20 mils)
	D_{ch}	38.1 mm (1.5 inch)
	L_t	35.6 mm (1.4 inch)
	D_t	5.10 mm (0.20 inch)
	L_{port}	6.35 mm (0.25 inch)
	D_{port}	3.05 mm (0.12 inch)
	L_o	50.8 mm (2 inch)
	D_o, D_i	19.05 mm (3/4 inch), 6.35 mm (1/4 inch)
Others		
	m_a, m_p	0.20 kg, 0.10 kg
	F_s, F_d	13.4 N (3 lbf), 4.5 N (1 lbf)
	K_d, K_s	1.8×10^3 N/m, 10.8×10^6 N/m

The frequency at which peak no-load performance occurs mainly depends on two properties, inertia and stiffness, of the actuation system. In general, the inertia of the system consists of the inertia of the pump piston, the output cylinder and the fluid being accelerated through the valves and manifold. When viewed as separate SDOF systems, the masses of the pump piston and the output cylinder (with no external load) are very small while the corresponding stiffnesses and driving forces are very large; hence, these systems have a high natural frequency and do not impose any limitations in our frequency range of operation. The fluid in the manifold, however, has a stronger inertia effect due to the long travel distance and the small cross-sectional area available in the compact manifold.

The fidelity of the model is also verified by comparing the actual displacement and strain data from the tests with the simulations. The displacements at 200 Hz and 300 Hz pumping frequencies are compared in Figure 3.24(a) and Figure 3.24(b) respectively, while the corresponding strains are shown in Figure 3.23(a) and Figure 3.23(b). A noticeable feature is the discrepancy in oscillatory behavior seen in the displacement data; while the experimental data at 200 Hz [Figure 3.24(a)] resembles a lightly damped system, the motion at 300 Hz seems to be more damped and does not show any oscillations[Figure 3.24(b)]. The model does a good job at capturing this variation in damping, as well as tracking the initial and final positions of the output piston in each pumping cycle. During numerical simulations, it was noted that this behavior was strongly dependent on the dynamics of the reed valves and the stiction behavior of the output piston.

The location of this peak depends on two main factors - inertia and stiffness

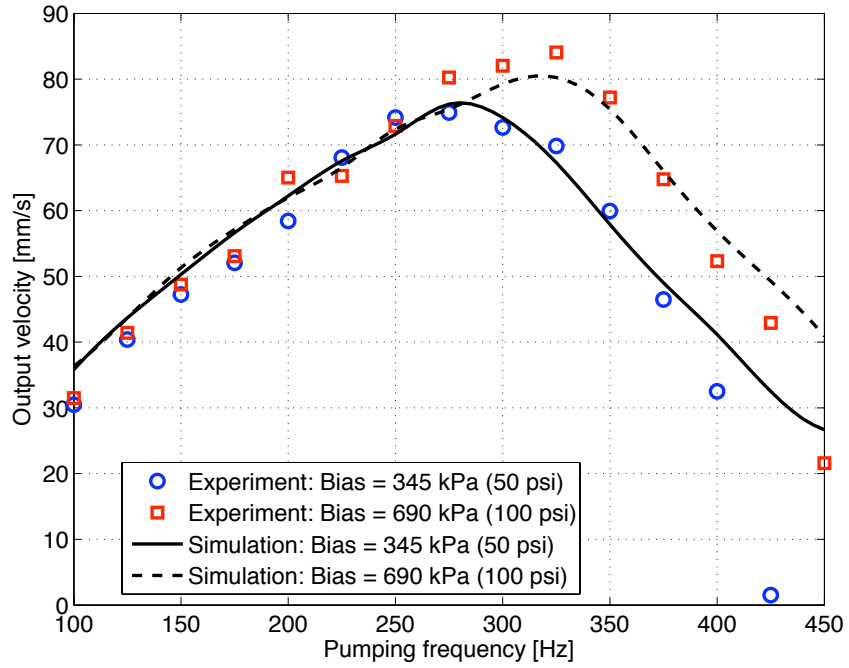

(a) 51 mm (2 inch) Terfenol-D rod

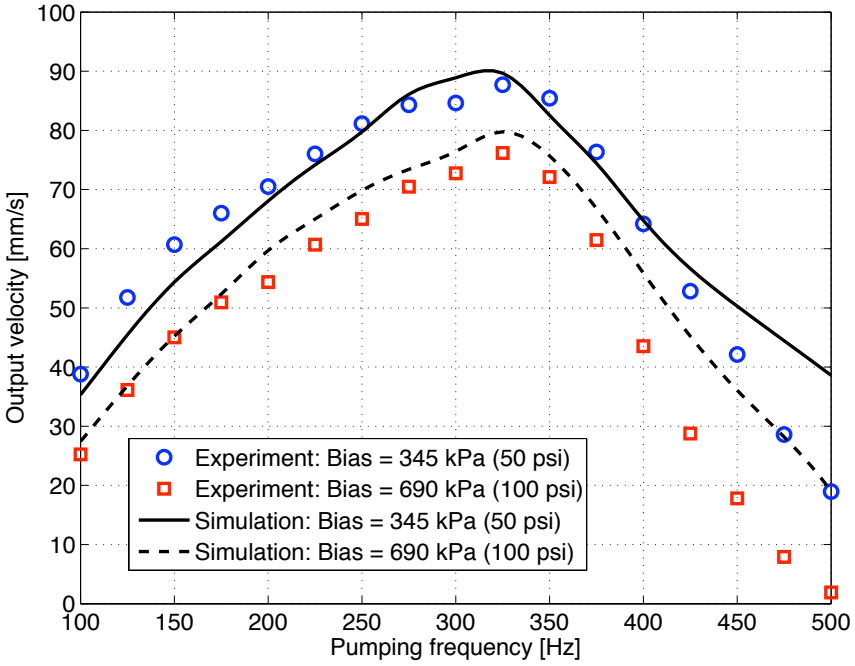

(b) 102 mm (4 inch) Terfenol-D rod

Figure 3.21: Comparison of experiment and simulation results obtained using LVC 623 amplifier

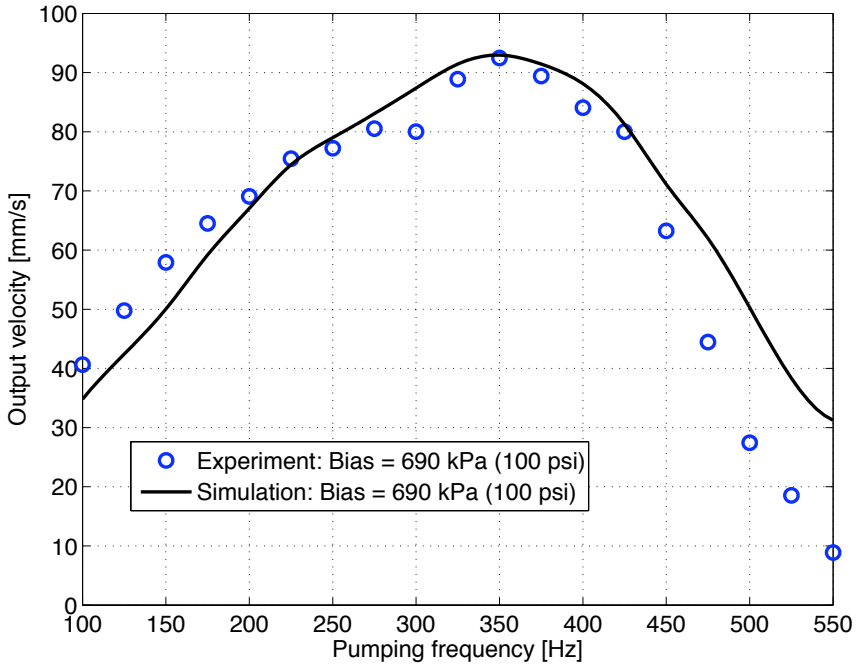

(a) 51 mm (2 inch) Terfenol-D rod

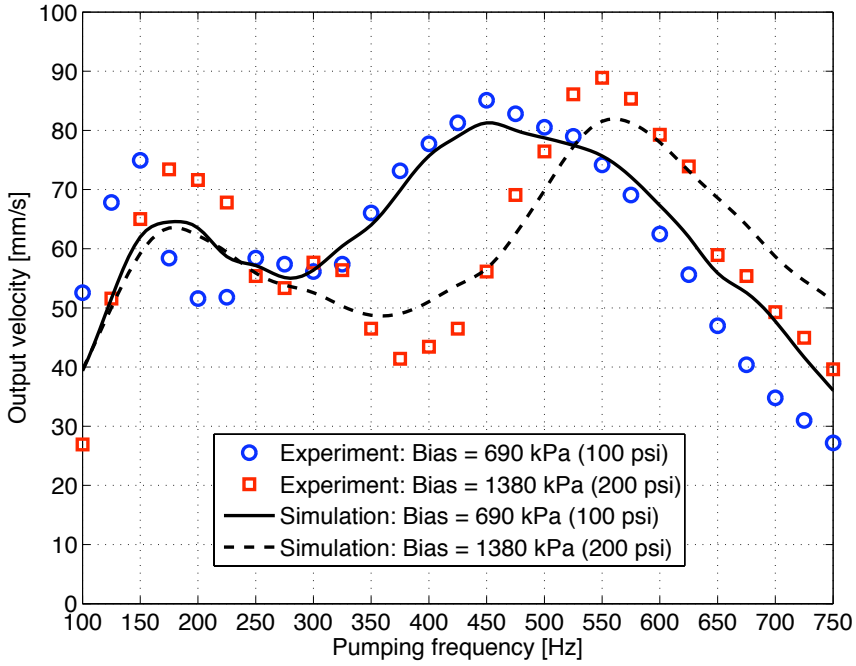

(b) 102 mm (4 inch) Terfenol-D rod

Figure 3.22: Comparison of experiment and simulation results obtained using LVC 5050 amplifier

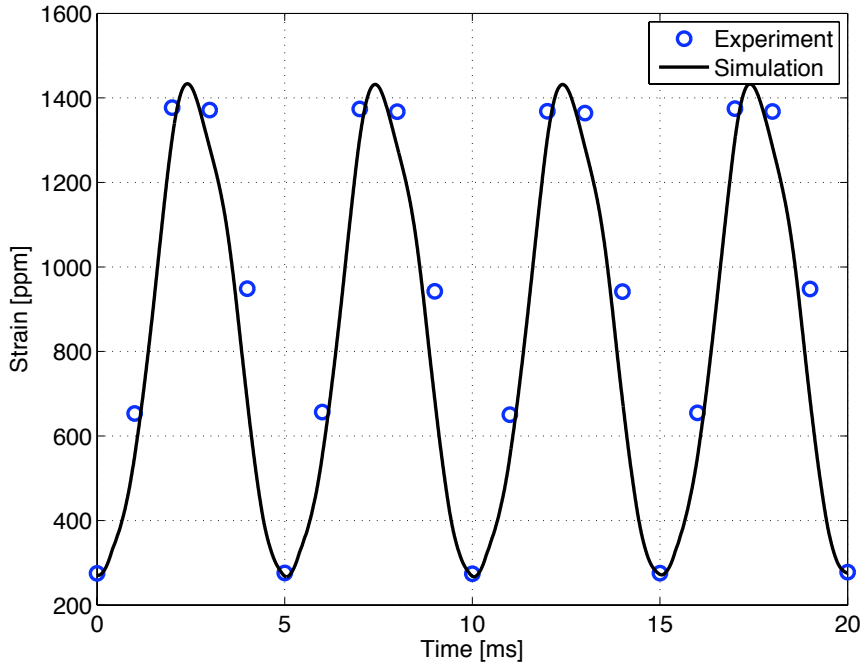

(a) 200 Hz

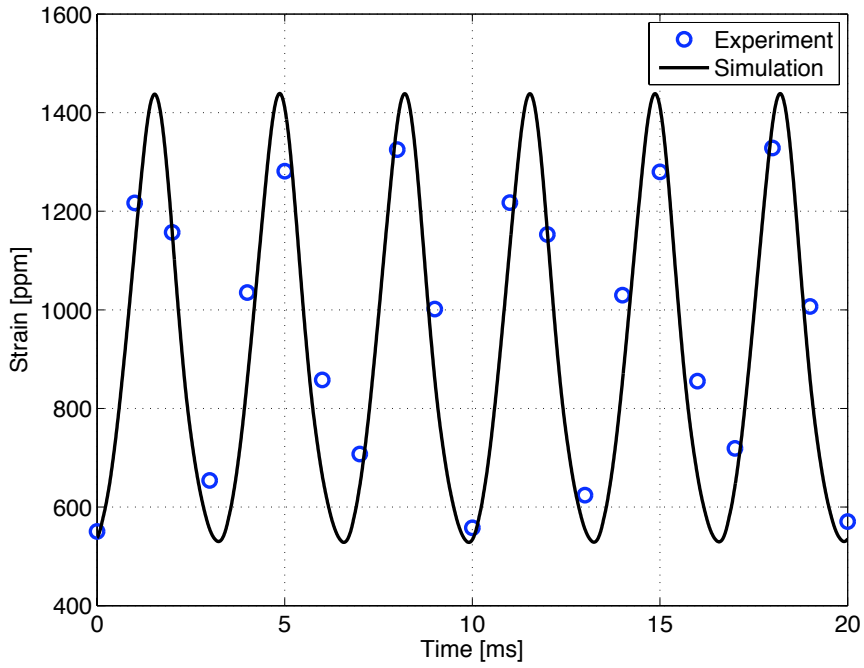

(b) 300 Hz

Figure 3.23: Comparison of actual strain between experiment data and simulation results for 51 mm (2 inch) Tefenol-D rod at two different pumping frequencies

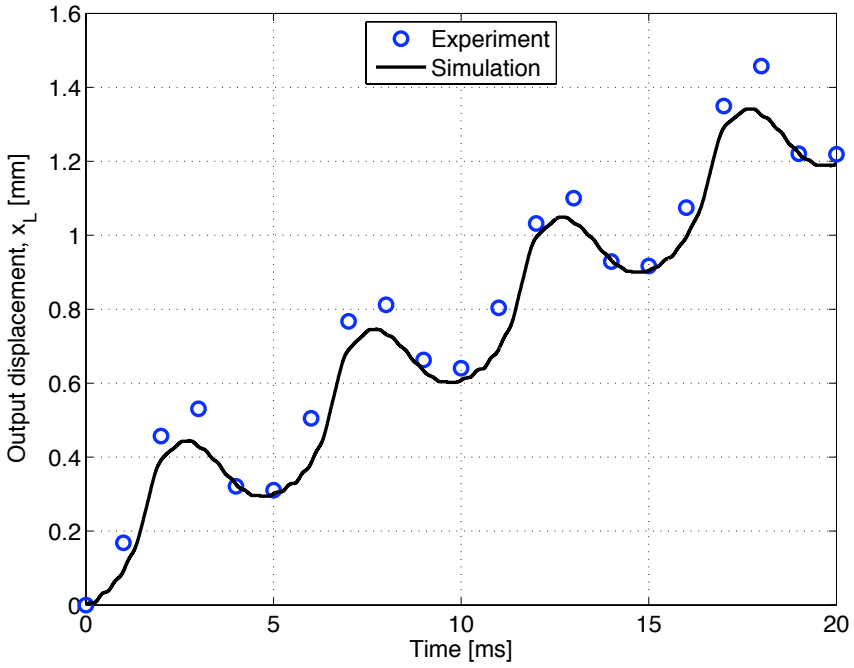

(a) 200 Hz

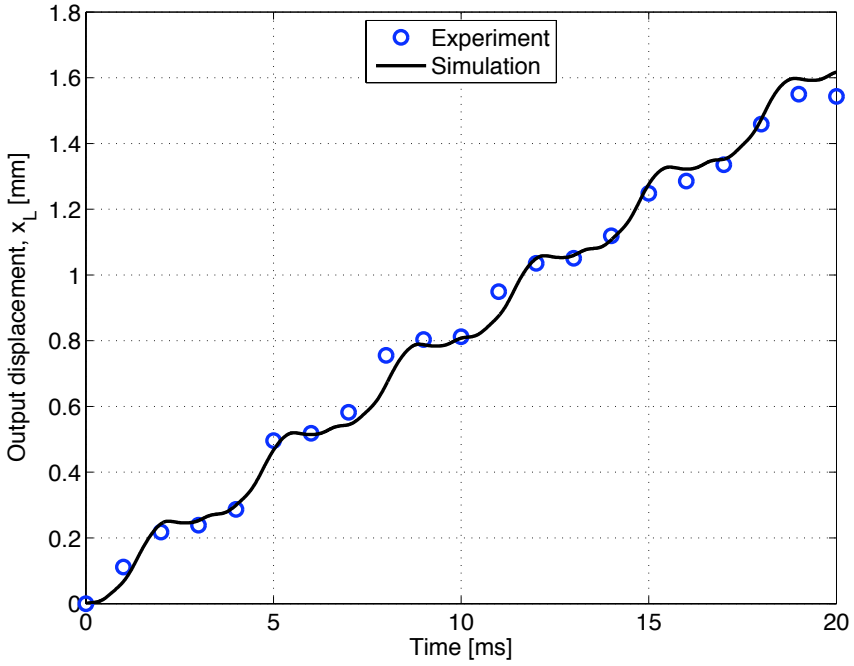

(b) 300 Hz

Figure 3.24: Comparison of output displacement between experiment data and simulation results for 51 mm (2 inch) Tefenol-D rod at two different pumping frequencies

of the actuation system. In general, the inertia of the system consists of the inertia of the pump piston, the output cylinder and the fluid being accelerated through the valves and manifold. The stiffness of the system arises from two primary factors:

1. Fluid compressibility i.e. bulk modulus.

2. Fluid accumulator characteristics.

The peak output frequency is highly sensitive to value of fluid bulk modulus, which should ideally be very high in order to transfer all the energy from the active material to the load. The presence of entrained air in the hydraulic oil increases the fluid compressibility [197, 262–264] and drastically reduces the bulk modulus, as seen in Figure 3.25. In practice, the oil is vacuumed after filling and then pressurized to minimize the effects of any entrained air within the fluidic system. The value of bulk modulus used in all our simulations with the first prototype driven by Terfenol-D was ∼68.9 MPa (10,000 psi). Increasing the value of bulk modulus will make the fluid stiffer, thus moving the resonant peak to a higher frequency, which is much lower than the manufacturer specified value of 1793 MPa (260,000 psi). Increasing the value of bulk modulus will make the fluid stiffer, thus moving the resonant peak to a higher frequency. In addition, a less compressible fluid causes lower pressure losses, since less force is lost in compressing the fluid volume in the manifold before it begins to move. The disadvantage is that the stiffness of the pumping chamber, K_{ch}, increases linearly with the value of bulk modulus and may result in lower induced strain from the actuator rod; as a consequence, the volume flow rates from the pumping chamber might reduce. Hence, the design of the actuator for particular specifications involves

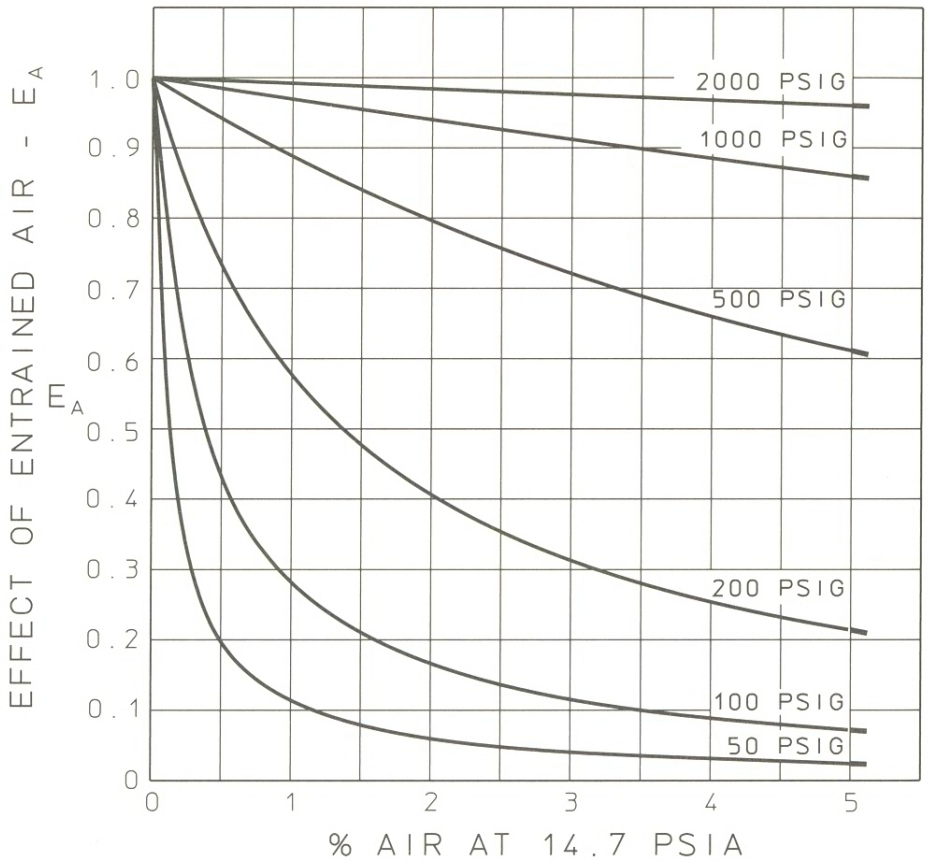

Figure 3.25: Effect of entrained air on the bulk modulus of a fluid [263]

a trade-off between the desired maximum pressure (i.e. blocked force) and maximum flow rate (i.e. no-load output velocity).

3.7 Conclusions

A comprehensive model of a hybrid hydraulic actuation system using Terfenol-D as the active driving element and hydraulic oil as the energy transmission medium has been developed in this section. The model was derived from a series of differential equations which represent the fluid properties in different sections of the system along

with displacements of the moving pieces. The active material stack and pump piston were modeled as a single degree of freedom systems. The driving signal for the entire system was provided by the magnetic field that actuated the magnetostrictive rod. Rate equations for fluid densities in different high pressure sections of the system were derived by taking into account the respective changes in fluid volumes and mass flow rates; the corresponding fluid pressures were calculated using the bulk modulus of the fluid. The output cylinder shaft was also modeled as a single degree of freedom system with stiction. A lumped model analogy was used to model the unsteady compressible fluid flow through the manifold passages and the driven side of the output piston. Simulation results of the model were compared with the experimental data to validate the model.

Chapter 4

Experimental Validation of a Hybrid Electrostrictive Hydraulic Actuator Analysis

4.1 Overview

A second-generation prototype of the compact hybrid actuator was built using the electrostrictive material PMN-PT. There are several advantages of using PMN-PT [chemical composition $(1-\mathrm{x})\mathrm{Pb}(\mathrm{Mg}_{1/3}\mathrm{Nb}_{2/3})\mathrm{O}_3 - \mathrm{xPbTiO}_3$] as the active material in a hybrid actuator: it has a uniquely low hysteretic response (implying reduced self heating) compared to piezoelectric ceramics thereby permitting high frequency operation while producing significantly higher strains (2 to 3 times higher) than piezoelectric ceramics [76, 152, 156]. The recent advancement in PMN-PT manufacturing and the corresponding reduction in price have made PMN-PT attractive for use in hybrid hydraulic pumps as a substitute for piezoelectric ceramics.

A hybrid actuator using the single crystal electrostrictive material PMN-32%PT as the driving element and hydraulic oil as the working fluid was recently developed in our laboratory. Two PMN stacks, each 12 mm in diameter and 30 mm long, were aligned end-to-end to obtain one single driving element and unipolar sinusoidal voltage with frequencies ranging from 100 Hz to 1 kHz was used to actuate the stacks. To characterize the behavior of the pre-stressed active material at high actuation

frequencies, we also carried out dynamic tests with the PMN stacks in the pump body and analyzed the frequency response; the fluidic subsystem was not connected during these tests. The axial velocity of the pump piston was also measured under similar conditions in order to detect any non-uniformity in the pumping motion. Tests at no-load and with external load were carried out to evaluate the overall actuator performance for unidirectional motion of the output piston. While the no-load tests yield the maximum possible volumetric flow rates under any combination of test conditions, the load tests allowed us to calculate the blocked force of the actuator. The peak velocity of the output shaft was measured to be 330 mm/s (13 in/s), corresponding to a volume flow rate of 42.5 cc/s, and was obtained at pumping frequencies between 600 Hz and 800 Hz, while the blocked load was around 63 N (14.1 lbf).

The primary objective of this chapter is to present an experimentally validated analysis of the hybrid actuator. The mechanical design of the new actuator and the measured performance are presented. These results are compared with simulation data, under no-load and externally loaded conditions, to validate the non-linear time-domain model developed earlier.

4.1.1 Active stack

The active material, PMN-32% PT, was manufactured by TRS Ceramics, Inc. Two cylindrical stacks were obtained, each being 12 mm in diameter and 30 mm long; each stack was composed of 100 layers of the electrostrictive material, each 0.3 mm

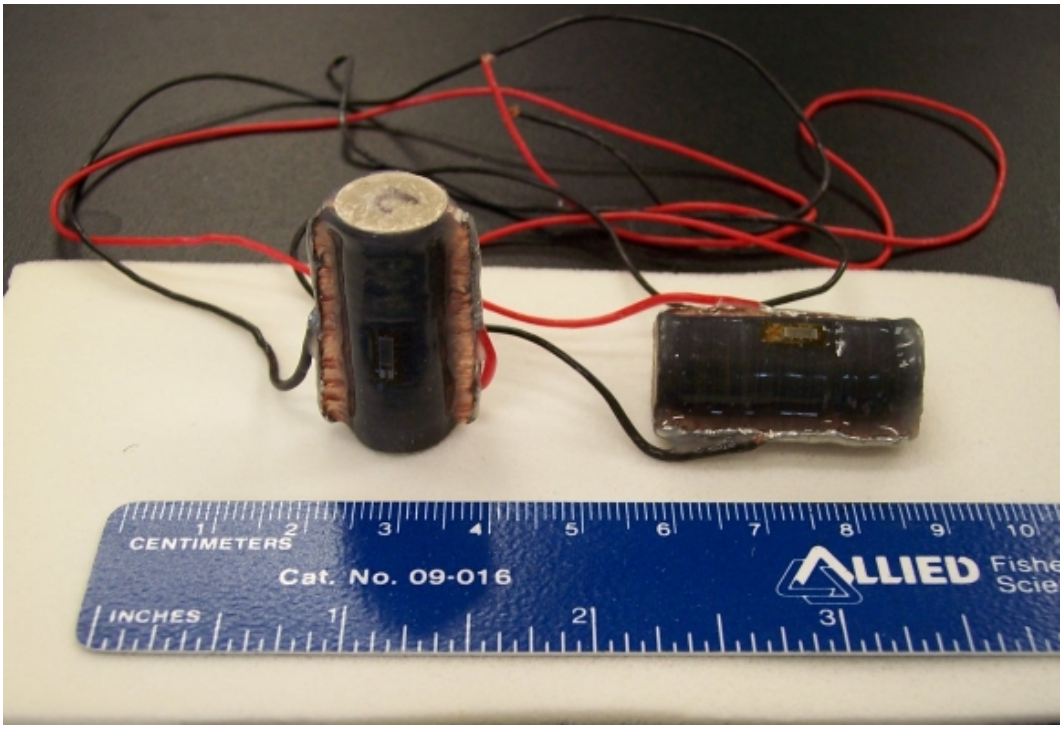

Figure 4.1: PMN stacks

thick. Figure 4.1 shows the two stacks with strain gages attached to them; a thin layer of insulating coating was also present over the entire circular surface to reduce arcing.

According to manufacturer supplied test data, the PMN stacks were capable of producing strains up to 2000 ppm when excited with a peak voltage of 500 V. This data was verified from static excitation tests conducted in our laboratory; the stack extensions and corresponding strains are shown in Figure 4.2.

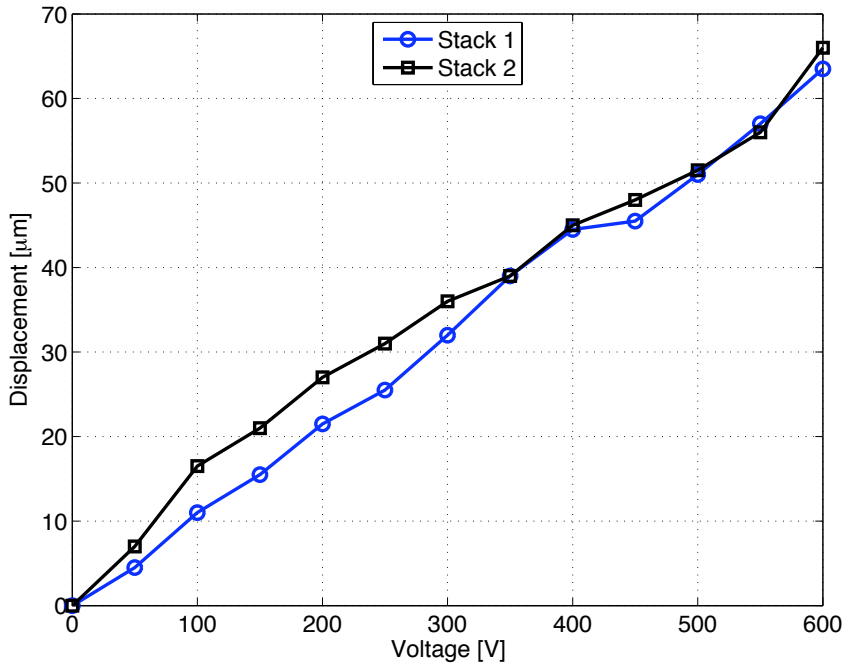

(a) Measured stack displacement

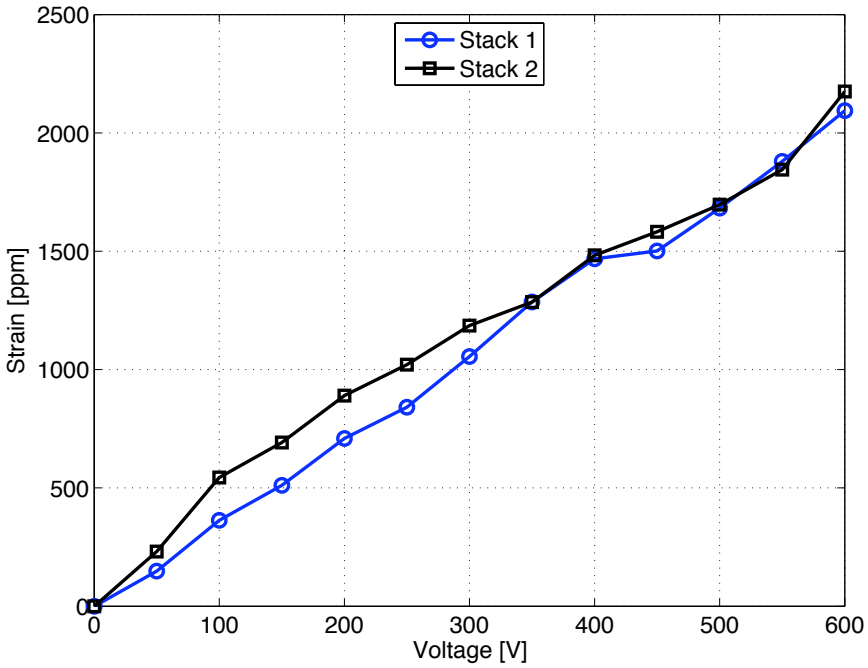

(b) Stack strain

Figure 4.2: PMN stack test results under static excitation

4.2 Actuator design steps

4.2.1 Ideal assumptions

The design of the actuator based on blocked force, F_b and no-load velocity, v_L specifications started with the calculation of the dimensions of the active material and geometry of the pumping device. The fluid in the manifold tubing was assumed to be incompressible while the fluid in the pumping chamber was compressible, the bulk modulus being denoted by β.

The maximum output volume flow rate Q is obtained from no-load velocity v_L as follows:

$$Q = A_o v_L \tag{4.1}$$

where $A_o = \pi(d_o^2 - d_i^2)/4$ is the cross-sectional area of the output cylinder with bore d_o and shaft diameter d_i. If f is the frequency of actuating signal to the actuator stack/rod with length L_a and strain ϵ, then this flow rate is given by:

$$Q = f \times \epsilon \times L_a \times A_{ch} \tag{4.2}$$

where $A_{ch} = \pi d_{ch}^2/4$ is the area of the pumping piston of diameter D_{ch}. For computing maximum no-load velocity, it is assumed that the entire induced free strain of the active material is available for moving the fluid. Equating 4.1 and 4.2, we get

$$x_{free} = \epsilon \times L_a = \left(\frac{A_o}{A_{ch}}\right)\left(\frac{v_L}{f}\right) \implies L_a = \frac{x_{free}}{\epsilon} \tag{4.3}$$

Figure 4.3 combines the above analysis assuming incompressible flow for three different lengths (1 inch, 2 inch and 4 inch) of PMN stacks actuated at different

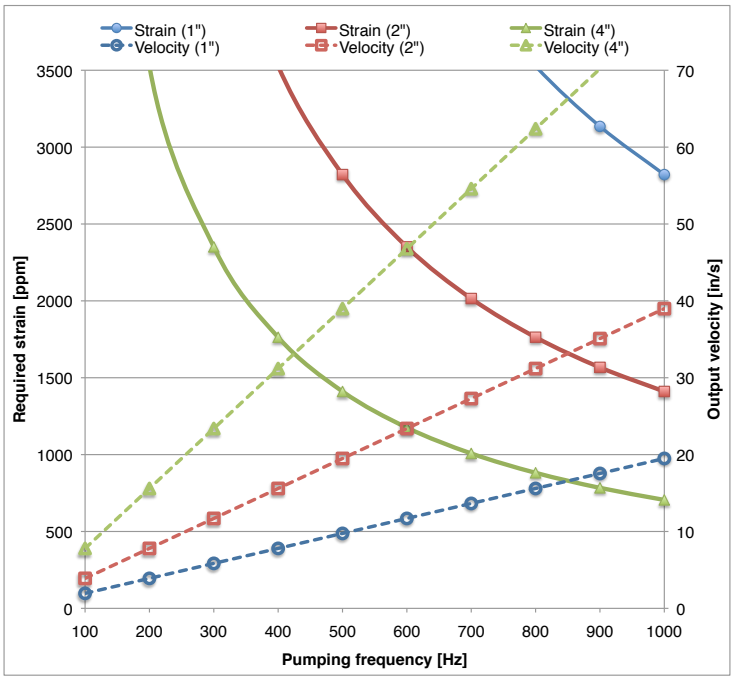

(a) Pumping chamber diameter = 1.5 in

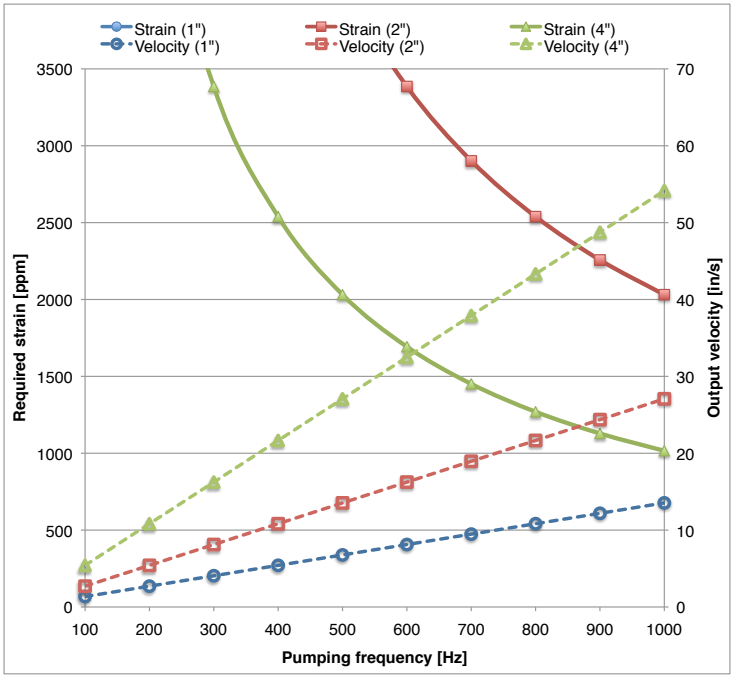

(b) Pumping chamber diameter = 1.25 in

Figure 4.3: Required free strain and calculated no-load velocities for different actuator lengths, ideal assumptions

pumping frequencies from 100 Hz to 1 kHz; the left hand axis (and the corresponding solid lines) represent the strain required to achieve specified no-load velocity of 25 inch/s (635 mm/s), while the right hand axis (dashed lines) represent the output velocities if free strain of 2200 ppm, as seen in the static induced strain tests (Figure 4.2), could be attained. The output cylinder has bore diameter (D_o) of 9/16 inch and a 1/4 inch diameter shaft (D_i). Two different pumping chamber sizes were considered, the first one with 1.5 inch (38.1 mm) diameter and the second with 1.25 inch (31.8 mm) diameter.

The analysis shows that the induced strain required is inversely proportional to the pumping frequency, thereby justifying the design of the actuator to operate at very high frequencies. The results in Figure 4.3(a) also suggest that the active stack length required to achieve the desired output velocity would have to be between 2 inch and 4 inch, and we would also need pumping frequencies in excess of 400 Hz to achieve our goal with the available material. The analysis also shows that the output velocity increases linearly with pumping frequency, for fixed induced strain, for any particular actuator length. When a smaller size pumping piston is used, the pumping frequency has to be increased to higher levels ($>$ 600 Hz) in order to achieve the no-load velocity goal (Figure 4.3(b)). Hence, the choice of stack length determines the operating frequency of the actuator. Though these conclusions are good for preliminary design sizing, it should be noted that the higher pumping frequencies and flow rates also imply higher losses (inertial and viscous) which have not been included in this simple calculation.

The pressure P_b in the fluid pumping chamber is related to the blocked force F_b

of the actuator, assuming no static friction in the output cylinder and incompressible fluid under ideal conditions, by the following expression:

$$P_b = \frac{F_b}{A_o} \tag{4.4}$$

Applying Equation 3.9 to a changing control volume with fixed cross-sectional area A_{ch} and normal displacement x, we get:

$$dP = \frac{A_{ch}dx}{A_{ch}\left(L_{ch} - x\right)} = \frac{dx}{\left(L_{ch} - x\right)}$$

where L_{ch} is the initial length if the control volume. Using the following boundary conditions,

$$P = 0 \quad \text{at} \quad x = 0$$

$$P = P_b \quad \text{at} \quad x = x_p$$

and integrating, we get

$$P_b = \beta ln\left(1 - \frac{x_p}{L_{ch}}\right) \tag{4.5}$$

which can rewritten using a series expansion of the logarithmic term, assuming $x_p \ll L_{ch}$, as

$$P_b = 1 - \left[1 - \left(\frac{x_p}{L_{ch}}\right) + \frac{1}{2}\left(\frac{x_p}{L_{ch}}\right)^2 - \frac{1}{3}\left(\frac{x_p}{L_{ch}}\right)^3 \ldots\right]$$

Neglecting the higher order terms, we get a linear relation between the pressure generated and the piston displacement:

$$P_b = \beta\frac{x_p}{L_{ch}} \tag{4.6}$$

where x_p is the induced displacement under blocked condition. Since the pressure calculated from Equation 4.4 is the same developed in the pumping chamber, hence,

combining it with Equation 4.6, we can write

$$x_p = \frac{F_b}{\beta A_o} L_{ch} = \frac{F_b}{K_{ch}} \lambda \tag{4.7}$$

where

$$K_{ch} = \frac{\beta A_{ch}}{L_{ch}} \quad \text{and} \quad \lambda = \frac{A_{ch}}{A_o}$$

are the stiffness of the fluid pumping chamber and the *input-output area ratio* (between pumping piston and output cylinder) respectively.

Based on the stiffnesses of the actuator stack/rod, K_a, and the pumping chamber, K_{ch}, the actual strain induced in the active material is obtained from static conditions [72, 185] as follows:

$$\begin{aligned} x_p &= \frac{K_a}{K_a + K_{ch}} x_{free} \\ \implies 1 + \frac{K_{ch}}{K_a} &= \frac{x_{free}}{x_p} \\ \implies K_a &= \frac{K_{ch}}{\frac{x_{free}}{x_p} - 1} \end{aligned} \tag{4.8}$$

From definition,

$$K_a = \frac{E_a A_a}{L_a}$$

for an actuator with cross-sectional area $A_a = \pi D_a^2/4$, where D_a is the diameter of the active rod/stack. Using this along with the value of L_a from Equation 4.3, we can find D_a from Equation 4.8.

This method was used to carry out a study of the variation of required stack diameter with change in pumping chamber diameter; this was important since the pumping piston was the interface between the solid actuation and the fluidic transmission modes and had to be carefully designed for best matching of mechanical

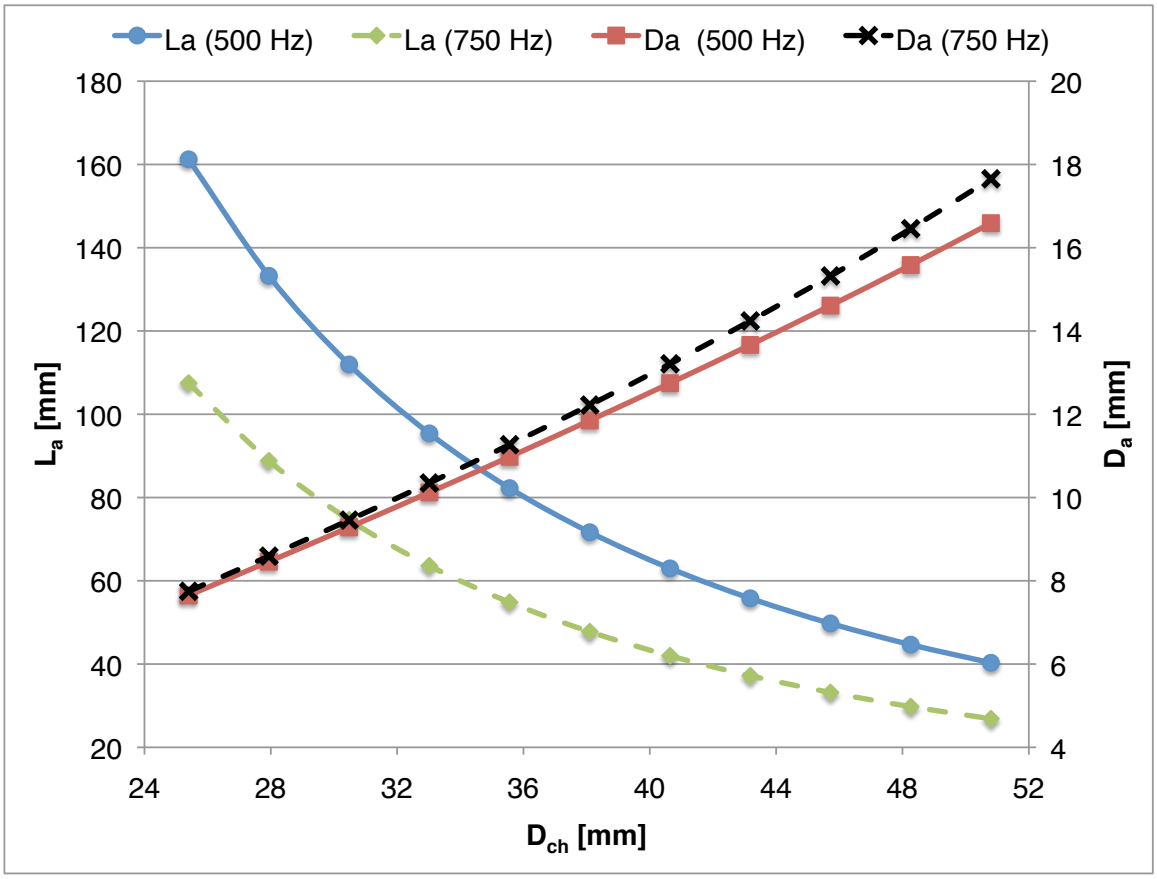

Figure 4.4: Required stack length and diameter for two pumping frequencies with specific no-load velocity and blocked force requirements, ideal assumptions

impedances. Using manufacturer specifications, the Young's modulus of the stacked PMN-32%PT actuator used for preliminary sizing was 20 GPa. The target no-load velocity and blocked force were 508 mm/s (20 in/s) and 267 N (60 lbf) respectively. Two different operating pumping frequencies, 500 Hz and 750 Hz, were studied and the results are shown in Figure 4.4. The results clearly show that while the required active stack length L_a decreases quadratically with rise in pumping piston diameter D_{ch}, the required stack diameter D_a increases almost linearly. This is because an

increase in chamber diameter causes a corresponding increase in the opposing force acting on the PMN-PT stack, leading to requirement of higher driving force from the stack, and vice versa. Hence, there must be a trade-off between achievable no-load velocity and blocked force of the actuator. We also notice a strong dependence of stack length on the pumping frequency; the effect of frequency on the required stack diameter is much less.

4.2.2 Dynamic considerations

To investigate the induced strain behavior of the PMN-32%PT material at high actuation frequencies, we carried out dynamic tests with two 7 mm diameter stacks inside the pre-stressed pump body. A disc spring with stiffness 1.82×10^7 N/m was used to prestress the stacks. Frequency sweeps from 100 Hz to 1 kHz were carried out at different applied voltages up to a maximum of 500 V and the corresponding induced strains were measured [265]. The frequency response is shown in Figure 4.5(a). We see that at any applied voltage, there is no appreciable change is response of the PMN material; this is very encouraging, since it implies that the material itself does not have any limitations on induced strain within our frequency range of interest. The induced strain vs. applied voltage curves at different actuation frequencies are shown in Figure 4.5(b); as the sizes of the loops are almost same, we can also conclude that the hysteresis in the PMN stacks, and hence, the amount of self heating, does not change much with frequency up to 1 kHz. This uniform hysteresis behavior makes the electrostrictive material much more attractive for high frequency

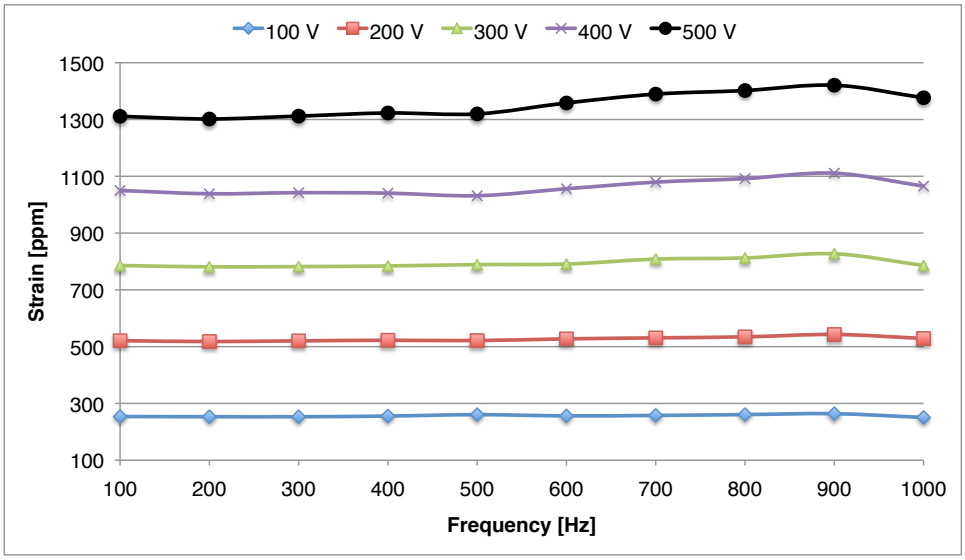

(a) Variation of induced strain with frequency at different levels of applied voltage

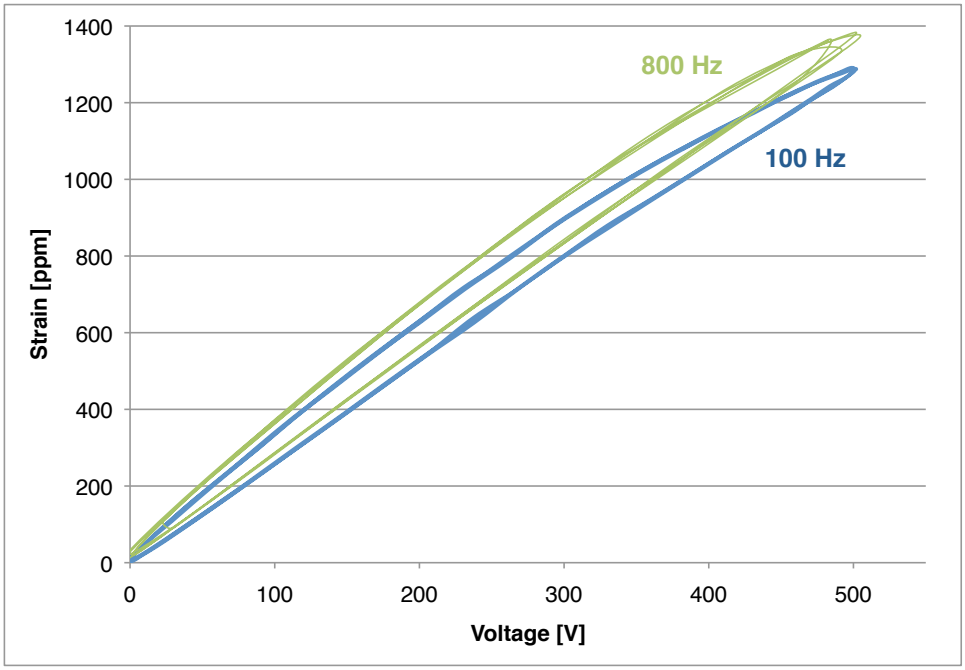

(b) Hysteresis in PMN under high frequency actuation

Figure 4.5: Results of dynamic tests with 7mm diameter PMN stacks

actuation than piezoceramics, which have been known to suffer from self-heating effects at high frequencies [72, 266–268]. Since the induced strain and hysteresis are intrinsic properties of the material, we can extend the same conclusions to PMN stacks having different dimensions too.

4.2.3 Vibrometer tests

The natural frequency of the PMN stacks under axial vibration can be calculated from the geometry and mechanical properties of the material, as derived in Equation 2.3. Using the Young's modulus (12 GPa) and density (7900 kg/m^3) [157, 269, 270], the first natural frequency for axial vibration was calculated to be 2.92 kHz.

Tests were carried out to measure the dynamic response of the 12 mm diameter PMN stack actuator when operated in isolation i.e. not connected to the fluidic system. The stack was prestressed within the pump body and the pumping piston was screwed on to the pre-stress connector piece; a disc spring with stiffness 1.64×10^6 N/m (McMaster part number 9713K68) was used for these dynamic characterization tests. The maximum peak voltage applied was 100 V, at frequencies 200 Hz, 500 Hz and 800 Hz. The strain in the stack was measured. In addition, a laser scanning vibrometer (PSV300 from Polytec Instruments) was used to measure the velocity at a point (selected as close to the center as possible) of the pumping piston. The velocity data was then integrated to obtain the displacement of the pumping piston; this was converted to an equivalent strain by dividing the pump piston dispacement by the overall length of the PMN stacks. The results are plotted in Figure 4.6. The black

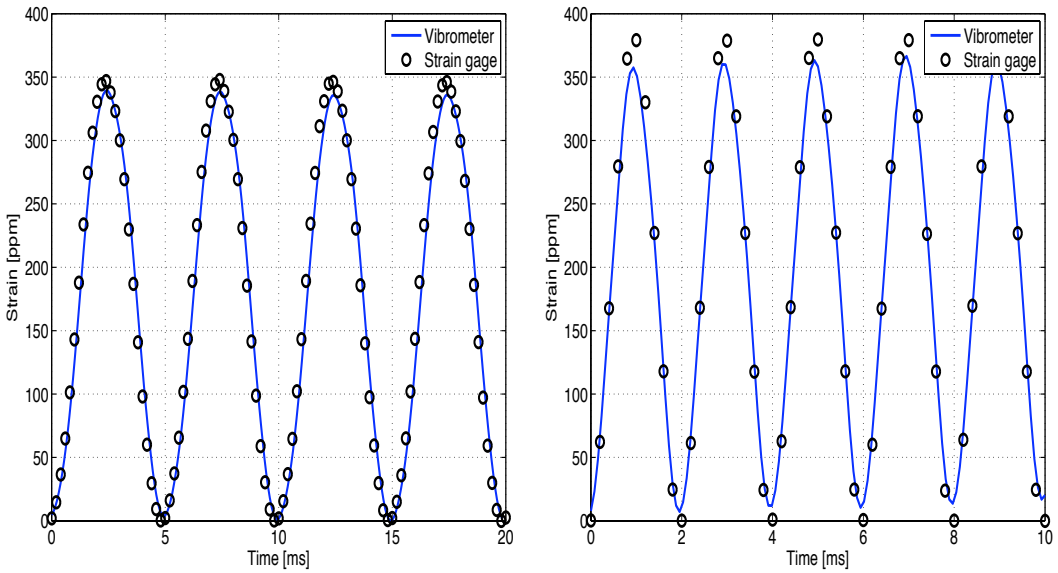

(a) 200 Hz

(b) 500 Hz

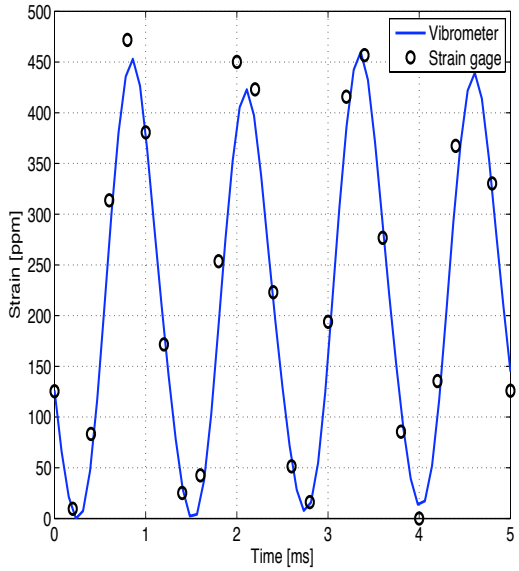

(c) 800 Hz

Figure 4.6: Comparison of stack strain and pumping piston displacement at different actuating frequencies

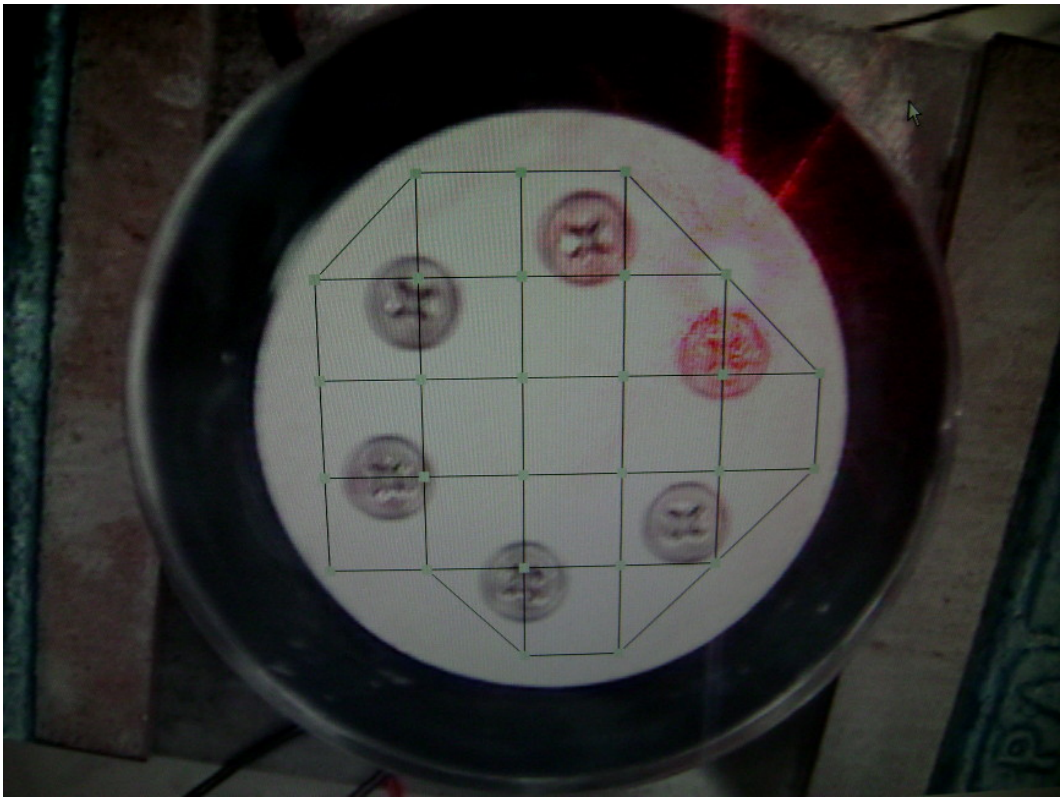

Figure 4.7: Scanning grid used for vibrometer measurements

circles show the strain gage data, while the solid blue lines represent equivalent strain of the piston. At 200 Hz pumping frequency, both measurements coincide almost completely with each other. However, a small difference in the two values is noted at the higher frequencies, with the actual material strain being higher in all cases. An increase in actual applied voltage, at a constant control voltage input to amplifier, was noticed; this is similar to the earlier dynamic test results shown in Figure 4.5(a).

The vibrometer tests clearly show that some of the induced strain in the stacks is lost due to compliance of internal parts within the pump body, as was explained earlier. However, by proper sizing of the components, we were able to limit the loss to less than 10% of the induced strain in the stacks.

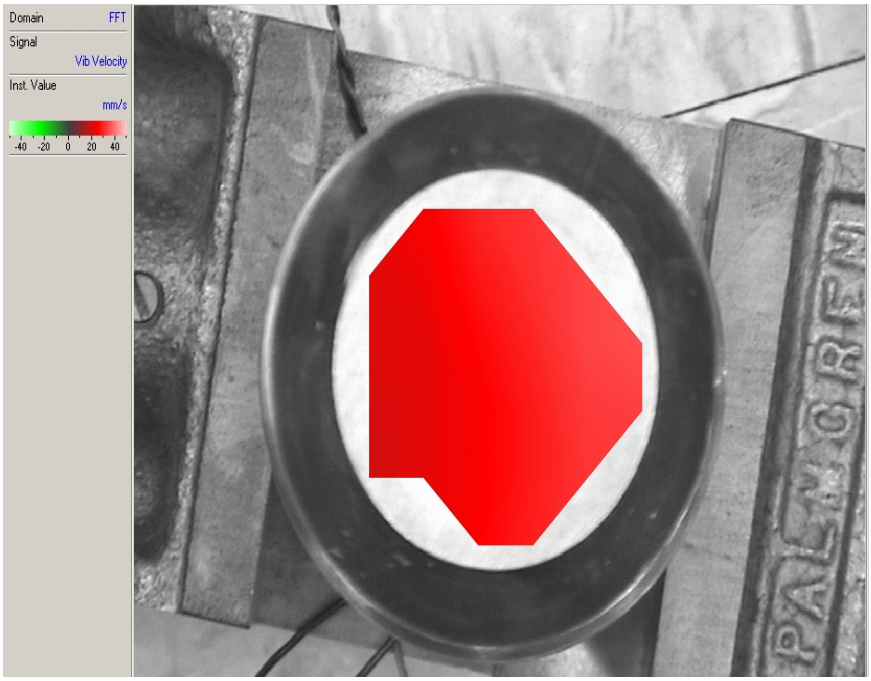

(a) Measured velocity distribution at the top surface of the pump piston at 500 Hz actuation frequency

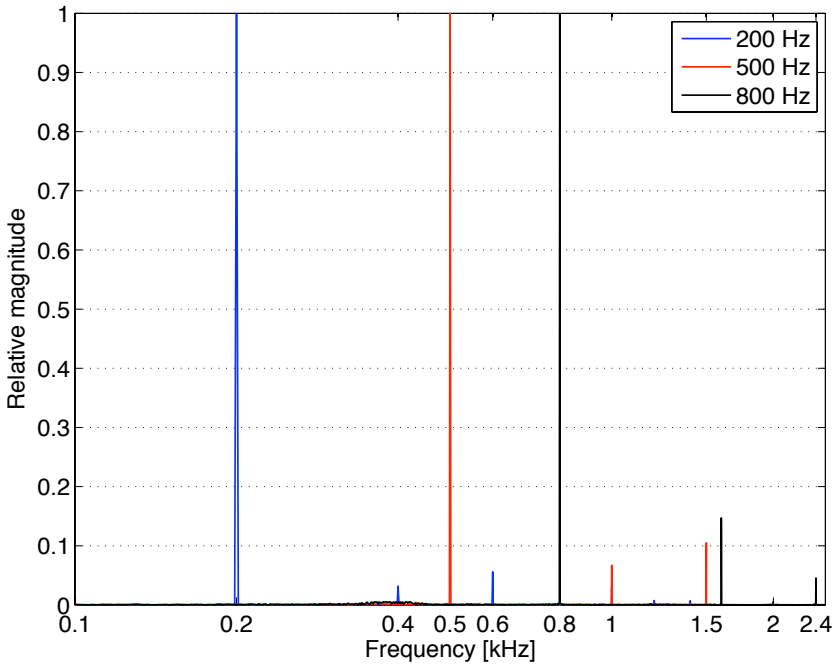

(b) FFT analysis of axial velocities of pump piston at three different actuation frequencies

Figure 4.8: Vibrometer test results

The vibrometer was also used in scanning mode to investigate the overall motion of the pumping piston. In this mode, the laser head was made to measure the velocity of points distributed over the entire piston surface while the PMN stacks were actuated at a fixed frequency (Figure 4.7). The applied voltage for these tests was 100 V; a lower voltage was used to reduce heating in the stacks, which might occur during the long time taken by the vibrometer to complete a scan. The actuation frequencies were 200 Hz, 500 Hz and 800 Hz. The results show that the highest amplitude of vibration corresponded to the frequency of actuation of the stacks. However, some motion could be attributed to higher frequencies which were integral multiples of the primary excitation frequency e.g. for actuation at 200 Hz, an FFT of the resulting displacement showed presence of 400 Hz and 600 Hz components too, which were, however, not more than 10% of the amplitude at 200 Hz (Figure 4.8(b)).

4.2.4 Final sizing

Two different configurations were chosen on the basis of the idealized static calculations, followed by dynamic analyses. These have been summarized in Table 4.1. The output cylinder length was chosen to be 51 mm (2 inch), as per minimum stroke requirements for the actuator. However, due to (i) frequent mechanical and electrical insulation failure of the PMN material and (ii) lower than expected elastic modulus of the PMN-PT material, we restricted our tests to the first configuration ($D_{ch} = 1.25$ inch) and the peak voltage to 400 V.

Table 4.1: PMN ACTUATOR SIZING

Parameter	Configuration 1	Configuration 2
Pumping chamber diameter, D_{ch}	31.8 mm (1.25 inch)	38.1 mm (1.5 inch)
Pumping chamber height, L_{ch}	1.27 mm (50 mils)	2.54 mm (100 mils)
Output cylinder bore, D_o	14.3 mm (9/16 inch)	14.3 mm (9/16 inch)
Output cylinder length, L_o	50.8 mm (2 inch)	50.8 mm (2 inch)
Manifold tubing diameter, D_t	5.1 mm (0.2 inch)	5.1 mm (0.2 inch)
Bulk modulus, β	0.69 GPa (100 ksi)	0.34 GPa (50 ksi)

4.3 Actuator description and test setup

4.3.1 Mechanical layout

The actuator assembly involves two distinct sections: the pump body containing the active material and the manifold assembly that includes the output hydraulic cylinder.

4.3.1.1 Pump

In the pump body, the active stack (PMN) was bonded to a 15.2 mm (0.6 inch) thick base plate and the electrical connections were properly made. The PMN stack has strain gages mounted on it. Note that due to the high voltages involved in actuation of electrostrictive PMN, we placed non-conducting caps made of Delrin at both ends (Figure 4.9). Though this led to additional compliance in the system since

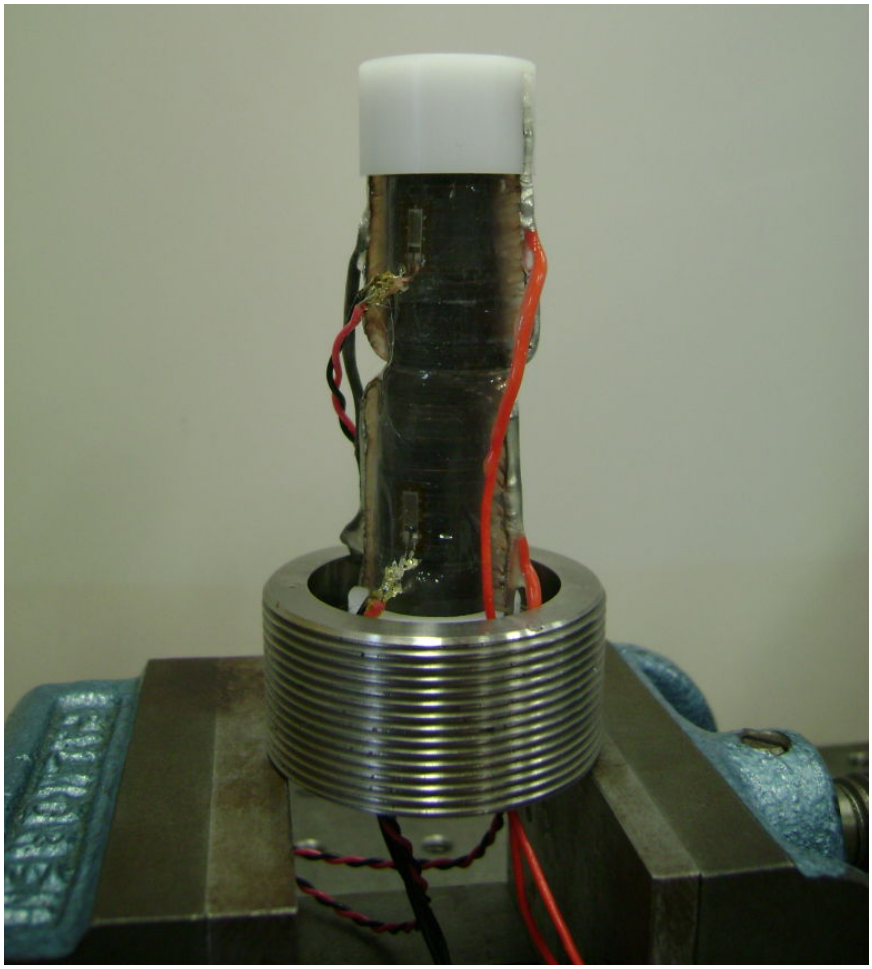

Figure 4.9: PMN stack mounted on base, with Delrin caps at both ends

Delrin had the lowest elastic modulus of all the materials, it was required to eliminate the risks of electrical shorts with the pump body. The base was then securely screwed to one end of the pump body, while a preload connector piece and disc springs were attached to the other end; this configuration allowed us to apply a controlled amount of preload to the stack. A cutaway drawing of the pump body assembly is shown in Figure 4.10.

During the initial design of the pump, the lower stiffness of the insulating caps placed at both ends of the stack as well as deflections of the base mount were of

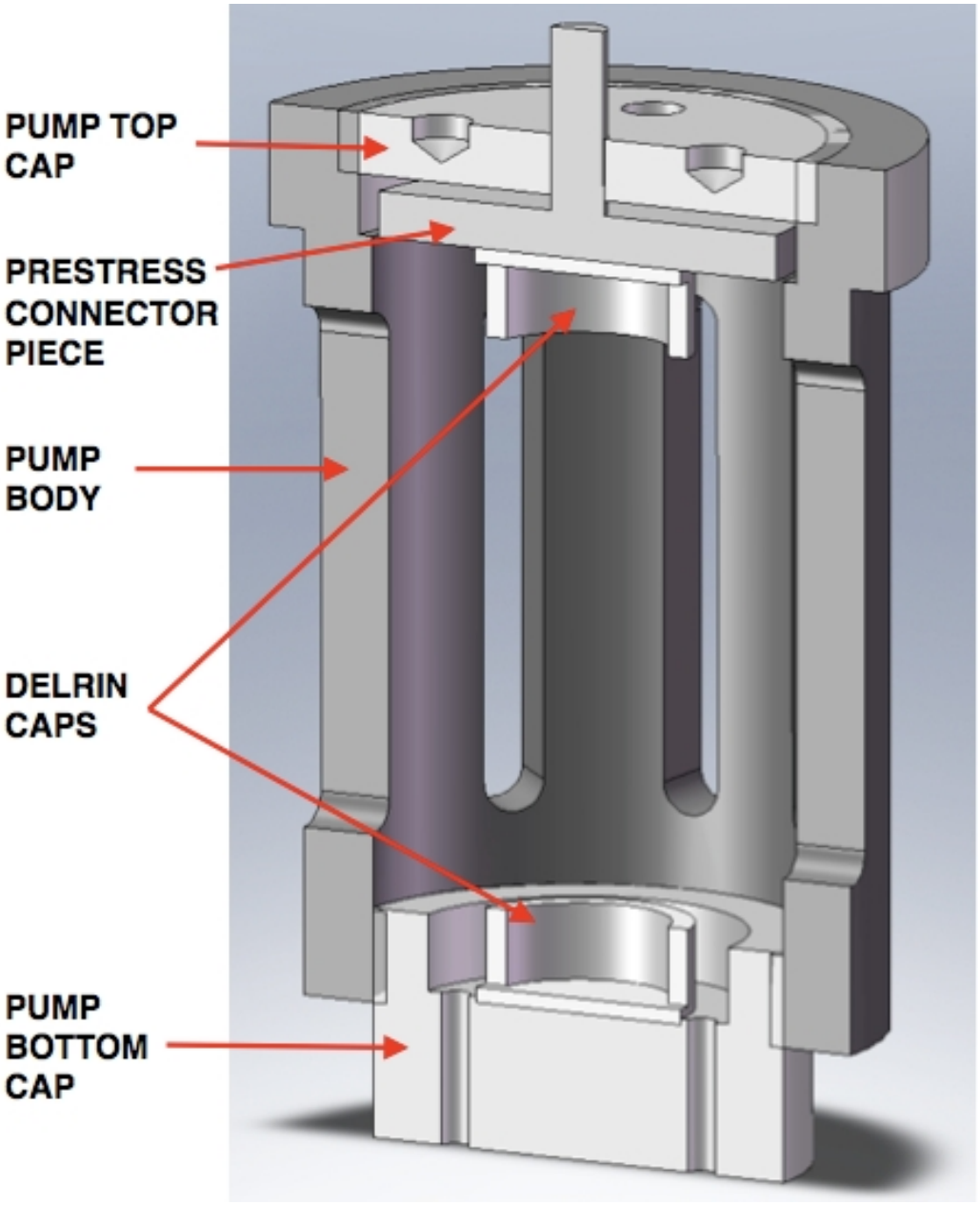

Figure 4.10: Section view of prestressed pump body for electrostrictive stack

concern because these mechanisms could result in reduction of final displacement of the pumping piston. The hybrid actuation system relies on very small displacements of the active driving element, hence any loss in the transfer of this motion to the hydraulic fluid would hamper performance. To reduce these effects, the Delrin caps were made as thin as possible to decrease their compliance without affecting their mechanical strength; the final thickness was 0.64 mm (0.025 in). A low thread pitch was chosen for the base mount so that a higher number of turns could engage with the pump body, thus preventing the base mount from deflecting when the PMN stacks were prestressed and actuated.

The pumping piston was the only moving part within the pumping section and had a two-fold job:

1. Separate and seal off the active material from the hydraulic fluid (using a metal diaphragm and o-rings).

2. Transfer the motion of the stack to the fluid in the pumping chamber (by the piston head).

The sizing of the pump piston head was based on the amount of flow rate required in the device and by matching the stiffness of the active material with the fluid in the pumping chamber.

The reed valves were made of 0.127 mm (5 mil) thick annealed spring steel sheets; this particular material was chosen because of its high fatigue resistance. Thicker reed valves (compared to the Terfenol-D pump) were chosen in order to raise the bandwidth of the vale system. Each reed was cut out using an EDM; this ensured

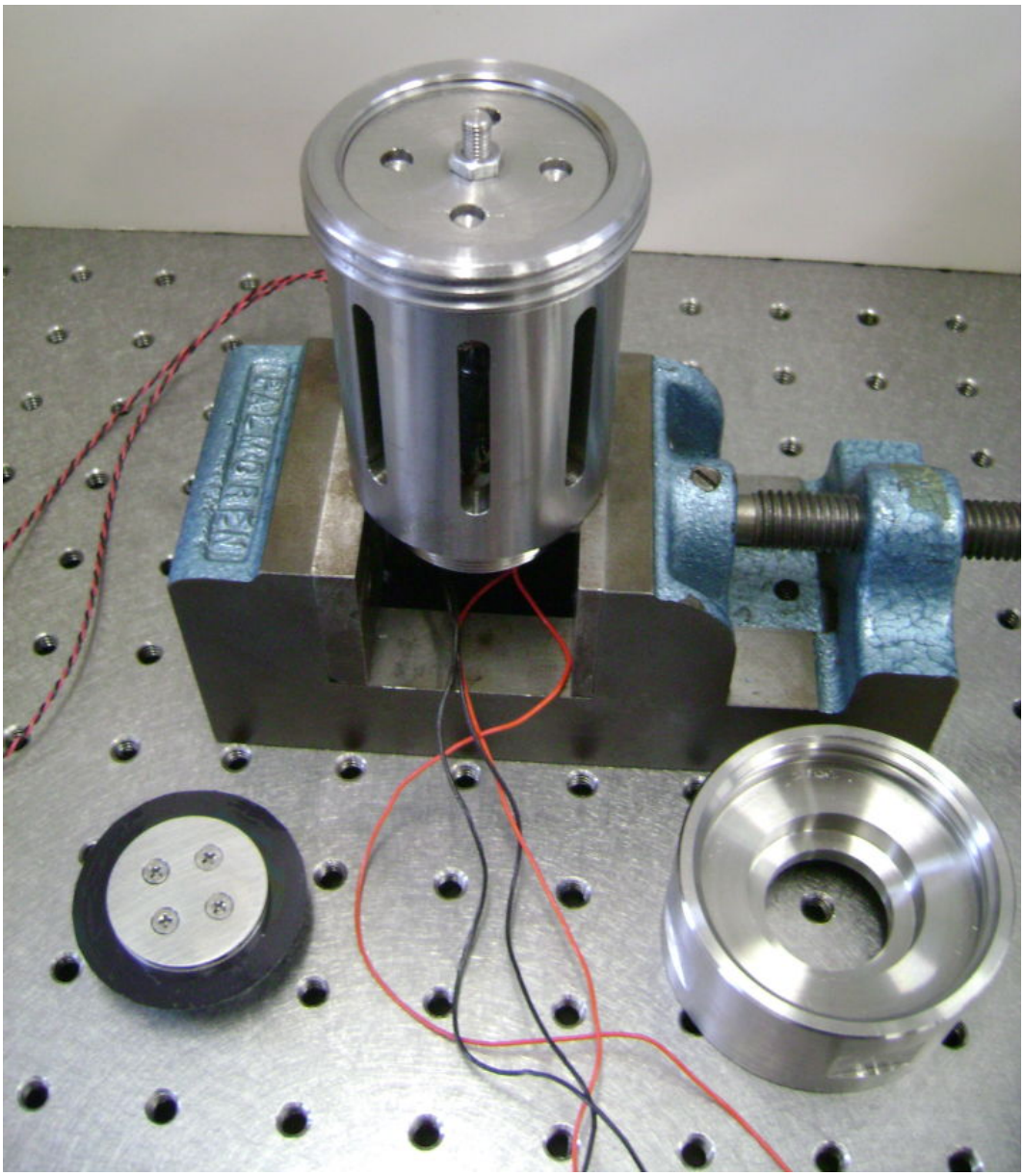

Figure 4.11: Parts of PMN pumping section

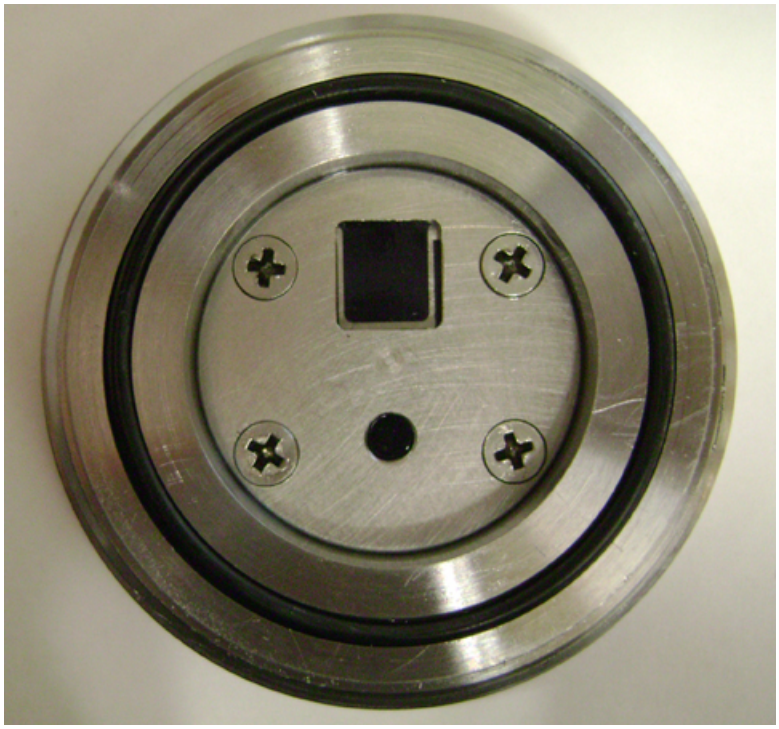

(a) New pump head assembly with discharge and intake reed ports

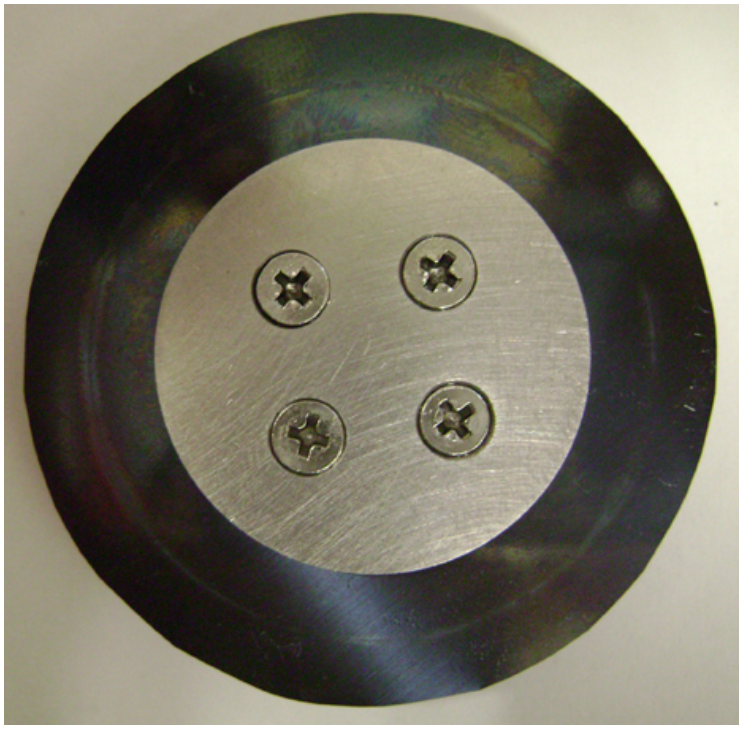

(b) New pumping piston assembly with metal diaphragm

Figure 4.12: Assembled parts of the new hybrid pump

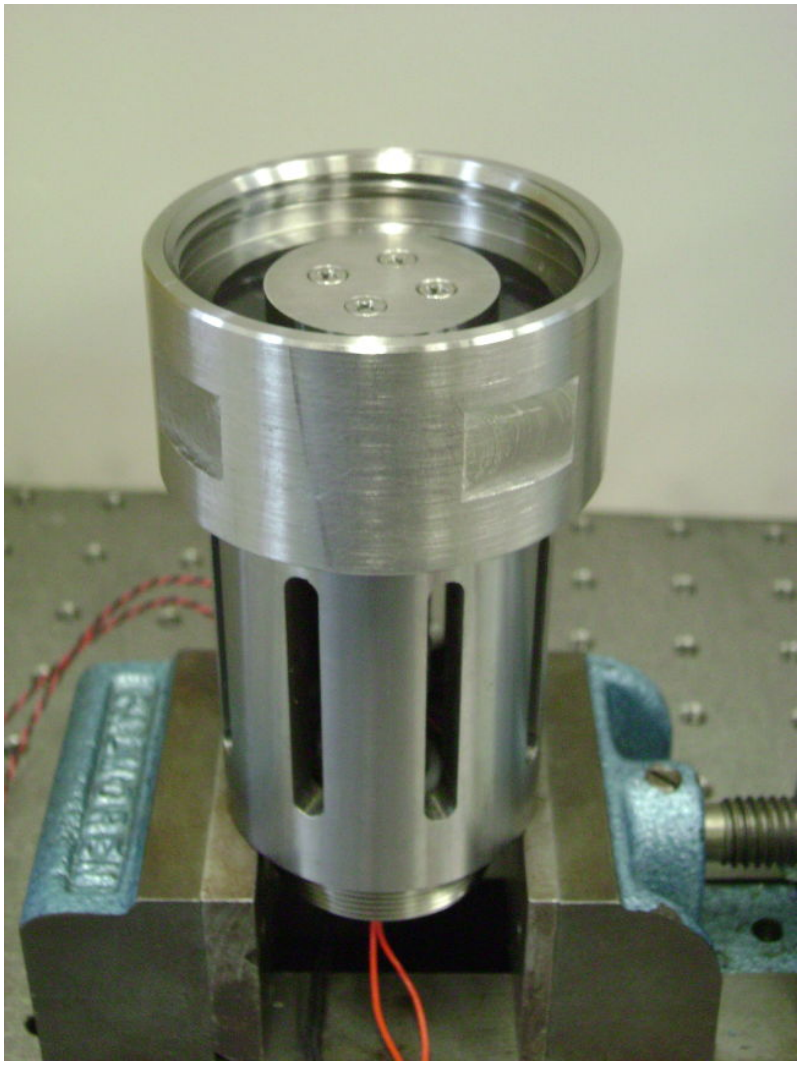

Figure 4.13: Assembled view of PMN pumping section

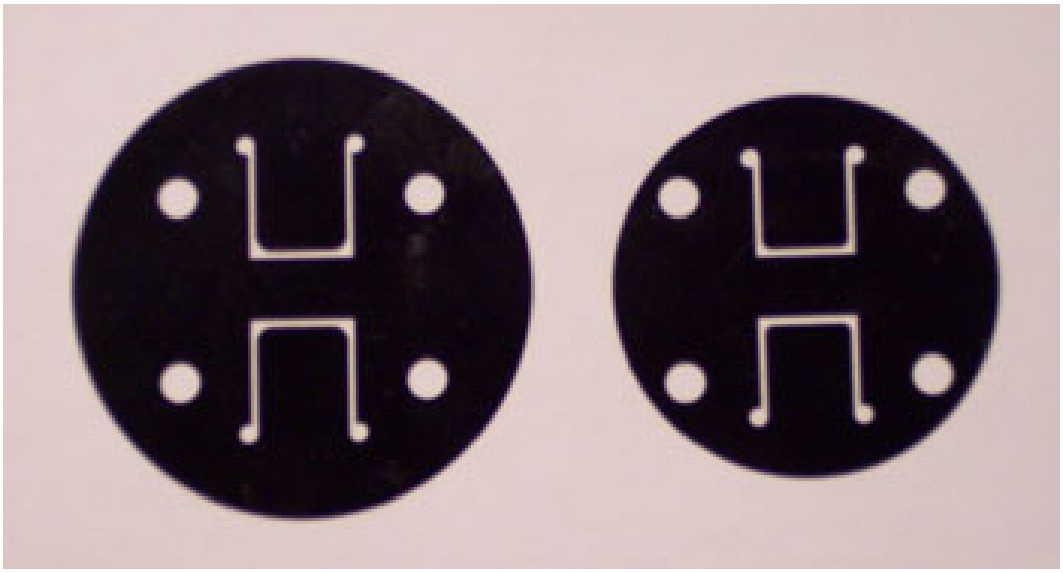

Figure 4.14: Reed valves with two different outer diameters: 38.1 mm (1.5 inch) and 31.8 mm (1.25 inch)

high precision (0.0001 inch) of the finished product, shown in Figure 4.14. The reed was then sandwiched between two steel plates and sealed using liquid sealant (Loctite 680); each reed plate had 1.52 mm (0.06 inch) deep slots cut inside to allow movement of the reeds in the direction of flow. This sealed assembly was then placed inside the pump head with the reed ports correctly aligned with the discharge and intake ports (Figure 4.15).

Since very high pressures are generated inside the pumping chamber during actuator and the flow rate per cycle is low, the seal around each reed port should be designed carefully to reduce loss of fluid pressure. During tests, it was noticed that improper sealing led to drastic drop in output performance. Though O-ring grooves were included in the reed valve assembly, we also used liquid sealant (Loctite 680) in order to get the best seal possible. The main issue with using such curable sealants

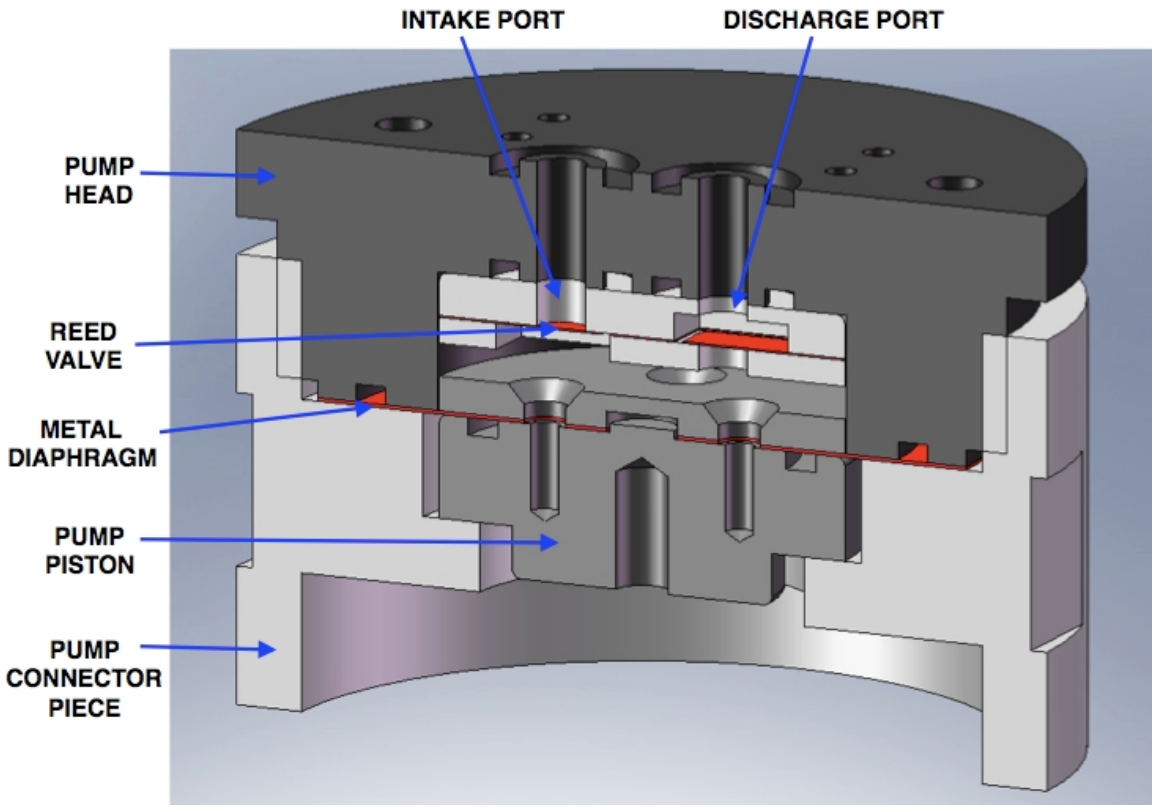

Figure 4.15: Section view of pump head assembly

is the time required for disassembly or re-asembly of the actuator; the curing time to achieve 100% strength using this sealant is almost 3 hours for steel surfaces [271].

4.3.1.2 Output manifold

The hybrid pump assembly described above was then mated to a manifold for delivery of the fluid pressure to an output cylinder. The new design included a pressure sensor in the manifold to measure the fluid pressure near the high pressure side of the output cylinder; this not only allowed us to monitor the pressure changes under operating conditions but also to calculate the instantaneous power output (as the product of pressure and volume flow rate) of the fluidic subsystem. An accumulator

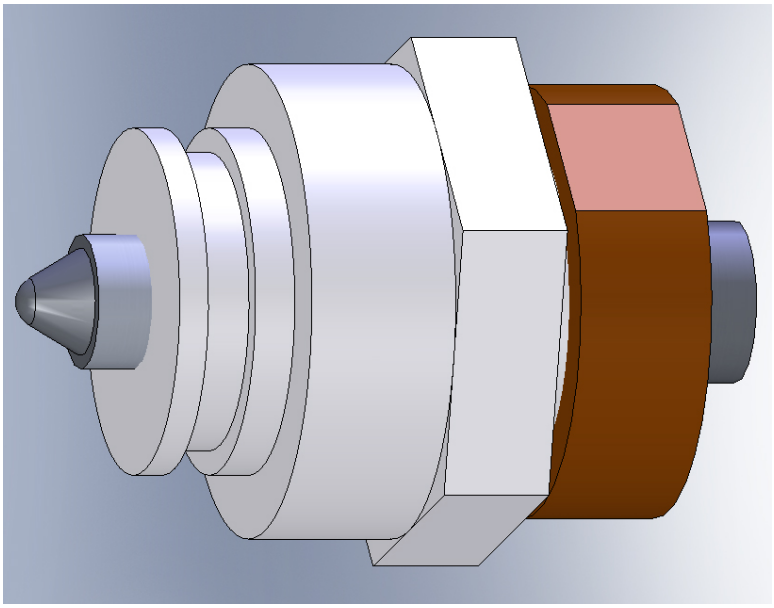

Figure 4.16: Needle valve used for output piston reset

was mounted on the low pressure return side of the manifold and acted as the fluid reservoir during the intake stroke. The accumulator port was also used to fill hydraulic oil into the fluidic subsystem and then apply the desired bias pressure. The hydraulic fluid used for the PMN pump tests was Mobil DTE-24. Since the current actuator test setup was built for unidirectional motion only, a return valve employing a threaded pin design (Figure 4.16) was present in the manifold to reset the output shaft to its original position at the end of one complete stroke.

Based on the observations from previous rotational tests [84], it was decided that the output cylinder should accommodate linear ball bearings within the housing of the cylinder to prevent any centrifugal loading from increasing friction at the contact points. The cylinder used in previous experiments has a brass bushing between the cylinder and the piston rod with 12.7 mm (0.5 inch) of surface contact. When the

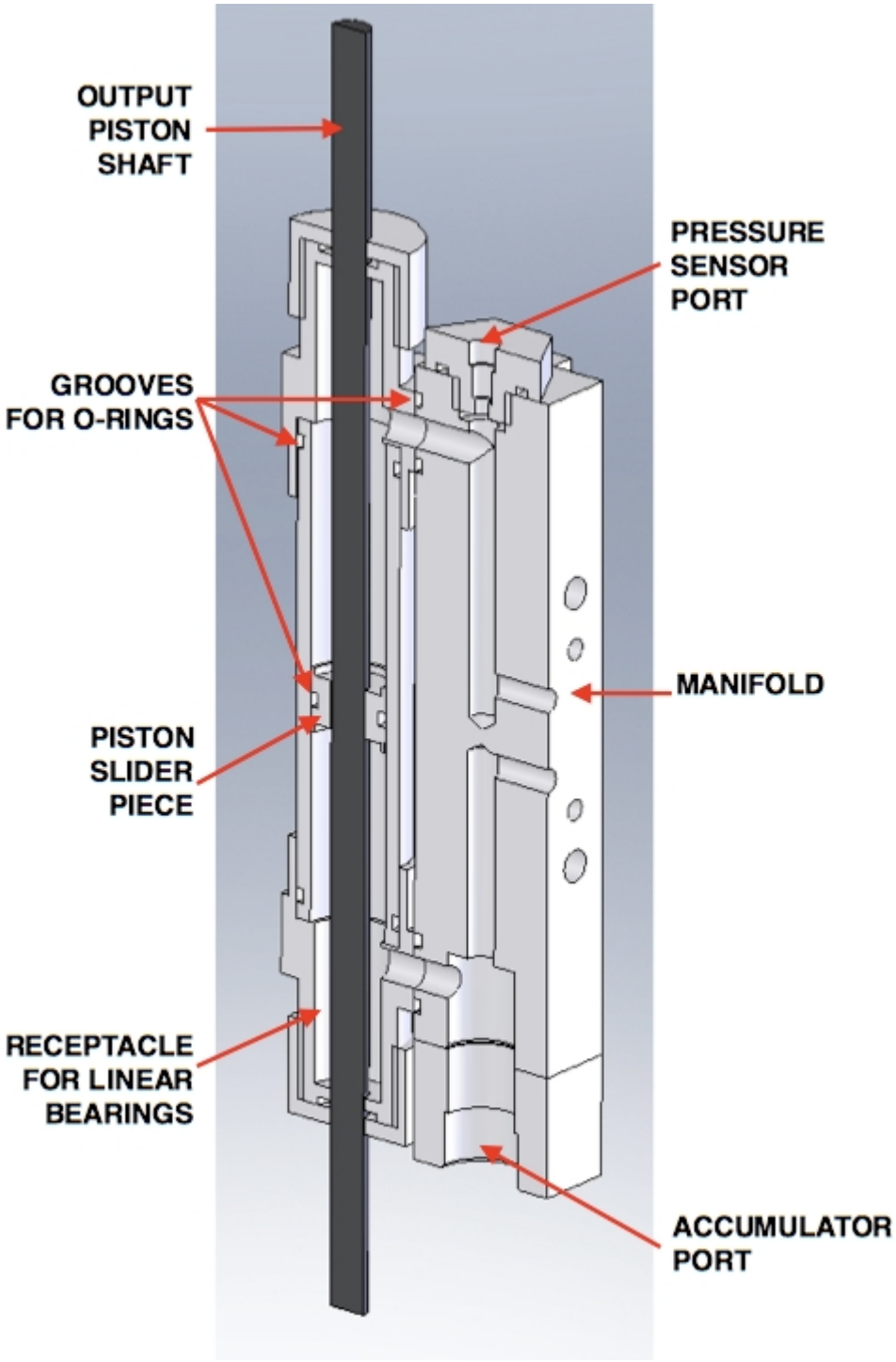

Figure 4.17: Section view of output manifold with hydraulic cylinder

actuator cylinder assembly was spun in the vacuum chamber, the piston rod pushed against the bushing, thus creating increased friction. The output hydraulic cylinder was redesigned and manufactured in-house instead of the one used in the previous tests with the Terfenol-D actuator. In the new design, shown in Figure 4.17, the brass bushing was replaced by a linear ball bearing. Linear ball bearings have a low coefficient of friction and can be used in high-speed applications; they usually require lubrication and perform best in contamination-free environments. Since our application involved hydraulic oil, the lubrication of the bearing was already taken into account. O-rings present on the piston assembly and all attachment points prevented any oil leakage and provided the ability to withstand very high fluid pressure levels.

The final hybrid actuator assembly is shown in Figure 4.18.

4.3.2 Electrical power input

The primary control signal to the PMN stacks was sinusoidal and produced using a function generator, Model 33220A 20 MHz Function / Arbitrary Waveform Generator from Agilent Technologies. This low voltage control input was applied to a voltage amplifier, LVC 3620, which produced a proportionally amplified output voltage. Since the maximum output voltage ratings of this amplifier were limited to 300 V (peak-to-peak), we used a step-up transformer to reach the desired voltage levels (up to 500V). The transformer was also useful since it allowed us to add a DC offset voltage, produced using the dc voltage supply module Genesys 1500W from Lambda Corporation, to the sinusoidally varying voltage. The resulting unipolar

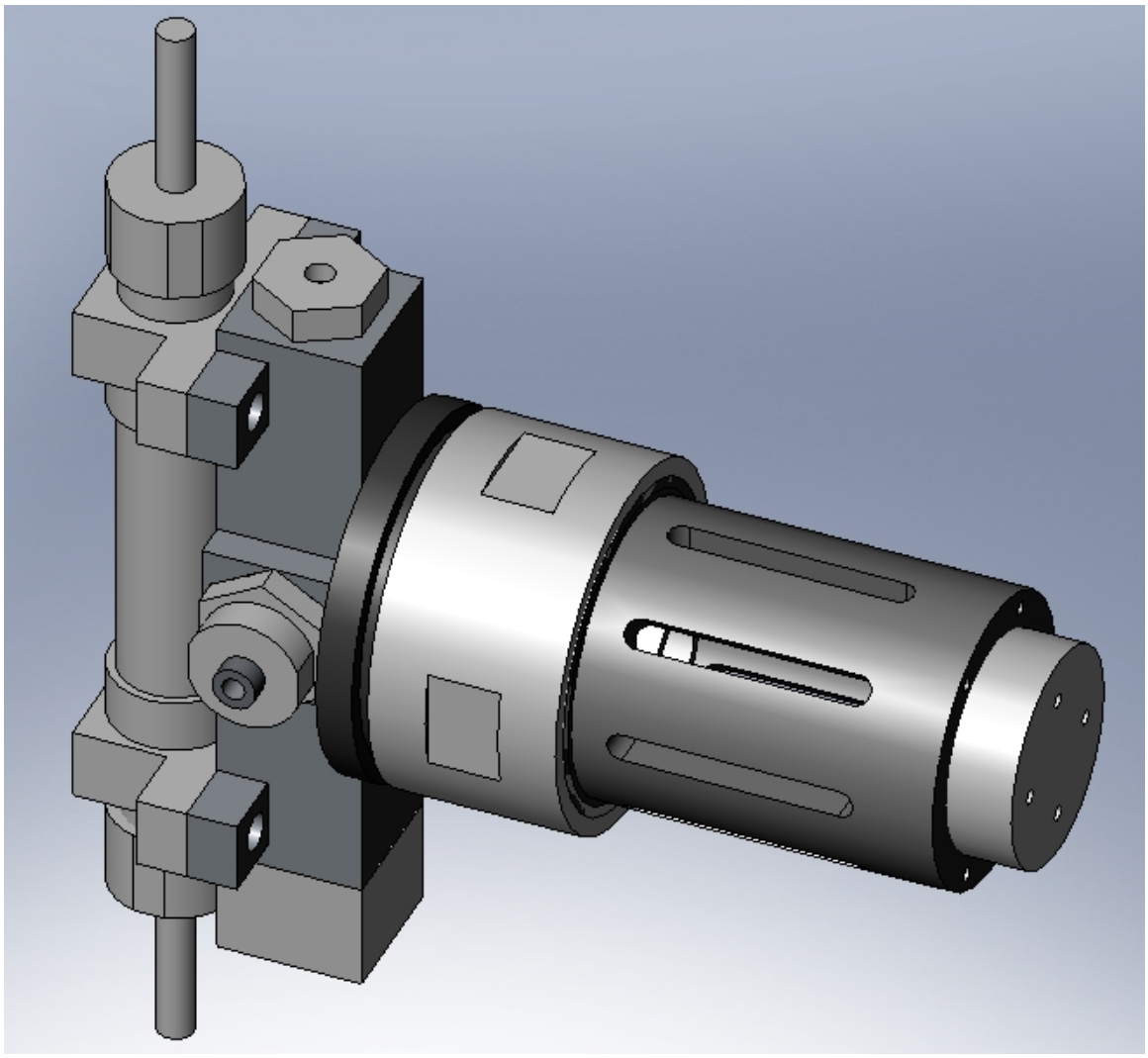

Figure 4.18: Assembled view of PMN-PT based hybrid hydraulic actuator

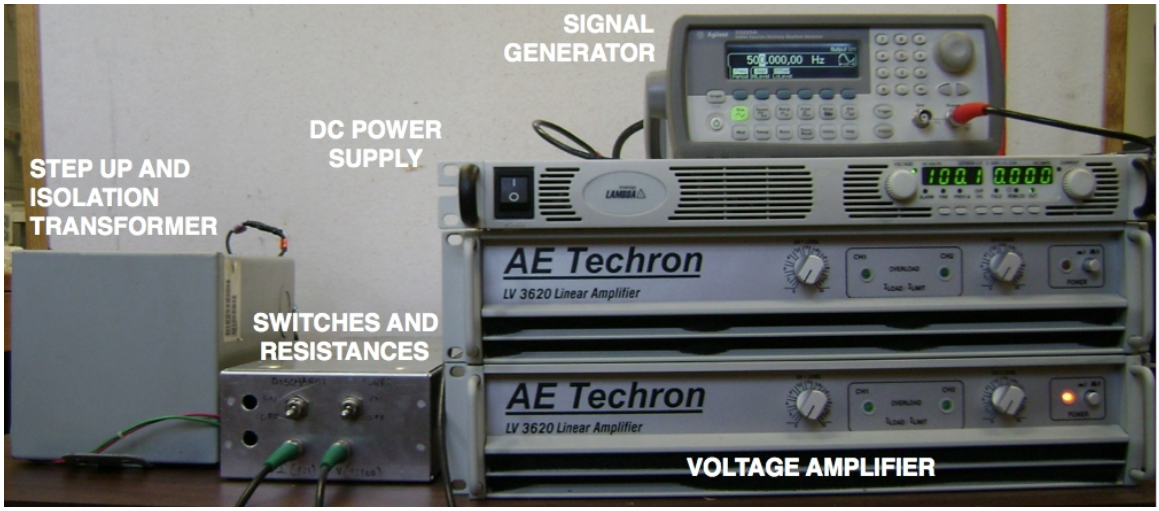

Figure 4.19: Electrical power input for PMN stacks

voltage signal was then applied to the PMN stacks.

4.3.3 Sensors and measuring instruments

The important parameters measured during the tests are as follows:

(i) Output shaft displacement: An LVDT was connected to the output shaft and produced a voltage proportional to the shaft displacement.

(ii) Input voltage: The actual voltage applied to the PMN stacks was also measured. However, to reduce the actual voltage to acceptable levels for the DAQ system, a voltage divider was included in the output. The divider was simply two high voltage resistors, 1 $k\Omega$ and 100 $k\Omega$, placed in series across the transformer output and resulted in a measurement voltage level that was approximately 1/100th of the actual voltage.

(iii) Input current: A high-precision high-wattage 1 Ω resistor was also included

in series in the output electrical circuit. The voltage across this resistor was measured and the current in the circuit is obtained.

(iv) Strain: Strain gages mounted on the stacks were used to measure the actual strain in the active material under operating conditions.

(v) Pressure: Fluid pressure in the high pressure driving side of the manifold was measured using a dynamic pressure sensor (model 105C12 from PCB Piezotronics).

4.4 Experiment results

The new actuator driven by the PMN stacks was tested under no-load conditions and also with external loads. The bias pressures were varied up to a maximum of 300 psi, since there was not much change beyond. The peak voltages applied to the stacks were 300V and 400V respectively; in order to prevent any damage to the electrical insulation, higher voltages were not used.

4.4.1 No-load tests

The first set of tests were carried out under no-load conditions. Here the output piston was allowed to move freely and the only opposing force was from friction between the output shaft and the wall of the hydraulic cylinder. From these tests, we calculated the maximum possible flow rate from the hybrid pumping device and the corresponding peak frequency. This provided a measure of the best performance of the actuation system. The peak control voltages applied to the stacks during each

frequency sweep were 300V and 400V; in order to prevent any damage to the electrical insulation, higher voltages were not used. Three different levels of bias pressures of 0.7 MPa (100 psi), 1.4 MPa (200 psi) and 2.1 MPa (300 psi) were applied to ascertain the effects of change in compressibility of the transmission fluid; since the compressibility of the bias pressure is related to the effective stiffness of the fluid, we expected to see a variation in the frequency response of the system.

The no-load tests were also aimed at achieving higher fluid flow rates from the hybrid pump compared to previous designs. Improving the stiffness match between the driving stack and the pumping chamber was a key design factor. Since the stiffness of the PMN stack was much lower than the Terfenol-D rods, the pumping chamber height was increased to 2.54 mm (100 mils) in order to make the fluid chamber more compliant and allow the PMN stack to expand more axially. Also, to improve high frequency operation of the device, thicker reed valves (5 mils) were used to increase the natural frequency of the valves. All seals were also replaced with new ones.

The test results show much improved performance over the magnetostrictive Terfenol-D based actuator, with the peak velocities being 223.5 mm/s (8.8 inch/s) and 330.2 mm/s (13.0 inch/s) at applied voltages of 300 V and 400 V and the peak performances being observed at 600 Hz and 800 Hz pumping frequencies respectively (Figure 4.20). We can clearly see the effect of increasing the bias pressure, thus lowering the fluid compliance, on the system performance. The output velocity variation with frequency was also seen to depend on the bias pressure applied; while the peak output occured between 500∼600 Hz at 0.7 MPa bias, it shifted to 600∼800 Hz when the bias pressure was raised to 2.1 MPa (300 psi). This behavior was noted at

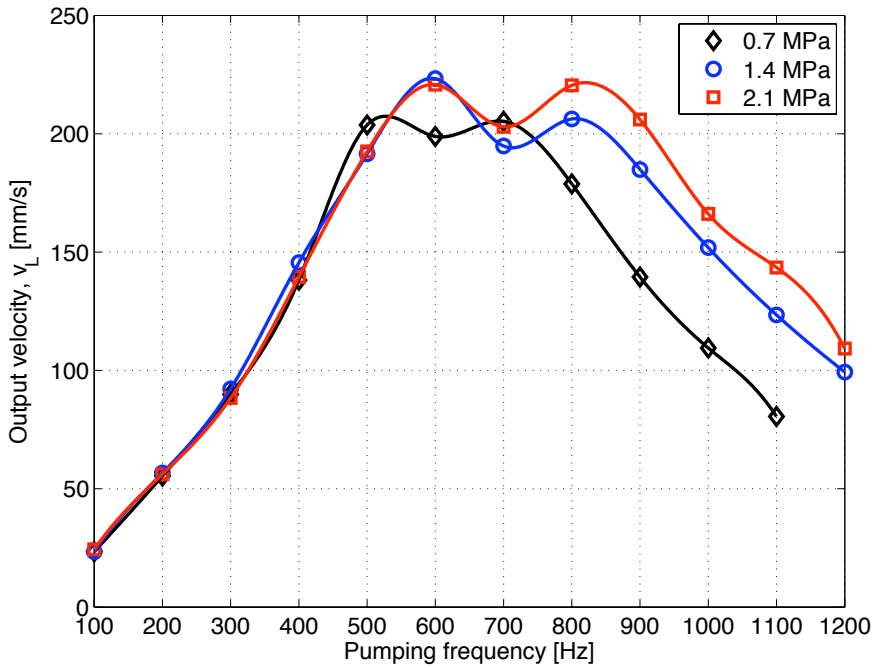

(a) 300 V

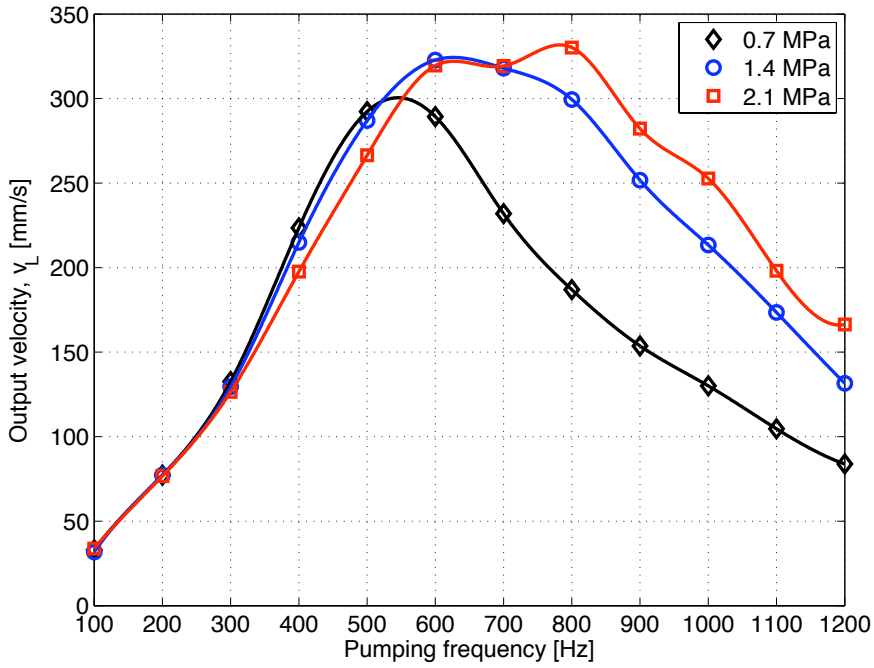

(b) 400 V

Figure 4.20: No-load velocity at different bias pressures and applied voltages

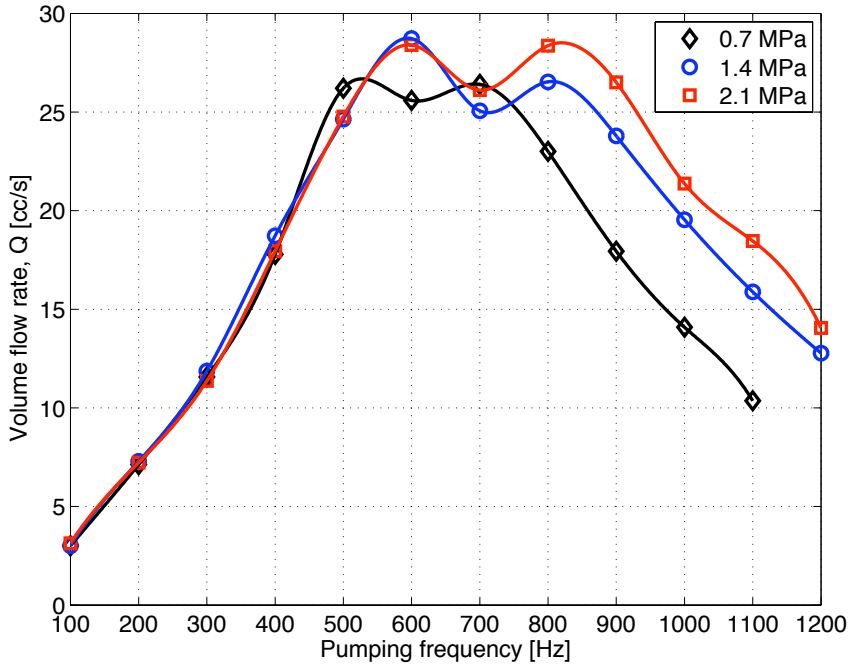

(a) 300 V

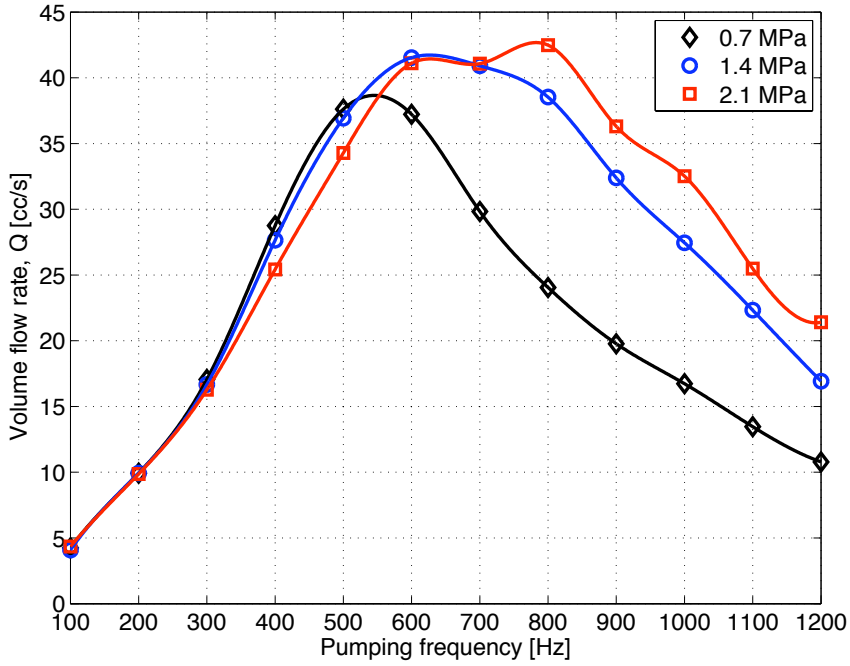

(b) 400 V

Figure 4.21: Volumetric flow rate at different bias pressures and applied voltages

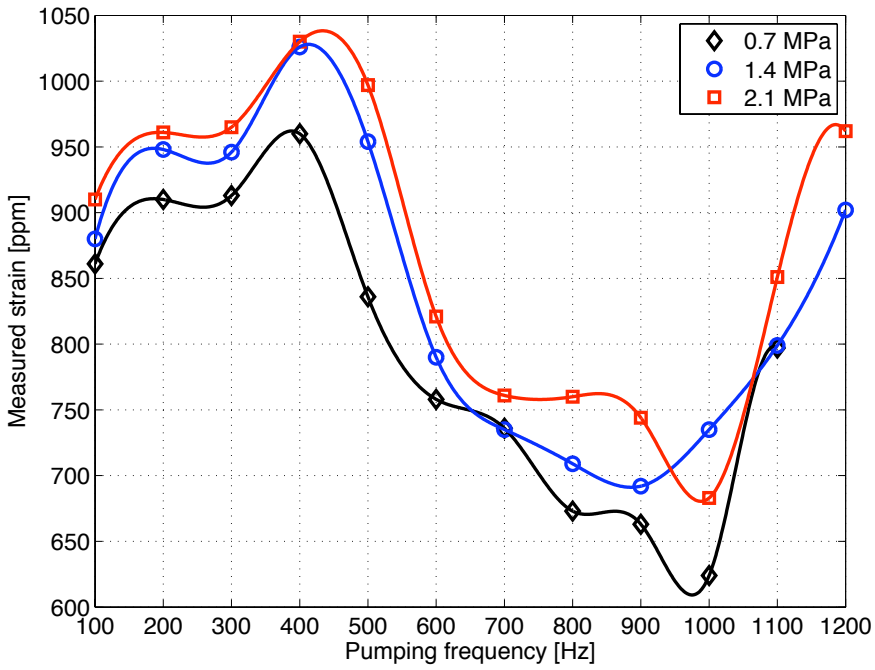

(a) 300 V

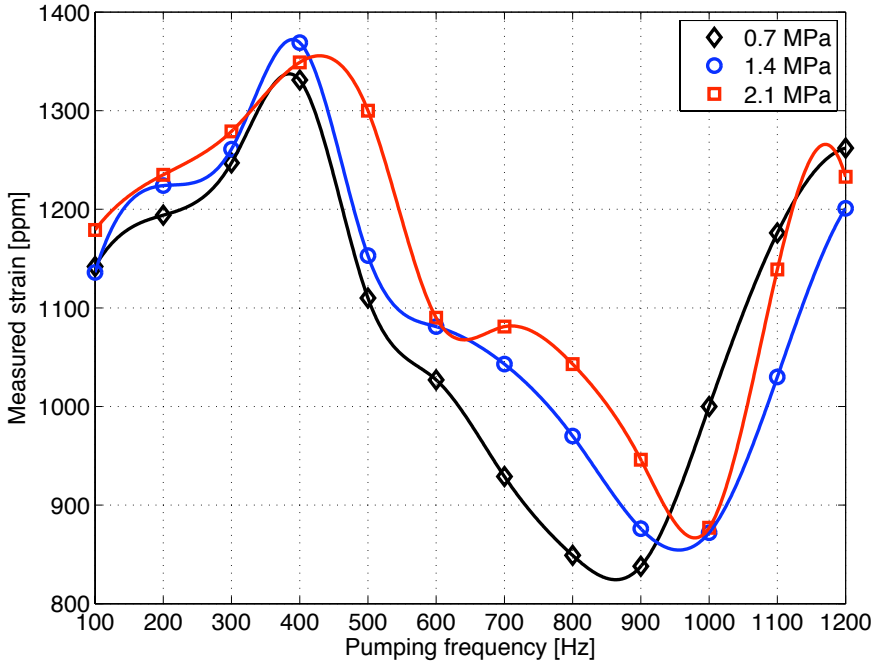

(b) 400 V

Figure 4.22: Measured strain at different bias pressures and applied voltages

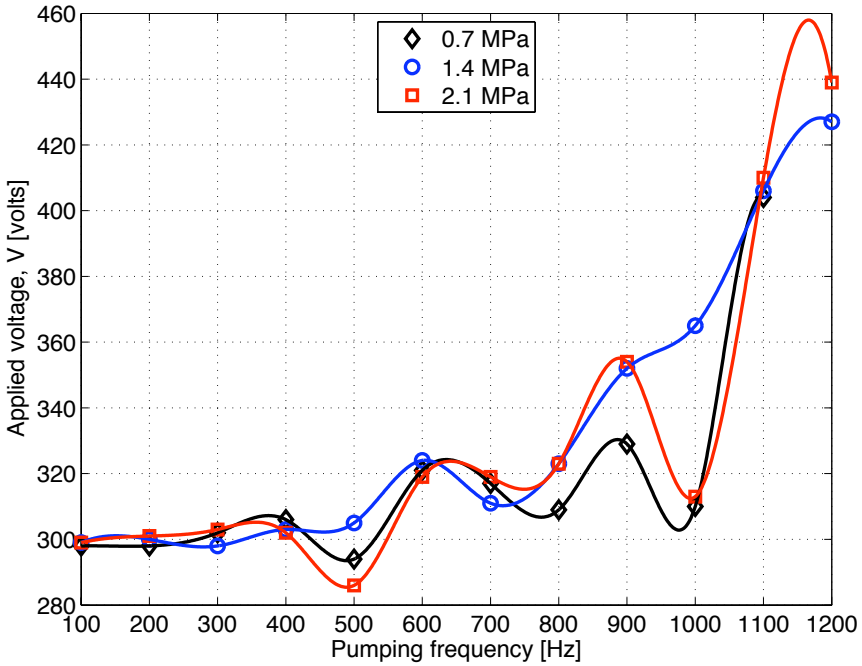

(a) 300 V

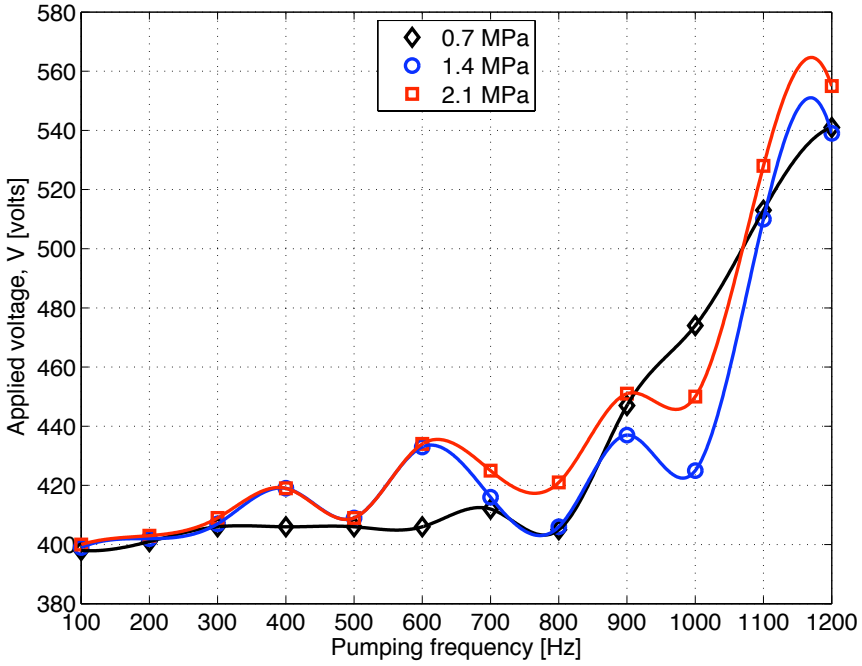

(b) 400 V

Figure 4.23: Actual voltage across stacks at different bias pressures and control voltages

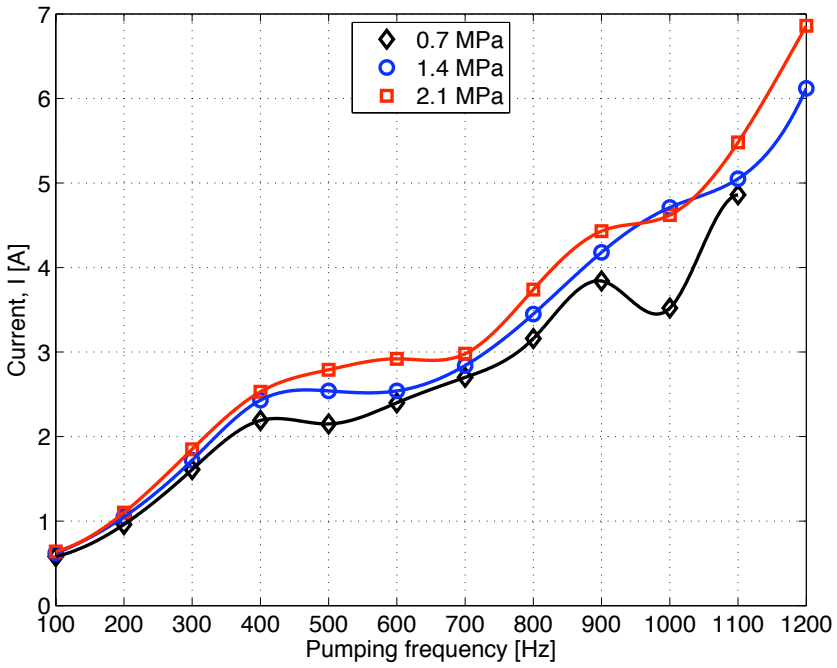

(a) 300 V

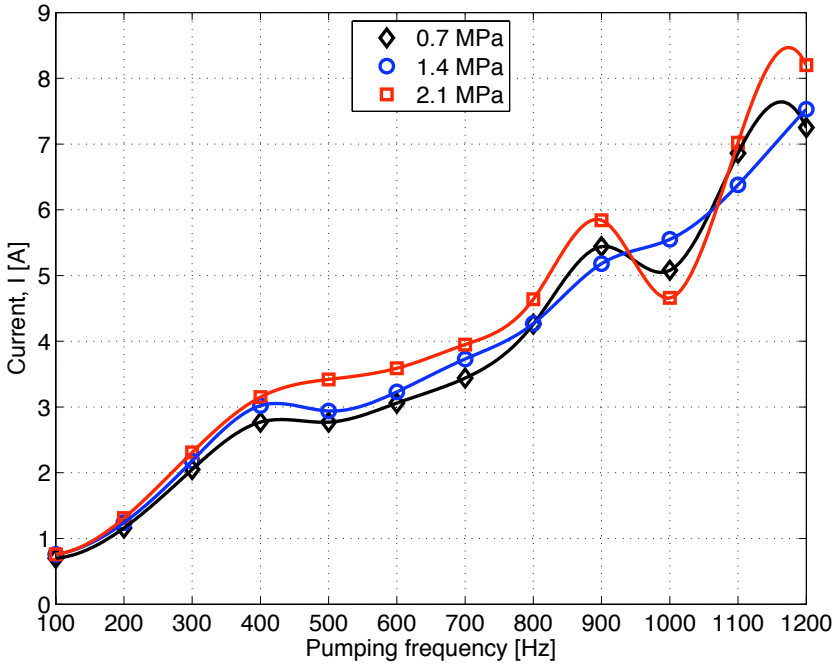

(b) 400 V

Figure 4.24: Input current at different bias pressures and applied voltages

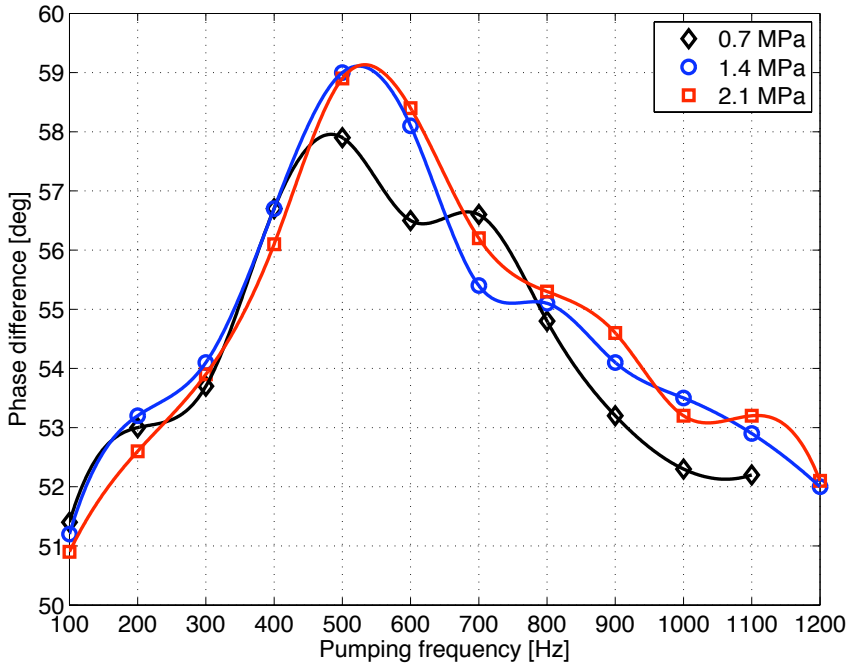

(a) 300 V

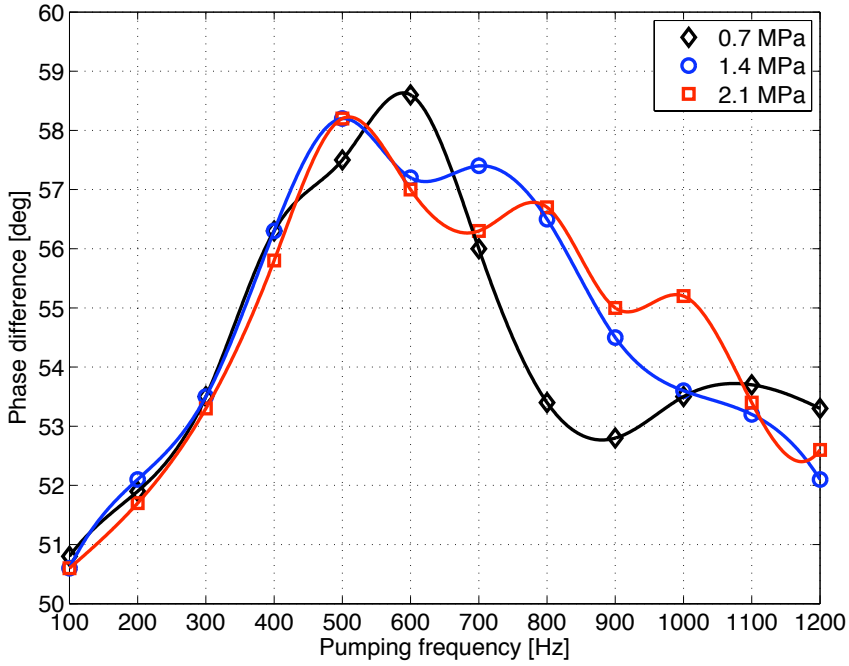

(b) 400 V

Figure 4.25: Phase difference at different bias pressures and applied voltages

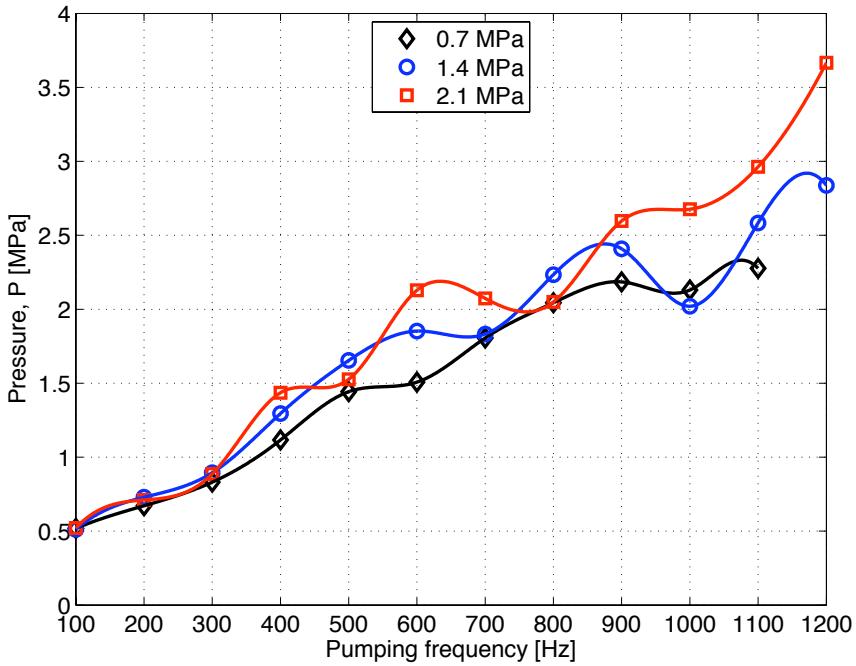

(a) 300 V

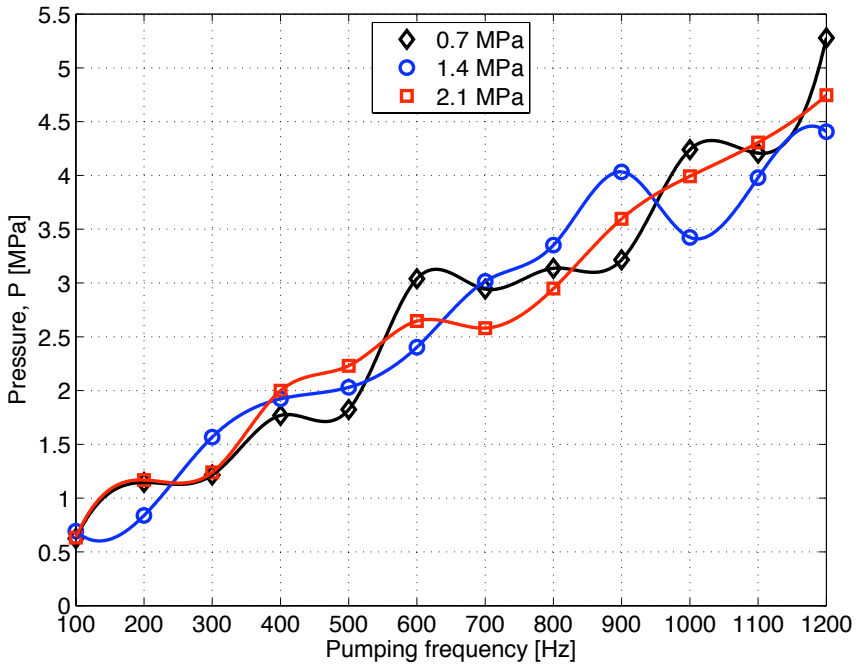

(b) 400 V

Figure 4.26: Manifold fluid pressure (peak-to-peak) at different bias pressures and applied voltages

both 300 V and 400 V actuation voltages. The frequency at which peak performance occurs for a particular bias pressure remains almost unchanged for the two different actuation voltage levels. This is accompanied by an improvement in the output velocity, mainly because lesser energy is lost in compressing the fluid and more is applied to translation of the fluid, ultimately resulting in higher volume flow rates from the pumping chamber to the output piston. However, there exists an optimal range of bias pressure, since the increase in fluid bulk modulus also increases the stiffness of the pumping chamber; hence, the strain induced in the active stack will reduce at excessive bias pressures.

The measured strains in the PMN stacks at different actuation frequencies and bias conditions are shown in Figure 4.22. The free strain of the PMN-32%PT stacks was 1120 ppm at 300 V and 1475 ppm at 400 V. During pump operation, the peak induced strains measured in the active material were 1030 ppm and 1370 ppm at 300 V and 400 V nominal input voltages respectively, with both peaks occurring at 400 Hz (Figure 4.22). The nature of high frequency ($>$ 900 Hz) behavior of the induced strain can be attributed to the voltage versus frequency characteristics of the electrical input, shown in Figure 4.23. As frequency increased, the peak-to-peak value of the measured voltage applied to the stack also increased (by nearly 25% over the entire range of frequencies tested) even though the input control voltage is kept constant. This effect was supported by measurements of the current in the amplifier output circuit too (Figure 4.24). The possible reason for such behavior could be the dynamics of the R-C circuit formed by the PMN stack; since the impedance Z of an

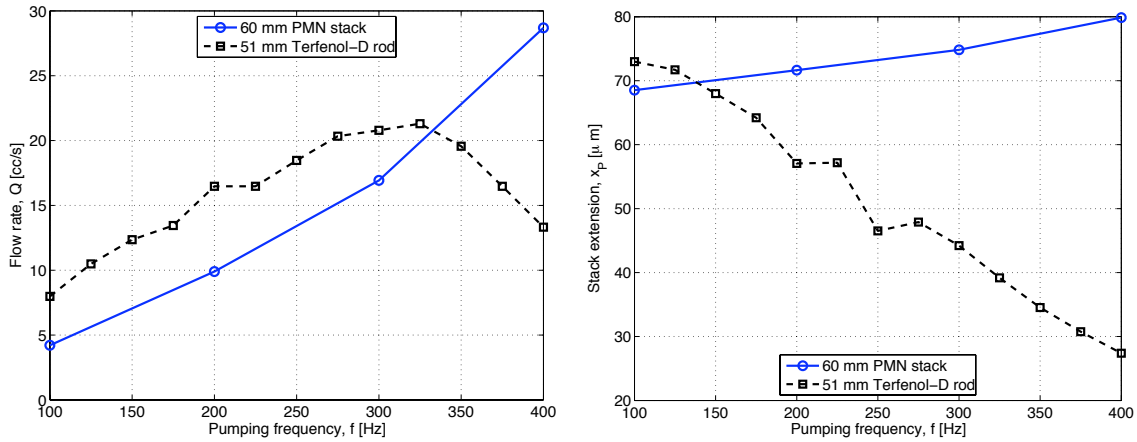

(a) Output flow rate

(b) Stack extension

Figure 4.27: Comparison of no-load performance between PMN-PT and Terfenol-D actuators

RC circuit decreases with frequency f,

$$Z = \sqrt{R^2 + \frac{1}{(2\pi f C)^2}}$$

it behaves much more efficiently at higher frequencies of operation.

Although different bore output cylinders can be used in actuators, a true comparison of no-load performance can be made by calculating the volume flow rates. For the PMN actuator setup, the maximum volume flow rate was calculated to be 42.5 cc/s (2.6 in^3/s), which is much higher than the previous designs at the University of Maryland that used PZT [72] or Terfenol-D [209] as the driving element. However, if we compare the flow rates from the PMN pump and the 51 mm Terfenol-D pump at the lower frequencies, shown in Figure 4.27(a), we see that the latter actually produces higher flow rates at the same frequency of actuation till ∼300 Hz. This is because the pumping chamber area of the Terfenol-D pump was 44 % more than the

PMN pump, while the actual pumping piston displacements due to extension of the active elements were almost same in this frequency range (Figure 4.27(b)). However, the induced strain in the magnetostrictive rod drops beyond this point, while the PMN material produces nearly same levels of induced strain up to much higher frequencies of actuation. Also, lower compliance of the fluid in the PMN pump markedly increases the bandwidth over the Terfenol-D pump.

Because voltage applied to the electrostrictive stacks was maintained nearly constant over the frequency range of interest, the roll-off in the performance was attributed to two major causes:

(i) Inertia of the fluid masses: The hybrid actuation system works by rectifying the fluid flow in every cycle, so that the hydraulic fluid in the manifold is accelerated in every cycle. This leads to considerable inertial effects at high frequencies, particularly because the required force increases quadratically with pumping frequency. Hence, beyond a certain pumping frequency, the additional inertia of the fluid mass overwhelms the increase in chamber pressure produced by motion of the active stacks (Figure 4.26), ultimately resulting in decrease of flow rate from the pumping device. The higher pressure in the pumping chamber also results in higher force acting on the active stacks, thus lowering the actual induced strain in the active stacks, and hence, reducing displacement of the pumping piston.

(ii) Dynamics of the reed valves: The passive reed valves used here can be modeled as cantilever beams oscillating in a fluid. Though the natural frequency of the

spring steel reeds, 7.62 mm (0.30 inch) long × 5.08 mm (0.20 inch) wide × 0.127 mm (0.005 inch) thick, vibrating in air is close to 1.7 kHz, the presence of a dense viscous hydraulic fluid reduces the resonant frequency into the range of pumping frequencies. From empirical relations [216], the modified natural frequency due to additional inertial effects was found to be ∼750 Hz; the dynamic response of the reed valve drops exponentially beyond this frequency, leading to higher losses in the reed ports. Since the natural frequency of the valves lay within the range of pumping frequencies used in our test setup, it was definitely a limiting factor in the pump performance.

The free strain of the PMN-32%PT stacks was 1120 ppm at 300 V and 1475 ppm at 400 V. During pump operation, the peak induced strains measured in the active material were 1030 ppm and 1370 ppm at 300 V and 400 V nominal input voltages respectively and occured around 400 Hz pumping frequency [Figure 4.22]. These values were lower than the free strains of the material at the respective electric fields and was due to the higher stiffness of the fluid chamber compared to the active stack.

The no-load test results clearly show a substantial reduction from the initial design predictions. This was expected, since the ideal, quasi-static calculations assumed maximum induced strain in the PMN-PT material and did not take into account any losses in the fluidic system due to viscosity, compressibility and inertia. Due to the high pumping frequency, the fluid mass was accelerated during every cycle, thus leading to high inertial losses. Moreover, the actual induced strains in the PMN stacks

during pump operation were much lower than the measurements under free conditions; this was due to the following reasons:

(i) The maximum voltage applied to the stacks was limited to 400 V to prevent chances of insulation failure during high frequency pumping operation. Since the free strain of 2200 ppm was observed at nearly 600 V, the reduction in operating voltage to 400 V resulted in an immediate drop of 33 % in the induced strain.

(ii) During actual pump operation, the pressure generated in the fluid pumping chamber opposes the axial motion of the stack; hence, the stack is unable to extend freely, and the resulting strain is lower than the maximum allowable free strain.

4.4.2 Tests with external loads

Tests were also carried out under load to investigate the performance of the actuator when an external load is attached and get a measure of the blocked force of the actuator. These tests were performed by attaching a fixture to the output shaft and then placing graduated weights; the experiment setup is shown in Figure 4.28. The fixture weighed 0.54 kg (1.2 lbs) and was fixed to the output piston shaft using a threaded connection.

The load tests were performed at input conditions where the best no-load performance was observed. The nominal applied voltage of 400 V, at 1.4 MPa (200 psi) bias pressure, over the entire frequency range for which appreciable output displacement was noted.

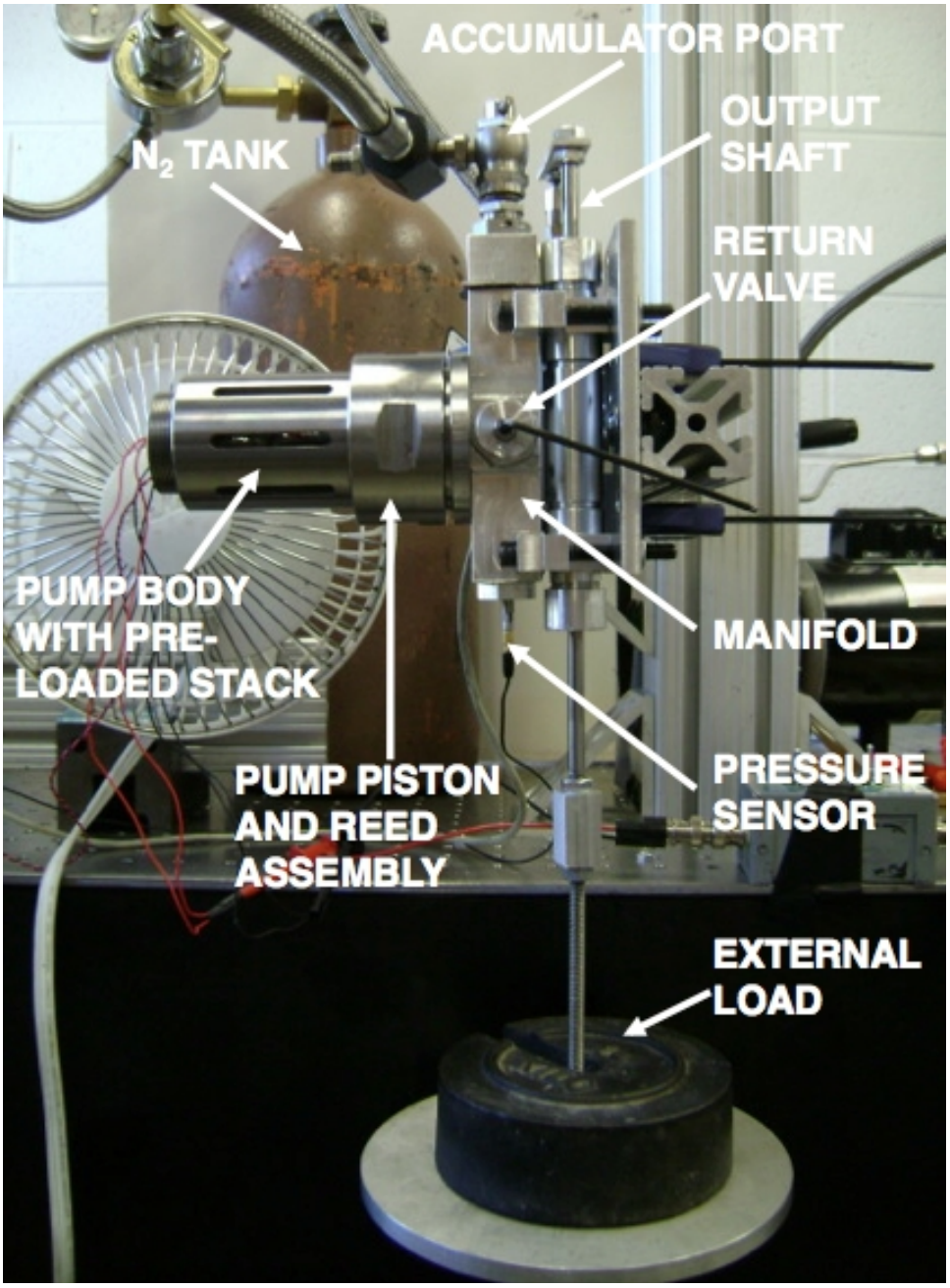

Figure 4.28: Test setup for PMN actuator with external loads

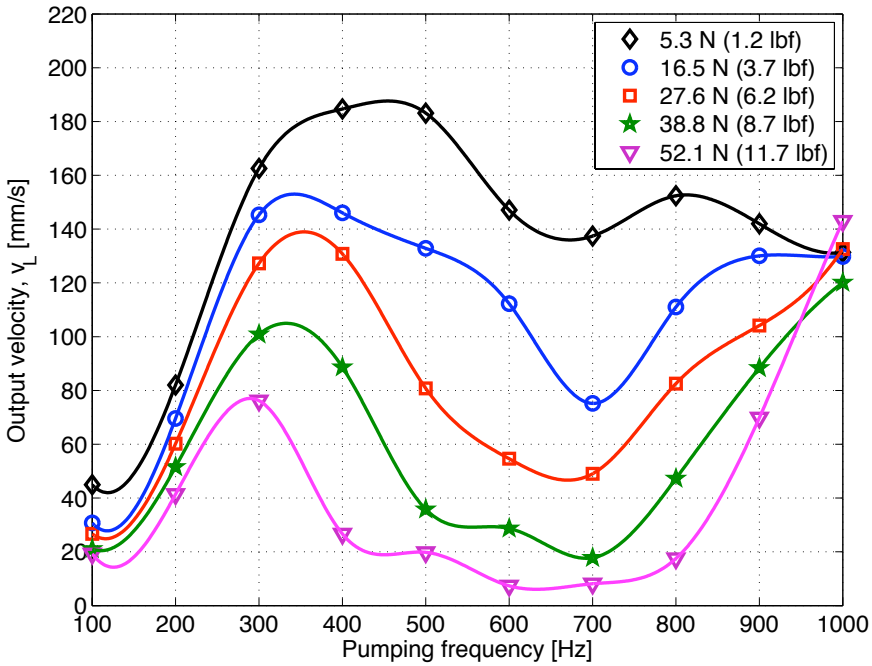

(a) Output velocity vs. pumping frequency for varying loads

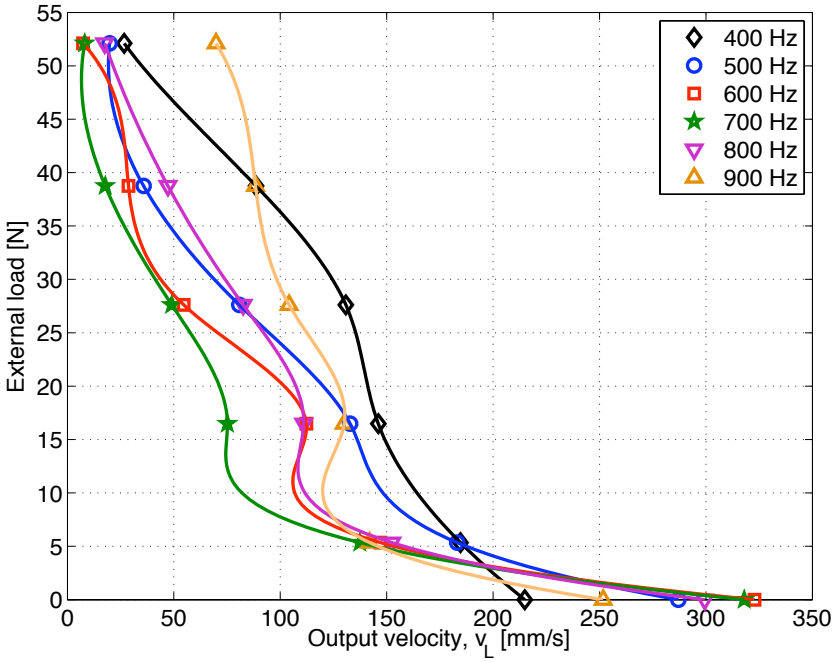

(b) Force vs. output velocity at different pumping frequencies

Figure 4.29: Results of load tests with PMN-PT actuator

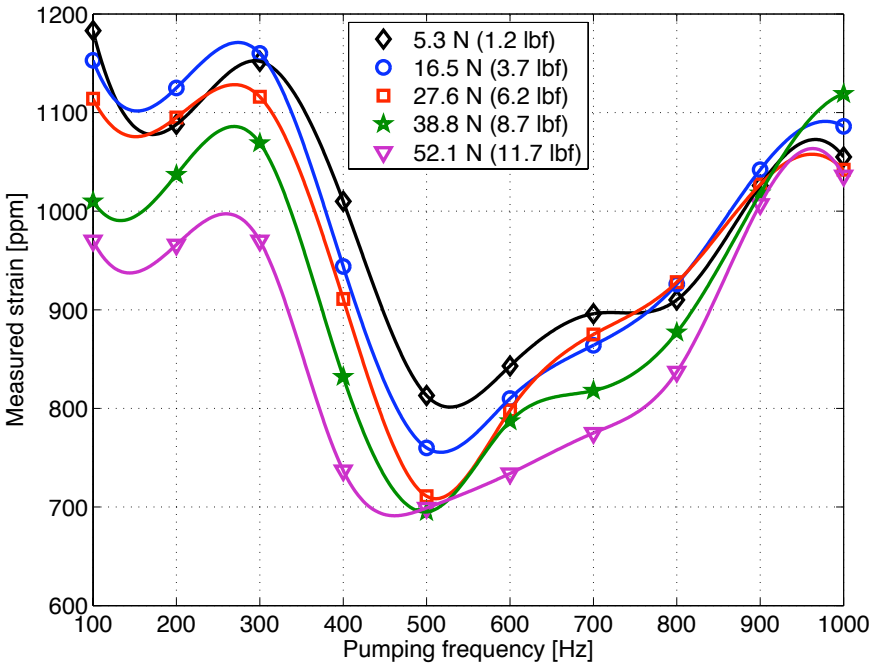

(a) Measured strain vs. pumping frequency for varying loads

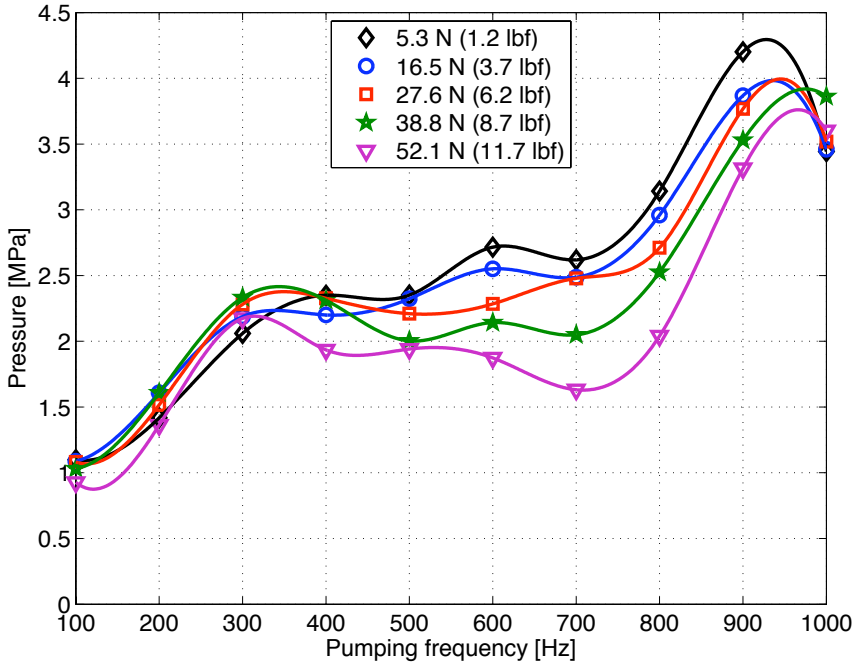

(b) Manifold pressure vs. pumping frequency for varying loads

Figure 4.30: Measurements from load tests with PMN-PT actuator

These tests results show a substantial drop in the output shaft velocity as we increase the external load from the no-load condition to the maximum value; just attaching the load-carrying fixture, which weighs 0.5 kg (1.2 lb), reduced the peak velocity to 185 mm/s, a drop of 44% from the peak performance (330 mm/s) measured in the absence of load. The frequencies at which the peak velocity was obtained shifted to lower values as the load was increased; this was expected because adding inertial load to the output shaft adds to the inertia of the system and effectively decreases its natural frequency. The actual strain in the active material is lower than the corresponding no-load conditions (Figure 4.30(a)), resulting in lower manifold pressure too, as seen in Figure 4.30(b).

The power output from the actuator was calculated at all the test points as the product of the load and the corresponding output shaft velocity i.e.

$$P_{out} = F_{ext} \times v_L, \quad F_{ext} = m_L g \tag{4.9}$$

The results are plotted in Figure 4.31(a). The corresponding electrical power input was calculated from the actual applied voltage and current measurements. The phase differences ϕ between the voltage and current signals were obtained from FFT calculations. The input power, P_{in}, was then written as:

$$P_{in} = \frac{1}{2} V_0 I_0 \cos\phi \tag{4.10}$$

The overall electromechanical efficiency was calculated from P_{in} and P_{out} and plotted in Figure 4.31(b).

From the results of the load tests, we extrapolated the force-velocity lines (Figure 4.29(b)) at each of the pumping frequencies to get a measure of the *blocked force*

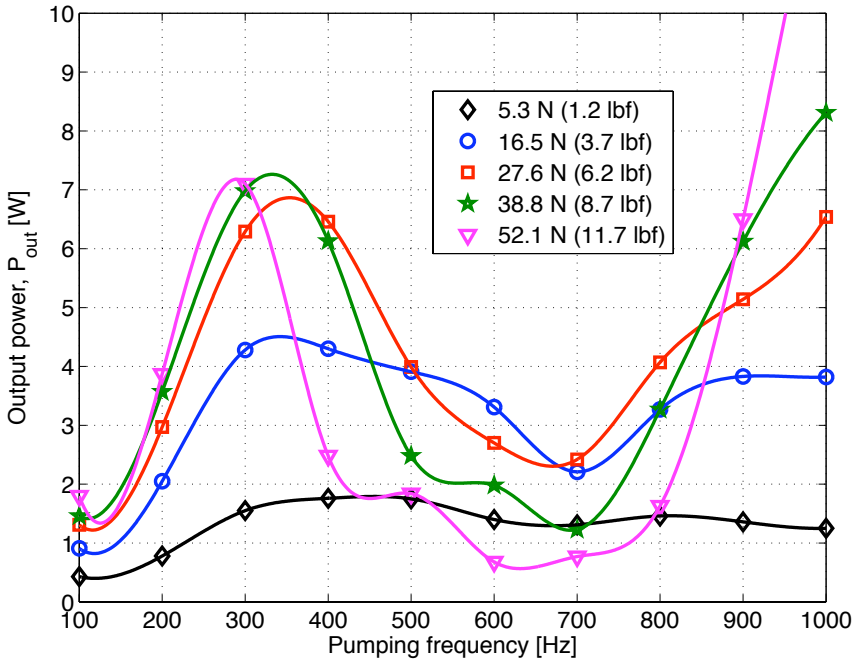

(a) Output power vs. pumping frequency for varying loads

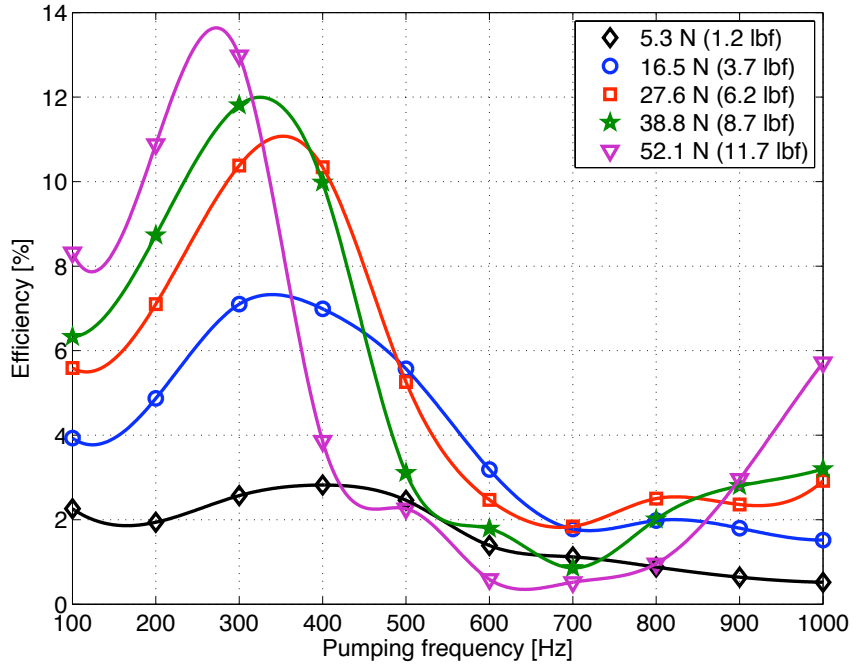

(b) Efficiency vs. pumping frequency for varying loads

Figure 4.31: Power and efficiency calculations for PMN-PT actuator

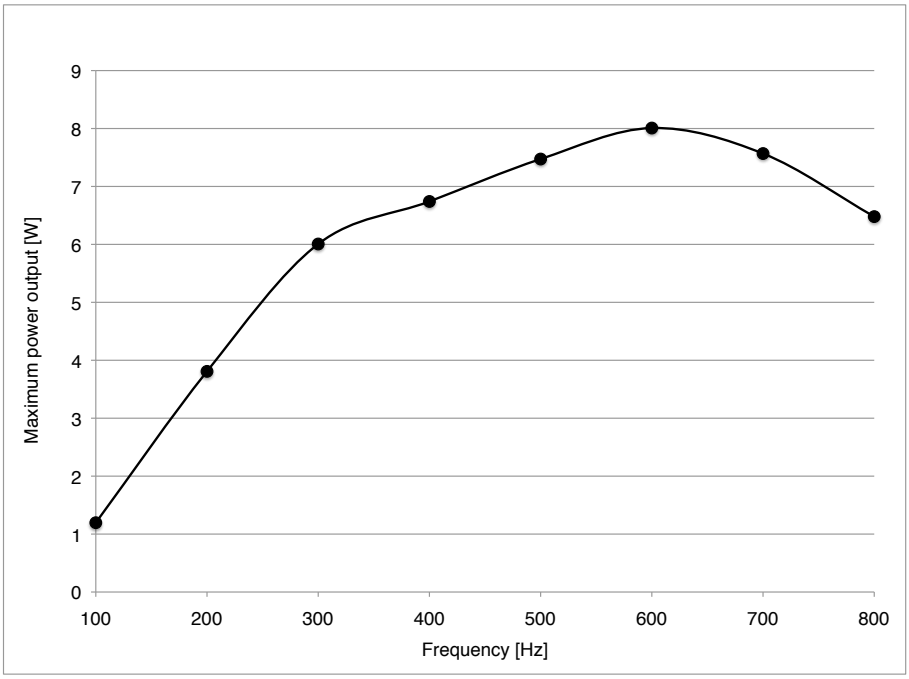

Figure 4.32: Maximum power output from PMN-PT actuator

of the actuator. The maximum blocked force considering all frequencies of actuation was calculated to be about 62.7 N, corresponding to an externally hung load mass of 6.4 kg (14.05 lb), for the current actuation system. Note that the blocked force of the actuator, which primarily depends on the stiffness of the active material, was the same at all pumping frequencies. Correspondingly, the maximum possible useful power output from the system was also calculated from the area under the force-velocity diagram at each distinct pumping frequency [72,86] using Equation 2.4. The results are shown in Figure 4.32, with the maximum possible power output found to be 8.0 W at 600 Hz pumping frequency.

4.4.3 Model validation

Results from performance tests with the PMN-PT driven actuator were used to validate the dynamic model derived earlier. The parameters used in the mode were changed to reflect the new design; the new values are given in Table 4.2.

The value of static friction, F_s, in the output cylinder was pre-determined by adding measured weights on to the output shaft (aligned vertically) and noting the point at which it started to move; the critical weight was found to be 2.27 kg (5 lb). Hence, the value of static friction, F_s, used in the simulations was 22.3 N. The value of the dynamic friction, F_d, was estimated to be 17.8 N (4 lbf) from the simulation studies.

The value free strain used for the model computations was 1200 ppm, corresponding to 400 V applied voltage. The corresponding free strain at 300 V was 25% lower.

The location of the actuator peak output was highly sensitive to value of fluid bulk modulus β, which should ideally be very high in order to transfer all the energy from the active material to the load. The presence of entrained air in the hydraulic oil increases the fluid compressibility and drastically reduced the bulk modulus [86, 92, 197, 262], as seen from the data sheet for hydraulic oil [263]. The value of bulk modulus used in the computations for the new PMN stack-based actuator was around 550 MPa (80 ksi) corresponding to a bias pressure of 1.38 GPa (200 psi), which is much lower than the manufacturer specified value of 1793 MPa (260 ksi). Increasing the value of bulk modulus stiffens the fluid, thus moving the resonant peak to a higher

Table 4.2: SIMULATION PARAMETERS

Properties		
	β	345 MPa (50 ksi)
	ρ_0	871 kg/m^3
	ρ_a	7900 kg/m^3
	ν	31.5 cSt
	E_A	12.0 GPa
Dimensions		
	L_a	60 mm (2.36 inch)
	D_a	12 mm (0.47 inch)
	L_{ch}	2.54mm (100 mils)
	D_{ch}	31.75 mm (1.25 inch)
	L_t	35.6 mm (1.4 inch)
	D_t	5.10 mm (0.20 inch)
	L_{port}	6.35 mm (0.25 inch)
	D_{port}	3.81 mm (0.15 inch)
	L_o	50.8 mm (2 inch)
	D_o, D_i	14.30 mm (9/16 inch), 6.35 mm (1/4 inch)
Others		
	m_a, m_p	0.10 kg, 0.075 kg
	F_s, F_d	22.3 N (5 lbf), 17.8 N (4 lbf)
	K_d, K_s	1.8×10^3 N/m, 1.8×10^5 N/m

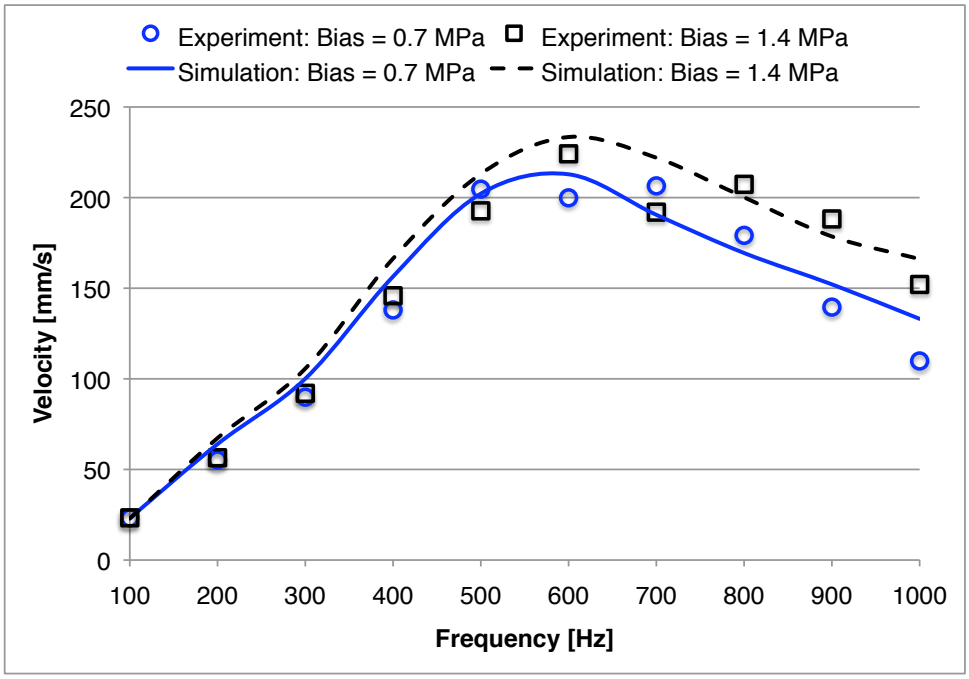

(a) 300 V peak applied voltage

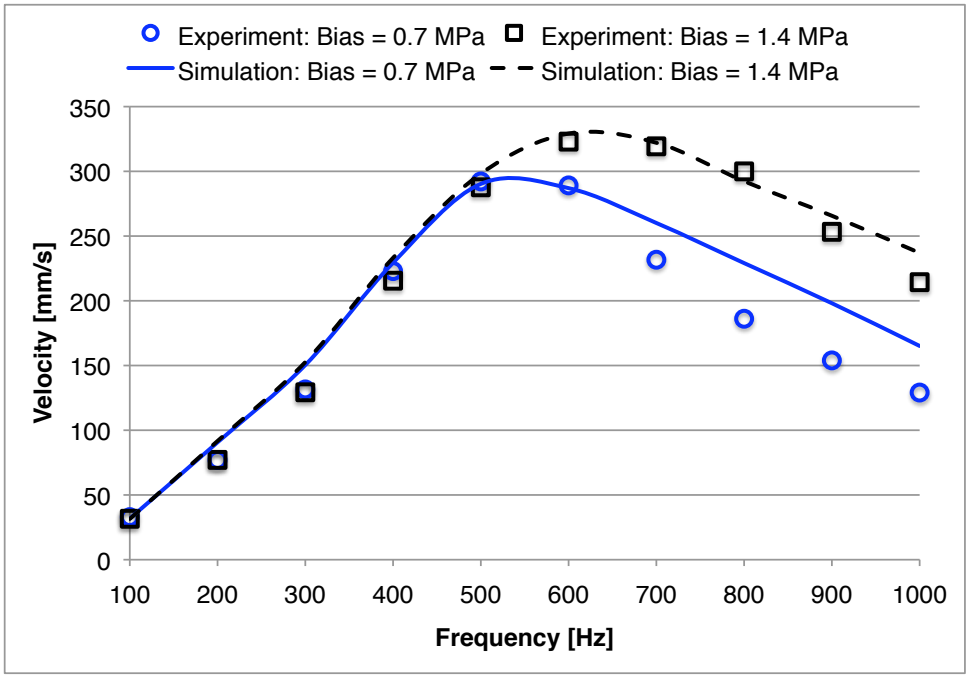

(b) 400 V peak applied voltage

Figure 4.33: Comparison of measured output velocity with simulation results at different voltage levels and bias pressures

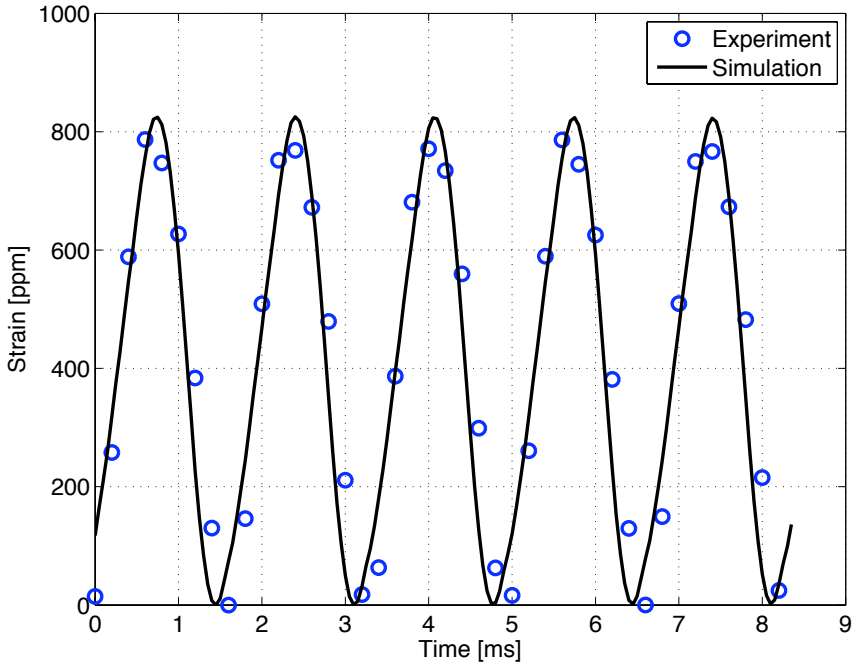

(a) Induced strain in PMN stack

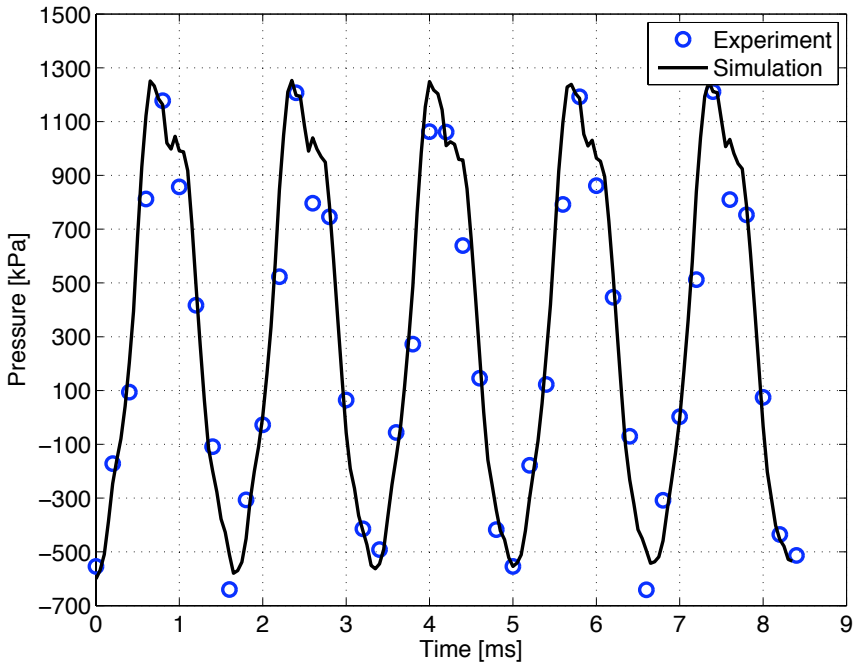

(b) Fluid pressure in manifold

Figure 4.34: Comparison of time-domain data at 600 Hz pumping frequency and 300 V peak applied voltage with simulation results

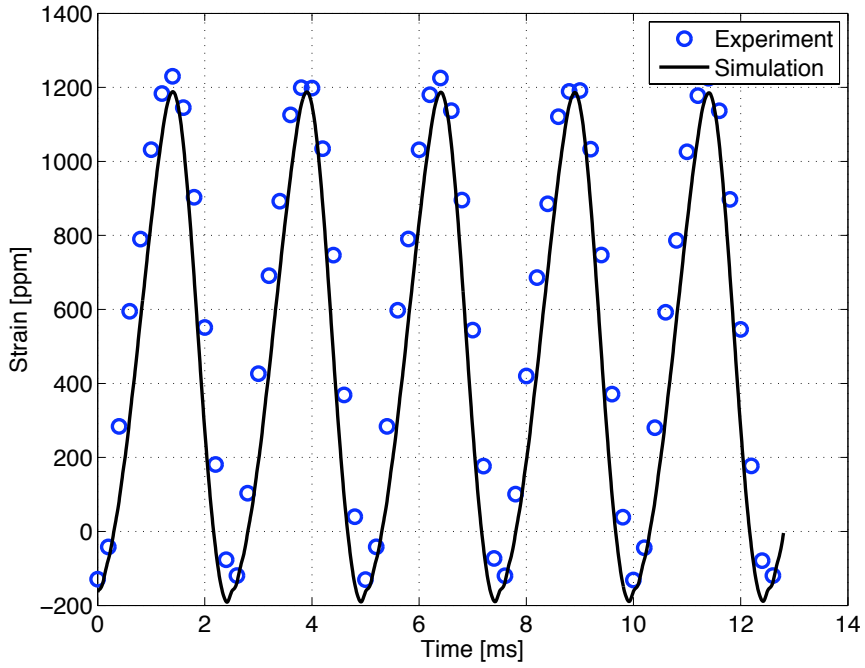

(a) Induced strain in PMN stack

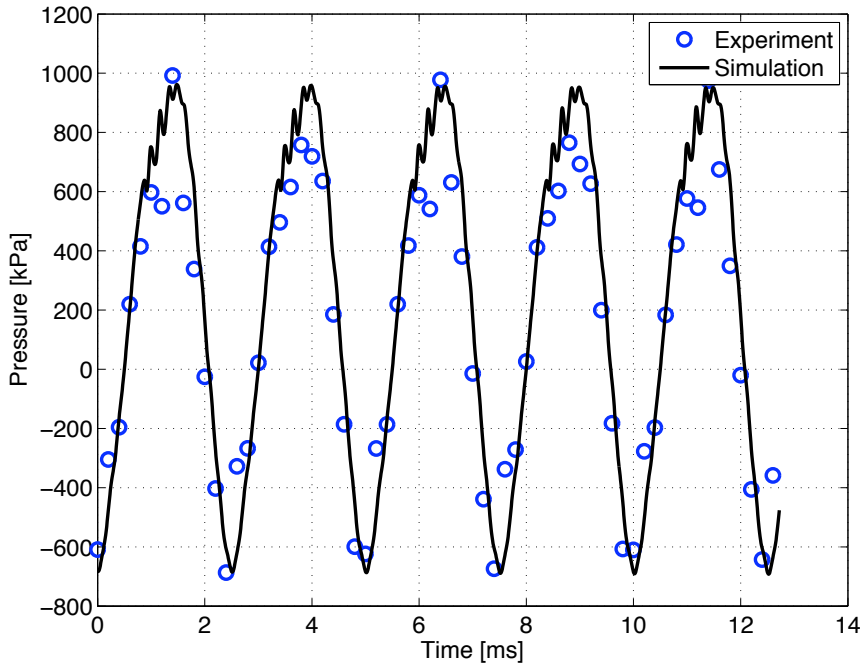

(b) Fluid pressure in manifold

Figure 4.35: Comparison of time-domain data at 400 Hz pumping frequency and 400 V peak applied voltage with simulation results

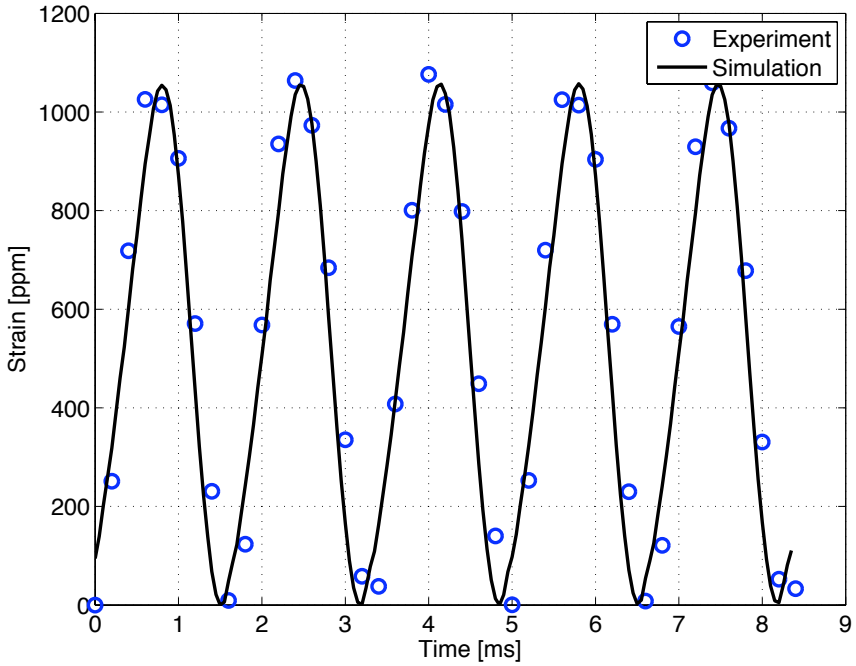

(a) Induced strain in PMN stack

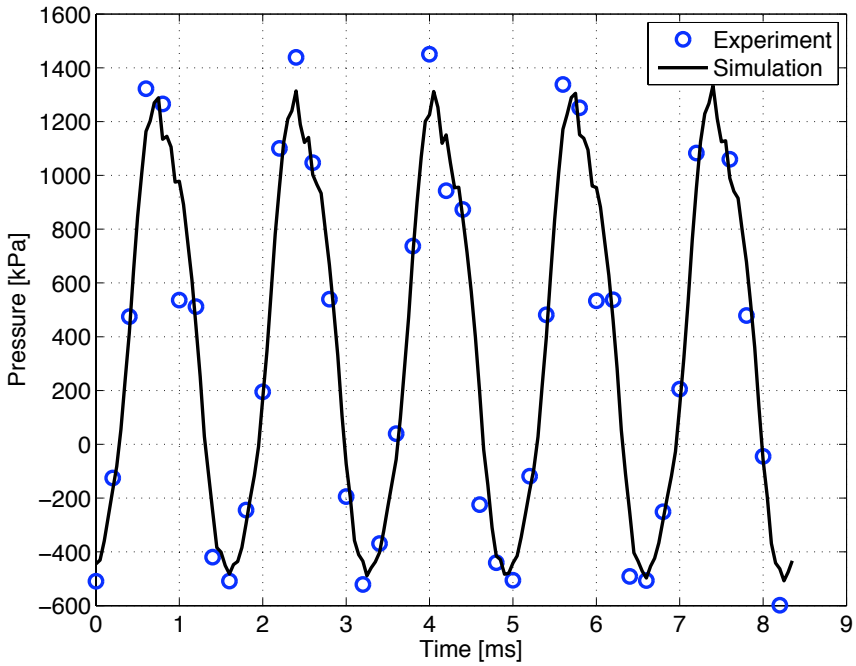

(b) Fluid pressure in manifold

Figure 4.36: Comparison of time-domain data at 600 Hz pumping frequency and 400 V peak applied voltage with simulation results

frequency. In addition, a stiffer fluid causes lower pressure losses, because less force is lost in compressing the fluid volume in the manifold before it begins to flow.

The simulated data is seen to match the experimentally obtained data very closely over the entire frequency range. The peak output velocity and the corresponding frequency are also captured accurately. To further verify the fidelity of the model, we also compared the time-domain measurements (5 complete cycles) of strain in the PMN stacks and fluid pressure in the driving side of the manifold for three combinations of applied voltage and pumping frequency as follows: (i) 300 V, 600 Hz, (ii) 400 V, 400 Hz, and (iii) 400 V, 600 Hz; the results are shown in Figure 4.34, Figure 4.35 and Figure 4.36 respectively. In all cases, we see a very good match between the test data and model simulation results.

The model was also used to validate the output velocity measurements from the tests with external loads with computational results from the model. Three cases were compared, at 400 Hz, 600 Hz and 800 Hz pumping frequencies, and the results are shown in Figure 4.37. At each pumping frequency, the simulations were carried out in steps of 0.25 kg up to 1 kg, and at 0.5 kg intervals beyond thereafter. The initial highly non-linear nature of the load-velocity curve is captured very accurately by the model and the blocked force was also accurately predicted; however, for the higher external load masses, where the output displacements (and velocities) become very small, the load-velocity curve becomes an asymptote to the load axis. This regime is difficult to predict accurately, probably because of (i) the increasing effects of stiction and (ii) change in fluid bulk modulus because of higher hydraulic pressures required to move the load mass. In our computations, zero velocity was observed when the

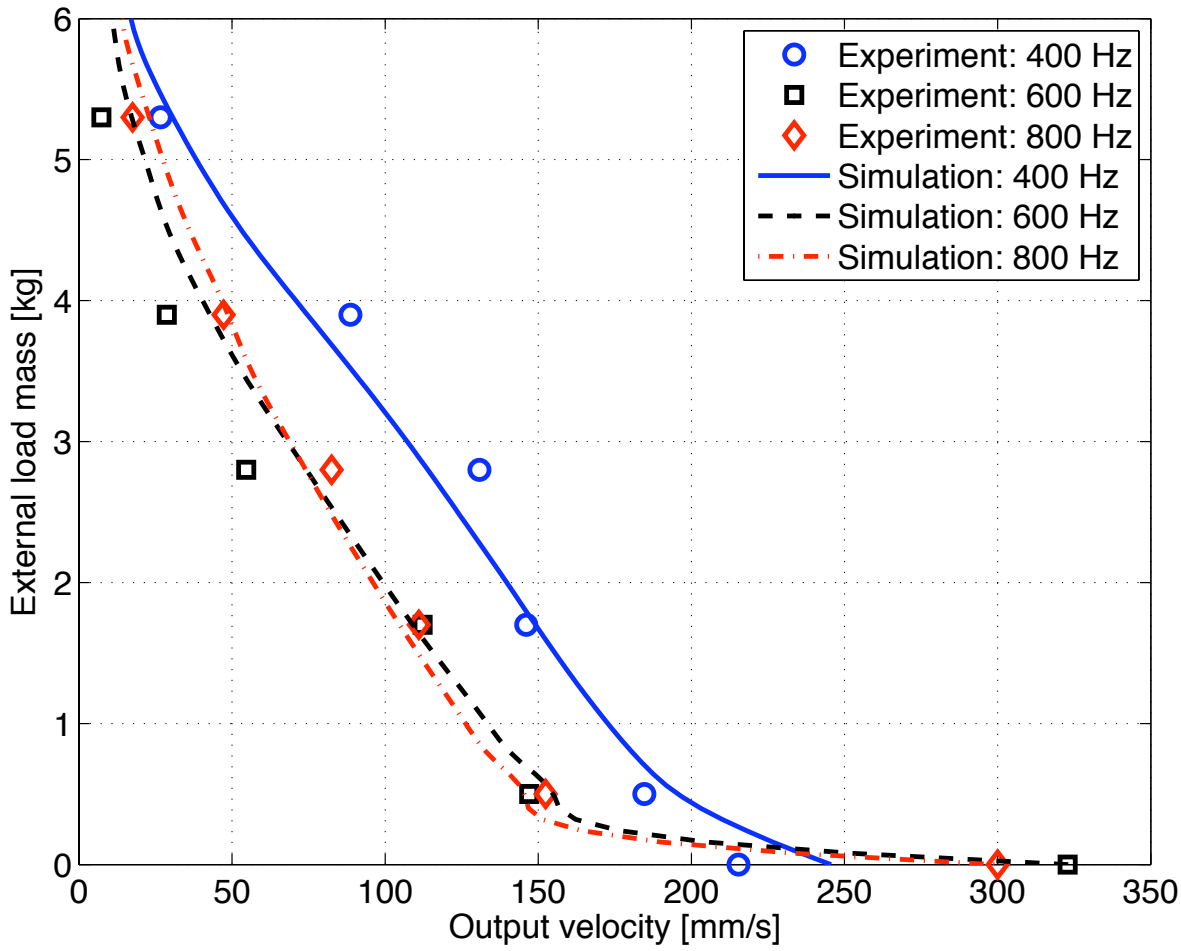

Figure 4.37: Comparison of measured output velocity with external loads and simulation results at different pumping frequencies

model was simulated with load mass of nearly 20 kg.

4.5 Conclusions

In this study, we presented the design and tests performed on a new compact hybrid actuation system using the electrostrictive material PMN-32%PT. Extensive experimental studies in uni-directional mode were performed on this actuation system. No-load and external load tests were carried out over a wide range of pumping frequencies to measure the performance as well as the identify the force limitations of such a hybrid actuation system. No-load testing established the maximum output velocity of the system to be 330 mm/s occurring at pumping frequencies close to 700 Hz; the corresponding flow rate was 42.5 cc/s. The blocked load of the actuator was calculated to be 63 N and the maximum power output was 8 W. Displacements of the pump piston due to stack actuation were also measured using a laser vibrometer and it was found that almost the entire induced strain is transferred to motion of the piston during actuation. The test data was also used to validate the time-domain model of the hybrid actuation system developed earlier by the authors.

Though these test results show that hybrid hydraulic actuation is possible using PMN as the driving material, there are a few noteworthy points. Self heating in the device tested was very low compared to previous experiences with PZT or TerfeNOL-D and so thermal stability should not be an issue for long duration applications. However, the single crystal material is extremely fragile and any misalignment during prestressing the sample led to immediate mechanical failure. High frequency opera-

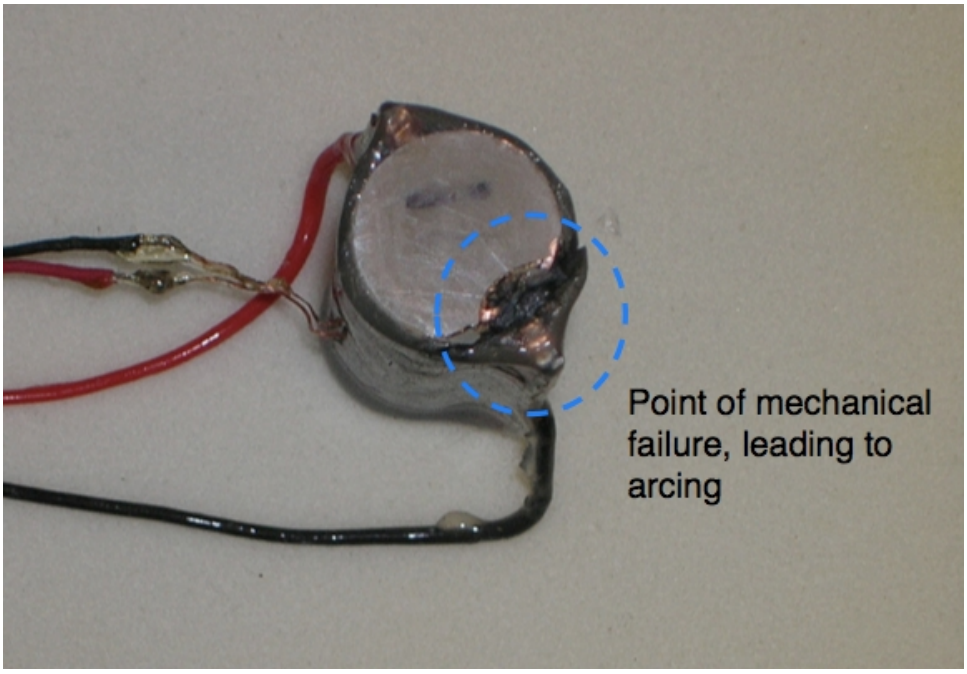

Figure 4.38: Mechanical failure of PMN stack

tion for long durations led to development of cracks and subsequent electrical failure on several occasions (Figure 4.38). The very high voltages needed to induce maximum strain from PMN sometimes led to arcing between the active layers or with the surrounding metallic body; to prevent this, characterization tests of the electrostrictive material have usually been carried out by placing the sample in a silicone oil bath [272]. The modulus of a stacked actuator made with PMN is also lower ($\sim$12 GPa) than other widely used smart materials; hence, the interface with the fluidic system has to be designed very carefully for good impedance matching and to utilize maximum induced strain from the material.

Chapter 5

Parametric Study

The comprehensive model developed in this dissertation takes into account several important physical parameters and phenomena occurring within the hybrid actuation system, for example, linear induced strain behavior of the active material, compressibility and inertia of the fluid, dynamics of the passive valves, and frequency-dependent characteristics of the input electrical and/or magnetic circuit. Although some of these features were also used in models developed previously in literature, the overall performance of the hybrid actuation mechanism could not be captured by one single model. The importance of some of these features, namely,

- Inertia of the fluid
- Reed valve dynamics
- Input circuit behavior

have been individually studied in this chapter and their phenomenological impact on the new model are justified.

The main parameters of the model can also be varied to find the sensitivity of the compact hybrid electro-hydraulic actuator performance. This study is important, since it helps in the identification of the specific material properties and geometric dimensions that can be manipulated during the design stage in order to attain certain

actuator requirements like no-load velocity, blocked force and frequency bandwidth. Due to the large variation in properties of active materials available in the market today (for example, from high strain, low stiffness PMN-PT to low strain, high stiffness GalFeNOL, to medium strain, medium stiffness PZT and TerFeNOL, and then to very high strain, low bandwidth shape memory alloys), it is extremely important to identify the correct induced strain actuation material for a specific purpose. The stiffness of the actuating material and the bulk modulus of the transmission fluid were previously identified as two of the important factors governing actuator performance and frequency of operation; this chapter also presents a brief study into the effects of parameter variations of certain material properties and geometric dimensions on these two parameters by using the comprehensive simulation model developed and validated in the earlier chapters.

5.1 Model features

5.1.1 Input circuit frequency response

The induced strain produced in a smart material depends on the driving electrical (for piezoelectrics and electrostrictives) or magnetic (magnetostrictives) signal. In case of the Terfenol-D actuator, it was seen that the flux density through the sample dropped rapidly with frequency and resembled the frequency characteristics of a low-pass filter, as shown in Figure 3.3; this was due to the inductive effect of the magnetizing coil and the behavior of the overall magnetic circuit. The decrease in magnetic flux was assumed to have a proportional decrease in the induced strain

behavior in the magnetostrictive material and was incorporated in the system model using estimated parameters listed in Table 3.1. In case of the PMN actuator, the voltage applied to the stacks increased at the higher frequencies and resulted in a slower roll-off beyond the peak frequency.

To verify the importance of the inclusion of input circuit dynamics, we simulated the model assuming a constant amplitude input at all frequencies. The experimental data for the 51 mm and 102 mm Terfenol-D rods were considered for this study and the results are shown in Figure 5.1. In both cases, we see that the model without input dynamics predicts much higher output velocity compared to the experimental results and the simulation results with input model. This is as expected, because the effect of including the input dynamics is to suppress the driving force, namely, the magnetic field driving the magnetostrictive material, at higher frequencies, thus resulting in lower free induced strain at higher frequencies.

5.1.2 Fluid inertia

Since the induced strain produced by the presently available active materials is very low, it is imperative to operate the pumping device at very high frequencies in order to maximize output performance. The compact hybrid actuators developed till date operate across a wide range of pumping frequencies, from as low as 10 Hz to as high as 1.2 kHz. This was seen to have considerable dependence on the actuator performance, especially when frequencies higher than 150 Hz were used.

The inertial forces arising due to unsteady flow are strongly dependent on the

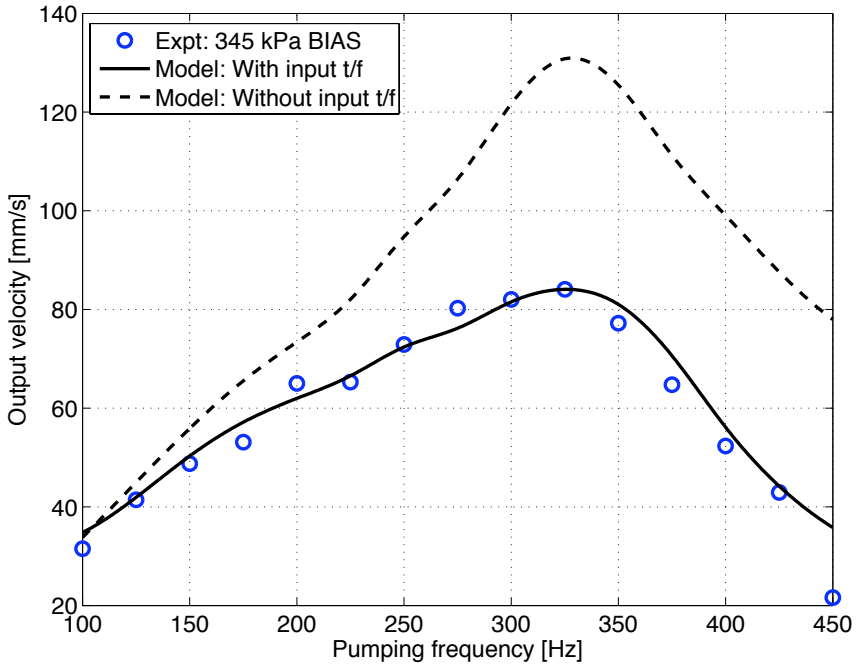

(a) 51 mm Terfenol-D rod

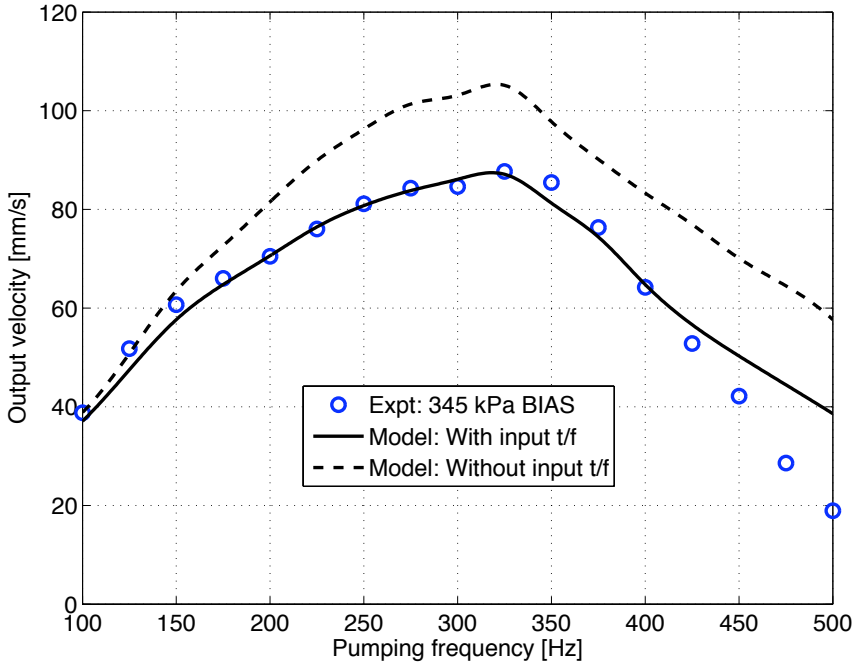

(b) 102 mm Terfenol-D rod

Figure 5.1: Comparison of measured output velocity with simulation results using model with and without input transfer function

frequency of operation, f. If we assume sinusoidally varying volumetric flow rate of a fluid i.e.

$$Q = Q_0 \sin(2\pi f t),$$

then the differential pressure, ΔP, required is proportional to the derivative of the flow rate [257, 262] i.e.

$$\begin{aligned} \Delta P &\propto \dot{Q} = (2\pi f) Q_0 \cos(2\pi f t) \\ \implies \Delta P &\propto f \end{aligned}$$

This clearly shows that the pressure has to increase proportional to the frequency in order to maintain the same flow rate. Most models developed previously in literature have failed to accurately capture the phenomenon at high frequencies. One of the main reasons was that they neglected the inertia of the fluid; only the frequency-domain model by Sirohi and Chopra [201] attempted to model the high-frequency (> 250 Hz) behavior by using a transmission line approach.

In order to show the characteristics of a model that neglected fluid inertia, we considered the model developed by Tan and Leo [69, 206]. This model took into account the compressibility of the fluid in the high pressure sections and also had a accurate representation of the minor losses. However, the model was formulated for an actuation system with active valves. In order to apply this model to the actuator developed in our laboratory, a passive reed valve model that operated (without any dynamics) on the basis of pressure difference was used. The modified model was simulated with material and geometrical parameters as used in the Terfenol-D actuators and the results are shown in Figure 5.2.

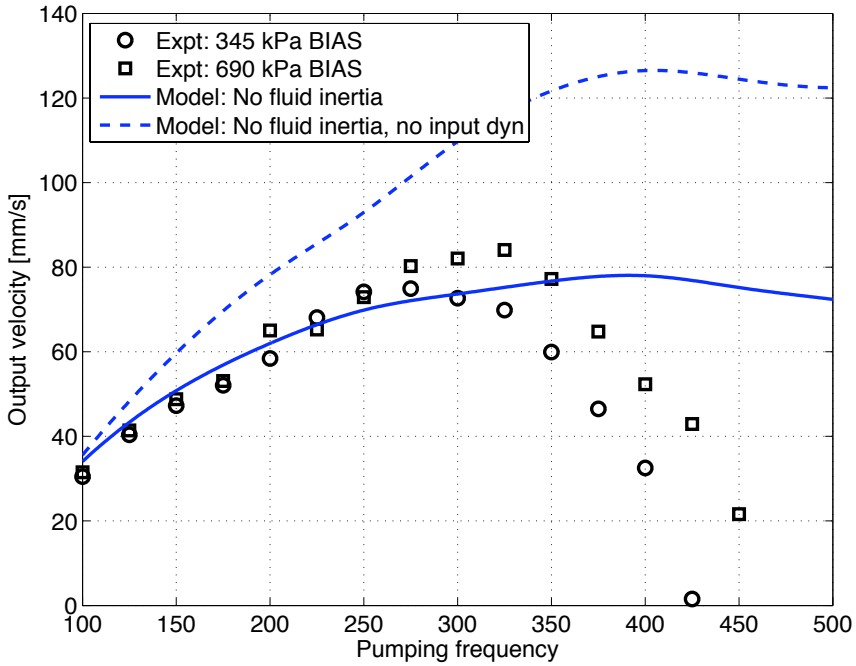

(a) 51 mm Terfenol-D rod

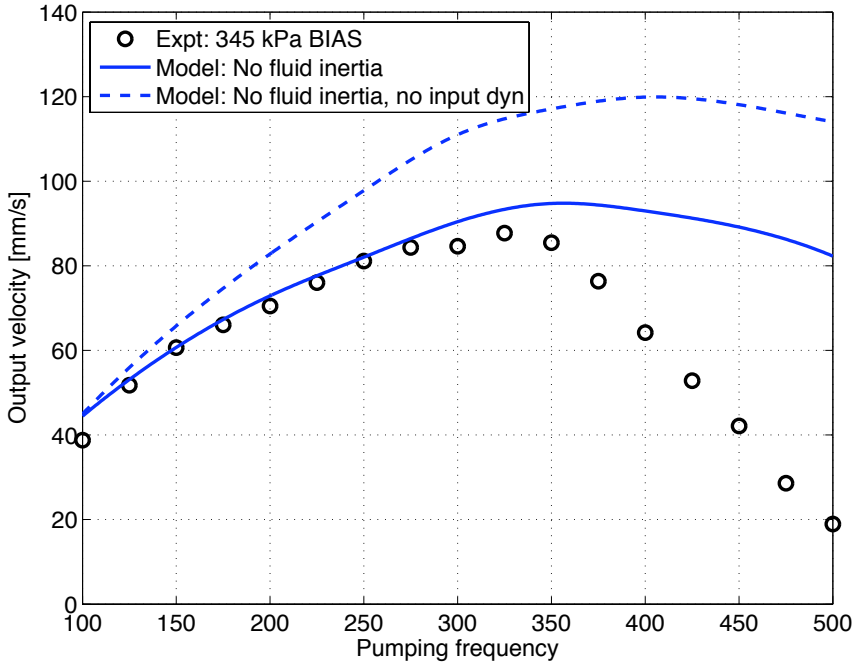

(b) 102 mm Terfenol-D rod

Figure 5.2: Comparison of measured output velocity with simulation results using a model that neglected fluid inertia

The numerical simulation results, shown with solid lines in both plots, prove the importance of fluid inertia in the actuator model. Though the reduced model captured the low frequency behavior (up to 300 Hz) very accurately for both the 51 mm (Figure 5.2(a)) and 102 mm (Figure 5.2(b)) long Terfenol-D actuators, it was unable to match the roll-off in output response at higher frequencies. Since the length of the manifold tubing is considerable and the volumetric flow rates are also high, the forces required to overcome the inertia of the fluid cannot be neglected in reality. These results are similar to the computational results obtained by Tan and Leo [69] for their own hybrid actuator, and they also indicated that the acceleration and inertia of the load and the fluid may influence the performance of the system at high frequencies.

The effect of the input circuit dynamics was also included in this stud and the predictions of the inertialess model that also excludes input dynamics have been shown with dashed lines in Figure 5.2. The results indicate that this simplified model, too, results in overestimation of actuator performance. The inclusion of frequency-dependent input behavior, therefore, is analogous to the application of a scaling factor to the driving force at all pumping frequencies.

5.1.3 Reed valve dynamics

According to tests conducted by previous researchers, the use of passive reed valves in the hybrid actuator leads to introduction of additional dynamics and frequency limitations of the device [72, 205]. It has also been suggested that at high

operating frequencies, the valves do not close completely and allow some fluid to leak back from the exhaust line into the pumping chamber [202, 204]. These analyses imply that a simple valve model that assumes perfect valve behavior and frequency-independent operation might not be sufficient. However, inclusion of valve dynamics using SDOF equations results in four additional states (two for each valve) in the overall model formulation, resulting in complicated coupling effects as well as higher computational load. In order to justify the importance of passive reed valve dynamics, the comprehensive model was also simulated without including dynamics of the reed valves; other model variables were modified accordingly in order to match the output velocity measurements from the tests.

Figure 5.3 shows a comparison between experimental measurements (shown with blue circles) and the simulation results without reed dynamics (shown with dashed red lines). The modified model does a fairly good job in tracking the initial and final positions of the output displacement variable, x_L, at each cycle, but it is unable to capture the frequency-dependent overshoot or slope of the response. The stepped motion of the output piston, however, is replicated in the simpler formulation. On the other hand, the calculated results from the mathematical model with reed dynamics included in the actuator model (plotted with solid black lines) are seen to track the measured shaft displacement at two different pumping frequencies more closely. From this study, we concluded that the inclusion of reed valve dynamics in the model was important to accurately capture the frequency-dependent behavior of output shaft displacement, x_L.

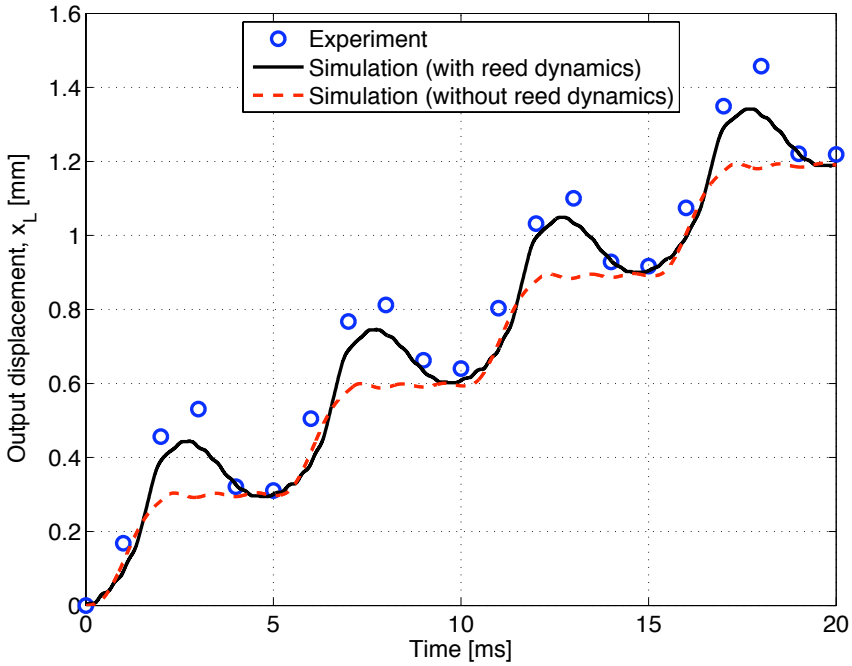

(a) Pumping frequency = 200 Hz

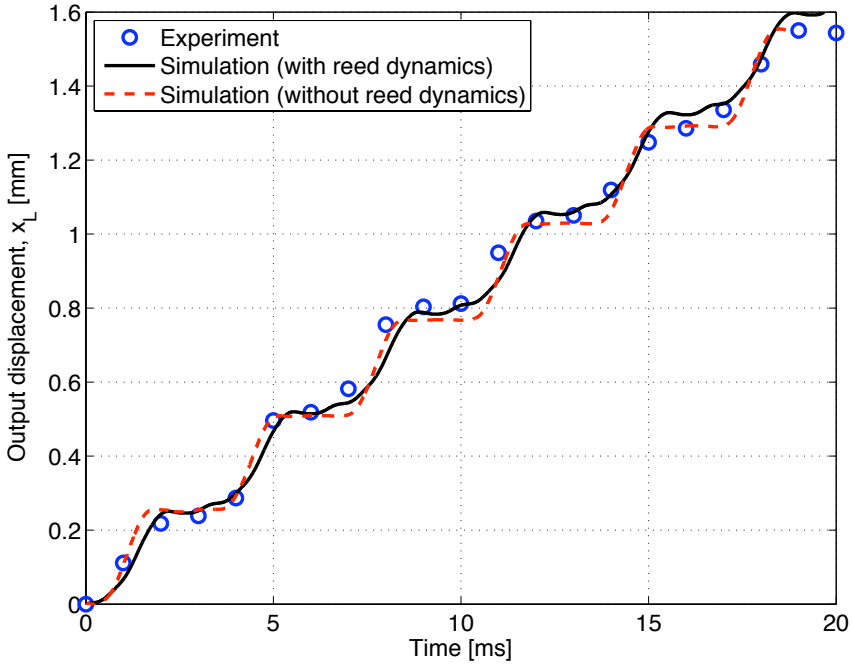

(b) Pumping frequency = 300 Hz

Figure 5.3: Comparison of measured output shaft displacement with simulation results, with and without reed valve dynamics

5.2 Sensitivity to pump design parameters

The comparative study in this chapter was carried out by first computing the simulated results of a hybrid actuator using PMN-PT as the driving material. The important geometrical dimensions used are listed in Table 5.1; these values are the same as in the device used for performance tests in Chapter 4. The free strain of the material was assumed to be 1600 ppm, corresponding to ideally induced free strain at 400 V applied voltage. To simplify the analysis and minimize the frequency-dependent effects from non-inertial sources, this strain (and applied voltage) was assumed to be constant over the entire frequency range while the natural frequency of the reed valves was assumed to be 1 kHz.

The importance of stiffness (or mechanical impedance) matching between the driving active material and the pressurized transmission fluid has been shown by earlier researchers (using a static idealized approach) as well as the experimental results of the current research. To recall, the stiffness of the actuator material is given by

$$K_a = \frac{E_a A_a}{L_a}, \quad A_a = \frac{\pi}{4} D_a^2$$

while the stiffness of the pumping chamber has been shown to be

$$K_{ch} = \frac{\beta A_{ch}}{L_{ch}}, \quad A_{ch} = \frac{\pi}{4} D_{ch}^2.$$

Hence, the stiffness of the same active material (i.e. constant E_a) can be altered by changing either D_a or L_a. The effect of changing any parameter, however, is coupled to the rest of the system and affects the performance in several ways. For example, an increase in fluid bulk modulus, β, results in higher pumping chamber stiffness which

Table 5.1: DESIGN SIZING AND MATERIAL PROPERTIES FOR THE BASELINE SYSTEM

Properties	
Free strain	1600 ppm
ρ_0	871 kg/m^3
ρ_a	7900 kg/m^3
ν	31.5 cSt
E_A	15.0 GPa
Dimensions	
L_a, D_a	60 mm, 12 mm
L_{ch}, D_{ch}	2.54mm (100 mils), 31.75 mm (1.25 inch)
L_t, D_t	35.6 mm (1.4 inch), 5.10 mm (0.2 inch)
L_{port}, D_{port}	6.35 mm (0.25 inch), 3.81 mm (0.15 inch)
L_o	50.8 mm (2 inch)
D_o, D_i	14.30 mm (9/16 inch), 6.35 mm (1/4 inch)

can lead to lower induced strain, while decreasing fluid compliance and increasing the frequency bandwidth of the device.

5.2.1 Bulk modulus, β

The bulk modulus of the hydraulic fluid is strongly dependent on the applied bias pressure as well as the entrained air volume [257, 263]. The effects of changing

bias pressure have been clearly shown in the test results for both actuators described in the earlier chapters. When simulated with the set of parameters in Table 5.1, we once again observe the frequency shift with change in compliance of the fluid, everything else remaining the same [Figure 5.4(a)]. The maximum output velocity was calculated to be 430 mm/s (16.9 inch/s) corresponding to 650 Hz pumping frequency. We considered this as the baseline configuration and all future velocity performance values were compared to the peak velocity, v_{max} = 430 mm/s; the *velocity ratio* is defined, in this case, as the ratio between the measured velocity v and peak baseline velocity i.e. $velocity\ ratio = v/v_{max}$. The maximum value of bulk modulus (β_{max}) of the hydraulic oil in the absence of any entrained is specified as 260 ksi; this value was used to non-dimensionalize the varying values of bulk modulus used in our simulation studies.

The results of the simulation clearly show the effect of bulk modulus, and hence, fluid compliance, on the output velocity (Figure 5.4(a)). As the value of bulk modulus is increased, the peak response location shifts to a higher frequency and the value of output velocity also increases. While the former effect is due to the increase of the stiffness of the fluidic subsystem, the latter effect is mainly due to lesser energy being wasted in compressing the fluid rather than accelerating it in every cycle.

When the velocity ratios are plotted at three different frequencies (400 Hz, 600 Hz and 800 Hz), shown in Figure 5.4(b), we notice that the improvement in output performance starts to saturate beyond a certain value of bulk modulus, β. At low pumping frequencies, the saturation occurs is noted to occur at much lower value of β/β_{max}; this supports the assumption that output performance of the hybrid actuator,

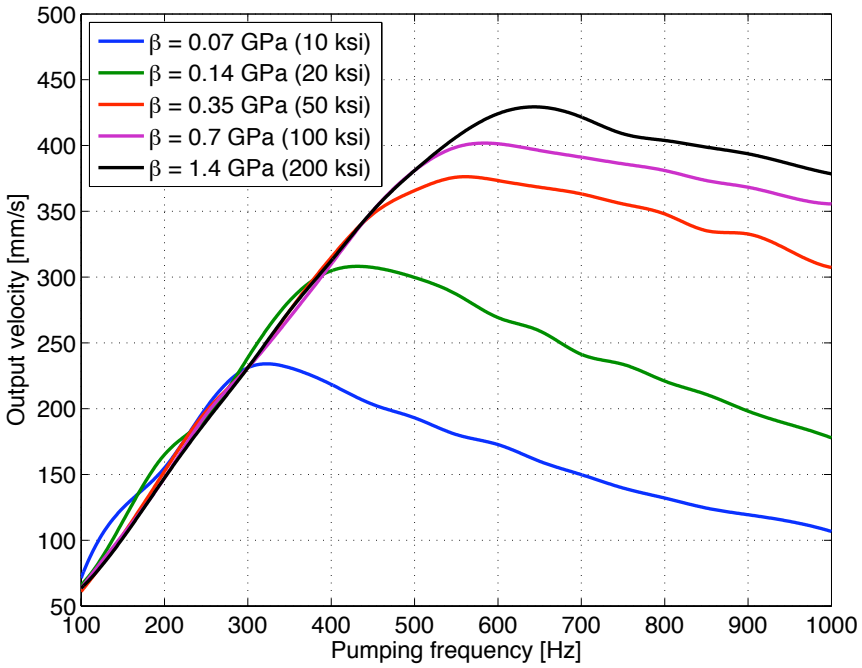

(a) Output velocity at different pumping frequencies

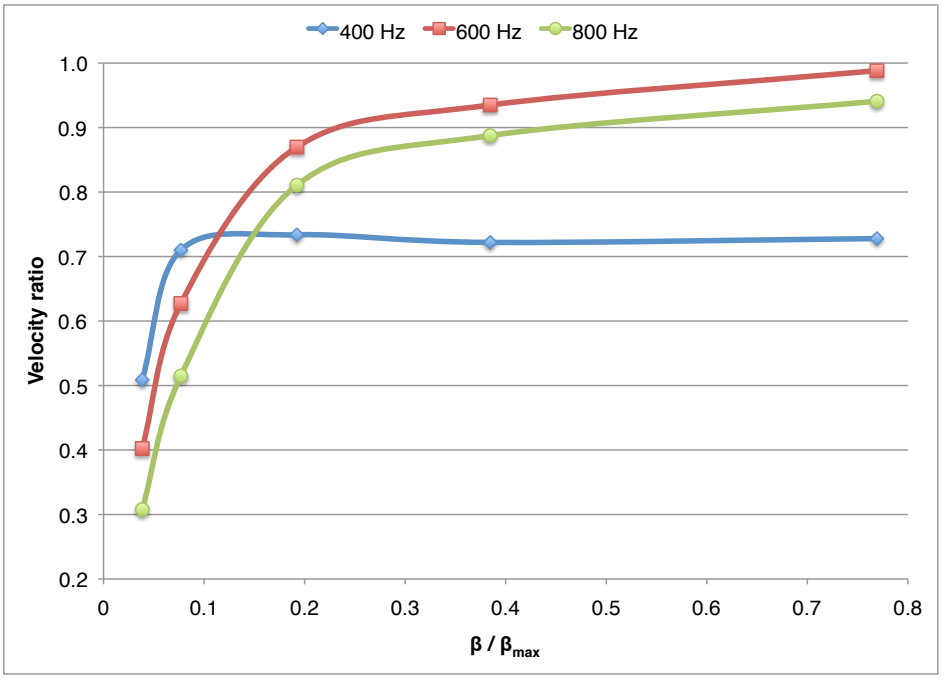

(b) Velocity ratio as a function of bulk modulus

Figure 5.4: Output performance for baseline configuration

in terms of peak operating frequency, is strongly dependent on the fluid bulk modulus, which, in turn, is a function of the applied bias pressure and entrained air.

This result can be used to determine the optimal range of bias pressures to be applied to the fluidic system in order to achieve desired performance at a certain range of pumping frequencies. In order to account for mechanical failure of the body parts and fluid sealing techniques, the mechanical design of the actuator becomes more complicated when the system pressure is increased. Smaller and lighter components can be used if the system pressure is maintained at a lower value. Moreover, because the bias pressure in the fluid directly affects the preload on the active stack/rod, especially in the case of magnetostrictives, an optimum value should be chosen to extract maximum induced strain from the driving material.

5.2.2 Actuator length L_a

The length of the active material is one of the key factors affecting the performance of the hybrid actuator. Increasing the length of the active stack/rod results in a proportional increase in the free displacement of the solid-fluid interface, thus leading to possible gains in volumetric displacement of the transmission fluid [Equation 4.2]. However, the stiffness of the stack is inversely proportional to the active length and hence, the force exerted by the material remains unchanged.

The results of numerical simulation with two different stack lengths, $L_a = 80$ mm and $L_a = 50$ mm, have been plotted in Figure 5.5(a) and Figure 5.5(b) respectively. The results at lower values of fluid bulk modulus, $\beta < 0.35$ GPa (50 ksi), show a

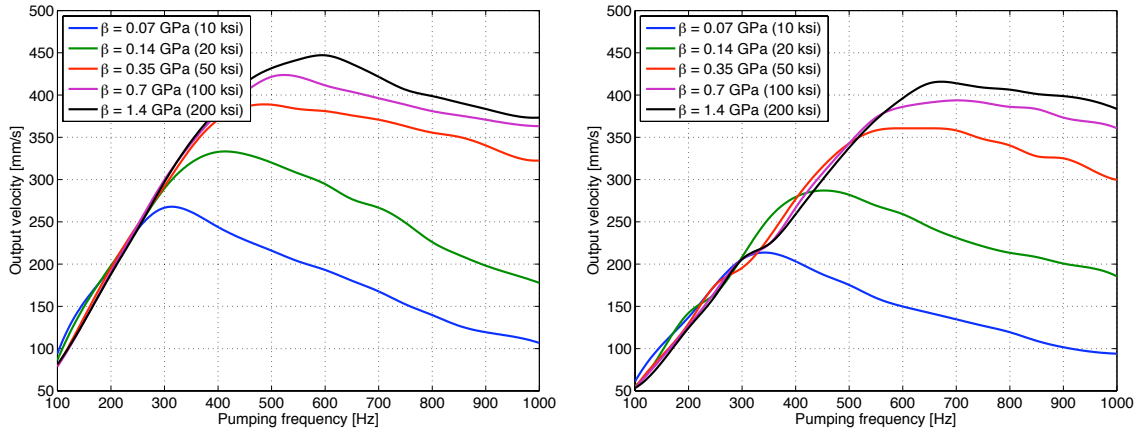

(a) $L_a = 80$ mm

(b) $L_a = 50$ mm

Figure 5.5: Output performance for two different active stack lengths

greater improvement in output velocity with increase in actuator length L_a when compared to the increase at higher bulk moduli. A reason for this behavior might be the sensitivity of the response to the stiffnesses of the actuating rod, K_a, and the fluid pumping chamber, K_{ch}.

A plot of the peak velocities calculated for the two stack lengths, along with the baseline case, is shown as a function of the fluid bulk modulus in Figure 5.6(a). The increase in output velocity with stack length and bulk modulus is expected, because of the increase in stack displacement per cycle and decrease in losses arising from fluid compliance. However, when we plot the ratio of peak velocities observed at the different bulk moduli versus the ratio of stiffnesses, K_{ch}/K_a, we see from Figure 5.6(b) that the results for all the three stack lengths ($L_a = 50$, 60, 80 mm) collapse on top of each other. This suggests that the blocked force of the actuating material (blocked force = elastic modulus $\times$ free strain $\times$ cross-sectional area), which is independent of the length, is a primary driving factor for the actuator. The greatest change

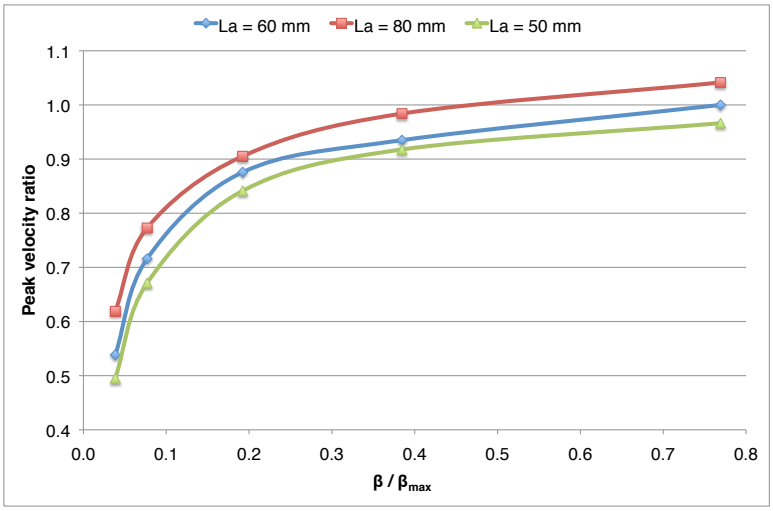

(a)

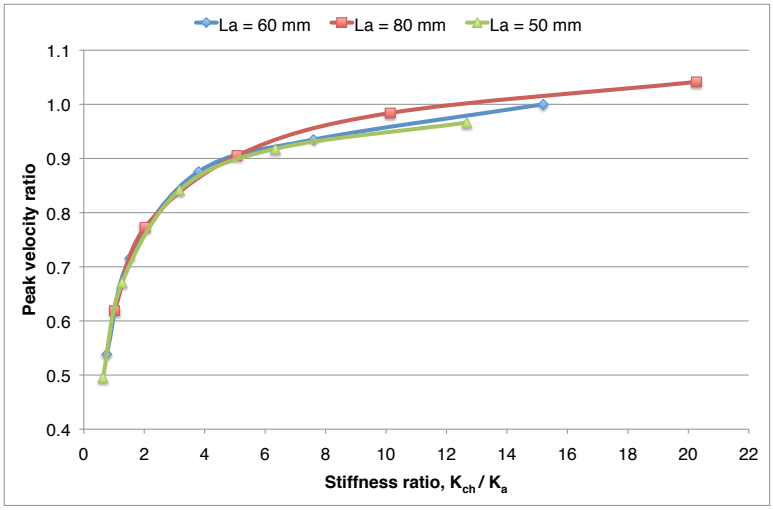

(b)

Figure 5.6: Comparison of peak velocities for different active stack lengths

in peak velocity (almost 40 %) was observed when the stiffnesses are comparable ($1 < K_{ch}/K_a < 5$), whereas the change in velocity beyond this was much lower (< 10 %). A reason for this behavior is that for a lower range of *stiffness ratios*, there is both an improvement in impedance matching between the driving active material and the driven fluid for the same actuator blocked force, as well as lower fluid pressure losses. Note that although it was predicted by previous research [27, 185] that maximum electro-mechanical conversion efficiency should be obtained when $K_{ch} = K_a$, those analyses were carried out for a completely blocked pumping chamber with no fluid flow and are not directly applicable for actual pump operation with flow in and out of the pumping chamber. For very high bulk moduli, there in no appreciable change in the actual strain induced during pump operation and the performance gains are only due to the lower losses from fluid compliance.

5.2.3 Actuator diameter, D_a

The actuator diameter is another key factor affecting the performance of the actuator. Since the stiffness of the active material is proportional to its cross-sectional area, the blocked force of the active stack/rod is strongly dependent on the diameter, D_a. Hence, everything else remaining unchanged, a smart stack/rod of higher diameter can apply greater force to pressurize the fluid in the moving chamber and move it through the manifold. The obvious effect of changing D_a is a change in output velocity of the hybrid actuator.

Simulations were carried out for two additional values of D_a (10 mm and 15

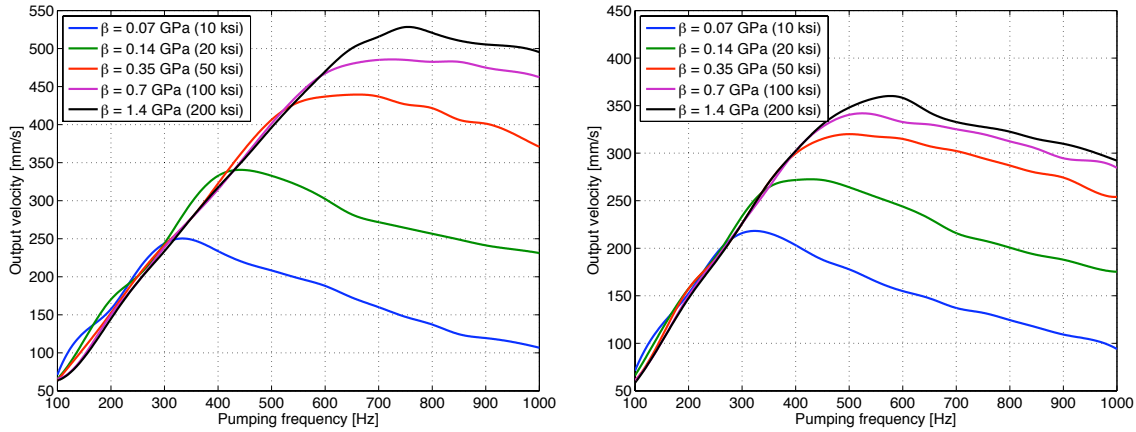

(a) $D_a = 15$ mm

(b) $D_a = 10$ mm

Figure 5.7: Output performance for two different active stack diameters

mm), and the results are shown in Figure 5.7. The maximum output velocities were found to be 358 mm/s, 429 mm/s and 528 mm/s for 10 mm, 12 mm and 15 mm diameters respectively. The frequencies at which the peaks occurred were seen to shift to higher frequencies with increasing D_a. When plotted with bulk modulus as the independent variable (Figure 5.8(a)), we can see the improvement in output performance with increase in both stack diameter and bulk modulus. Unlike the previous comparative study with varying stack length, L_a, the blocked force of the active element varies as the square of the stack diameter, D_a, leading to completely different actuation characteristics when plotted as a function of the stiffness ratios (Figure 5.8(b)).

5.2.4 Pumping chamber diameter, D_{ch}

The pumping chamber diameter, D_{ch}, which is also equal to the pumping piston diameter, governs the amount of fluid that is displaced in every actuation cycle. It

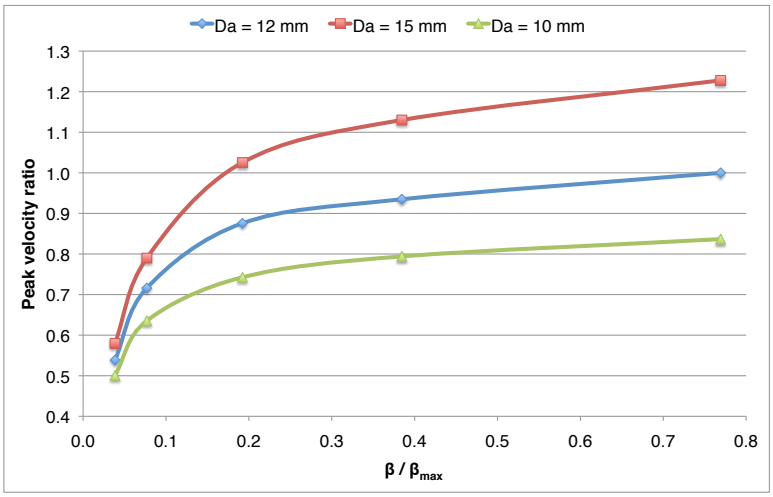

(a)

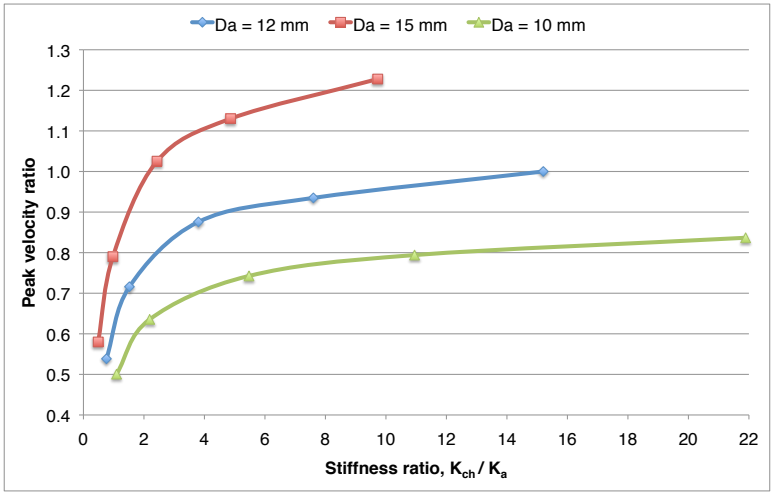

(b)

Figure 5.8: Comparison of peak velocities for different active stack diameters

also directly controls the stiffness of the fluid pumping chamber, K_{ch}, and is, thus, one of the main factors directly affecting the opposing force on the active material and the frequency at which peak output velocity is observed.

The simulation results with two different chamber diameters, 1.5 inch and 1.0 inch, plotted in Figure 5.9, show a huge difference in output velocity of the hybrid actuator. For the higher values of bulk modulus, the peak velocities with the smaller chamber are nearly 40 % more than that with the larger chamber, and occur at much higher pumping frequencies. This difference, however, is much less at lower values of β and at lower pumping frequencies. The plots with stiffness ratio as the independent variable are similar to those with varying D_a, except that better results are noted with lower chamber diameter (which imply lower forces opposing active stack motion). Although the results suggest that a smaller chamber diameter is more suited for the particular stack size considered in these calculations, there are practical limits on the mechanical design; the chamber has to accommodate the reed ports for intake and exhaust, hence there are lower bounds on the usable geometry.

5.2.5 Manifold passage diameter, D_t

The size of the manifold tubing, D_t, is also an important consideration, since it affects pressure losses due to both inertial and viscous effects. The change in volume flow rate, Q, through the tube depends on the product of the cross-sectional area, A_t, and fluid pressure difference, ΔP. Hence, the change in flow rate will be much faster if a tubing of greater area is used. The viscous losses are also lower for higher

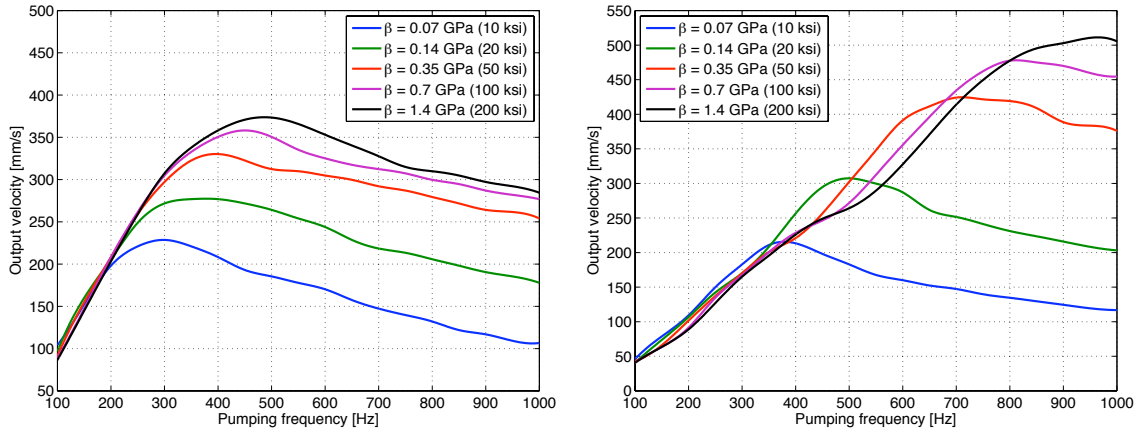

(a) D_{ch} = 1.5 inch

(b) D_{ch} = 1.0 inch

Figure 5.9: Output performance for two different pumping chamber diameters

A_t, as seen in Equation 3.26. On the other hand, the pressure change is inversely proportional to A_t (Equation 3.29); hence, smaller cross-sectional area is desirable for faster rise in manifold fluid pressure. Due to these opposing effects, it is difficult to choose a particular tubing size during the mechanical design of the manifold. To study the effect of D_t, the calculated peak output velocities for three different values (D_t = 0.1, 0.3, 0.4 inch) were plotted along with the baseline design (D_t = 0.2 inch) in Figure 5.11(a). The numerical simulations were carried out at five different values of bulk modulus, β.

From the results, we see that the smallest tubing diameter has worst performance in terms of output velocity. Though the calculated velocity initially rises with increase in D_t, there is an optimum value of D_t beyond which the performance starts to degrade once again. The negative effects at higher tubing diameters can be alleviated, however, by increasing the bulk modulus of the fluid as seen in Figure 5.11(b).

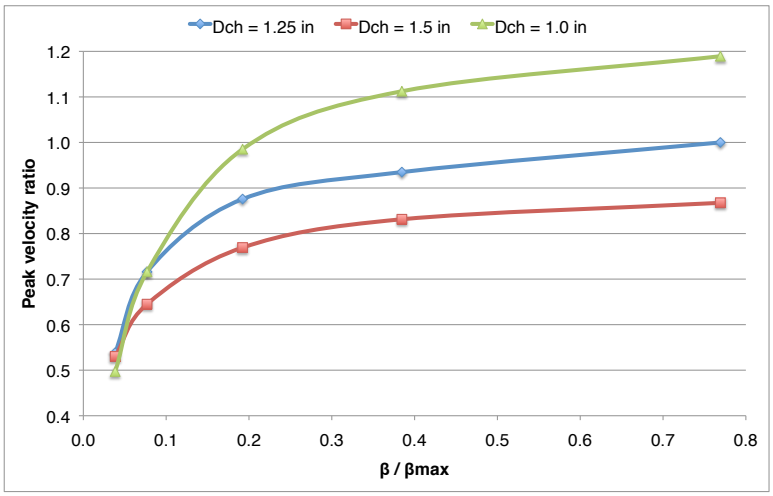

(a)

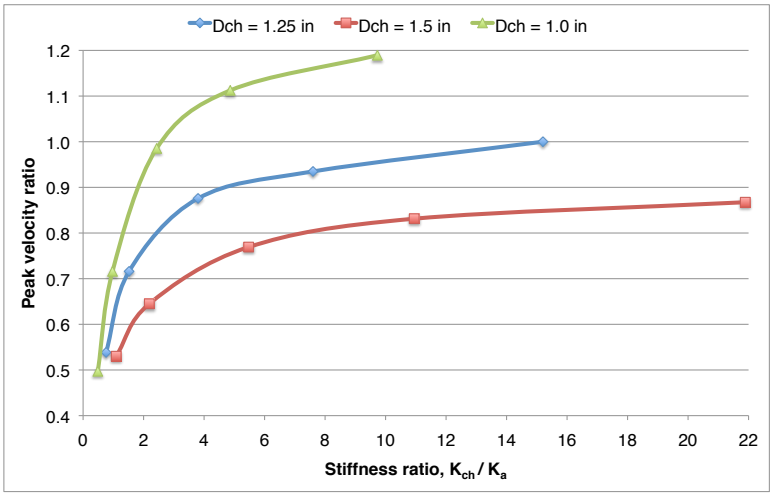

(b)

Figure 5.10: Comparison of peak velocities for different pumping chamber diameters

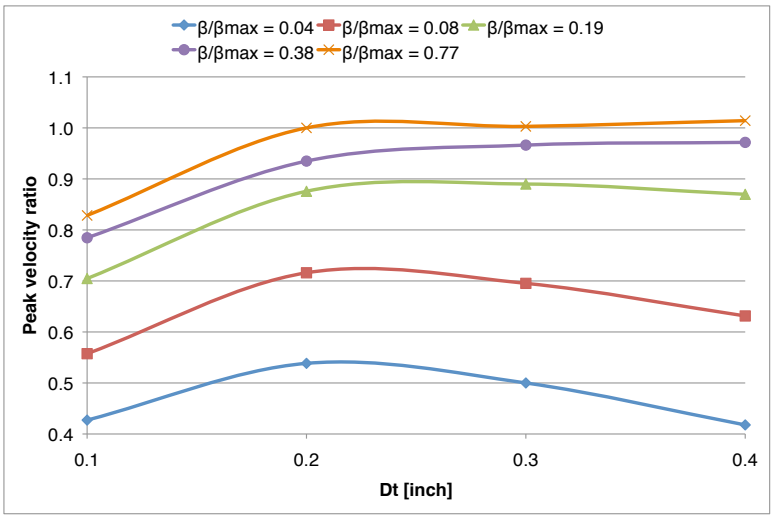

(a)

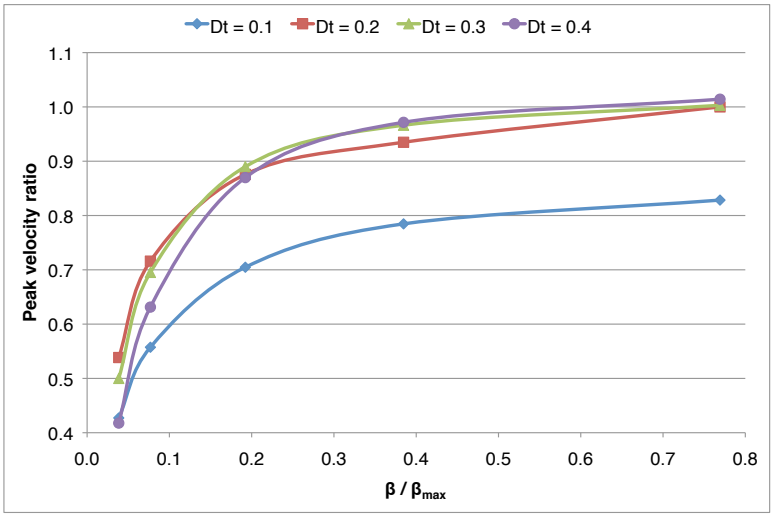

(b)

Figure 5.11: Peak velocity ratios for different tubing diameters

Hence, we can conclude that the selection of the manifold geometry is also dependent on the physical properties of the fluid as well as the dimensions of the pumping chamber.

5.3 Conclusions

In this chapter, we compared the results of simpler model formulations that neglected the input frequency response, fluid inertia and reed valve dynamics. Each of these features results in added complexity in the model and greater numerical computation loads. The importance of including each of these features in the overall formulation was shown by comparing the results of previously derived models with experimental measurements, where we noticed large deviations from the experimental measurements of actuator performance for the simplified models.

A study of the effects of certain physical properties and geometrical dimensions of the hybrid electro-hydraulic actuation system was also presented in this chapter. Results show that the physical properties and geometrical sizes are intricately connected, and design of the overall actuator requires optimal selection of all these. This helped us to identify the parameters that affect the output performance, and hence, optimize the actuator design.

Chapter 6

Conclusions and Future Work

6.1 Summary of research

The design, test and modeling of a compact smart material based compact hybrid electro-hydraulic actuator was described in this dissertation. The basic motivation for developing the hybrid smart actuation concept was to increase the energy density and operational bandwidth of actuators based on active materials. The overall design combines the high energy density of magnetostrictive and electrostrictive materials with the power transmission versatility of a hydraulic system. The operation of the actuator was based on the high frequency extension/contraction of the active material actuated by an electric or magnetic field which, in turn, drove a pressurized hydraulic fluid through a manifold to an output device. The oscillatory action of the driving force was converted to unidirectional fluid flow rate by using a set of passive reed valves to perform frequency rectification. This configuration converted the high frequency, small displacement motion of the active material to low frequency, high stroke motion of the output device connected to the fluidic system.

The first prototype hybrid actuator was operated using the giant magnetostrictive material Terfenol-D ($Tb_{0.3}Dy_{0.7}Fe_{1.92}$) as the driving element and tests were performed to measure the output performance. Two different Terfenol-D rods were used; the first one was 51 mm (2 inch) long with 12.7 mm (0.5 inch) diameter, while the

second one was 102 mm (4 inch) long with 12.7 mm (0.5 inch) diameter. Both the rods were laminated (5 laminations) to minimize the effects of eddy currents. Passive reed valves made of spring steel were used to rectify the fluid flow initiated by cyclic motion of the Terfenol-D rods. A hydraulic cylinder with 19.05 mm (3/4 inch) bore and 6.35 mm (1/4 inch) stroke was used as the output device. The pumping frequency was varied by controlling the electrical input signal to the magnetizing coil. The displacement of the output shaft was measured using an LVDT and the mean velocity was computed as the slope of a linear fit to the displacement data. Tests, without load and with externally attached load, were carried out to measure the maximum flow rate and the blocked force of the actuator respectively. Dynamic tests, with only the driving rod in the pump body, were also performed to characterize the strain and magnetic flux variation with frequency; this set of tests involved frequency sweeps carried out at different control voltages and the induced strain and magnetic flux density in the respective Terfenol-D rods were measured.

A non-linear time-domain model was formulated for the hybrid actuators designed and tested in our laboratory. The active material was modeled using linearized quasi-static equations, because the natural frequency of this section was found to be much higher than our frequency range of interest. The model took into account the motion of the pumping piston head mass assembly and the output shaft, along with any load mass, by considering them as individual SDOF systems and applying the governing force-balance equations. Friction in the output hydraulic cylinder was represented using the Karnopp model. Further, compressibility of the fluid in the pumping chamber, the high pressure driving side and the manifold tubing was taken

into account by incorporating the bulk modulus of the fluid. A lumped parameter approach was used to represent coupled inertia and compliance of the hydraulic fluid in the long manifold passages and the low-pressure driven side of the output cylinder. In order to model the continuously varying openings of the passive reed valves in contrast to on-off type valves, two non-dimensional dynamic variables were introduced to express the opening of the reed valves as a function of the time-varying pressure difference across the reed ports. This feature allowed us to simulate the frequency dependent behavior of the output piston motion and also captured the back flow through the pressure-dependent passive valves. Two-dimensional CFD models with fluid-structure coupling were used for the first time to estimate the critical pressures required for opening the reed valves in these hybrid devices, while their dynamic response characteristics were obtained from empirical results. The pressure losses incurred in the manifold passages were also computed by applying CFD to three-dimensional models of the respective flow paths. The models for fluid flow though these valve ports included pressure losses due to inertia effects as well as minor losses. The bandwidth of the power amplifier and the frequency response of the magnetic/electric circuit were also included in the overall system model. Simulations were carried out and results were compared with experimental data from Terfenol-D pump tests to validate the model.

A second-generation hybrid actuator using the single crystal electrostrictive material PMN-32%PT as the driving element and hydraulic oil as the working fluid was then designed. Two PMN stacks, each 12 mm in diameter and 30 mm long, were aligned end-to-end to obtain one single driving element and unipolar sinusoidal

voltage with frequencies ranging from 100 Hz to 1 kHz was used to actuate the stacks. The initial mechanical design was carried out by studying the effects of different physical parameters and pump geometry using the simple idealized analytical model. Dynamic tests with the PMN stacks in the pump body were carried out to characterize the behavior of the pre-stressed active material at high actuation frequencies in the absence of fluid loads. The axial velocity of the pump piston was also measured under similar conditions in order to detect any non-uniformity in the pumping motion. Tests at no-load, and with external loads, were carried out to evaluate the overall actuator performance for unidirectional motion of the output piston. While the no-load tests yielded the maximum possible volumetric flow rates under any combination of test conditions, the load tests allowed us to calculate the blocked force of the actuator. The peak velocity of the output shaft was measured to be 330 mm/s (13 in/s), corresponding to a volume flow rate of 42.5 cc/s, and was obtained at pumping frequencies between 600 Hz and 800 Hz, while the blocked load was around 63 N (14.1 lbf). The maximum operational efficiency was almost 14 %, which was much higher than results from the earlier prototype with magnetostrictive rods. These results were compared with simulation data, under no-load and externally loaded conditions, to validate the non-linear time-domain model developed earlier.

Studies were also carried out to justify the inclusion of certain features in the comprehensive model, namely, frequency response of input, inertia of the fluid in manifold passages, and dynamics of the reed valves. The numerical simulation results in the absence of these physical phenomena show large deviations from the experimental measurements of actuator performance. A comparison of the effects of different

actuator design parameters, mainly those affecting the stiffnesses of the driving and driven elements, was also reported. Results show that the physical properties and geometrical sizes are intricately connected, and design of the overall actuator requires optimal selection of all these parameters.

Maximization of the output performance of such a hybrid electrohydraulic system requires operation of the smart material at very high frequencies. Several challenges exist to operate the pump at high pumping frequencies, some of which are listed as follows:

(i) Inertia and compliance of the fluidic system

(ii) Characteristics of the input electrical and/or magnetic circuit

(iii) Dynamics of the valve system

(iv) Sealing of the fluidic subsystem to minimize leakage

(v) Hysteresis and self-heating

The physics-based model derived in this dissertation takes a macroscopic look at the operation of the hybrid pump and combines it with the dynamics of the different sections of the output using a time-domain approach. This allows the engineer to get an accurate measure of a particular design without actually building and testing a prototype by using easily obtainable material property values and even allows for optimizing the design. Important physical variables in different sections of the actuation system were identified and the equations governing their time rate of change were derived.

6.2 Future work

Availability of smart materials in large sizes is essential to building full-scale versions of the hybrid electrohydraulic actuator that can replace currently used electrical or hydraulic drives.

Though the model formulated in this thesis does a very good job at calculating the performance of the hybrid actuator built using various smart materials over a large frequency range and varying loading conditions, improvements can be made to obtain a better and more comprehensive model. Some possible ideas are as follows:

- The induced strain in the active material varies non-linearly in reality, especially when the material is actuated over its entire range. A complete model of the active material that accurately reflects the induced strain behavior should be developed for more accuracy; such a model should take into account the operational dynamics by incorporating quantities like the strain rate and hysteretic behavior. In our formulation, the linearized model was deemed sufficient in our formulation because it was simpler to implement and reduced the computational loads that usually accompany the material models. The mechanical and electrical properties of smart materials, especially magnetostrictives and electrostrictives, have been shown to be highly dependent on the mechanical stresses and electro-magnetic fields applied; these can be included in the model for a more accurate representation of material physics.

- An accurate estimation of the bulk modulus is extremely important and can be done by measuring pressure at multiple sites in the actuator, especially the

pumping chamber. This might be very difficult in practice, especially in a device of such small dimensions. Some further refinements to the analysis could be made if additional fluid pressure measurements were made at certain alternate locations (e.g. discharge port, driving side of output cylinder, intake manifold) during pump operation and compare the data with simulated results. However, it should also be kept in mind that any pressure tap will act as a source of compliance in the fluidic system and reduce the effective bulk modulus. Prior characterization of the working fluid can also be used to derive a mathematical form of the dependence of bulk modulus on fluid pressure.

- A complete 3-D coupled simulation of the reed valve port can be carried out to obtain accurate values of the loss coefficients therein. The pressure loss in the reed ports, even when fully open, are significant and there are ways to reduce them by efficient mechanical design and optimization for specific pressures and flow rates; the coupled interactions involved during high frequency oscillations of a thin metal reed in a highly viscous fluid have to be investigated.

- Modeling of friction in the output hydraulic cylinder can be done using more involved schemes, especially dynamic approaches. A complete experimental study of the force - displacement characteristics of the hydraulic output cylinder are required to estimate the higher-order coefficients and apply such advanced models.

Appendix A
Simulation code for hybrid actuator
Main program

```
#include <iostream.h>
#include <stdio.h>
#include <math.h>
#include <stdlib.h>
#include "common.h"

// Fluid assumed as compressible in exhaust line
// Fluid inside driven side of piston assumed compressible
// Transmission line model applied to driving line, exhaust port and output cyl (lumping by length)
// Mass flow rate to/from pumping chamber, volume flow rate in tubes
// Reed valve opening modeled using 2nd order ODE

int main(int narg)
{

/* a: actuator, ch: chamber, p: piston, tube: tubing, l: load, acc: accumulator */
FILE *fop1, *fop2;// Input & Output files
double La, Lch, Lo, Lacc, Lport, Lporto;
// Lengths (actuator, chamber, output cylinder, accumulator, reed ports)
double Ltube, Ltubeo; // Tube lengths (central, output side)
double Ma, Mp, Ml0, Ml; // Masses
double Cp, Cl; // Damping cofficients
double Ka, Kch, Ks, Kd, Kacc; // Stiffnesses
double KLvalveo, KLvalvei, KLbend, KLentry, KLchA = 0, KLchB = 0;
// Loss coeff (reed valves, pipe bend, entry, chamber[from cfd])
double da, dch, dout, din, dtube, dtubeo, dport, dacc; // Diameters
double Yr, rhor, Lr, br, tr, wnreed, etareed = 0.71; // Reed valve properties and dimensions
double rhoa, Ya, Da; // Material properties
double Vpeak = 100, Vac, Vdc, gain = 1, tau = 1e-5;
double Rtube, Rtubeo, Rport, Rcyl;
// Visocus loss coefficients (tubing, tube output, ports, output cylinder)
double wn, avgvl; // Natural frequency of pumping section, Average load velocity

double f, fsim, w, dt; // Frequencies (actuation, simulation, angular), Time step (simulation)
double ncycles; // Number of cycles
long int i, n; // Simulation counter, total number of steps

// States & other variables
double *t, *V, *xp, *vp, *xl, *vl, *Pacc, *Pch, *Ph, *Mdotout, *Mdotin, *roh, *rol, *rohd, *rold;
double *Php, *Qhp, *Pht, *Qht, *Pho, *Qho, *Plo, *Qlo;
double Vapp, delP, *Pl, *Ql, *Pthi, *Ptho, *Ptpo, *Qthi, *Qtho, *Qtpo, *Qh, *ropenh, *ropenl, *Sblock;

double sysode(int *,double *,double *,double *,double,double *,double *,double *,
                            double *,double *,double *,double *);

//**********   Terfenol-D **********
/* // Diameters
da = 0.5 * in2m; dch = 1.5 * in2m; dout = 0.75 * in2m; din = 0.25 * in2m;
dtube = 0.20 * in2m; dtubeo = 0.26 * in2m; dport = 0.12 * in2m; dacc = 0.5 * in2m;
// Lengths
La = 2 * in2m; Lch = .5e-3; Lo = 2.0 * in2m; Lacc = 0.5 * in2m;
Ltube = 1.7 * in2m; Ltubeo = 0.5 * in2m; Lport = Ltubeo; Lporto = 0.2 * in2m;
// Properties
nu = 21.0e-6; rho = 860.0;
Ya = 30e9; rhoa = 9250; freestrain = 1600e-6; Da = freestrain / Vpeak; // d_33 // TerfD
// Reed properties
Yr = 180e9; rhor = 7800; Lr = 0.45 * in2m; br = 0.2 * in2m; tr = 4e-3 * in2m; etareed = 0.71;
```

```
// Masses
Mp = 0.2; Ml0 = 0.1;
// Stiffnesses
Ks = 10.8e6; Kd = platestiffness(180e9,1.55*in2m/2,dch/2,.002*in2m);//1.8e3; */
//**********  PMN ***********
// Diameters
da = 12e-3; dch = 1.25 * in2m; dout = 0.5625 * in2m; din = 0.25 * in2m;
dtube = 0.2 * in2m; dtubeo = 0.2 * in2m; dport = 0.15 * in2m; dacc = 0.5 * in2m;
// Lengths
La = 60e-3; Lch = 100e-3 * in2m; Lo = 2.8 * in2m; Lacc = 0.5 * in2m;
Ltube = 1.4 * in2m; Ltubeo = 0.5 * in2m; Lport = Ltubeo; Lporto = 0.1 * in2m;
// Physical properties
nu = 31.5e-6; rho = 871.0;
Ya = 15e9; rhoa = 7900; freestrain = 1200e-6; Da = freestrain / Vpeak; // d_33 // PMN
// Reed dimensions
Yr = 200e9; rhor = 7800; Lr = 0.30 * in2m; br = 0.28 * in2m; tr = 5e-3 * in2m; etareed = 0.71; // 1.25in
// Yr = 200e9; rhor = 7800; Lr = 0.35 * in2m; br = 0.30 * in2m; tr = 5e-3 * in2m; etareed = 0.71; // 1.50in
// Masses
Mp = 0.23 * .454; Ml0 = 0.07;
// Stiffnesses
Ks = 1.6e6; Kd = platestiffness(180e9,1.3*in2m/2,dch/2,.002*in2m);//1.8e3;

cout << "\nEnter load [kg]: "; cin >> Ml;
// Properties
beta = 50e3 * psi2Pa; Pbias = 0 * psi2Pa;
// Cross sectional areas
double Aa = csa(da), Ach = csa(dch), At = csa(dtube), Ato = csa(dtubeo), Aport = csa(dport);
double Ao = csa(dout) - csa(din), Aacc = csa(dacc);
// Masses
Ma = rhoa * Aa * La;
// Stiffnesses
Ka = (Ya * Aa) / La; Kch = (beta * Ach) / Lch; Kacc = (1e-3 * beta * Aacc) / Lacc;
// Damping coefficients
wn = sqrt((Ka + Kch + Kd + Ks) / Mp); Cp = 2 * 0.01 * wn * Mp; Cl = 0;
f_s = 3 * lbf2N; f_d = 1 * lbf2N; vmin = .001; vs = 10.0e-3; // Karnopp model parameters
// Loss coeficients
KLvalveo = 15; KLvalvei = 10; KLbend = 0.75; KLentry = 0.75;
// Reed valve properties
double Popen = 5 * psi2Pa, Pclose = Popen;
double mr = (rhor * br * tr) + (.25 * pi * rho * br * br), Ir = (br * tr * tr * tr) / 12;
wnreed = (Yr * Ir) / (mr * Lr * Lr * Lr * Lr); wnreed = 1.875 * 1.875 * sqrt(wnreed);
etareed = 4;// wnreed = 2 * pi * 200;
// Prestrain due to prestress & bias pressure respectively
double xprestrain = 0, xprebias = -(Pbias * Ach) / Ka; xpretotal = xprestrain + xprebias;
// Simulation parameters
cout << "\nEnter actuation frequency [Hz]: "; cin >> f; w = 2 * pi * f;
fsim = 1.0e6; ncycles = 10; rmin = 0.0001;
dt = 1.0 / fsim; n = int((ncycles * fsim) / f);
// vmin = vmincalc(f,100,0.001,300,10e-3); vs = vmin * 10;

int nlumpp = 2, nlumpt = 8, nlumpto = 2, nlumpo = 2; // #lumps (port, tube, output piston)
int npstates = 14, nstates = npstates + 2*nlumpp + 2*nlumpt + 2*nlumpto + 2*nlumpo;
// #states (primary, total)
int j, k, dblsize = sizeof(double); double tempt, *tempx, *x, *xdot, *rk;

t = (double *)malloc(dblsize * n); // Time
// States (memory allocation)
V = (double *)malloc(dblsize * n); // Applied voltage
xp = (double *)malloc(dblsize * n); // Pumping piston displacement
vp = (double *)malloc(dblsize * n); // Pumping piston velocity
xl = (double *)malloc(dblsize * n); // Output displacement
vl = (double *)malloc(dblsize * n); // Output velocity
Pacc = (double *)malloc(dblsize * n); // Accumulator pressure
Pch = (double *)malloc(dblsize * n); // Pumping chamber pressure
Ph = (double *)malloc(dblsize * n); // Driving side pressure
Mdotout = (double *)malloc(dblsize * n); // Exhaust flow rate
Mdotin = (double *)malloc(dblsize * n); // Intake flow rate
roh = (double *)malloc(dblsize * n); // Exhaust valve opening ratio, actual
```

```
rol = (double *)malloc(dblsize * n); // Intake valve opening ratio, actual
rohd = (double *)malloc(dblsize * n); // Exhaust valve opening ratio derivative
rold = (double *)malloc(dblsize * n); // Intake valve opening ratio derivative
Php = (double *)malloc(dblsize * nlumpp); // Driving side port pressure
Qhp = (double *)malloc(dblsize * nlumpp); // Driving side port flow rate
Pht = (double *)malloc(dblsize * nlumpt); // Driving side tubing pressure
Qht = (double *)malloc(dblsize * nlumpt); // Driving side tubing flow rate
Pho = (double *)malloc(dblsize * nlumpto); // Driving side tubing output pressure
Qho = (double *)malloc(dblsize * nlumpto); // Driving side tubing output flow rate
Plo = (double *)malloc(dblsize * nlumpo); // Output piston driven side pressure
Qlo = (double *)malloc(dblsize * nlumpo); // Output piston driven side flow rate
// Other variables
Pl = (double *)malloc(dblsize * n); // Output piston driven side pressure
Ql = (double *)malloc(dblsize * n); // Flow rate between piston & accumulator
Pthi = (double *)malloc(dblsize * n); // Driving side tubing entry pressure
Qthi = (double *)malloc(dblsize * n); // Driving side tubing entry flow rate
Ptho = (double *)malloc(dblsize * n); // Driving side tubing exit pressure
Qtho = (double *)malloc(dblsize * n); // Driving side tubing exit flow rate
Ptpo = (double *)malloc(dblsize * n); // Driving side port exit pressure
Qtpo = (double *)malloc(dblsize * n); // Driving side port exit flow rate
Qh = (double *)malloc(dblsize * n); // Driving side entry flow rate
ropenh = (double *)malloc(dblsize * n); // Exhaust valve opening ratio
ropenl = (double *)malloc(dblsize * n); // Intake valve opening ratio
Sblock = (double *)malloc(dblsize * n); // Blocked strain

x = (double *)malloc(dblsize * nstates); // State vector
xdot = (double *)malloc(dblsize * nstates); // Differentiated state vector
tempx = (double *)malloc(dblsize * nstates); // Temporary state vector
rk = (double *)malloc(dblsize * nstates * 4); // Vectors for RK-4 method

double M[4], C[2], K[5], L[8], D[7], A[7], prop[15], ro[2], Vin[2]; int N[5];
t[0] = 0;
N[0] = npstates; N[1] = nlumpp; N[2] = nlumpt; N[3] = nlumpto; N[4] = nlumpo;
M[0] = Ma; M[1] = Mp; M[2] = Ml0; M[3] = Ml;
C[0] = Cp; C[1] = Cl;
K[0] = Ka; K[1] = Kd; K[2] = Ks; K[3] = Kch; K[4] = Kacc;
A[0] = Aa; A[1] = Ach; A[2] = At; A[3] = Ao; A[4] = Aacc; A[5] = Aport; A[6] = Ato;
L[0] = La; L[1] = Lch; L[2] = Ltube; L[3] = Lo; L[4] = Lacc; L[5] = Lport; L[6] = Ltubeo; L[7] = Lporto;
D[0] = da; D[1] = dch; D[2] = dtube; D[3] = dout; D[4] = dacc; D[5] = dport; D[6] = dtubeo;
// Other variables
KLchA = (6*mu*log(dch/dport)) / (pi*Lch*Lch*Lch);
KLchB = .6*rho*((dch*dch)/(dport*dport)-1) / (pi*pi*Lch*Lch*dch*dch);
Rtube = (8 * pi * nu) / (At * At); // Loss coefficient in tubing (per unit length and density)
Rtubeo = (8 * pi * nu) / (Ato * Ato); // Loss coefficient in tubing output (per unit length and density)
Rport = (8 * pi * nu) / (Aport * Aport); // Loss coefficient in ports (per unit length and density)
Rcyl = (8 * pi * nu) / (Ao * Ao); // Loss coefficient in output cylinder (per unit length and density)
// Input characteristics
inputv(Vin,f); Vac = Vin[0]; Vdc = Vin[1];
// Initialize (primary) states
V[0] = 0; xp[0] = xpretotal; vp[0] = 0; xl[0] = 0.005; vl[0] = 0;
Pacc[0] = Pbias; Pch[0] = Pbias; Ph[0] = Pbias; Mdotout[0] = 0; Mdotin[0] = 0;
roh[0] = 0; rol[0] = 0; rohd[0] = 0; rold[0] = 0;
// Initialize other variables
ropenh[0] = 0; ropenl[0] = 0; Sblock[0] = 0;
Pl[0] = Pbias; Pthi[0] = Ph[0]; Ptho[0] = Ph[0]; Ptpo[0] = Ph[0];
Ql[0] = 0; Qthi[0] = 0; Qtho[0] = 0; Qtpo[0] = 0; Qh[0] = 0;
for (j = 0; j < nlumpp; j++){ Php[j] = Ph[0]; Qhp[j] = 0; }
for (j = 0; j < nlumpt; j++){ Pht[j] = Ph[0]; Qht[j] = 0; }
for (j = 0; j < nlumpto; j++){ Pho[j] = Ph[0]; Qho[j] = 0; }
for (j = 0; j < nlumpo; j++){ Plo[j] = Ph[0]; Qlo[j] = 0; }
// Initialize state vector
x[0] = V[0]; x[1] = xp[0]; x[2] = vp[0]; x[3] = xl[0]; x[4] = vl[0];
x[5] = Pacc[0]; x[6] = Pch[0]; x[7] = Ph[0]; x[8] = Mdotout[0]; x[9] = Mdotin[0];
x[10] = roh[0]; x[11] = rol[0]; x[12] = rohd[0]; x[13] = rold[0];
for (j = 0; j < nlumpp; j++){ x[npstates+j] = Php[j]; x[npstates+nlumpp+j] = Qhp[j]; }
for (j = 0; j < nlumpt; j++){ x[npstates+2*nlumpp+j] = Pht[j]; x[npstates+2*nlumpp+nlumpt+j] = Qht[j]; }
for (j = 0; j < nlumpto; j++)
{ x[npstates+2*nlumpp+2*nlumpt+j] = Pho[j]; x[npstates+2*nlumpp+2*nlumpt+nlumpto+j] = Qho[j]; }
```

```
for (j = 0; j < nlumpo; j++)
{ x[npstates+2*nlumpp+2*nlumpt+2*nlumpto+j] = Plo[j];
x[npstates+2*nlumpp+2*nlumpt+2*nlumpto+nlumpo+j] = Qlo[j]; }
// Properties
prop[0] = gain; prop[1] = tau; prop[2] = Da;
prop[3] = KLvalveo; prop[4] = KLvalvei; prop[5] = KLbend;
prop[6] = KLentry; prop[7] = KLchA; prop[8] = KLchB;
prop[9] = Rtube; prop[10] = Rport; prop[11] = Rcyl; prop[12] = Rtubeo;
prop[13] = wnreed; prop[14] = etareed;

// Start time-stepped solution
for(i = 1; i < n; i++){

delP = Pch[i-1] - Pthi[i-1]; ropenh[i] = valveopen(delP,Popen,Pclose); // Exhaust valve opening
delP = Pacc[i-1] - Pch[i-1]; ropenl[i] = valveopen(delP,Popen,Pclose); // Intake valve opening
ro[0] = ropenh[i]; ro[1] = ropenl[i];

t[i] = t[i-1] + dt; Vapp = absval(0.5 * Vpeak * (Vdc - Vac * cos(w * t[i])));
// if (Vapp > Vpeak) Vapp = Vpeak; // Saturation

// Steps for Runge-Kutta Order 4
for(j = 0; j < 4; j++){
tempt = rkmethodt(t[i],dt,j+1); tempx = rkmethodx(j,nstates,x,rk);
Sblock[i] = sysode(N,xdot,tempx,prop,Vapp,M,C,K,A,L,D,ro);
for(k = 0; k < nstates; k++) rk[(j*nstates) + k] = dt * xdot[k];
}
for(k = 0; k < nstates; k++) x[k] = x[k] + (rk[k] + 2*rk[nstates+k] + 2*rk[2*nstates+k] + rk[3*nstates+k])/6;

if(x[3] < xl[0]) { x[3] = xl[0]; x[4] = 0; } // Prevent output undershoot
if(x[3] > Lo) { x[3] = Lo; x[4] = 0; } // Prevent output overshoot
x[10] = valveopenlimit(x[10]); x[11] = valveopenlimit(x[11]); // Bound limits of ropen
if(x[10] <= rmin) x[8] = 0; if(x[11] <= rmin) x[9] = 0;
if((x[10] == 0 && x[12] < 0) || (x[10] == 1 && x[12] > 0)) x[12] = 0; // stop valve motion beyond limits
if((x[11] == 0 && x[13] < 0) || (x[11] == 1 && x[13] > 0)) x[13] = 0; // stop valve motion beyond limits
// Update states
V[i] = x[0]; xp[i] = x[1]; vp[i] = x[2]; xl[i] = x[3]; vl[i] = x[4];
Pacc[i] = x[5]; Pch[i] = x[6]; Ph[i] = x[7]; Mdotout[i] = x[8]; Mdotin[i] = x[9];
roh[i] = x[10]; rol[i] = x[11]; rohd[i] = x[12]; rold[i] = x[13];
for (j = 0; j < nlumpp; j++){ Php[j] = x[npstates+j]; Qhp[j] = x[npstates+nlumpp+j]; }
for (j = 0; j < nlumpt; j++){ Pht[j] = x[npstates+2*nlumpp+j]; Qht[j] = x[npstates+2*nlumpp+nlumpt+j]; }
for (j = 0; j < nlumpto; j++)
{ Pho[j] = x[npstates+2*nlumpp+2*nlumpt+j];
Qho[j] = x[npstates+2*nlumpp+2*nlumpt+nlumpto+j]; }
for (j = 0; j < nlumpo; j++)
{ Plo[j] = x[npstates+2*nlumpp+2*nlumpt+2*nlumpto+j];
Qlo[j] = x[npstates+2*nlumpp+2*nlumpt+2*nlumpto+nlumpo+j]; }
// Calculate other variables
Pl[i] = meanval(nlumpo,Plo); Ql[i] = Qlo[nlumpo-1];// Pl[i] = Plo[0];
Pthi[i] = Php[0]; Qthi[i] = Qhp[0]; Ptho[i] = Pht[nlumpt-1]; Qtho[i] = Qht[nlumpt-1];
Ptpo[i] = Php[nlumpp-1]; Qtpo[i] = Qhp[nlumpp-1]; Qh[i] = Qho[nlumpto-1];
}
avgvl = linearslope(t,xl,n);
printf("\nFrequency = %.1f Hz, Load = %.1f kg (%.1f lbs), Avg velocity = %.3f mm/sec (%.3f in/sec) \n",
f,Ml,Ml*2.2,avgvl*1e3,avgvl/in2m);

cout << "\nFile write .... ";
// Open files to write
fop1 = fopen("results.txt","w+");
for(i = 0; i < n; i++)
fprintf(fop1,"%8.4f %7.2f %7.2f %7.2f %7.3f %10.3f %10.3f %7.1f %7.1f %7.1f %7.1f %7.1f %7.1f %7.1f
%7.3f %7.3f %7.3f %7.3f %7.3f %7.3f %7.3f %6.2f %6.2f %8.3f %8.3f %8.3f %8.3f %7.1f %7.3f %7.3f \n",
t[i]*1000,V[i]*Da*1e6,(xp[i]-xpretotal)*1e6/La,Sblock[i]*1e6,xl[i]*1e3,vp[i]*1e3,vl[i]*1e3,
Pch[i]/psi2Pa,Pthi[i]/psi2Pa,Ptho[i]/psi2Pa,Ph[i]/psi2Pa,Pl[i]/psi2Pa,Pacc[i]/psi2Pa,(Pch[i]-Pthi[i])/psi2Pa,
(Mdotout[i]/rho)*1e6,Qthi[i]*1e6,Qtho[i]*1e6,Ao*vl[i]*1e6,Ql[i]*1e6,(Mdotin[i]/rho)*1e6,Ach*vp[i]*1e6,
ropenh[i],ropenl[i],roh[i]*100,rol[i]*100,rohd[i],rold[i],
Ptpo[i]/psi2Pa,Qtpo[i]*1e6,Qh[i]*1e6);
fclose(fop1);
```

```
fop2 = fopen("simparams.txt","w+");
fprintf(fop2,"Frequency: Actuation = %.1f Hz, Simulation = %.1f kHz \n",f,fsim*1e-3);
fprintf(fop2,"Mean output velocity = %.3f mm/sec\t (%.3f in/sec)\n",avgvl*1e3,avgvl/in2m);
fprintf(fop2,"Material properties: Youngs modulus = %.1f GPa, Free strain = %.0f ppm \n",Ya*1e-9,freestrain*1e6);
fprintf(fop2,"Fluid properties: Bulk modulus = %.1f ksi (%.2f MPa), Density = %6.1f kg/m^3,
Kin viscosity = %.3e Pa-s \n", beta/6895e3,beta*1e-6,rho,nu);
fprintf(fop2,"Input characteristics: Gain = %.2f, Time constant = %.3f ms\n",gain,tau*1000);
fprintf(fop2,"Strain conditions [ppm]: prestrain = %.2f, bias = %.2f",xprestrain*1e6/La,xprebias*1e6/La);
fprintf(fop2,"Others: Pbias = %.3f psi, Popen = %.3f psi \n",Pbias/psi2Pa,Popen/psi2Pa);
fprintf(fop2,"Masses [kg]: Rod/stack = %.3f, Piston (pumping, output)= %.3f %.3f, Load = %.3f\n",Ma,Mp,Ml0,Ml);
fprintf(fop2,"Viscous coefficients [Ns/m]: Piston = %.2f, Load = %.2f\n",Cp,Cl);
fprintf(fop2,"Output piston friction: %.2f  %.2f [lbf], %.2f [in/s] \n",f_s/lbf2N,f_d/lbf2N,vmin/in2m);
fprintf(fop2,"Minor loss coeff: Reed valve = %.2f %.2f, Pipe bend = %.2f, Pipe entry = %.2f,
Chamber = %.4f, %.3f \n",KLvalveo,KLvalvei,KLbend,KLentry,KLchA,KLchB);
fprintf(fop2,"Lengths [in]: Actuator = %.2f, Chamber = %.3f, Tube = %.2f, Output = %.2f, Port = %.2f,
Tube-Piston = %.2f, Port-out = %.2f\n",La/in2m,Lch/in2m,Ltube/in2m,Lo/in2m,Lport/in2m,Ltubeo/in2m,Lporto/in2m);
fprintf(fop2,"Diameters [in]: Actuator = %.2f, Chamber = %.2f, Tubing = %.2f, Tubing out = %.2f, Output
(bore, shaft) = %.3f %.3f, Port = %.2f\n",da/in2m,dch/in2m,dtube/in2m,dtubeo/in2m,dout/in2m,din/in2m,dport/in2m);
fprintf(fop2,"Stiffnesses [N/m]: Actuator = %.2e, Chamber = %.2e, Spring = %.2e, Diaphragm = %.2e,
Accumulator = %.2e\n",Ka,Kch,Ks,Kd,Kacc);
fprintf(fop2,"Number of lumps (port,tube,tubeout,driving side) = %d, %d, %d, %d \n",nlumpp,nlumpt,nlumpto,nlumpo);
fprintf(fop2,"Reed properties: Natural freq = %.3f Hz, Damping coeff = %.3f \n",wnreed/(2*pi),etareed);
fclose(fop2);
cout << "complete. \n";

if(fsim*1e-6 >= 1) printf("Frequency: Actuation = %.1f Hz, Simulation = %.1f MHz \n",f,fsim*1e-6);
else printf("Frequency: Actuation = %.1f Hz, Simulation = %.1f kHz \n",f,fsim*1e-3);
printf("Reed valve natural frequency [Hz] = %.1f \n",wnreed/(2*pi));
printf("Bias conditions: Pressure [psi] = %.0f, Bulk modulus [ksi] = %.1f \n",Pbias/6895,beta/6895000);
printf("Strain conditions [ppm]: prestrain = %.2f, bias = %.2f",xprestrain*1e6/La,xprebias*1e6/La);
printf("Stack size [in]: Height = %.3f, Diameter = %.3f \n",La/in2m,da/in2m);
printf("Chamber size [in]: Height = %.3f, Diameter = %.3f \n",Lch/in2m,dch/in2m);
printf("Output piston size [in]: Bore = %.3f, Shaft = %.3f \n",dout/in2m,din/in2m);
printf("Masses [g]: Rod/stack = %.1f, Piston (pumping, output)= %.1f %.1f, Load = %.1f\n",
Ma*1e3,Mp*1e3,Ml0*1e3,Ml*1e3);
printf("Stiffness [N/m]: Ka = %.3e, Kch = %.3e, Kacc = %.3e, Ks = %.3e, Kd = %.3e \n",Ka,Kch,Kacc,Ks,Kd);
printf("Output piston friction: %.2f  %.2f [lbf], %.2f [in/s] \n",f_s/lbf2N,f_d/lbf2N,vmin/in2m);
printf("Minor loss coeff: Reed valve = %.2f %.2f, Pipe bend = %.2f, Pipe entry = %.2f, Chamber = %.4f, %.3f \n",
KLvalveo,KLvalvei,KLbend,KLentry,KLchA,KLchB);

// Deallocate memory
free(t); free(V); free(xp); free(xl); free(vp); free(vl); free(Mdotout); free(Mdotin);
free(Pacc); free(Pch); free(Ph);
free(Pl); free(Ql); free(Php); free(Qhp); free(Pht); free(Qht); free(Pho); free(Qho); free(Plo); free(Qlo);
free(Pthi); free(Qthi); free(Ptho); free(Qtho); free(Ptpo); free(Qtpo); free(Qh);
free(ropenh); free(ropenl); free(roh); free(rol); free(rohd); free(rold);

return 0;
}

double sysode(int *n,double *ydot, double *y,double *pro,double vapp,double *m,double *c,double *k,
double *a,double *l,double *d, double *ropen)
// pro: properties
// x = [v xp vp xl vl Pacc Pch Ph Mdotout Mdotin roh rol rohd rold Php Qhp Pht Qht Pho Qho Plo Qlo]
{
double g = pro[0], tc = pro[1], d33 = pro[2];
double Klvo = pro[3], Klvi = pro[4], Klb = pro[5], Kle = pro[6];//, KlA = pro[7], KlB = pro[8];
double rtube = pro[9], rport = pro[10], rcyl = pro[11], rtubeo = pro[12], wnr = pro[13], etar = pro[14];
double ma = m[0], mp = m[1], ml0 = m[2], ml = m[3];
double cp = c[0], cl = c[1];
double ka = k[0], ks = k[2], kacc = k[4];
double ach = a[1], at = a[2], ao = a[3], aacc = a[4], ap = a[5], ato = a[6];
double la = l[0], lch = l[1], lt = l[2], lo = l[3], lp = l[5], lto = l[6], lpo = l[7];
double dtube = d[2], dacc = d[4];
double rh = ropen[0], rl = ropen[1];
double r, Klec, xblock, F, v, temp;
// fluid density, loss coeff due to sudden expansion/contraction, blocked disp
int nps = n[0], np = n[1], nt = n[2], nto = n[3], no = n[4], ns = nps+2*np+2*nt+2*nto+2*no;
```

```
// #primary states,#lumps(port,tubing,output),#total states

ydot[0] = (g * vapp - y[0]) / tc; // V

ydot[1] = y[2]; // xp
xblock = (d33 * y[0] * la) - y[1] + xpretotal;
// xblock = (terfdstrain(y[0]) * la) - y[1] + xpretotal;
ydot[2] = ((ka * (xblock-xpretotal)) - (y[6] * ach) - (ks * y[1]) - (cp * y[2])) / (mp + (ma/3)); // vp

F = (y[7] - y[nps+2*np+2*nt+2*nto])*ao - ml*9.81;
ydot[3] = y[4]; // xl
ydot[4] = (F - stiction(F,y[4]) - cl*y[4]) / (ml0 + ml); // vl;

ydot[5] = kacc * (y[ns-1] - (y[9] / rho)) / (aacc * aacc); // Pacc

r = rho * exp((y[6] - Pbias) / beta);
ydot[6] = beta * ((r * ach * y[2]) - y[8] + y[9]) / (r * ach * (lch - y[1])); // Pch
ydot[7] = beta * (y[nps+2*np+2*nt+2*nto-1] - ao * y[4]) / (ao * y[3]); // Ph

if (y[10] > rmin){
temp = 0.5 * (y[6] + y[nps]); r = rho * exp((temp - Pbias) / beta);
v = y[8] / (r * ap);
ydot[8] = (y[6] - y[nps]) - (Klvo/y[10])*(0.5 * r * absval(v) * v);
ydot[8] = ydot[8] * (ap / lpo);
}
else ydot[8] = 0; // Mdotout

if (y[11] > rmin){
temp = dtube / dacc; Klec = 0.42 * (1 - temp*temp);
v = y[9] / (rho * ap);
ydot[9] = (y[5] - y[6]) - (rtube*lt + rport*lp)*y[9]
- (Klec*(ap/at)*(ap/at) + Klb + (Klvi/y[11]))*(0.5 * rho * absval(v) * v);
ydot[9] = ydot[9] / (lt/at + lp/ap);
}
else ydot[9] = 0; // Mdotin

ydot[10] = y[12]; // roh
ydot[11] = y[13]; // rol

ydot[12] = (rh - (2*etar*y[12])/wnr - y[10]) * wnr * wnr; // rohd
ydot[13] = (rl - (2*etar*y[13])/wnr - y[11]) * wnr * wnr; // rold

r = rho * exp((y[nps] - Pbias) / beta);
tubeflowq(np,ydot+nps,y+nps,ap,lp,Klb,rport,y[8]/r,y[nps+2*np],1); // Php, Qhp

tubeflowq(nt,ydot+nps+2*np,y+nps+2*np,at,lt,Klb,rtube,y[nps+2*np-1],y[nps+2*np+2*nt],1);
// Pht, Qht
tubeflowq(nto,ydot+nps+2*np+2*nt,y+nps+2*np+2*nt,ato,lto,Kle,rtubeo,y[nps+2*np+2*nt-1],y[7],1);
// Pho, Qho
temp = (ao/at) * (ao/at);
tubeflowq(no,ydot+nps+2*np+2*nt+2*nto,y+nps+2*np+2*nt+2*nto,
                  ao,lo-y[3],temp*Kle,rcyl,ao*y[4],y[5]*(at/ao),1);
// Plo, Qlo

return (xblock/la);
}
```

Functions

```
#define pi M_PI
double in2m = 0.0254, psi2Pa = 6895.0, lbf2N = 0.454 * 9.81, rmin;
double Pbias, beta, nu, rho; // Fluid properties
double freestrain; // Max induced strain in active material
double xpretotal; // Total prestrain + bias induced displacement
double f_s, f_d, vmin, vs; // static & dynamic friction values, sticking velocity, stribeck velocity

void inputv(double *vin,double fr)
{
double w = 2 * pi * fr;
vin[0] = 1.05 / sqrt((1 - w*w*2.461e-7)*(1 - w*w*2.461e-7) + (w*.001)*(w*.001)); vin[1] = 1.1; // 2" 623
// 50psi, 4" 623
// vin[0] = 1.00 / sqrt((1 - w*w*1.142e-7)*(1 - w*w*1.142e-7) + (w*.00067)*(w*.00067)); vin[1] = 1.02;
// 100psi, 4" 623
// vin[0] = 0.92 / sqrt((1 - w*w*1.258e-7)*(1 - w*w*1.258e-7) + (w*.00064)*(w*.00064)); vin[1] = 1.02;
// 2" 5050
// vin[0] = 1.03 / sqrt((1 - w*w*2.421e-7)*(1 - w*w*2.421e-7) + (w*8.07e-4)*(w*8.07e-4)); vin[1] = 1.03;
// 4" 5050
// vin[0] = 1/sqrt((1 - w*w*5.163e-8)*(1 - w*w*5.163e-8) + (w*3.636e-4)*(w*3.636e-4)); vin[1] = 1.0;
// load, 2" 5050
// vin[0] = 1/sqrt((1 - w*w*1.479e-7)*(1 - w*w*1.479e-7) + (w*7.63e-4)*(w*7.63e-4)); vin[1] = 1.05;
// vin[0] = 1/sqrt((1 - w*w*2.551e-7)*(1 - w*w*2.551e-7) + (w*4.747e-4)*(w*4.747e-4));
// vin[1] = 1;//((-7.6e-9*fr+1.2e-5)*fr-.0048)*fr+1.4; // load, 4" 5050
// pmn 12mm, 400V
// vin[0] = (((7.831e-13*fr - 1.179e-9)*fr + 4.972e-7)*fr + 4.297e-5)*fr + 0.9877; vin[1] = vin[0];
// vin[0] = (1.342e-7*fr - 2.651e-5)*fr + 1.008; vin[1] = vin[0]; // pmn 12mm, 400V
// pmn 12mm, 300V
// vin[0] = (((2.015e-13*fr + 3.109e-10)*fr - 4.831e-7)*fr + 1.789e-4)*fr + 0.9819; vin[1] = vin[0];
// vin[0] = 1.977e-7 * pow(fr,1.947) + 0.989; vin[1] = vin[0]; // pmn 12mm, 300V
}

double absval(double x) { return (x < 0) ? -x : x; }

double sign(double x) { return (x < 0) ? -1 : 1; }

double csa(double d) { return (0.25 * pi * d * d); }

double valveopen(double dP, double Po, double Pc)
{
double value;
if (dP < 0) value = (absval(dP) > Pc) ? -1 : (dP / Pc);
else value = (dP > Po) ? 1 : (dP / Po);
return value;
}

double stiction(double F, double v)
// F: applied force, v: velocity, force: friction force
{
double force;//, temp;
// Karnopp model
if (absval(v) < vmin) force = (absval(F) <= f_s) ? F : (sign(F) * f_s); // stiction
else force = sign(v) * f_d; // slippage
return force;
}

void tubeflowq(int N,double *xdot,double *x,double A,double L,double KL,double Rf, double Qin,
double Pend,int endtype)
// for volume flow rates
// ENDTYPE = 1, if line ends in reservoir, 0 otherwise
{
int i; double r, lumpvol = (A * L) / N, tmp = (N * A) / L;

for (i = 0; i < N; i++){
if (i == 0) xdot[i] = ((Qin - x[N+i]) * beta) / lumpvol;
else xdot[i] = ((x[N+i-1] - x[N+i]) * beta) / lumpvol;
```

```
r = rho * exp((x[i] - Pbias) / beta);
if (i == N-1)
xdot[N+i] = ((x[i] - Pend)*tmp)/r - (Rf*A*x[N+i]) - endtype*(0.5*KL*absval(x[N+i])*x[N+i])/lumpvol;
else xdot[N+i] = ((x[i] - x[i+1])*tmp)/r - (Rf*A*x[N+i]);
}
}

double fluidchamber(double vol, double volchgrate, double netqflowin)
// volchgrate is POSITIVE for decrease and NEGATIVE for increase
{ return beta * (volchgrate + netqflowin) / vol; }

double valveopenlimit(double x)
{
double value;
if (x <= 0) value = 0;
else { value = (x > 1) ? 1 : x; }
return value;
}

double platestiffness(double Y,double ro,double ri,double t)
//Y: modulus, ro,ri: radii(outer, loaded), t: thickness
{
double temp;
temp = ri / ro; temp = 1 - (temp*temp) * (temp*temp + 4*log(temp)); temp = temp*3*(1 - 0.3*0.3)/16;
return ((pi*Y*t*t*t) / (temp*ri*ri));
}

double rkmethodt(double t1, double t2, int r)
{
double t3;
if(r == 1) t3 = t1;
else if (r == 4) t3 = t1 + t2;
else t3 = t1 + 0.5 * t2;
return t3;
}

double * rkmethodx(int step,int ns,double *y,double *rky)
{
int i;
double *tempy; tempy = (double *)malloc(sizeof(double) * ns);

switch(step){
case 0:
tempy = y; break;
case 3:
for(i = 0; i < ns; i++) tempy[i] = y[i] + 0.5 * rky[(step*ns)+i]; break;
default:
for(i = 0; i < ns; i++) tempy[i] = y[i] + rky[(step*ns)+i]; break;
}

return tempy;
}

double linearslope(double *t,double *x,long int N)
{
long int i;
double xmean, tmean, Sx = 0.0, Stt = 0.0, Sxt = 0.0;

tmean = (t[0] + t[N-1]) / 2;
for(i = 0; i < N; i++) Sx = Sx + x[i];
xmean = Sx / N;
for(i = 0; i < N; i++){
Stt = Stt + (t[i] - tmean) * (t[i] - tmean);
Sxt = Sxt + (x[i] - xmean) * (t[i] - tmean);
}
return double(Sxt/Stt);
}
```

```
double meanval(int n, double *x)
{
double value = 0.0; int i;
for(i = 0; i < n; i++) value = value + x[i];
return (value/n);
}
```

Appendix B
Mechanical design drawings

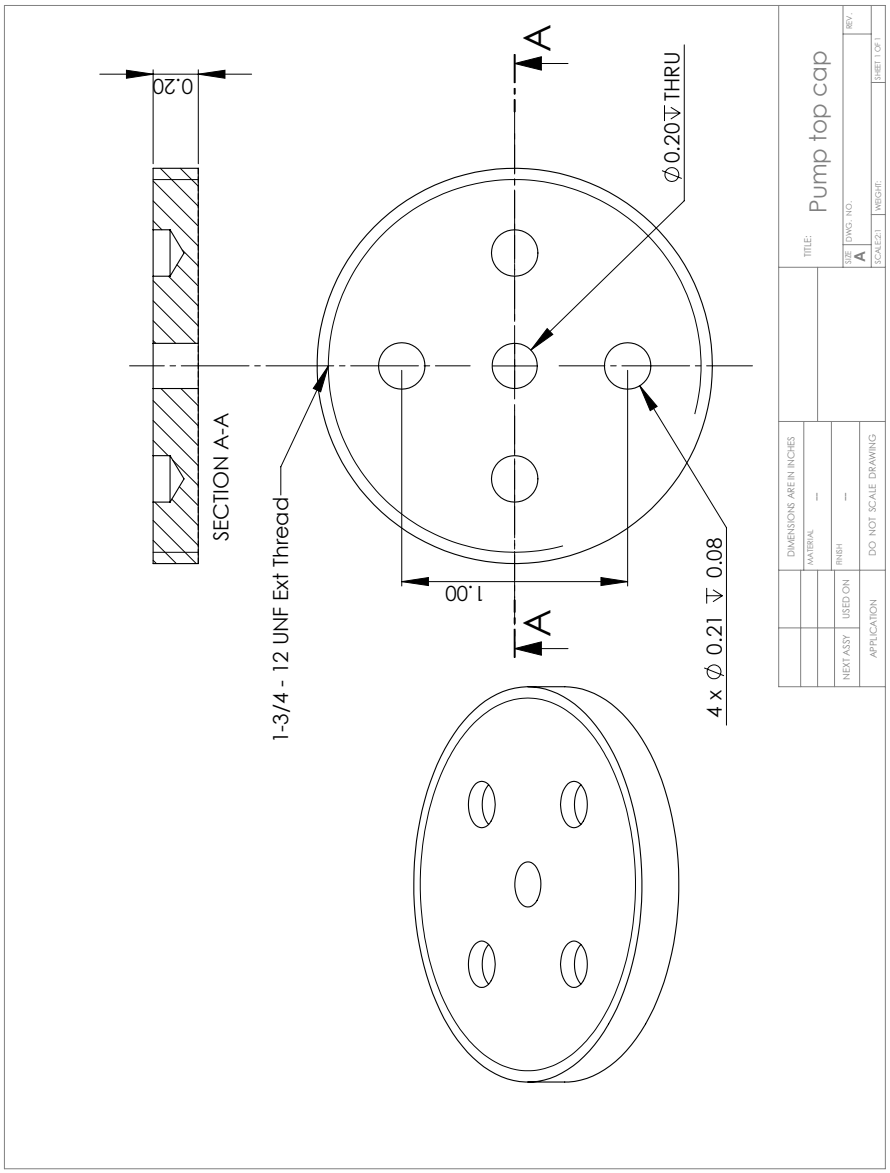

Figure B.1: Pump top cap

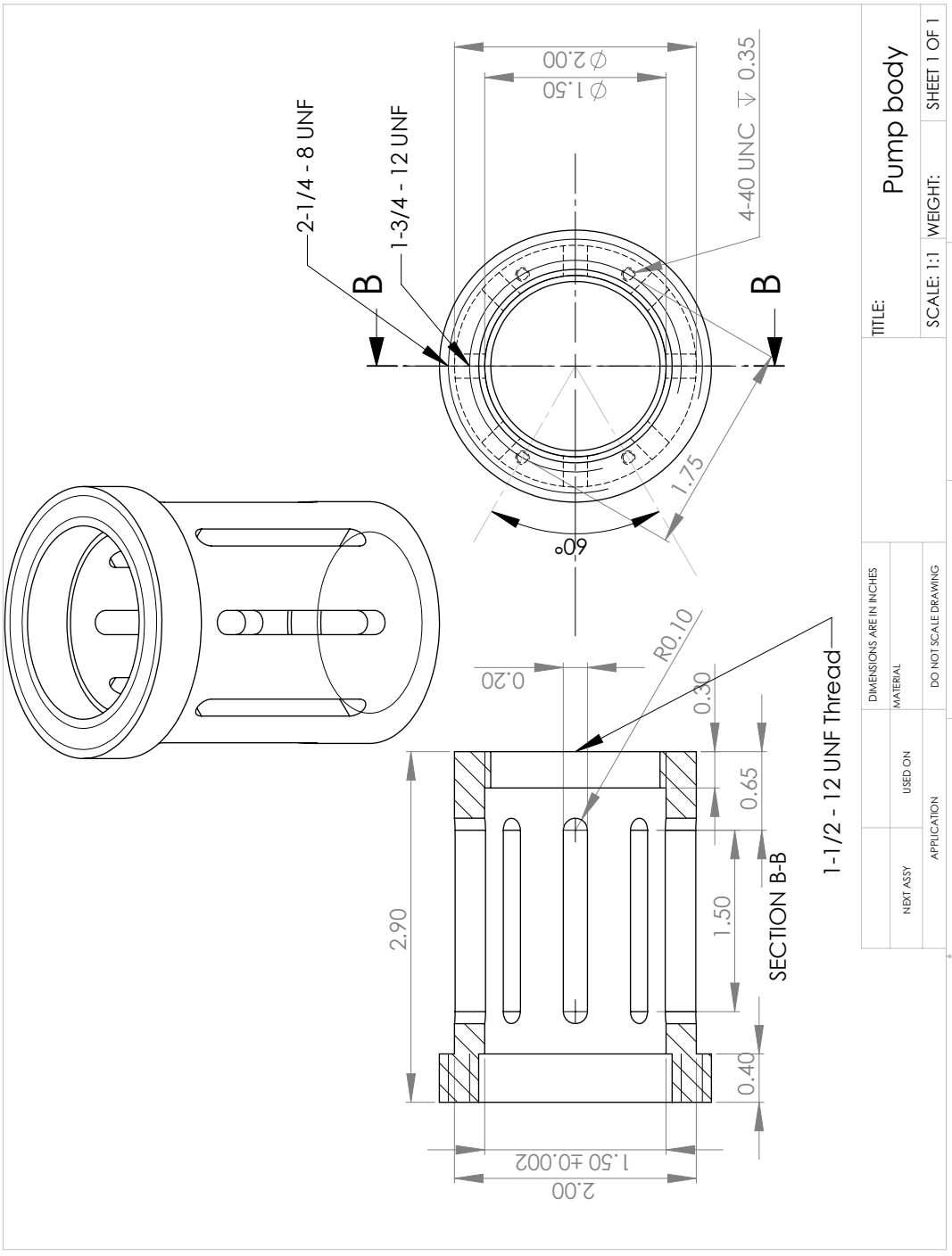

Figure B.2: Pump body

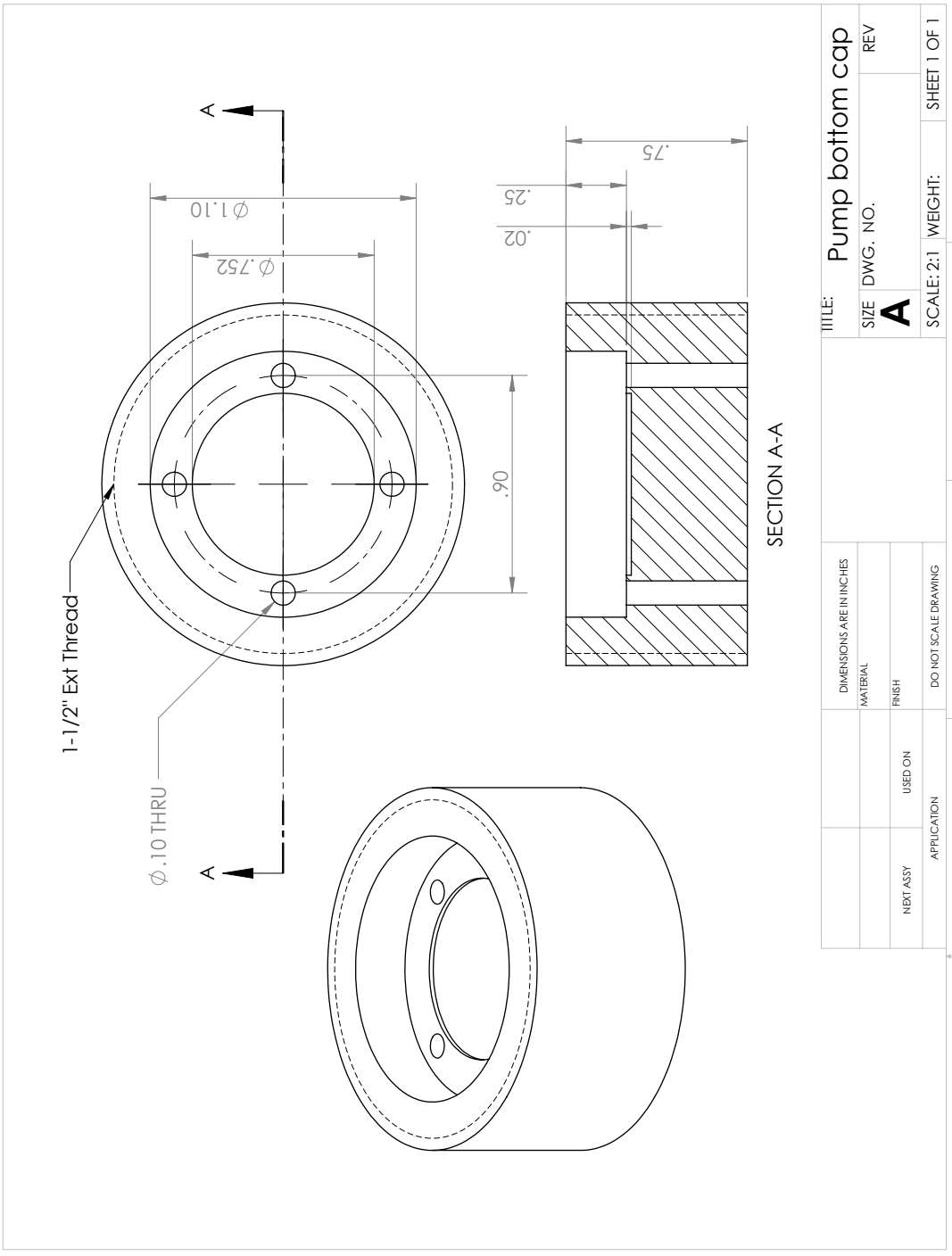

Figure B.3: Pump bottom cap

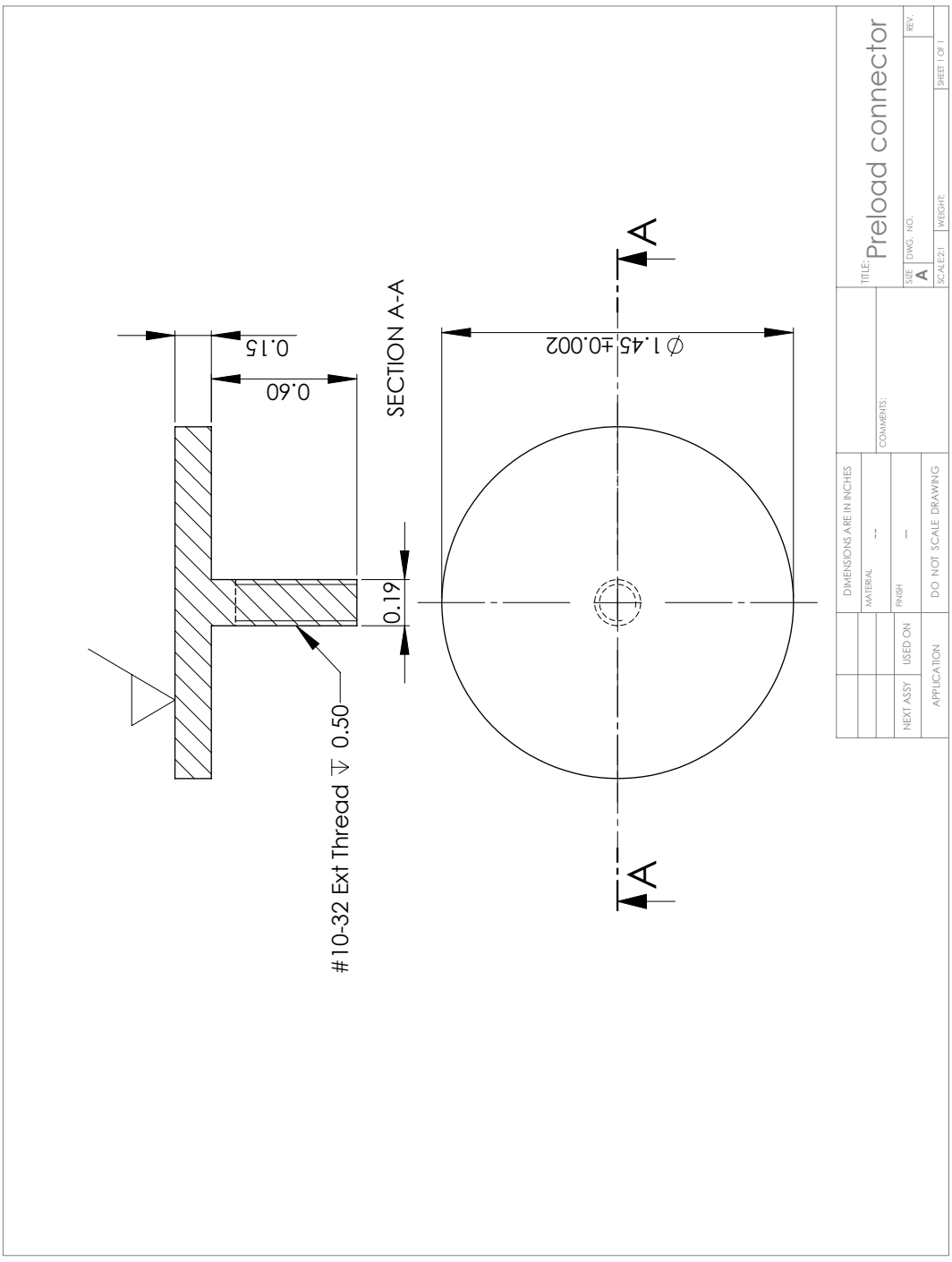

Figure B.4: Preload connector

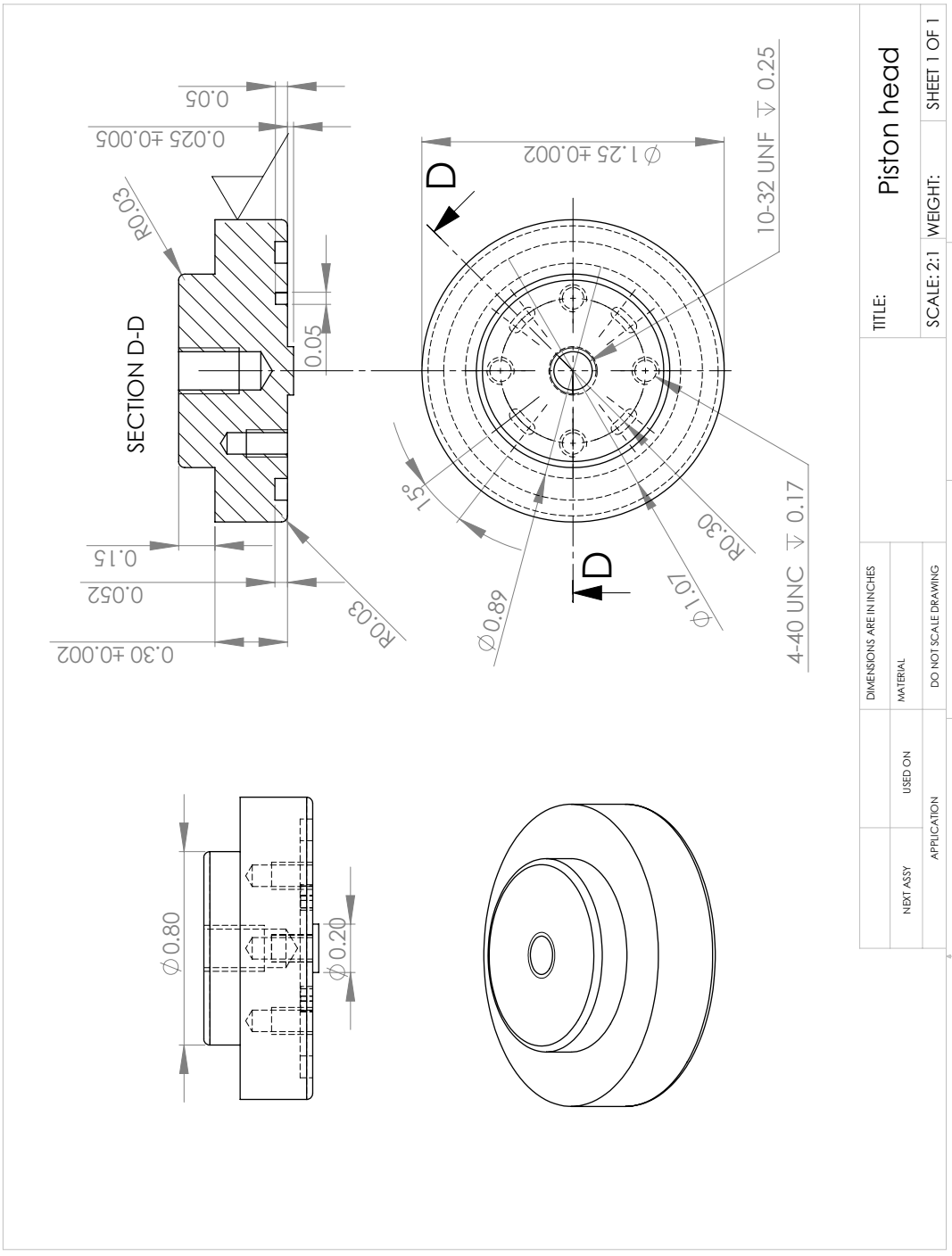

Figure B.5: Pumping piston head

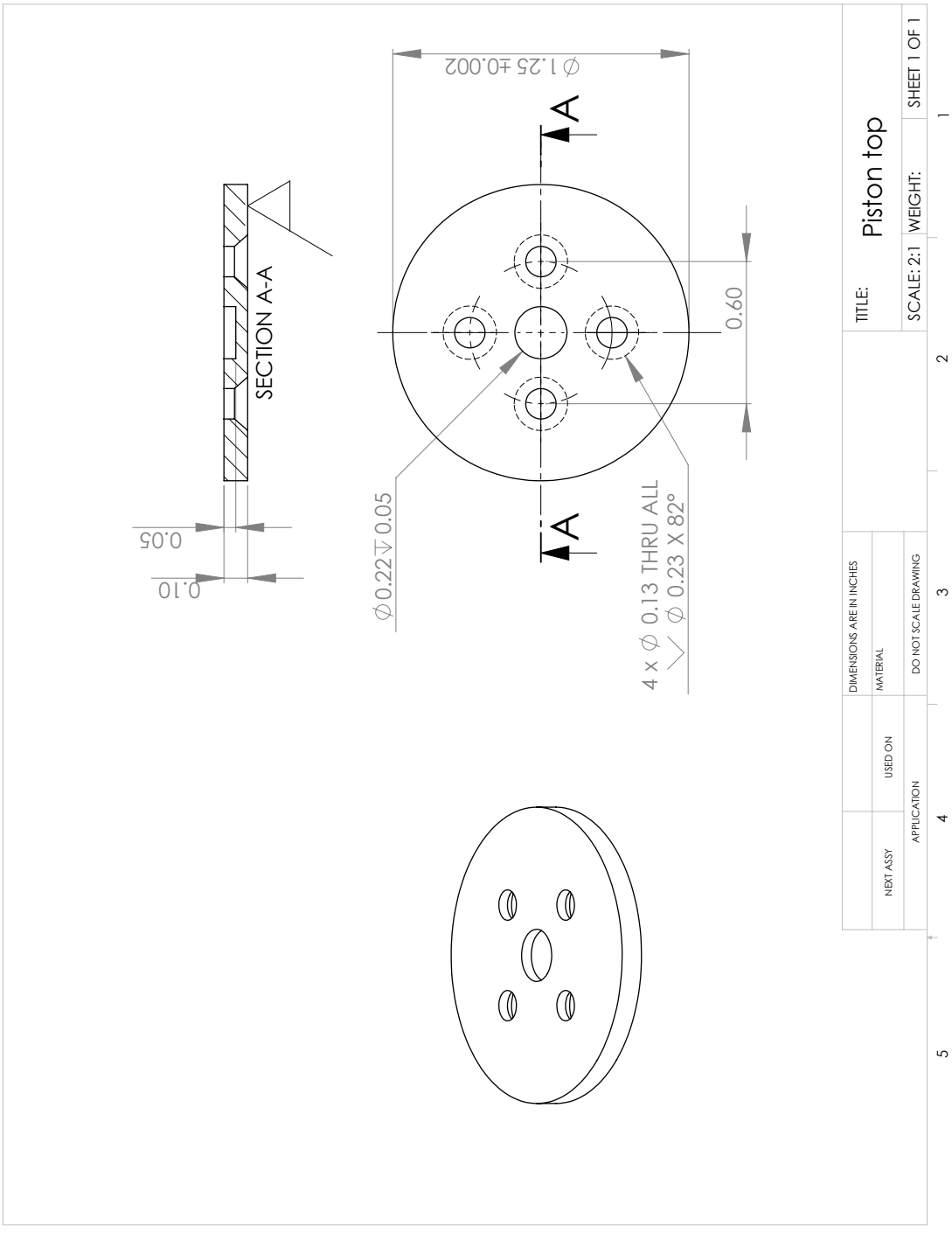

Figure B.6: Pumping piston top

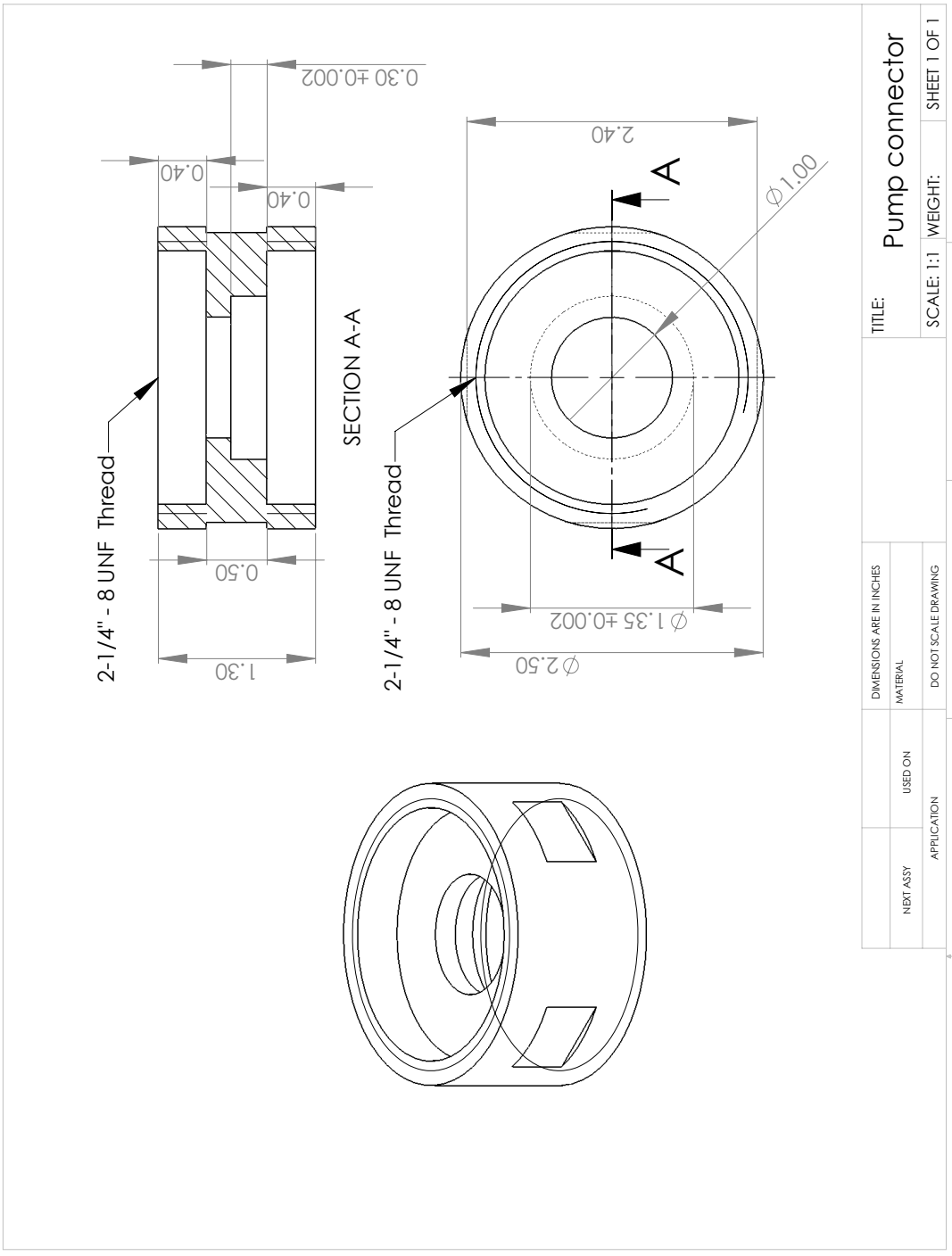

Figure B.7: Pump connector piece

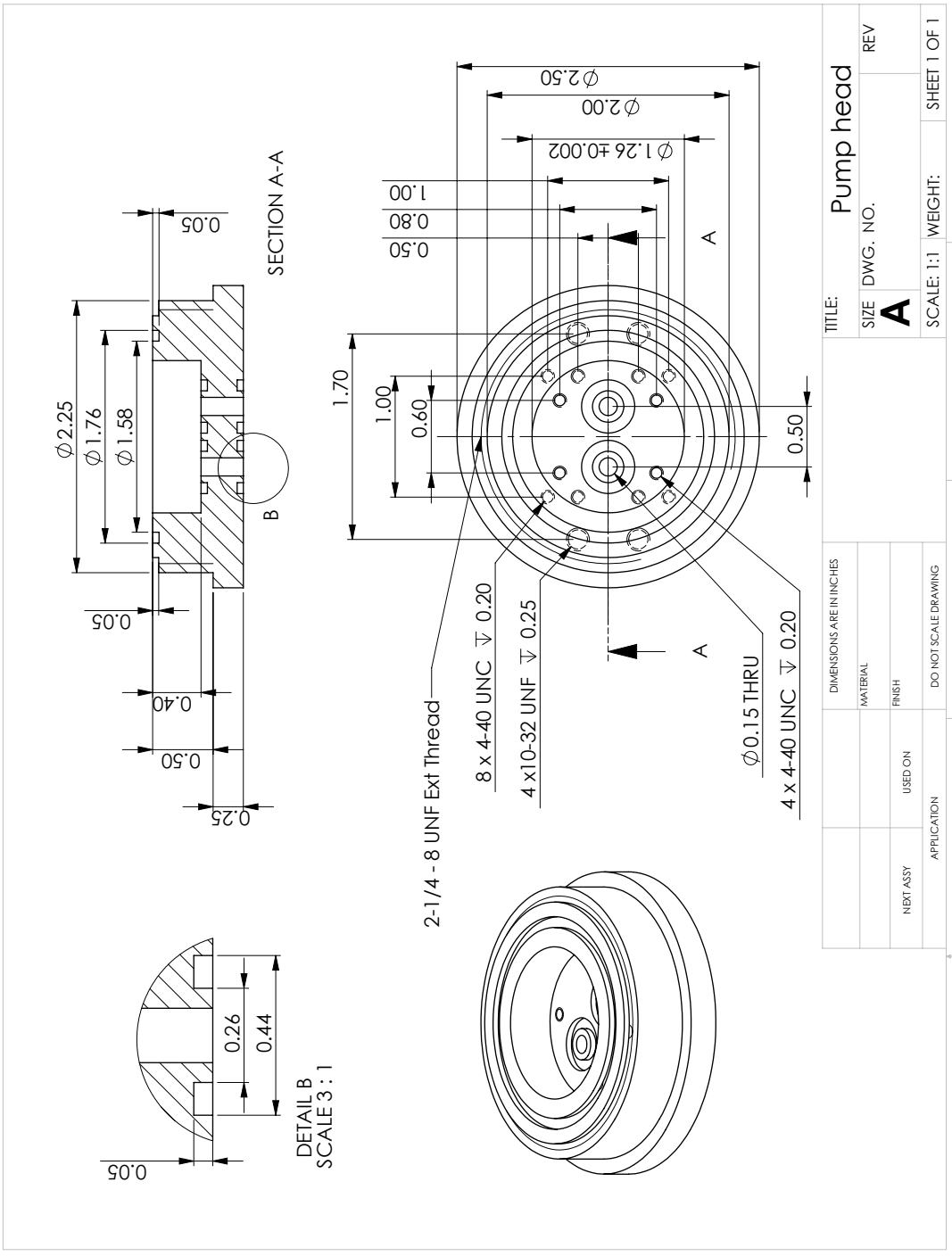

Figure B.8: Pump head

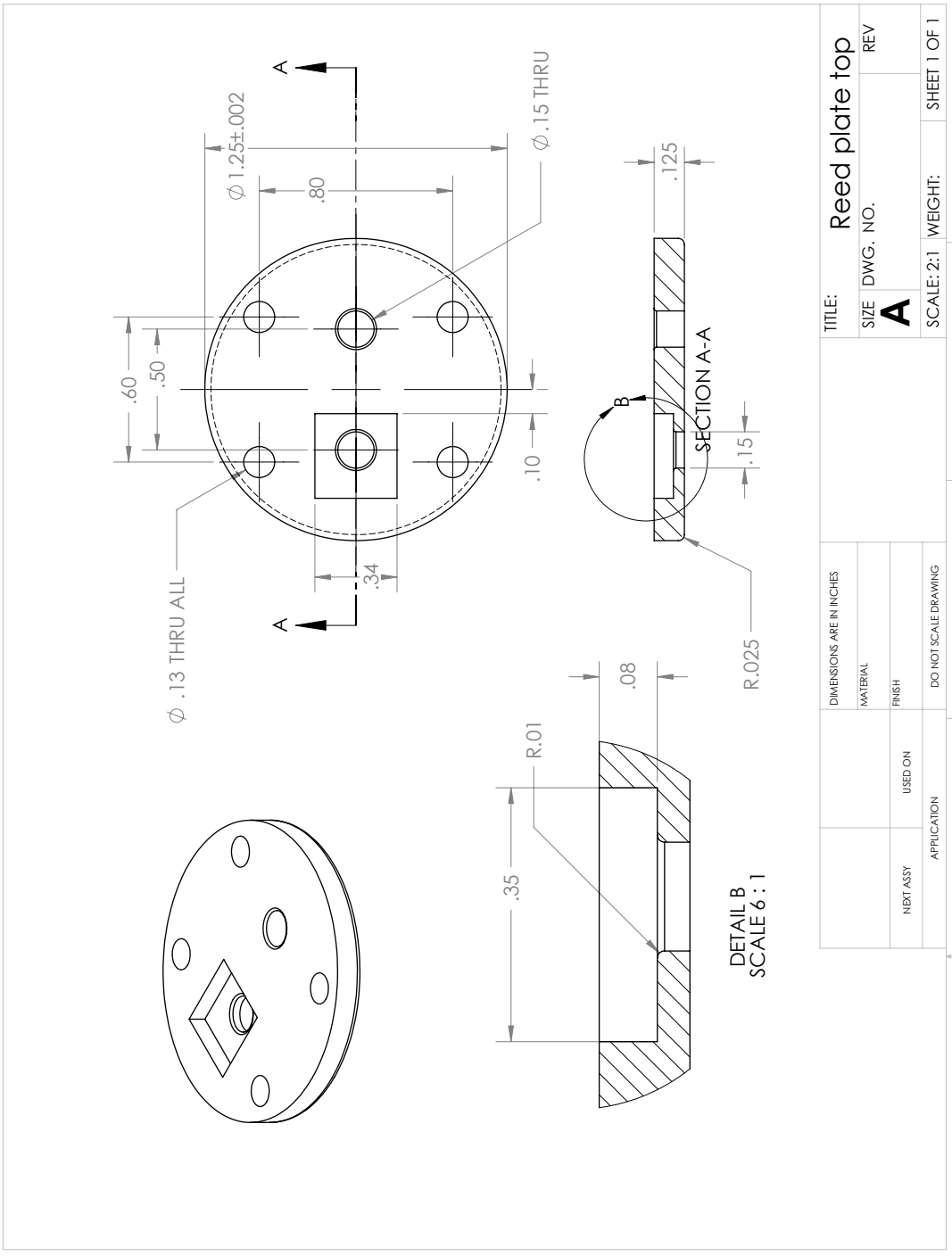

Figure B.9: Top reed plate

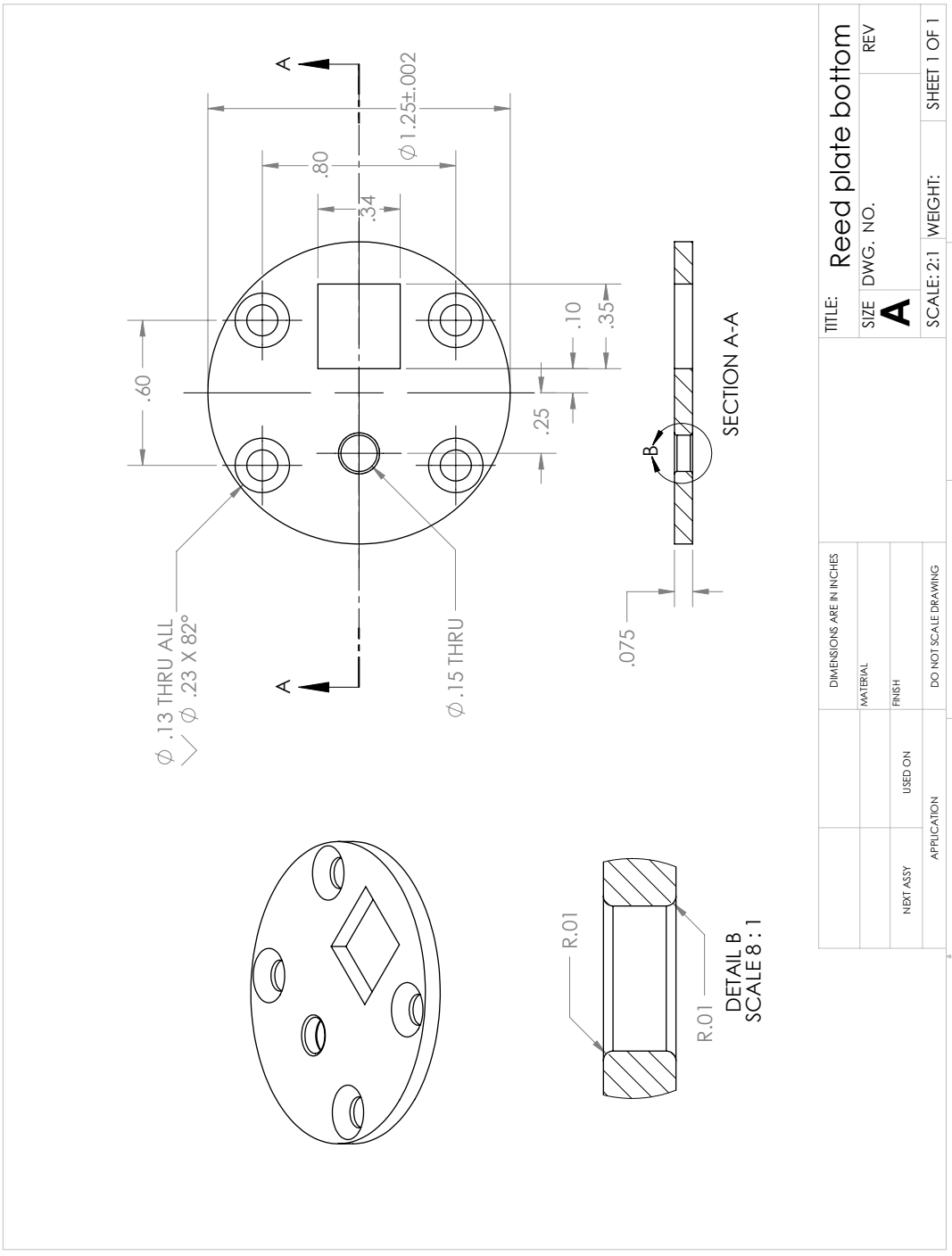

Figure B.10: Bottom reed plate

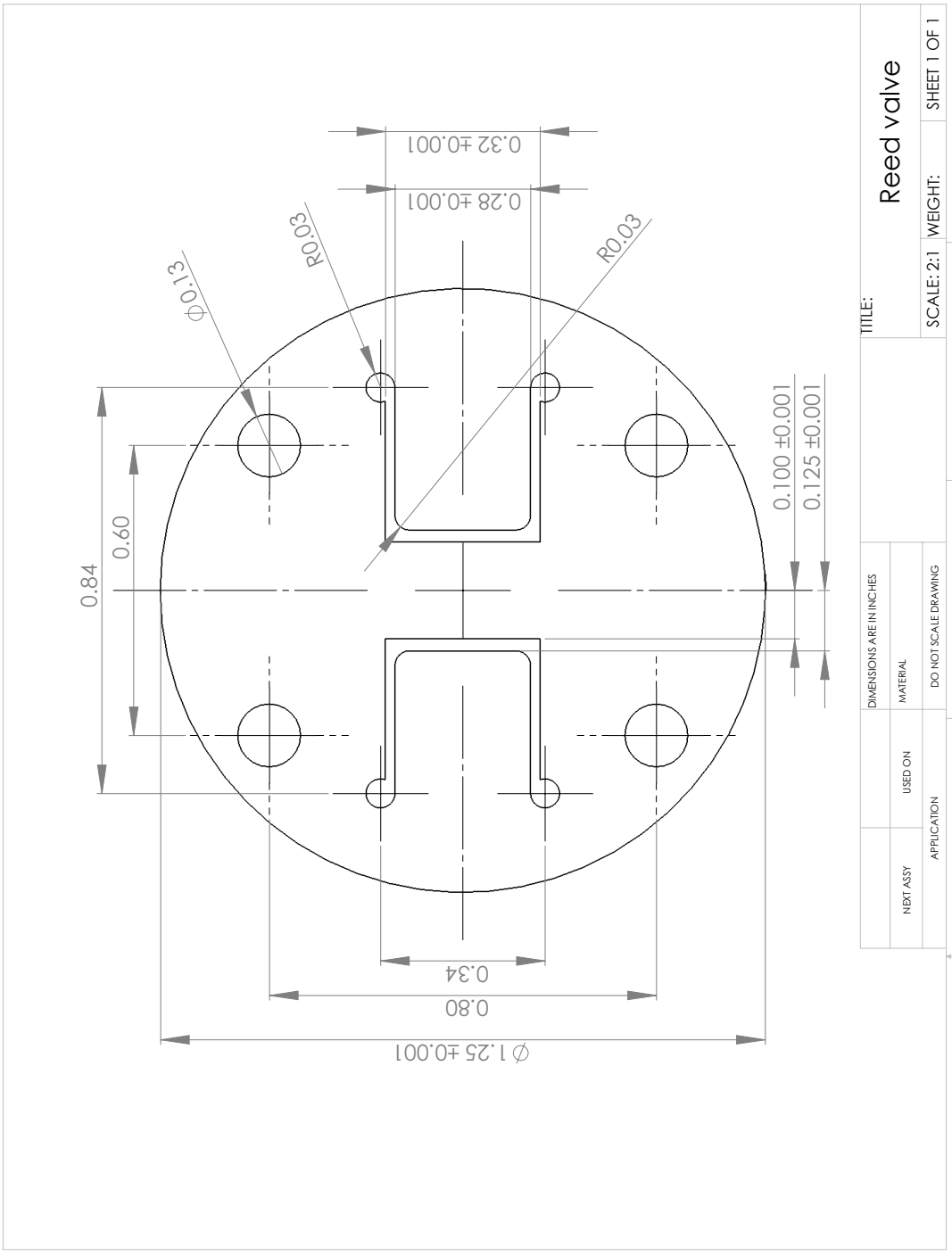

Figure B.11: Reed valve

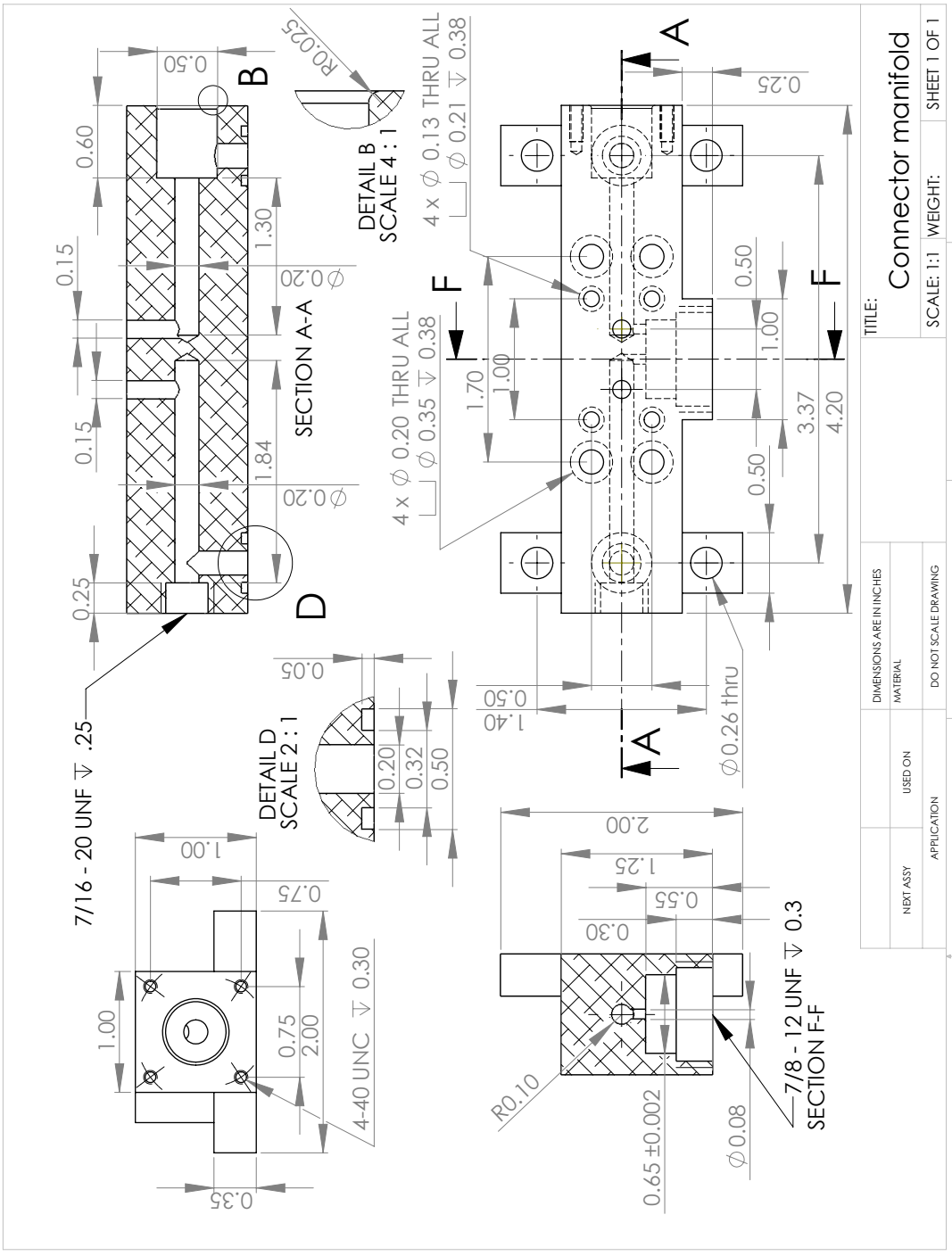

Figure B.12: Manifold

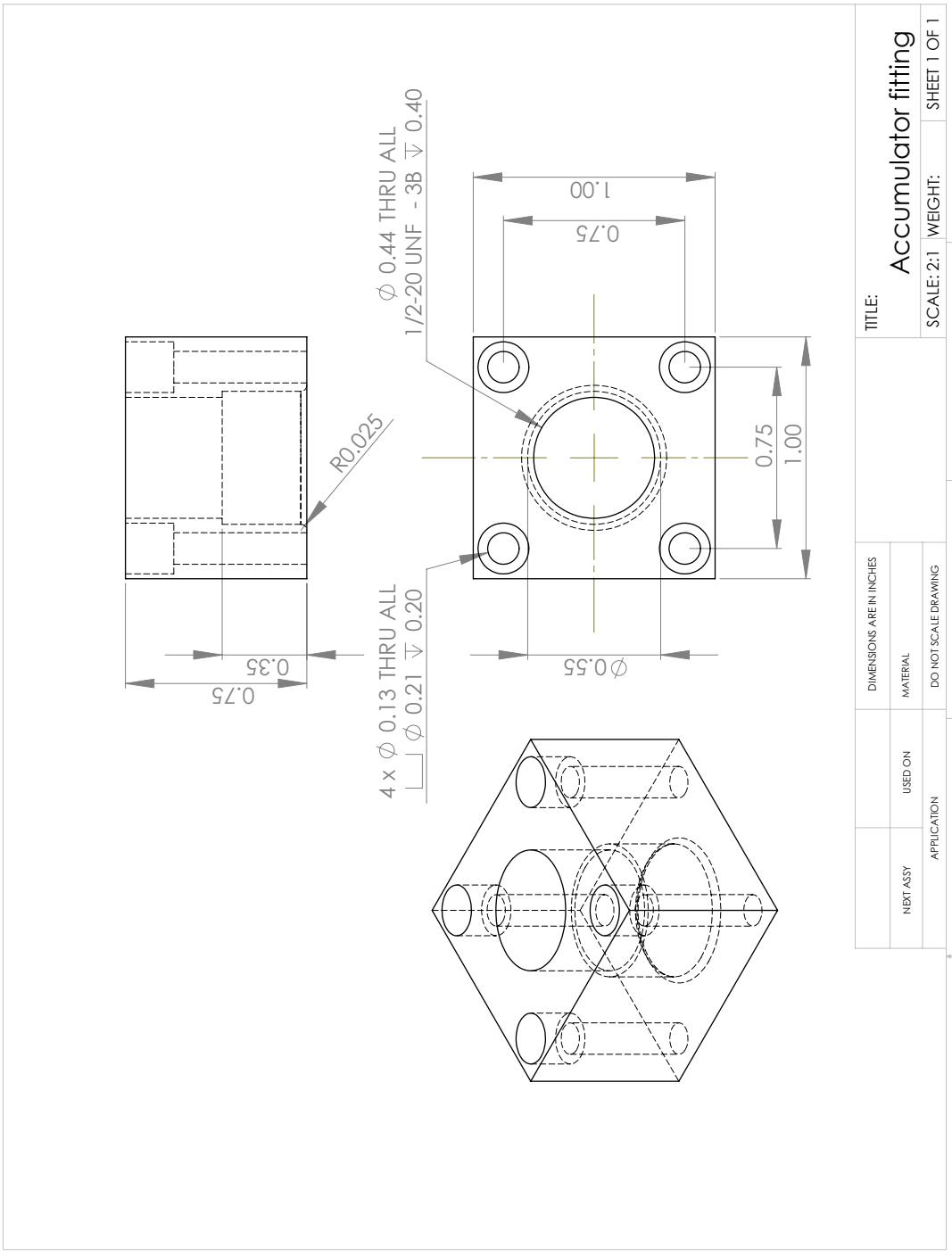

Figure B.13: Accumulator fitting

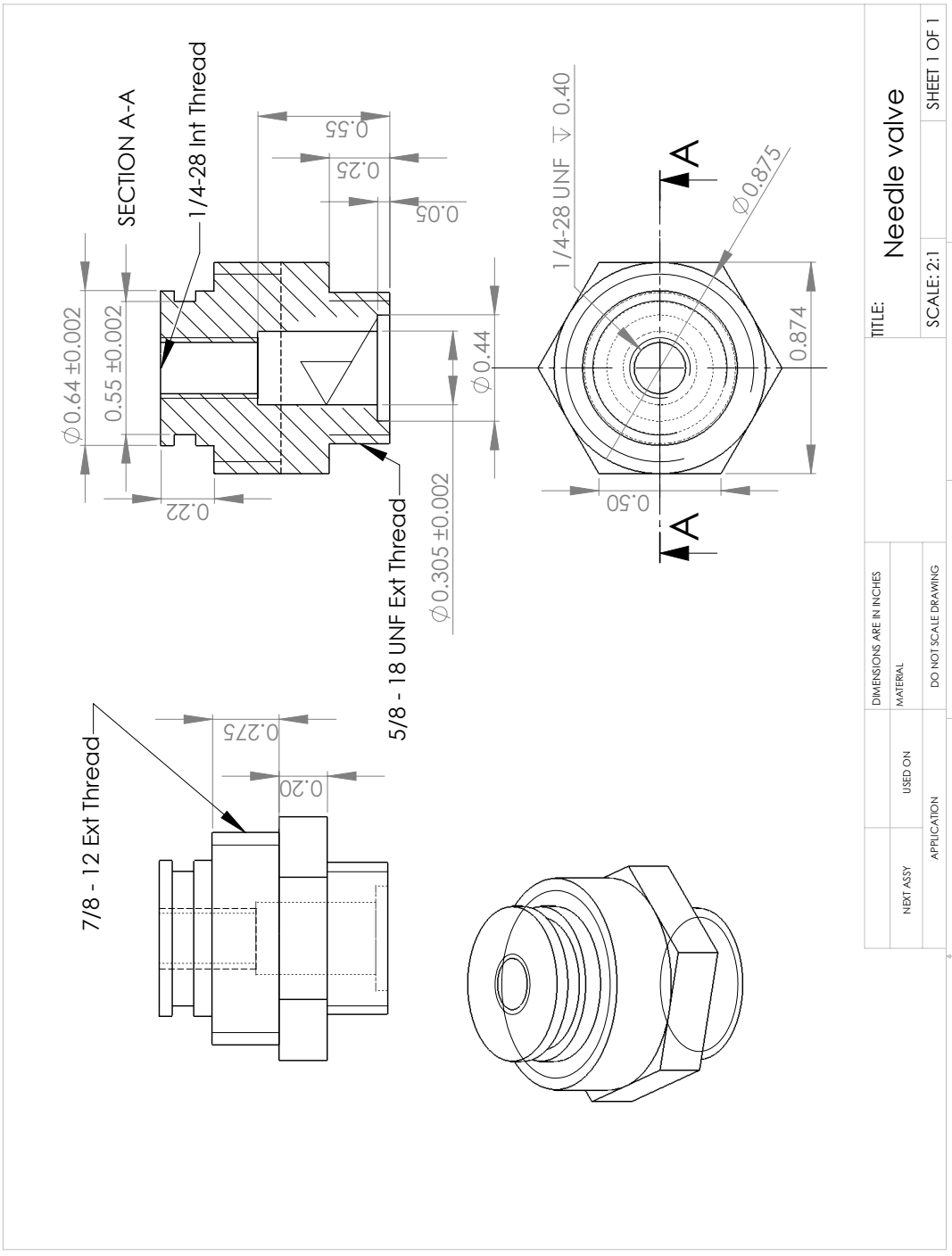

Figure B.14: Needle valve

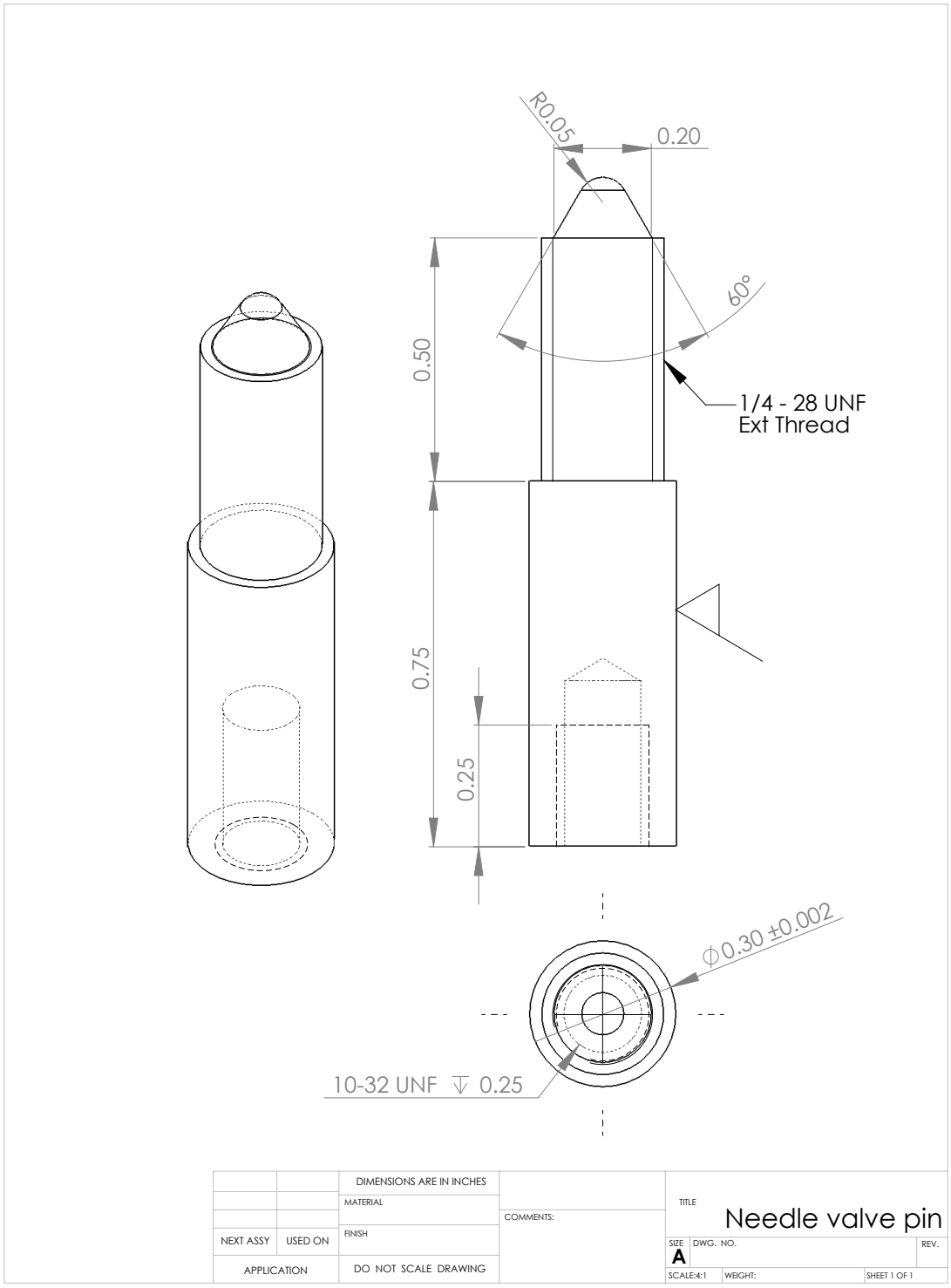

Figure B.15: Needle valve pin

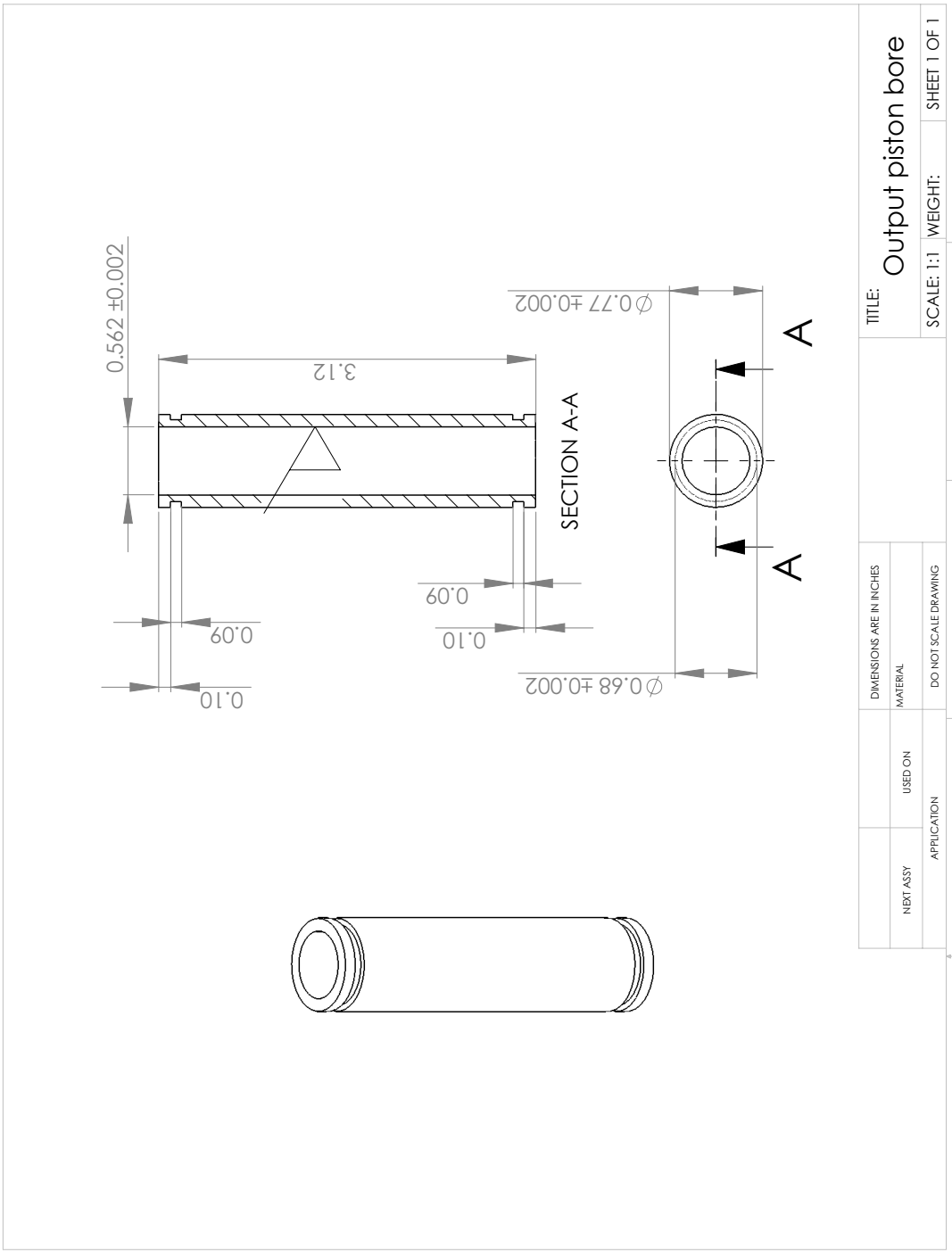

Figure B.16: Output piston bore

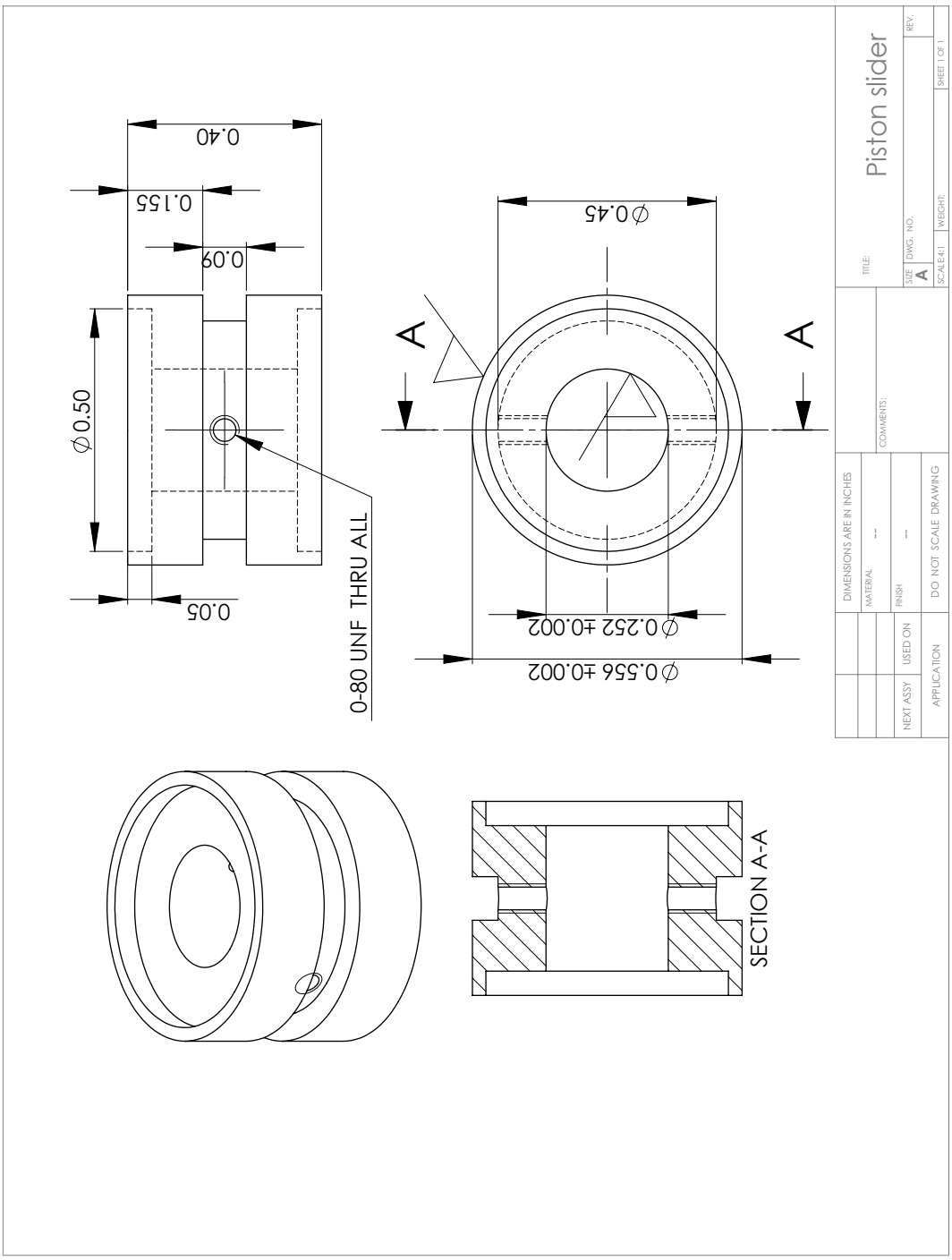

Figure B.17: Output piston slider

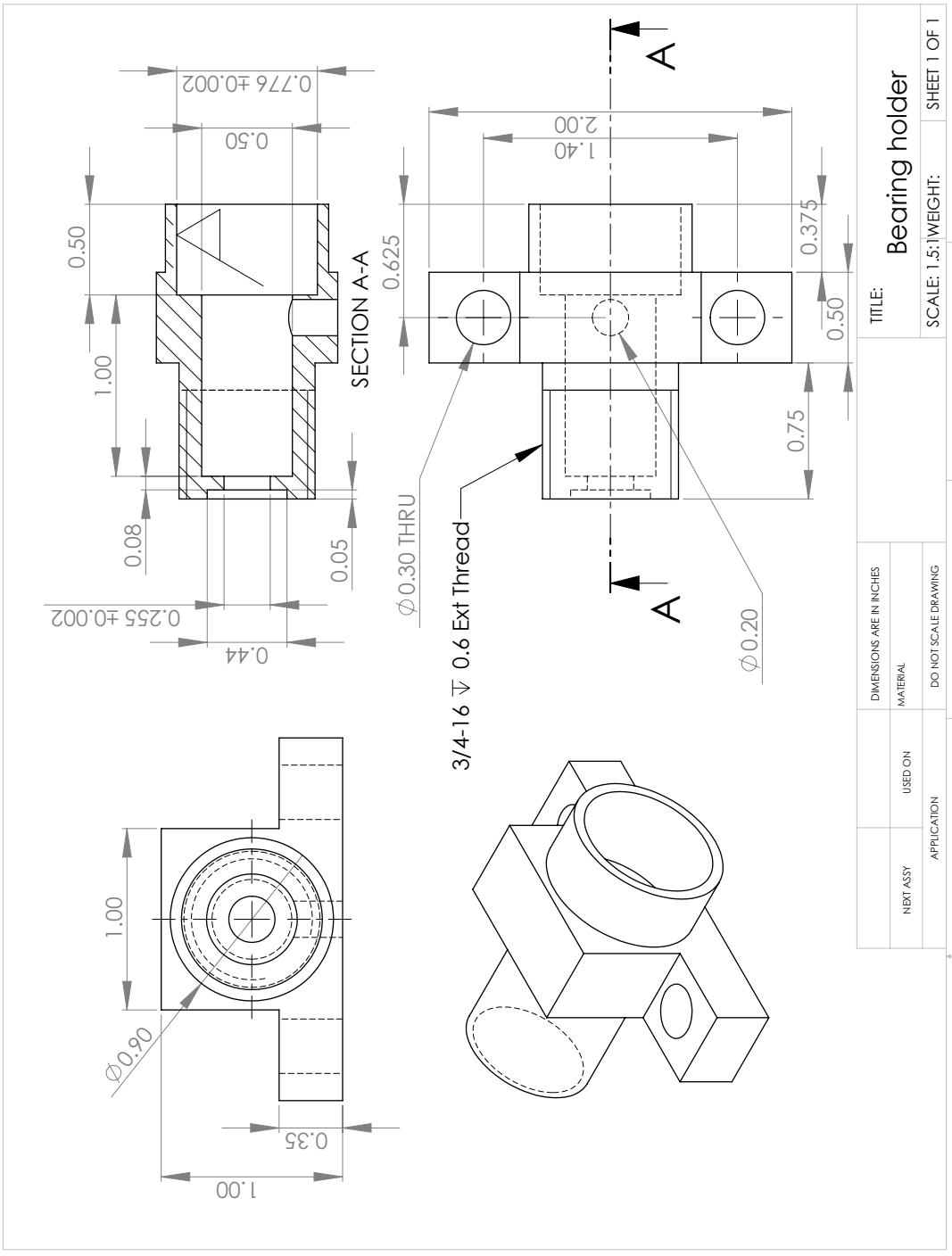

Figure B.18: Bearing holder

Bibliography

[1] R. G. Loewy. Recent developments in smart structures with aeronautical applications. *Smart Materials and Structures*, 6(5):R11–R42, 1997.

[2] R. G. S. Barsoum. Active materials and adaptive structures. *Smart Materials and Structures*, 6(1):117–122, 1997.

[3] E. F. Crawley. Intelligent structures for aerospace - A technology overview and assessment. *AIAA Journal*, 32(8):1689–1699, 1987.

[4] V. Giurgiutiu, Z. Chaudhry, and C. A. Rogers. Engineering feasibility of induced strain actuators for rotor blade active vibration control. *Journal of Intelligent Material Systems and Structures*, 6(5):583–597, 1995.

[5] M. A. Hopkins, D. J. Dolvin, D. B. Paul, E. R. Anselmo, and J. V. Zweber. Structures technology for future aerospace systems. In *39th AIAA/ASME/ASCE/AHS/ASC Structures, Structural Dynamics and Materials Conference*, Long Beach, CA, 1998.

[6] V. Giurgiutiu, R. Pomirleanu, and C. A. Rogers. Energy-based comparison of solid-state actuators. Technical Report USC-ME-LAMSS-2000-102, University of South Carolina, Columbia, SC, March 2000.

[7] V. Giurgiutiu. Review of smart-materials actuation solutions for aeroelastic and vibration control. *Journal of Intelligent Material Systems and Structures*, 11(7):525–7544, 2000.

[8] I. Chopra. Review of state of art of smart structures and integrated systems. *AIAA Journal*, 40(11):2145–2187, 2002.

[9] E. Anderson, G. L. Bales, and E. V. White. Application of smart material - hydraulic actuators. In *Proceedings of the SPIE*, volume 5054, pages 73–84, San Diego, CA, March 2003.

[10] S. G. Wax, G. M. Fischer, and R. R. Sands. The past, present, and future of DARPA's investment strategy in smart materials. *Journal of the Minerals Metals and Materials Society*, 55(12):17–23, 2003.

[11] A. Yousefi-Koma and D. G. Zimcik. Applications of smart structures to aircraft for performance enhancement. *Canadian Aeronautics and Space Journal*, 49(4):163–172, 2003.

[12] B. Sanders, R. Crowe, and E. Garcia. Defense Advanced Research Projects Agency - Smart Materials and Structures Demonstration Program Overview. *Journal of Intelligent Material Systems and Structures*, 15(4):227–233, 2004.

[13] H. P. Monner. Smart materials for active noise and vibration reduction. In *Proceedings of Novem – Noise and Vibration: Emerging Methods*, Saint-Raphaël, France, April 2005.

[14] A. B. Flatau and K. P. Chong. Dynamic smart material and structural systems. *Engineering Structures*, 24(3):261–270, 2002.

[15] E. F. Crawley and J. Deluis. Use of piezoelectric actuators as elements of intelligent structures. *AIAA Journal*, 25(10):1373–1385, 1987.

[16] N. W. Hagood and A. von Flotow. Damping of structural vibrations with piezoelectric materials and passive electrical networks. *Journal of Sound and Vibration*, 146(2):243–268, 1991.

[17] I. Chopra. Status of application of smart structures technology to rotorcraft systems. *Journal of American Helicopter Society*, 45(4):228–252, 2000.

[18] F. K. Straub, D. K. Kennedy, D. B. Domzalski, A. A. Hassan H. Ngo, V. Anand, and T. Birchette. Smart material actuated rotor technology - SMART. In *41st AIAA/ASME/ASCE/AHS/ASC Structures, Structural Dynamics and Materials Conference*, Atlanta, GA, 2000.

[19] W. B. Facey, N. C. Rosenfeld, Y. T. Choi, and N. M. Wereley. Design and testing of a compact magnetorheological damper for high impulsive loads. *International Journal of Modern Physics B*, 19(7–9):1549–1555, 2005.

[20] Y. T. Choi and N. M. Wereley. Shock isolation systems using magnetorheological dampers. *Journal of Vibration and Acoustics*, 130(2), 2008.

[21] S. Sherrit. Smart material/actuator needs in extreme environments in space. In *Proceedings of the SPIE*, volume 5761, San Diego, CA, 2005.

[22] J. Chandra, V. Rao, R. Butler, and R. Damle. Multidisciplinary research in smart structures: A survey. In *Proceedings of the American Control Conference*, volume 6, pages 4167–4172, 1995.

[23] W. B. Spillman Jr, J. S. Sirkis, and P. T. Gardiner. Smart materials and structures: What are they? *Smart Materials and Structures*, 5(3):247–254, 1996.

[24] P. Janker, F. Claeyssen, B. Grohmann, M. Christmann, T. Lorkowski, R. LeLetty, O. Sosniki, and A. Pages. New actuators for aircraft and space applications. In *11th International Conference on New Actuators*, Bremen, Germany, June 2008.

[25] G. Akhras. Smart materials and smart systems for the future. *Canadian Military Journal*, 1(3):25–32, 2000.

[26] A. V. Srinivasan and D. M. McFarland. *Smart Structures: Analysis and Design*. Cambridge University Press, 2001.

[27] V. Giurgiutiu and C. A. Rogers. Power and energy characteristics of solid-state induced-strain actuators for static and dynamic application. *Journal of Intelligent Material Systems and Structures*, 8(9):738–750, 1997.

[28] P. C. Chen and I. Chopra. Hover testing of smart rotor with induced-strain actuation of blade twist. *AIAA Journal*, 35(1):6–16, 1997.

[29] P. Wierach, H. P. Monner, A. Schoenecker, and J. K. Duerr. Application-specific design of adaptive structures with piezoceramic patch actuators. In *Proceedings of the SPIE*, volume 4698, pages 333–341, 2002.

[30] D. K. Samak and I. Chopra. Design of high force, high displacement actuators for helicopter rotors. *Smart Materials and Structures*, 5(1):58–67, 1996.

[31] F. K. Straub. A feasibility study of using smart materials for rotor control. *Smart Materials and Structures*, 5(1):1–10, 1996.

[32] C. Near. Piezoelectric actuator technology. In *Proceedings of the SPIE*, volume 2717, pages 246–258, San Diego, CA, 1996.

[33] S. A. Wise and M. W. Hooker. Characterization of multilayer piezoelectric actuators for use in active isolation mounts. Technical Report NASA-TM-4742, Langley Research Center, NASA, Hampton, VA, March 1997.

[34] F. K. Straub, H. T. Ngo, V. Anand, and D. B. Domzalski. Development of a piezoelectric actuator for trailing edge flap control of full scale rotor blades. *Smart Materials and Structures*, 10(1):25–34, 2001.

[35] R. Pomirleanu and V. Giurgiutiu. Full-stroke static and dynamic analysis of high-power piezoelectric actuators. *Journal of Intelligent Material Systems and Structures*, 13(5):275–289, 2002.

[36] E. V. Ardelean, D. G. Cole, and R. L. Clarke. High performance "V-stack" piezoelectric actuator. *Journal of Intelligent Material Systems and Structures*, 15(11):879–889, 2004.

[37] S. W. Meeks and R. W. Timme. Rare earth iron magnetostrictive underwater sound transducer. *Journal of the Acoustical Society of America*, 62(5):1158–1164, 1977.

[38] R. D. Greenough, M. P. Schulze, A. G. I. Jenner, and A. J. Wilkinson. Actuation with Terfenol-D. *IEEE Transactions on Magnetics*, 27(6):5346–5348, 1991.

[39] J. L. Butler, S. C. Butler, and A. E. Clark. Unidirectional magnetostrictive/piezoelectric hybrid transducer. *Journal of the Acoustical Society of America*, 88(1):7–11, 1990.

[40] P. R. Downey and M. J. Dapino. Extended frequency bandwidth and electrical resonance tuning in hybrid Terfenol-D/PMN-PT transducers in mechanical series configuration. *Journal of Intelligent Material Systems and Structures*, 16(9):757–772, 2005.

[41] A. Dogan, J. Tressler, and R. E. Newnham. Solid-state ceramic actuator designs. *AIAA Journal*, 39(7):1354–1362, 2001.

[42] P. M. Flick, M. H. Love, and P. S. Zink. The impact of active aeroelastic wing technology on conceptual aircraft design. In *RTO AVT Specialists' Meeting on "Structural Aspects of Flexible Aircraft Control"*, Ottawa, Canada, October 1999.

[43] F. Austin, M. J. Siclari, M. Kesselman, and G. N. Weisensel. Smart TERFENOL-D-powered trailing-edge experiment. In *Proceedings of the SPIE*, volume 3326, pages 282–293, June 1998.

[44] D. Moorhouse, B. Sanders, M. von Spakovsky, and J. Butt. Benefits and design challenges of adaptive structures for morphing aircraft. *The Aeronautical Journal*, 110(1105):157–162, 2006.

[45] J. N. Kudva, C. A. Martin, L. B. Scherer, A. P. Jardine, A. R. McGowan, R. C. Lake, G. P. Sendeckyj, and B. P. Sanders. Overview of the DARPA/AFRL/NASA Smart Wing program. In *Proceedings of the SPIE*, volume 3674, pages 230–236, July 1999.

[46] J. N. Kudva. Overview of the DARPA Smart Wing Project. *Journal of Intelligent Material Systems and Structures*, 15(4):261–267, 2004.

[47] R. Vos, R. De Breuker, R. Barrett, and P. Tiso. Morphing wing flight control via postbuckled precompressed piezoelectric actuators. *Journal of Aircraft*, 44(4):1060–1068, 2007.

[48] T. Ford. Advances in rotorcraft. *Aircraft Engineering and Aerospace Technology*, 69(5):447–452, 1997.

[49] A. D. Jacot. Smart structures for rotorcraft control (SSRC). In *Proceedings of the SPIE*, volume 3044, pages 114–122, May 1997.

[50] A. D. Jacot and L. Dadone. Smart structures for rotorcraft control (SSRC) II. In *Proceedings of the SPIE*, volume 3326, pages 272–281, June 1998.

[51] I. Chopra. Smart Structures Technology: Innovations and Applications to Rotorcrafts Systems (final report). Technical Report ARO 30380.90-EG-URI, University of Maryland, May 2000.

[52] S. Kota, J. A. Hetrick, and R. F. Osborn. Adaptive structures: Moving into the mainstream. *Aerospace America*, 44(9):16–18, September 2006.

[53] J. S. Vipperman. Simultaneous qualitative health monitoring and adaptive piezoelectric sensoriactuation. *AIAA Journal*, 39(9):1822–1825, 2001.

[54] B. Culshaw, C. Michie, P. Gardiner, and A. McGown. Smart structures and applications in civil engineering. *Proceedings of the IEEE*, 84(1):78–86, 1996.

[55] G. W. Housner, L. A. Bergman, and T. K. Caughey. Structural control: Past, present, and future. *Journal of Engineering Mechanics*, 123(9):897–971, 1997.

[56] C. A. Rogers, V. Giurgiutiu, and C. K. Y. Leung. *Emerging Materials for Civil Infrastructure - State of the Art*, chapter 1: Smart Materials for Civil Engineering Applications. ASCE Press, 2000.

[57] B. F. Spencer and S. Nagarajaiah. State of the art of structural control. *Journal of Structural Engineering*, 129(7):845–856, 2003.

[58] G. Song, V. Sethi, and H.-N. Li. Vibration control of civil structures using piezoceramic smart materials: A review. *Engineering Structures*, 28(11):1513–1524, 2006.

[59] T. T. Hyde and G. Agnes. Adaptive structures. *Aerospace America*, 38(12):68–68, December 2000.

[60] E. Anderson and D. P. Garg. Active vibration control in rotorcraft systems using smart actuators. In *43rd AIAA/ASME/ASCE/AHS/ASC Structures, Structural Dynamics, and Materials Conference*, Denver, CO, April 2002.

[61] K. Konishi, T. Yoshimura, K. Hashimoto, and N. Yamamoto. Hydraulic actuators driven by piezoelectric elements (1st report, trial piezoelectric pump and its maximum power). *Journal of Japanese Society of Mechanical Engineering (C)*, 59(564):213–220, 1993.

[62] K. Konishi. Hydraulic actuators driven by piezoelectric elements. In *Proceedings of the International Symposium on Microsystems, Intelligent Materials and Robots*, Sendai, Japan, September 1995.

[63] P. Tang, A. B. Palazzolo, A. F. Kascak, G. Montague, and W. Li. Combined piezoelectric-hydraulic actuator based active vibration control for rotordynamic system. *Journal of Vibration and Acoustics*, 117(3):285–293, 1995.

[64] M. J. Gerver, J. H. Goldie, J. R. Swenbeck, R. Shea, P. Jones, R. T. Ilmonen, D. M. Dozor, S. Armstrong, R. Roderick, F. E. Nimblett, and R. Iovanni. Magnetostrictive water pump. In *Proceedings of the SPIE*, volume 3329, pages 694–705, 1998.

[65] L. D. Mauck and C. S. Lynch. Piezoelectric hydraulic pump. In *Proceedings of the SPIE*, volume 3668, pages 844–852, 1999.

[66] L. D. Mauck, J. Menchaca, and C. S. Lynch. Piezoelectric hydraulic pump development. In *Proceedings of the SPIE*, volume 3985, pages 729–739, 2000.

[67] L. D. Mauck and C. S. Lynch. Piezoelectric hydraulic pump development. *Journal of Intelligent Material Systems and Structures*, 11(10):758–764, 2000.

[68] K. Nasser, D. J. Leo, and H. H. Cudney. Compact piezohydraulic actuation system. In *Proceedings of the SPIE*, volume 3991, pages 312–322, 2000.

[69] H. Tan, W. Hurst, and D. Leo. Performance modeling of a piezohydraulic actuation system with active valves. *Smart Materials and Structures*, 14(1):91–110, 2005.

[70] J. Sirohi. *Piezoelectric Hydraulic Hybrid Actuator for a Potential Smart Rotor Application*. PhD thesis, Department of Aerospace Engineering, University of Maryland, College Park, MD, 2002.

[71] J. Sirohi and I. Chopra. Development of a compact piezoelectric-hydraulic hybrid actuator. In *Proceedings of the SPIE*, volume 4327, pages 401–412, 2001.

[72] J. Sirohi and I. Chopra. Design and development of a high pumping frequency piezoelectric-hydraulic hybrid actuator. *Journal of Intelligent Material Systems and Structures*, 14(3):135–147, 2003.

[73] J. A. Ellison, J. Sirohi, and I. Chopra. Design and testing of a bidirectional magnetostrictive-hydraulic hybrid actuator. In *Proceedings of the SPIE*, volume 5390, pages 483–494, San Diego, CA, 2004.

[74] J. Ellison. Investigation of active materials as driving elements in a hydraulic-hybrid actuator. Master's thesis, University of Maryland, College Park, MD, 2004.

[75] S. John, J. Sirohi, and N. M. Wereley. Comparison of piezoelectric, magnetostrictive and electrostrictive hybrid hydraulic actuators. In *Proceedings of the ASME International Mechanical Engineering Congress and Exposition*, Chicago, IL, Nov 2006.

[76] S. John, J. Sirohi, G. Wang, and N. M. Wereley. Comparison of piezoelectric, magnetostrictive, and electrostrictive hybrid hydraulic actuators. *Journal of Intelligent Material Systems and Structures*, 18(10):1035–1048, 2007.

[77] D. G. Lee, S. W. Or, and G. P. Carman. Design of a piezoelectric-hydraulic pump with active valves. *Journal of Intelligent Material Systems and Structures*, 15(2):107–115, 2004.

[78] R. M. Tieck, G. P. Carman, Y. Lin, and C. O'Neill. Characterization of a piezohydraulic actuator. In *Proceedings of the SPIE*, volume 5764, pages 671–679, May 2005.

[79] A. Ullmann and I. Fono. The piezoelectric valve-less pump - improved dynamic model. *Journal of Microelectromechanical Systems*, 11(6):655–664, 2002.

[80] E. G. Chapman, S. L. Herdic, C. A. Keller, and C. S. Lynch. Development of miniaturized piezo-hydraulic pumps. In *Proceedings of the SPIE*, volume 5762, San Diego, CA, May 2005.

[81] J.-H. Yoo, J. Sirohi, N. M. Wereley, and I. Chopra. A magnetorheological hydraulic actuator driven by a piezopump. In *Proceedings of the SPIE*, volume 5056, pages 444–456, San Diego, CA, 2003.

[82] J.-H. Yoo and N. M. Wereley. Performance of a magnetorheological hydraulic power actuation system. *Journal of Intelligent Material Systems and Structures*, 15(11):847–858, 2004.

[83] J.-H. Yoo, J. Sirohi, and N. M. Wereley. A magnetorheological piezohydraulic actuator. *Journal of Intelligent Material Systems and Structures*, 16(11–12):945–953, 2005.

[84] S. John. *Development of a Magnetorheological Fluid Based Hybrid Actuator*. PhD thesis, Department of Aerospace Engineering, University of Maryland, College Park, MD, 2007.

[85] S. John, J. H. Yoo, and N. M. Wereley. A magnetorheological actuation system - Part I: Testing. In *Proceedings of the ASME IDETC*, Las Vegas, NV, September 2007.

[86] S. John, A. Chaudhuri, and N. M. Wereley. A magnetorheological actuation system: Test and model. *Smart Materials and Structures*, 17(2), 2008.

[87] D. T. Nosse and M. J. Dapino. Magnetorheological valve for hybrid electrohydrostatic actuation. *Journal of Intelligent Material Systems and Structures*, 18(11):1121–1136, 2007.

[88] J.-H. Yoo and N. M. Wereley. Design of a high-efficiency magnetorheological valve. *Journal of Intelligent Material Systems and Structures*, 13(10):679–685, 2002.

[89] K. Bridger, J. M. Sewell, A. V. Cooke, J. L. Lutian, D. Kohlhafer, G. E. Small, and P. M. Kuhn. High pressure magnetostrictive pump development: A comparison of prototype and modeled performance. In *Proceedings of the SPIE*, volume 5388, pages 246–257, 2004.

[90] E. Anderson, J. Lindler, and M. Regelbrugge. Smart material actuator with long stroke and high power output. In *43rd AIAA/ASME/ASCE/AHS/ASC Structures, Structural Dynamics, and Materials Conference*, Denver, CO, April 2002.

[91] J. E. Lindler, E. H. Anderson, and M. E. Regelbrugge. Design and testing of piezoelectric-hydraulic actuators. In *Proceedings of the SPIE*, volume 5054, pages 96–107, San Diego, CA, 2003.

[92] R. Sneed, R. R. Smith, M. F. Cash, G. L. Bales, and E. H. Anderson. Development of smart material - hydraulic pumps and actuators. In *Proceedings of ASME International Mechanical Engineering Congress and Exposition*, Chicago, IL, Nov 5-10 2006.

[93] R. Sneed, R. R. Smith, M. F. Cash, and E. H. Anderson. Smart-material based hydraulic pump system for actuation of a morphing wing. In *15th AIAA/ASME/AHS Adaptive Structures Conference*, Honululu, Hawaii, April 2007.

[94] Kinetic Ceramics Inc. Piezoelectric fluid pumps. http://www.kineticceramics.com/piez_fluid.html.

[95] J. B. Beckman and M. J. Blickstein. Apparatus and method for piezoelectric pump. *US Patent Specification 4,449,893*, 1984.

[96] J. B. Beckman and M. J. Blickstein. Piezoelectric pump with internal load sensor. *US Patent Specification 4,519,751*, 1985.

[97] G. W. Culp and V. Nuys. Apparatus and method for piezoelectric pump. *US Patent Specification 5,192,197*, 1993.

[98] R. F. Cusack. Magnetostrictive pump with hydraulic cylinder. *US Patent Specification 4,726,741*, 1988.

[99] F. E. Sager and C. J. Matice. Piezoelectric pumps. *US Patent Specification 5,798,600*, 1998.

[100] K. Ogawa, Y. Yoshida, M. Nishizawa, N. Kamehara, A. Yano, A. Miyaki, M. Ono, Y. Numata, K. Kurihara, and K. Watanabe. Piezoelectric pumps. *US Patent Specification 5,798,600*, 1999.

[101] R. P. Bishop, B. R. Face, S. A. Face, S. E. Clark, and N. S. Rose. Piezoelectrically actuated piston pump. *US Patent Specification 6,071,088*, 2000.

[102] K. Bridger, A. V. Cooke, F. J. Crowne, J. J. Lutian, J. M. Sewell, and G. L. Small III. Compact hybrid actuator. *US Patent Specification 6,751,954*, 2004.

[103] V. Giurgiutiu, C. A. Rogers, and Z. Chaudhry. Energy-based comparison of solid-state induced-strain actuators. *Journal of Intelligent Material Systems and Structures*, 7(1):4–14, 1996.

[104] V. Giurgiutiu and C. A. Rogers. Dynamic power and energy capabilities of commercially-available electro-active induced-strain actuators. *Journal of Intelligent Material Systems and Structures*, 7(6):656–667, 1996.

[105] C. M. Friend. Smart materials: The emerging technology. *Materials World*, 4(1):16–18, 1996.

[106] C. M. Friend. Smart materials and structure - The emerging technology. *Interdisciplinary Science Reviews*, 21(3):195–198, 1996.

[107] J. Atulasimha. *Characterization and Modeling of the Magnetomechanical Behavior of Iron-Gallium Alloys*. PhD thesis, Department of Aerospace Engineering, University of Maryland, College Park, MD, 2006.

[108] S. Ashley. Magnetostrictive actuators. *Mechanical Engineering*, 120(6):68–70, 1998.

[109] W. D. Armstrong. Magnetization and magnetostriction processes in $Tb_{(0.27-0.30)}Dy_{(0.73-0.70)}Fe_{(1.9-2.0)}$. *Journal of Applied Physics*, 81(5):2321–2326, 1997.

[110] A. E. Clark. Magnetostrictive transducers. *US Patent Specification 4,158,368*, 1979.

[111] A. E. Clark, J. P. Teter, M. Wun-Fogle, M. Moffett, and J. Lindberg. Magnetomechanical coupling in bridgman-grown $Tb_{0.3}Dy_{0.7}Fe_{1.9}$ at high drive levels. *Journal of Applied Physics*, 67(9):5007–5009, 1990.

[112] A. E. Clark (Editor E. P. Wohlfarth). *Ferromagnetic Materials*, volume 1, chapter 7: Magnetostrictive Rare Earth-Fe_2 Compounds. North-Holland Publishing Company, 1980.

[113] H. T. Savage, A. E. Clark, and O. D. McMasters. Rare earth-iron magnetostrictive materials and devices using these materials. *US Patent Specification 4,308,474*, 1981.

[114] J. G. Webster, editor. *Wiley Encyclopedia of Electrical and Electronics Engineering*, chapter Magnetostrictive Devices, pages 278–305. John Wiley & Sons Inc., 1999.

[115] M. Goodfriend. High-strain magnetostrictive alloy for transducers and actuators. *Journal of the Minerals Metals and Materials Society*, 42(7):49–49, 1990.

[116] M.J. Goodfriend and K.M. Shoop. Adaptive characteristics of the magnetostrictive alloy, Terfenol-D, for active vibration control. *Journal of Intelligent Material Systems and Structures*, 3(2):245–254, 1992.

[117] A. B. Flatau, D. H. Hall, and J. M. Schlesselman. Magnetostrictive vibration control systems. *Journal of Intelligent Material Systems and Structures*, 4(4):560–565, 1993.

[118] W. S. Oates and R. C. Smith. Nonlinear optimal control techniques for vibration attenuation using magnetostrictive actuators. *Journal of Intelligent Material Systems and Structures*, 19(2):193–209, 2008.

[119] Z. Qingxin, W. Fengxiang, and W. Xinjie. A novel magnetostrictive linear motor and control system. In *6th International Conference on Electrical Machines and Systems*, volume 1, pages 180–182, November 2003.

[120] Z. Qingxin, W. Fengxiang, W. Xinjie, and L. Wenjunand J. Lusheng. A novel inchworm type linear magnetostrictive motor. In *4th International Power Electronics and Motion Control Conference*, volume 2, pages 557–559, August 2004.

[121] J. L. Butler and S. J. Closek. Rare earth iron octagonal transducer. *Journal of the Acoustical Society of America*, 67(5):1809–1811, 1980.

[122] Y. Murata and H. Yamada. Magnetostrictive brake. *US Patent Specification 5,826,683*, 1998.

[123] Y. Naerheim. Magnetostrictive brake actuation mechanism. *US Patent Specification 6,170,921*, 2001.

[124] W. Wang and I. Busch-Vishniac. A high precision micropositioner based on magnetostriction principle. *Review of Scientific Instruments*, 63(1):249–254, 1992.

[125] B. T. Yang, M. Bonis, H. Tao, C. Prelle, and F. Lamarque. A magnetostrictive mini actuator for long-stroke positioning with nanometer resolution. *Journal of Micromechanics ad Microengineering*, 16(7):1227–1232, 2006.

[126] R. G. Deschamps. Magnetostrictive rod filters. *US Patent Specification 4,257,022*, 1981.

[127] F. Claeyssen, N. Lhermet, and R. L. Letty. High power magnetostrictive Tonpilz transducers. In *Proceedings of the Institute of Acoustics*, volume 17, pages 1193–1204, 1995.

[128] F. T. Calkins, A. B. Flatau, and M. J. Dapino. Overview of magnetostrictive sensor technology. *Journal of Intelligent Material Systems and Structures*, 18(10):1057–1066, 2007.

[129] K. B. Hathaway and A. E. Clark. Magnetostrictive materials. *MRS Bulletin*, 18(4):34–41, 1993.

[130] J. Bomba and J. Kaleta. Giant Magnetostrictive Materials (GMM): facilitate of sensor and actuator constructions. In *AMAS Workshop on Smart Materials and Structures*, pages 337–342, September 2003.

[131] L. Kvarnsjö and G. Engdahl. Examination of eddy current influence on the behavior of a giant magnetostrictive functional unit. *Journal of Applied Physics*, 67(9):5010–5012, 1990.

[132] L. Kvarnsjö and G. Engdahl. Examination of the interaction between eddy currents and magnetoelasticity in Terfenol-D. *Journal of Applied Physics*, 69(8):5783–5785, 1991.

[133] J. L. Butler. *Application Manual for the Design of ETREMA Terfenol-D Magnetostrictive Transducers*. Etrema Products, Inc., Ames, IA 50010, USA, 1988.

[134] F. Stillesjo, G. Engdahl, and A. Bergqvist. A design technique for magnetostrictive actuators with laminated active material. *IEEE Transactions on Magnetics*, 34(4):2141–2143, 1998.

[135] IEEE. IEEE standard on magnetostrictive materials: Piezomagnetic nomenclature. Technical Report IEEE Std 319-1990 (Revision of IEEE Std 319-1971), The Institute of Electrical and Electronics Engineers, Inc., 345 East 47th Street, New Yrk, NY 10017, USA, 1990.

[136] G. P. Carman and M. Mitrovic. Nonlinear constitutive relations for magnetostrictive materials with applications to 1-D problems. *Journal of Intelligent Material Systems and Structures*, 6(5):673–683, 1995.

[137] M. J. Dapino, F. T. Calkins, A. B. Flatau, and D. L. Hall. Measured Terfenol-D material properties under varied applied magnetic field levels. In *Proceedings of the SPIE*, volume 2717, pages 697–708, 1996.

[138] M. J. Dapino, A. B. Flatau, and F. T. Calkins. Statistical analysis of Terfenol-D material properties. In *Proceedings of the SPIE*, volume 3041, pages 256–267, San Diego, CA, 1997.

[139] M. J. Dapino, F. T. Calkins, and A. B. Flatau. Identification and analysis of fundamental issues in Terfenol-D transducer modeling. In *Proceedings of the SPIE*, volume 3329, pages 185–197, 1998.

[140] Y. Wan, D. Fang, A. K. Soh, and K. C. Hwang. Experimental and theoretical study of the nonlinear response of a giant magnetostrictive rod. *Acta Mechanica Sinica*, 19(4):324–329, 2003.

[141] Etrema Products Inc. Terfenol-D datasheet. http://www.etrema-usa.com/documents/Terfenol.pdf.

[142] F. T. Calkins, M. J. Dapino, and A. B. Flatau. Effect of prestress on the dynamic performance of a Terfenol-D transducer. In *Proceedings of the SPIE*, volume 3041, pages 293–304, San Diego, CA, 1997.

[143] L. E. Faidley, B. J. Lund, A. B. Flatau, and F. T. Calkins. Terfenol-D elastomagnetic properties under varied operating conditions using hysterisis loop analysis. In *Proceedings of the SPIE*, volume 3329, pages 856–865, 1998.

[144] A. E. Clark and H. T. Savage. Magnetostriction of rare earth-Fe_2 compunds under compressive stress. *Journal of Magnetism and Magnetic Materials*, 31–34(Feb):849–851, 1983.

[145] A. E. Clark, M. L. Spano, and H. T. Savage. Effect of stress on the magnetostriction and magnetization of Rare Earth-$Fe_{1.95}$ alloys. *IEEE Transactions on Magnetics*, 19(5):1964–1966, 1983.

[146] K. Uchino, S. Nomura, L. E. Cross, S. J. Jang, and R. E. Newnham. Electrostrictive effect in lead magnesium niobate single crystals. *Journal of Applied Physics*, 51(2):1142–1145, 1980.

[147] C. L. Hom and N. Shankar. A fully coupled constitutive model for electrostrictive ceramic models. *Journal of Intelligent Material Systems and Structures*, 5(6):795–801, 1994.

[148] H. Cao and A. G. Evans. Nonlinear deformation of ferroelectric ceramics. *Journal of the American Ceramic Society*, 76(4):890–896, 1993.

[149] D. Viehland, L. Ewart, J. Powers, and J.-F. Li. Stress dependence of the electromechanical properties of 001-oriented $Pb(Mg_{1/3}Nb_{2/3})O_3 - -PbTiO_3$ crystals: Performance advantages and limitations. *Journal of Applied Physics*, 90(5):2479–2483, 2001.

[150] D. Viehland, J.-F. Li, E. McLaughlin, J. Powers, R. Janus, and H. Robinson. Effect of uniaxial stress on the large-signal electromechanical properties of electrostrictive and piezoelectric lead magnesium niobate lead titanate ceramics. *Journal of Applied Physics*, 95(4):1969–1972, 2004.

[151] K. G. Webber, R. Zuo, and C. S. Lynch. Ceramic and single-crystal (1 – x)PMN–xPT constitutive behavior under combined stress and electric field loading. *Acta Materialia*, 56(6):1219–1227, 2008.

[152] S. E. Park and W. Hackenberger. High performance single crystal piezoelectrics: Applications and issues. *Current Opinion in Solid State and Materials Science*, 6(1):11–18, 2002.

[153] T. Liu and C. S. Lynch. Domain engineered relaxor ferroelectric single crystals. *Continuum Mechanics and Thermodynamics*, 18(1–2):119–135, 2006.

[154] E. A. McLaughlin, T. Liu, and C. S. Lynch. Relaxor ferroelectric PMN-32%PT crystals under stress, electric field and temperature loading: I-32-mode measurements. *Acta Materialia*, 52(13):3849–3857, 2004.

[155] E. A. McLaughlin, T. Liu, and C. S. Lynch. Relaxor ferroelectric PMN-32%PT crystals under stress, electric field and temperature loading: Ii-33-mode measurements. *Acta Materialia*, 53(14):4001–4008, 2005.

[156] A. Hall, M. Allahverdi, and E. K. Akdogan. Development and electromechanical properties of multimaterial piezoelectric and electrostrictive PMN-PT monomorph actuators. *Journal of Electroceramics*, 15(2):143–150, 2005.

[157] A. Amin. Electromechanical properties of high coupling single crystals funder large electric drive and uniaxial compression. *IEEE Transactions on Ultrasonics, Ferroelectrics, and Frequency Control*, 52(10):1632–1637, 2005.

[158] IEEE. IEEE standard on piezoelectricity. Technical Report ANSI/IEEE Std 176-1987, The Institute of Electrical and Electronics Engineers, Inc., 345 East 47th Street, New Yrk, NY 10017, USA, 1987.

[159] IEEE. IEEE standard on magnetostrictive materials: Piezomagnetic nomenclature. Technical report, The Institute of Electrical and Electronics Engineers Inc., 345 East 47 Street, New York, NY 10017, 1971.

[160] G. Engdahl and L. Svensson. Simulation of the magnetostrictive performance of Terfenol-D in mechanical devices. *Journal of Applied Physics*, 63(8):3924–3926, 1988.

[161] L. Kvarnsjö and G. Engdahl. Nonlinear 2-D transient modeling of Terfenol-D rods. *IEEE Transactions on Magnetics*, 27(6):5349–535, 1991.

[162] X. J. Zheng and X. E. Liu. A nonlinear constitutive model for Terfenol-D rods. *Journal of Applied Physics*, 97(5), 2005.

[163] J. Zheng, S. Cao, and H. Wang. Modeling of magnetomechanical effect behaviors in a giant magnetostrictive device under compressive stress. *Sensors and Actuators A: Physical*, 143(2):204–214, 2008.

[164] R. C. Smith. Modeling techniques for magnetostrictive actuators. In *Proceedings of the SPIE*, volume 3041, pages 243–253, 1997.

[165] M. J. Dapino. *Nonlinear and Hysteretic Magnetomechanical Model for Magnetostrictive Transducers*. PhD thesis, Department of Aerospace Engineering and Engineering MechanicsEngineering Mechanics, Iowa State University, Ames, IA, 1999.

[166] D. C. Jiles. Theory of the magnetomechanical effect. *Journal of Physics D: Applied Physics*, 28(8):1537–1546, 1995.

[167] R. C. Smith. A nonlinear physics-based optimal control method for magnetostrictive actuators. Technical Report NASA/CR-1998-206905, ICASE Report No. 98-4, North Carolina State University, January 1998.

[168] R. Venkataraman. *Modeling and adaptive control of magnetostrictive actuators*. PhD thesis, University of Maryland, College Park, 1999.

[169] D. C. Jiles and D. L. Atherton. Theory of ferromagnetic hysteresis. *Journal of Magnetism and Magnetic Materials*, 61(1–2):48–60, 1986.

[170] F. T. Calkins, R. C. Smith, and A. B. Flatau. Energy-based hysteresis model for magnetostrictive transducers. *IEEE Transactions on Magnetics*, 36(2):429–439, 2000.

[171] W. Huang, B. Wang, S. Cao, Y. Sun, L. Weng, and H. Chen. Dynamic strain model with eddy current effects for giant magnetostrictive transducer. *IEEE Transactions on Magnetics*, 43(4):1381–1384, 2007.

[172] X. Tan and J. S. Baras. Modeling and control of hysteresis in magnetostrictive actuators. *Automatica*, 40(9):1469–1480, 2004.

[173] F. T. Calkins, R. C. Smith, and A. B. Flatau. An energy-based hysteresis model for magnetostrictive transducers. Technical Report NASACR-97-206246, ICASE-97-60, Langley Research Center, NASA, Hampton, VA, November 1997.

[174] M. J. Dapino, R. C. Smith, L. E. Faidley, and A. B. Flatau. A coupled structural-magnetic strain and stress model for magnetostrictive transducers. *Journal of Intelligent Material Systems and Structures*, 11(2):135–152, 2000.

[175] M. J. Dapino, R. C. Smith, F. T. Calkins, and A. B. Flatau. A coupled magnetomechanical model for magnetostrictive transducers and its application to Villari-effect sensors. *Journal of Intelligent Material Systems and Structures*, 13(11):737–747, 2002.

[176] M. Goldfarb and N. Celanovic. Modeling piezoelectric stack actuators for control of micromanipulation. *IEEE Control Systems*, 17(3):69–79, 1997.

[177] M. Goldfarb and N. Celanovic. A lumped parameter electromechanical model for describing the nonlinear behavior of piezoelectric actuators. *ASME Journal of Dynamic Systems, Measurement and Control*, 119(3):478–485, 1997.

[178] J. C. Piquette and S. E. Forsythe. A nonlinear material model of lead magnesium niobate (PMN). *Journal of the Acoustical Society of America*, 101(1):289–296, 1997.

[179] C. L. Hom, S. M. Pilgrim, N. Shankar, K. Bridger, M. Massuda, and S. R. Winzer. Calculation of quasi-static electromechanical coupling coefficients for electrostrictive ceramic materials. *IEEE Transactions on Ultrasonics, Ferroelectrics, and Frequency Control*, 41(4):542–551, 1994.

[180] S. M. Pilgrim, M. Massuda, J. D. Prodey, and A. P. Ritter. Electromechanical properties of some $Pb(Mg_{1/3}Nb_{2/3})O_3 - PbTiO_3 - (Ba, Sr)TiO_3$ ceramics: 1. *Journal of the American Ceramic Society*, 75(7):1964–1969, 1992.

[181] C. L. Hom and N. Shankar. Modeling the dynamic behavior of electrostrictive actuators. In *Proceedings of the SPIE*, volume 3041, pages 268–280, San Diego, CA, June 1997.

[182] B. Deng. Dynamic behavior of a ferroelectric actuator. *Mathematics and Mechanics of Solids*, 4(1):89–107, 1999.

[183] J.-C. Debus, B. Dubus, and J. Coutte. Finite element modeling of lead magnesium niobate electrostrictive materials: Static analysis. *Journal of the Acoustical Society of America*, 103(6):3336–3343, 1998.

[184] J. Coutte, J.-C. Debus, B. Dubus, and R. Bossut. Finite-element modeling of lead magnesium niobate electrostrictive materials: Dynamic analysis. *Journal of the Acoustical Society of America*, 109(4):1403–1411, 2001.

[185] V. Giurgiutiu, C. A. Rogers, and Z. Chaudhry. Design of displacement-amplified induced-strain actuators for maximum energy output. *Journal of Mechanical Design*, 119(4):511–517, 1997.

[186] D. J. Leo. Energy analysis of piezoelectric-actuated structures driven by linear amplifiers. *Journal of Intelligent Material Systems and Structures*, 10(1):36–45, 1999.

[187] D. E. Heverly II, K. W. Wang, and E. C. Smith. Dual-stack piezoelectric device with bidirectional actuation and improved performance. *Journal of Intelligent Material Systems and Structures*, 15(7):565–574, 1995.

[188] C. Liang, F. P. Sun, and C. A. Rogers. Electro-mechanical impedance modeling of active material systems. *Smart Materials and Structures*, 5(2):171–186, 1996.

[189] C. Liang, F. P. Sun, and C. A. Rogers. An impedance method for dynamic analysis of active material systems. *Journal of Intelligent Material Systems and Structures*, 8(4):323–334, 1997.

[190] C. Liang and C. A. Rogers. Transient electro-mechanics of piezoelectric actuator-driven active mechanical systems. *Journal of Intelligent Material Systems and Structures*, 8(4):374–379, 1997.

[191] V. Giurgiutiu and R. Pomirleanu. Modeling and characterization of piezoelectric and magnetostrictive induced strain actuators. In *Proceedings of the SPIE*, volume 4327, pages 610–619, August 2001.

[192] C. Cadou and B. Zhang. Performance modeling of a piezo-hydraulic actuator. *Journal of Intelligent Material Systems and Structures*, 14(3):149–160, 2003.

[193] P. Szymanski. Some exact solutions of the hydrodynamic equations of a viscous fluid in the case of a cylindrical tube. *Journal of Mathematics Pures Appl.*, 11(9):67, 1932.

[194] S. Uchida. The pulsating viscous flow superposed on the steady laminar motion of incompressible fluids in a circular pipe. *Zeitschrift für Angewandte Mathematik und Physik*, 7(5):403–422, 1956.

[195] D. Das and J. H. Arakeri. Unsteady laminar duct flow with a given volume flow rate variation. *Journal of Applied Physics*, 67(2):274–281, 2000.

[196] P. Tang, A. B. Palazzolo, A. F. Kascak, and G. Montague. Electromechanical modeling of hybrid piezohydraulic actuator system for active vibration control. *ASME Journal of Dynamic Systems, Measurement and Control*, 119(1):10–18, 1997.

[197] W. S. Oates and C. S. Lynch. Piezohydraulic hydraulic pump system dynamic model. *Journal of Intelligent Material Systems and Structures*, 12(11):737–744, 2001.

[198] A. Ullmann, I. Fono, and Y. Taitel. The piezoelectric valve-less pump - dynamic model. *ASME Journal of Fluids Engineering*, 123(1):92–98, 2001.

[199] K. Nasser and D. J. Leo. Efficiency of frequency-rectified piezohydraulic and piezopneumatic actuation. *Journal of Intelligent Material Systems and Structures*, 11(10):798–814, 2000.

[200] J. Sirohi, C. Cadou, and I. Chopra. Frequency domain modeling of a piezohydraulic actuator. In *44th AIAA/ASME/ASCE/AHS/ASC Structures, Structural Dynamics and Materials Conference*, Norfolk, VA, April 2003.

[201] J. Sirohi, C. Cadou, and I. Chopra. Investigation of the dynamic characteristics of a piezohydraulic actuator. *Journal of Intelligent Material Systems and Structures*, 16(6):481–492, 2005.

[202] M. J. Rupinsky and M. J. Dapino. Smart material electrohydrostatic actuator for intelligent transportation systems. In *Proceedings of the ASME International Mechanical Engineering Congress and Exposition*, Chicago, IL, Nov 2006.

[203] K. Nasser. Development and analysis of the lumped parameter model of a piezohydraulic actuator. Master's thesis, Virginia Polytechnic Institute and State University, 2000.

[204] K. Nasser, N. Vujic, D. J. Leo, and H. H. Cudney. Modeling and testing of a piezohydraulic actuation system. In *Proceedings of the SPIE*, volume 4327, pages 354–365, August 2001.

[205] M. E. Regelbrugge, J. Lindler, and E. H. Anderson. Design model for piezohydraulic actuators. In *44th AIAA/ASME/ASCE/AHS/ASC Structures, Structural Dynamics and Materials Conference*, volume 3, pages 2163–2171, Norfolk, VA, April 2003.

[206] H. Tan. Performance modeling and efficiency analysis for a piezoelectric pump with active valves. Master's thesis, Virginia Polytechnic Institute and State University, Blacksburg, VA, 2002.

[207] S. John, C. Cadou, J.-H. Yoo, and N. M. Wereley. Application of CFD in the design and analysis of a piezoelectric hydraulic pump. *Journal of Intelligent Material Systems and Structures*, 17(11):967–979, 2006.

[208] A. Chaudhuri, J.-H. Yoo, N. M. Wereley, and N. Nerssesian. Scaling-up issues with a magnetostrictive hydraulic pump. In *Proceedings of the ASME International Mechanical Engineering Congress and Exposition*, Chicago, IL, Nov 2006.

[209] A. Chaudhuri, J.-H. Yoo, and N. M. Wereley. Development of a hybrid magnetostrictive hydraulic actuator - Part I: Unidirectional tests. *submitted*, 2008.

[210] M. J. Dapino. On magnetostrictive materials and their use in adaptive structures. *Structural Engineering and Mechanics*, 17(3–4):303–329, 2004.

[211] A. Chaudhuri and N. M. Wereley. Dynamic model of a hybrid hydraulic actuator utilizing different smart materials. In *Proceedings of the ASME International Mechanical Engineering Congress and Exposition*, Seattle, WA, Nov 2007.

[212] M. B. Moffett, A. E. Clark, M. Wun-Fogle, J. Lindberg, J. P. Teter, and E. A. McLaughlin. Characterization of Terfenol-D for magnetostrictive transducers. *Journal of the Acoustical Society of America*, 89(3):1448–1455, 1991.

[213] X. Zhao, G. Wu, J. Wang, K. Jia, and W. Zhan. Stress dependence of the magnetostrictions and strains in ¡111¿-oriented single crystals of Terfenol-D. *Journal of Applied Physics*, 79(8):6225–6227, 1996.

[214] L. E. Faidley, M. J. Dapino, and A. B. Flatau. Characterization of a small Terfenol-D transducer in mechanically blocked configuration. In *Proceedings of the SPIE*, volume 4327, pages 521–532, 2001.

[215] S. Chakraboty and G. R. Tomlinson. An initial experimental investigation into the change in magnetic induction of a Terfenol-D rod due to external stress. *Smart Materials and Structures*, 12(5):763–768, 2003.

[216] R. D. Blevins. *Formulas for Natural Frequency and Mode Shape*. Van Nostrand Reinhold Company, New York, 1979.

[217] D. M. Zhang. Magnetic skin effect in silicon-iron core at power frequency. *Journal of Magnetism and Magnetic Materials*, 221(3):414–416, 2000.

[218] O. Bottauscio, M. Chiampi, and L. Rege. Influence of skin effect on magnetic flux distribution in voltage driven devices with laminated cores. *Journal of Magnetism and Magnetic Materials*, 254–255:234–236, 2003.

[219] D. Kendall and A. R. Piercy. The frequency dependence of eddy current losses in Terfenol-D. *Journal of Applied Physics*, 73(10):6174–6176, 1993.

[220] H. Janocha and J. Schafer. Design rules for magnetostrictive actuators. In *ACTUATOR*, 1996.

[221] D. L. Hall and A. B. Flatau. Nonlinearities, harmonics, and trends in dynamic applications of Terfenol-D. In *Proceedings of the SPIE*, volume 1917, pages 929–939, 1993.

[222] M. J. Dapino, R. C. Smith, and A. B. Flatau. A model for the ΔE effect in magnetostrictive transducers. In *Proceedings of the SPIE*, volume 3985, pages 174–185, 2000.

[223] M. J. Dapino, A. B. Flatau, and F. T. Calkins. Statistical analysis of Terfenol-D material properties. *Journal of Intelligent Material Systems and Structures*, 17(7):587–599, 2006.

[224] M. E. H. Benbouzid, G. Reyne, and G. Meunier. Finite element modelling of magnetostrictive devices: Investigations for the design of the magnetic circuit. *IEEE Transactions on Magnetics*, 31(3):1813–1816, 1995.

[225] G. Cunningham, R. J. Kee, and R. G. Kenny. Reed valve modelling in a computational fluid dynamics simulation of the two-stroke engine. *Proceedings of the Institution of Mechanical Engineers – Part D – Journal of Automobile Engineering*, 213(1):37–45, 1999.

[226] D. Karnopp. Computer simulation of stick-slip friction in mechanical dynamic systems. *ASME Journal of Dynamic Systems, Measurement and Control*, 107(1):100–103, 1985.

[227] B. Armstrong-Hélouvry, P. Dupont, and C. C. de Wit. A survey of models, analysis tools and compensation methods for the control of machines with friction. *Automatica*, 30(7):1083–1138, 1994.

[228] C. C. de Wit, H. Olsson, K. J. Astrom, and P. Lischinsky. A new model of control of systems with friction. *IEEE Transactions on Automatic Control*, 40(3):419–425, 1995.

[229] H. Olsson, K. J. Astrom, C. Canudas de Wit, M. Gafvert, and P. Lischinsky. Friction models and friction compensation. *European Journal of Control*, 4(3):176–195, 1998.

[230] A. Chaudhuri, J.-H. Yoo, and N. M. Wereley. Dynamic modeling of a magnetostrictive hydraulic pump. In *Proceedings of the ASME International Mechanical Engineering Congress and Exposition*, Chicago, IL, Nov 2006.

[231] I. Chopra. *Lecture notes for ENAE651:Smart Structures*. University of Maryland, College Park, 2003.

[232] R. A. Kellogg and A. B. Flatau. Blocked-force characteristics of Terfenol-D transducers. *Journal of Intelligent Material Systems and Structures*, 15(2):117–128, 2004.

[233] E. E. Galloni and M. Kohen. Influence of the mass of the spring on its static and dynamic effects. *American Journal of Physics*, 47(12):1076–1078, 1979.

[234] Y. Yamamoto. Spring's effective mass in spring mass system free vibration. *Journal of Sound and Vibration*, 220(3):564–570, 1999.

[235] M. Gurgoze. On the representation of a cantilevered beam carrying a tip mass by an equivalent spring-mass system. *Journal of Sound and Vibration*, 282(1–2):538–542, 2005.

[236] M. Gurgoze. On the eigenfrequencies of a cantilever beam carrying a tip spring-mass system with mass of the helical spring considered. *Journal of Sound and Vibration*, 282(3–5):1221–1230, 2005.

[237] E. J. Berger. Friction modeling for dynamic system simulation. *Applied Mechanics Reviews*, 55(6):535–577, 2002.

[238] P. R. Dahl. A solid friction model. Technical Report TOR-0158(3107-18), The Aerospace Corporation, El Segundo, CA, 1968.

[239] P. R. Dahl. Solid friction damping of mechanical vibrations. *AIAA Journal*, 14(12):1675–1682, 1976.

[240] D. A. Haessig and B. Friedland. On the modeling and simulation of friction. *ASME Journal of Dynamic Systems, Measurement and Control*, 13(3):354–362, 1991.

[241] T. Lai and P. Kay. Breakaway frictions of dynamic O-rings in mechanical seals. *Lubrication Engineering*, 49(5):349–356, 1993.

[242] D. B. Wassink, V. G. Lenss, J. A. Levitt, and K. C. Ludema. Physically based modeling of reciprocating lip seal friction. *Journal of Tribology*, 123(2):404–412, 2001.

[243] F. M. M. Al-Ghathian and M. S. Tarawneh. Friction forces in O-ring sealing. *American Journal of Applied Sciences*, 2(3):626–632, 2005.

[244] S. Andersson, A. Soderberg, and S. Bjorklund. Friction models for sliding dry, boundary and mixed lubricated contacts. *Tribology International*, 40(7):580–587, 2007.

[245] Parker Hannifin Corporation, Cleveland, OH. *Parker O-Ring Handbook*, 2001.

[246] EPM Inc., Stockbridge, GA 30281, USA. *The Seal Man's O-Ring Handbook*, 2004.

[247] L Ravanbod-Shirazi and A. Besancon-Voda. Friction identification using the Karnopp model, applied to an electropneumatic actuator. *Proceedings of the Institution of Mechanical Engineers Part I - Journal of Systems and Control Engineering*, 217(2):123–138, 2003.

[248] R. Morselli. Modelling and simulation of static and Coulomb friction in a class of autonomous systems. *International Journal of Control*, 79(5):508–520, 2006.

[249] C. Richard, M. R. Cutkosky, and K. MacLean. Friction identification for haptic display. In *Proceedings of the ASME International Mechanical Engineering Congress and Exposition*, Nashville, TN, November 1999.

[250] F. M. White. *Fluid Mechanics*. McGraw-Hill Book Company, New York, 1979.

[251] E. O. Doeblin. *System Modeling and Response: Theoretical and Experimental Approaches*. John Wiley & Sons Inc., New York, 1980.

[252] E. B. Wylie and V. L. Streeter. *Fluid Transients*. FEB Press, Ann Arbor, MI, 1983.

[253] F. M. White. *Viscous Fluid Flow*. McGraw-Hill Book Company, NY, 1979.

[254] Z. Wang and S. T. Tan. Coupled analysis of fluid transients and structural dynamic responses of a pipeline system. *Journal of Hydraulic Research*, 35(1):119–131, 1997.

[255] M. S. Ghidaoui. On the fundamental equations of water hammer. *Urban Water Journal*, 1(2):71–83, 2004.

[256] J. Watton. *Fluid Power Systems: Modeling, simulation, analog and microcomputer control*. Prentice Hall, UK, 1989.

[257] N. D. Manring. *Hydraulic Control Systems*. John Wiley & Sons Inc., New York, 2005.

[258] R. Courant, K. Friedrichs, and H. Lewy. On the partial difference equations of mathematical physics. *IBM Journal of Research and Development*, 11(2):215–234, 1967.

[259] F. Fleissner, T. Gaugele, and P. Eberhard. Applications of the discrete element method in mechanical engineering. *Multibody System Dynamics*, 18(1):81–94, 2007.

[260] S. John, A. Chaudhuri, and N. M. Wereley. A magnetorheological actuation system - Part II: Modeling. In *Proceedings of the ASME IDETC*, Las Vegas, NV, September 2007.

[261] R. D. Blevins. *Flow Induced Vibration*. Van Nostrand Reinhold Company, New York, 2nd edition, 1990.

[262] H. E. Merritt. *Hydraulic Control Systems*. John Wiley & Sons Inc., New York, 1967.

[263] The Lee Company, Westbrook, CN. *Technical Hydraulic Handbook*, 2006.

[264] C. Niezrecki, J. K. Schueller, and K. Balasubramanian. Piezoelectric-based fluid bulk modulus sensor. *Journal of Intelligent Material Systems and Structures*, 15(12):893–899, 2004.

[265] N. Nersessian, A. Chaudhuri, S. John, G. Wang, and N. M. Wereley. Blocked force and free displacement characterization of PMN-32% PT stacks. In *Proceedings of the SPIE*, volume 6526, San Diego, CA, 2007.

[266] P. Ronkanen, P. Kallio, M. Vilkko, and H. N. Koivo. Self heating of piezoelectric actuators: Measurement and compensation. In *Proceedings of the 2004 International Symposium on Micro-Nanomechatronics and Human Science*, pages 313–318. IEEE, 2004.

[267] R. Keoschkerjan, M. Harutyunyan, and H. Wurmus. Analysis of self-heating phenomenon of piezoelectric microcomponents actuated harmonically. *Microsystem Technologies*, 9(1–2):75–80, 2002.

[268] S. Bashash and N. Jalili. Underlying memory-dominant nature of hysteresis in piezoelectric materials. *Journal of Applied Physics*, 100(1):014103(1–6), 2006.

[269] L. M. Ewart, E. A. McLaughlin, H. C. Robinson, A. Amin, and J. J. Stace. Mechanical and electromechanical properties of PMN-PT single crystals for naval sonar transducers. In *ISAF 2007, Sixteenth IEEE International Symposium on Applications of Ferroelectrics*, pages 553–556, May 2007.

[270] L. M. Ewart, E. A. McLaughlin, H. C. Robinson, J. J. Stace, and A. Amin. Mechanical and electromechanical properties of PMN-PT single crystals for naval sonar transducers. *IEEE Transactions on Ultrasonics, Ferroelectrics, and Frequency Control*, 54(12):2469–2473, 2007.

[271] Henkel Loctite Americas. Loctite 680: Technical data sheet, 2005.

[272] R. Yimnirun, S. Ananta, A. Ngamjarurojana, and S. Wongsaenmai. Uniaxial stress dependence of ferroelectric properties of xPMN-(1-x)PZT ceramic systems. *Applied Physics A: Materials Science & Processing*, 81(6):1227–1231, 2005.